APPLICATION OF LUMINESCENCE TECHNIQUES TO COASTAL STUDIES AT THE ST. JOSEPH PENINSULA, GULF COUNTY, FLORIDA

APPLICATION OF LUMINESCENCE TECHNIQUES TO COASTAL STUDIES AT THE ST. JOSEPH PENINSULA, GULF COUNTY, FLORIDA

By

Beth M. Forrest, B.Sc.

A Thesis

Submitted to the School of Graduate Studies

In Partial Fulfillment of the Requirements

For the Degree

Master's of Science

McMaster University

Master's of Science (2003) McMaster University
Hamilton, Ontario

TITLE: Application of Luminescence Techniques to Coastal Studies at the St. Joseph Peninsula, Gulf County, Florida

AUTHOR: Beth M. Forrest

SUPERVISOR: Dr. W.J. Rink

NUMBER OF PAGES: ix, 217

ABSTRACT

The main objectives of this study are to use optically stimulated luminescence (OSL) to date quartz samples collected from dune ridges on the St. Joseph Peninsula, to test the feasibility of dating quartz from heavy mineral layers as a solution to the problems associated with the low luminescence signal inherent to young samples and to use the natural residual thermoluminescence (NRTL) signal in littoral zone quartz to study sediment transport in the nearshore zone.

All samples were collected from the St. Joseph Peninsula, part of a barrier island chain that stretches across the northern Gulf of Mexico. Dune ridge samples and offshore samples were collected from various locations along the length of the peninsula.

Frequency histograms, showing the distribution of equivalent doses (D_E's), were plotted for each of the dune ridge samples. Several samples have large D_E's relative to their D_E distributions. There are two ways of obtaining grains with large doses and, therefore, large D_E's. The first is by proximity to other grains that are delivering high doses. The second is by incomplete zeroing. These possibilities are explored.

Based on the geometry of the ridges on the peninsula, the youngest dune ridges should be closest to the gulf side of the peninsula and the oldest ridges should be on the bay side. This is tested by obtaining OSL dates for a series of samples from the north end of the peninsula.

Two samples from storm deposits of a known age were collected. Results show that it is possible to date young samples by using quartz collected from heavy mineral

layers. The high radiation dose delivered to the quartz by the heavy minerals makes it possible to obtain accurate dates on "modern" deposits.

The natural residual thermoluminescence (NRTL) signal of the littoral samples was analysed for trends related to grain size and sample position relative to longshore drift. This study shows that NRTL is a useful tool in studies of sediment transport in the nearshore and can be used as an alternative to other sediment tracing methods.

The results of this study are a significant contribution to both luminescence dating and coastal geology.

ACKNOWLEDGEMENTS

I would first like to thank my supervisor, Dr. W.J. Rink, for his guidance. I would also like to thank Dr. J. Donoghue, from Florida State University, for providing useful information and offering many useful suggestions over the course of this research. Discussions with Tammy Rittenour from the University of Nebraska about collecting samples from dune ridges using vibracoring techniques were very helpful. The suggestions and advice offered by members of the luminescence dating community, too numerous to mention, were also greatly appreciated.

Much of this work would not have been possible without the assistance of others. Ann Harvey and Cyndy Emerich, Park manager and Assistant Park Manager, at the T.H. Stone Memorial St. Joseph Peninsula State Park were patient with our many requests and offered much needed logistical support. The rangers and staff at the state park were also very accommodating and helpful. Thanks are also extended to Tom Watters and the Florida Department of Environmental Protection (FDEP) for providing maps, benchmark locations and other data relevant to this research. The assistance provided by Jenn Etherington in preparing the multitude of littoral samples was appreciated. Karl Keizars' help with the tedious task of editing was also much appreciated.

Finally, I would like to thank my family and friends for their unending support and encouragement.

Financial support was provided by the Natural Sciences and Engineering Research Council of Canada (NSERC) in the form of a postgraduate scholarship.

TABLE OF CONTENTS

LIST OF FIGURES

LIST OF TABLES

CHAPTER 1- INTRODUCTION

1.1 Purpose of Study

The first objective of this study is to use optically stimulated luminescence (OSL) techniques to obtain ages for quartz samples collected from dune ridges on the northern half of the St. Joseph peninsula, within the T.H. Stone Memorial St. Joseph Peninsula State Park. Samples were collected using both trenching and vibracoring techniques. The results of both sampling methods are compared to determine whether the method of sample collection has an effect on the results.

The second objective involves the dating of young deposits. Dating these deposits is often problematic because of the low OSL signal intensity that is characteristic of young samples. There is, however, an exception to this. Quartz that has received a high radiation dose during burial will have a high OSL signal relative to samples of the same age that received lower doses. Samples that have received a high radiation dose include those that are in close proximity to high radioactivity minerals (i.e. heavy minerals). Heavy mineral deposits are common in coastal environments and typically represent high-energy events, such as storms. The second objective of this research is to improve the accuracy of dating modern samples by using these heavy mineral deposits. OSL is used to date samples collected from heavy mineral rich layers of a known age to assess the feasibility of using quartz extracted from heavy mineral rich sands to date young deposits.

The third objective of this research is to use the residual thermoluminescence (TL) signal in littoral zone quartz to monitor the transport of sediment in the nearshore zone.

The natural residual thermoluminescence, or NRTL, is the part of the TL signal that is not easily removed by exposure to sunlight. The magnitude of this residual is variable. It depends on the position of the sample on the beach surface, the type of quartz and the total transport history since the last burial of significant length. This project attempts to use this residual to distinguish between native sands transported from the Gulf of Mexico shoreline and the Apalachicola River Delta and sands obtained from beach nourishment projects and dredging activities along the northwest coast of Florida. An attempt is also made to characterize the relationship between the NRTL signal, grain size and the location of the sample relative to longshore drift.

1.2 Significance of Study

The results of the OSL dating component of this project are applicable to the reconstruction of the evolution of coastal environments. Approximately 50 % of the global population lives within 60 km of the coast (Woodroffe, 2002). Understanding coastal sand transport, the processes that shape the shoreline and changes that occur along the coast is important. With so much of the world's population living along the shoreline, it is important to be able to manage coastal resources.

This study is the first to use quartz grains extracted from heavy mineral lamina to date young samples using single aliquot OSL techniques. The lower limit for OSL dating is approximately 50 years (Berger, 1995). However, recent studies are promising (i.e. Ballarini et al. (2003)), as they have obtained much younger ages with low associated errors. There are many problems associated with dating "modern" samples. The results of this study are a significant step towards lowering the minimum age obtainable by OSL.

This high precision dating of young samples used in conjunction with the standard OSL dating of dune ridges is important in the reconstruction of the most recent part of the study area and will be an asset in future studies.

The most common methods of measuring longshore sediment transport are sediment tracers (Komar and Inman, 1970, Duane and James, 1980) and impoundment (Johnson, 1957, Bruno and Goble, 1977). Sediment characteristics have also been used to trace sediment transport and to distinguish between native and nourishment sands (Reed and Wells, 2000). Currently, remote sensing techniques are being applied to sediment transport studies in various locations. Kunte et al. (2003) used remote sensing techniques to study sediment transport in the Gulf of Kutch. Few studies have examined the possibility of using NRTL in the bedload as an alternative to other sediment tracing methods. This is the first study to analyse NRTL on a fine resolution. It is also the first study to analyse the relationship between the residual TL signal, grain size and longshore transport.

1.3 Luminescence Dating

Luminescence techniques can provide ages for deposits not datable by other geochronometric methods (Berger, 1988). Figure 1 outlines the basis of luminescence. At the time of sedimentation, the luminescence signal that was acquired in the past is set to zero. This zeroing is a response to the daylight or sunlight exposure that occurs during erosion and transport. Exposure to light releases electrons from traps and defects in the crystal structure. After deposition, exposure to radiation repopulates the traps (Huntley

and Lian, 1999). This repopulation continues until the sediment is exposed to sunlight during another sedimentation cycle.

Luminescence is explained using the conduction band model (Figure 2). It is based on the accumulation of electrons in atomic lattice sites called defects or traps (Aitken, 1998). These sites are associated with impurities or structural defects in the crystal lattice that were incorporated during crystallization. In some cases, they are associated with radiation damage (Hutt and Raukas, 1995). Ionizing radiation is produced by the decay of radioactive nuclides including ^{40}K, the uranium-series and the thorium-series elements and cosmic ray muons (Aitken, 1998). As this radiation passes through a mineral, it ionizes the mineral's binding electrons and excites them above their ground states. As these electrons return to their ground states, some become trapped in the defects and cannot be removed without an input of energy (Aitken, 1998). If the defect is large enough electrons can be held for long periods of geological time. Over time, defect sites accumulate electrons. These electrons are released from the defects by exposure to light or heat. Not all electron traps have an equal probability of being emptied (Huntley, 1985). Such differences could be a result of attenuation of light while passing through a mineral grain or a result of differences in the physical properties of the traps (Huntley, 1985). The detrapping process produces light. The amount of light emitted is proportional to the number of trapped electrons, which in turn, is related to the time lapsed since the sediment was last exposed to light (Aitken, 1998). If the detrapping mechanism is light, the method is referred to as optically stimulated luminescence (OSL). If heat is used, the method is called thermoluminescence (TL).

OSL was developed in 1985 (Huntley et al., 1985) as a method of determining when sediments were last exposed to sunlight. The method involves exciting the trapped electrons in sediment by shining light on grains isolated from a sample and measuring the amount of light emitted in response. The intensity of the emitted light is a measure of the number of electrons trapped and, thus, the radiation dose accumulated since the last sunlight exposure (Huntley and Lian, 1999). To calculate OSL ages, the paleodose is divided by the annual dose rate. The dose rate is the rate at which energy is absorbed from the incoming flux of radiation (Aitken, 1998). It's three components are environmental beta and cosmic radiation, external and internal beta radiation from K and Rb in the crystal lattice and internal alpha radiation from U and Th embedded in the grains (Mejdahl and Christiansen, 1994). There are also minor contributions to the dose rate from gamma radiation. The dose rate is determined by measuring the radioactivity of the sediment. The paleodose is the amount of radiation received since the traps were last emptied during a bleaching event (Smith et al., 1986). The laboratory equivalent of the paleodose is the equivalent dose (D_E), which is the laboratory dose of radiation that is needed to induce a luminescence signal equal to that acquired by the sample after the most recent bleaching event (Aitken, 1998). The D_E is evaluated using either the additive dose method or the regenerative dose method. For the additive dose method, the aliquots being measured are divided into several groups. One group is used to measure the natural OSL. The remaining groups are given different radiation doses before being measured. Dose is added with each cycle to build a response curve (Folz and Mercier, 1999). Figure 3 summarizes the additive dose method. Each point on the graph represents the average

OSL for a group of aliquots. The equivalent dose is estimated by extrapolating the line to its point of intersection with the dose axis. In the regeneration method, all aliquots are bleached to near zero and then given a laboratory dose. The natural aliquots are not given a radiation dose. The natural OSL is then compared to the OSL resulting from aliquots that received a dose. Figure 4 summarizes this method.

Luminescence dating has several advantages over other dating methods. The age range for OSL is approximately 50 to 800,000 years B.P. (Berger, 1995). For some samples, both quartz and feldspar have sufficient sensitivity to produce ages as young as one year, but currently there are no reliable techniques for doing this (Huntley and Lian, 1999).

Carbon-14 is another commonly used geochronometric technique. It is based on the beta decay of ^{14}C atoms produced in the upper atmosphere (Bard, 1998). This method has numerous disadvantages. It is not possible to measure the ratio between the parent isotope, ^{14}C, and the daughter product, ^{14}N (Bard, 1998). To be able to calculate a true calendar age the initial $^{14}C/^{12}C$ ratio of each sample must be known. A calibration is, therefore, needed. This involves evaluating past variations of atmospheric $^{14}C/^{12}C$. For the Holocene period (the past 10,000 years) it is possible to find fossil pines and oaks and compare ^{14}C levels to tree ring counts (Bard, 1998). Beyond the Holocene, calibration becomes difficult because there are few fossil trees. Other types of records are used to continue the calibration method. These include the use of laminated sediment and corals from tropical islands that can be cross-dated by spectrometric techniques. By combining these techniques, it has been possible to obtain maximum ages of 45,000 years B.P.

However, OSL dating has a wider age range and does not require extensive calibration. Another drawback of radiocarbon dating is that it can only be used to resolve differences on the order of a few hundred years (Stapor et al., 1991). Another advantage of OSL over radiocarbon is that it can be used in areas where quartz is more abundant than organic or shell material.

OSL dating also has many advantages over TL dating. One of the main disadvantages of TL is that the TL signal is only partially reset during light exposure (Berger, 1990). OSL requires less sunlight exposure prior to burial to empty the traps than TL. This means that at deposition the luminescence signal is smaller (Aitken, 1994). Therefore, OSL does not have the large residual signal that TL has. Another advantage is that in OSL, only the light sensitive traps that are easily emptied by sunlight are sampled (Huntley and Lian, 1999). In TL, both light sensitive and non-light sensitive traps are emptied (Aitken, 1994).

The second part of this project focuses on TL. TL is a property of crystals and non-conductive materials, which emit light when heated if they have been previously irradiated (Lalou and Valladas, 1989). The phenomenon of TL was recognized as early as 1663 when Sir Robert Boyle described the emission of light by diamonds when heated (Lalou and Valladas, 1989). In 1930, Urbach, who studied electron traps in crystals, became the first to use TL and to interpret TL glow curves (Lalou and Valladas, 1989). The TL method is applied to events where the TL signal is reduced to a non-zero level (Berger, 1988). This non-zero level, which is also known as the natural residual TL (NRTL), can be used to study coastal processes. UV radiation is filtered by seawater

(Spooner, 1987). Past studies have shown that the TL signal is most effectively depleted by UV light (Spooner, 1987). Therefore, the residual signal is much larger when grains are underwater, and shielded from UV light, than when they are onshore and exposed to the full solar spectrum. Consequently, grains on a beach surface have a more efficient reduction of TL than subaqueous grains (Rink, 1999). Grains sourced from distant locations experience increasing solar radiation exposure with time. Therefore, the residual TL decreases with increasing distance from the sediment source. This property can be applied to the study of sediment transport in the nearshore zone.

1.4 Previous Studies

1.4.1 Optically stimulated luminescence studies

Many different techniques have been used to date coastal deposits. For example, Stapor and Tanner (1973) analysed thirteen sediment samples from coastal deposits from the Apalachicola region and from nearshore sands seaward of pre-holocene barriers using radiocarbon dating. They obtained ages ranging between 22,000 and 40,000 years B.P. A study by Missimer (1973) looked at dune ridges on Sanibel Island, a barrier island located 100 miles south of Tampa, Florida. The island has seven to twelve sets of subparallel ridges, which have been used to estimate the growth rate of the island. The age relationships between the ridge sets were determined using radiocarbon dates obtained from aragonitic mollusc shells. The dates range between 547 and 4,310 years B.P. All ridges have been deposited in the past 4,300 years and it is estimated that it takes 14-18 years for each ridge to fully develop.

As an alternative to these methods, several studies have applied OSL dating to coastal deposits. Wintle et al. (1998) collected fifteen samples of dune sand and three samples from a core taken in the beach face of a sand spit that protrudes into Dingle Bay in southwest Ireland. Feldspar grains were dated using a single aliquot luminescence protocol for infrared stimulated luminescence (IRSL). No ages over 600 years were obtained. The youngest age obtained was 150 years. These ages are consistent with the belief that the majority of dunes in Ireland formed within the last 6,000 years (Carter et al., 1989).

Jungner et al. (2001) collected eight sediment samples from a parabolic dune in Cape Kiwanda, which is a part of a complex of four dunes formed by onshore winter storm winds. Seven samples were collected from exposed paleosols and one sample was collected from the base of the dune. Quartz within the 100-200 μm size fraction was dated using the single aliquot regenerative (SAR) method. The resulting dates cover a period ranging from a few hundred years to 7,000 years. Radiocarbon dates were also obtained for charcoal and wood samples collected at various locations in the dune profile. The OSL and radiocarbon ages fall in the correct stratigraphic order.

Richardson (2001) used IRSL to determine the D_E's of modern sediments from coastal environments in England and Wales. This study focused on the residual IRSL signal. Certain coastal environments have been proven datable by OSL techniques but once the intertidal zone is reached, light exposure at deposition is unreliable and, therefore, the success of OSL is limited. This study used IRSL to analyse the degree of zeroing at deposition.

It is often difficult to obtain reliable chronologies for depositional events in coastal environments, particularly in the case of dune ridges. This is because the sedimentary components dated may not represent the time of deposition. The approaches most commonly taken to date such deposits include the radiocarbon dating of skeletal carbonate sands and the dating of whole shells. Murray-Wallace et al. (2002) used the OSL of quartz sampled from relict beach ridges to evaluate the utility of applying OSL to studies of dune dynamics and coastal progradation rates. It became the first study to examine the potential of using OSL to date Holocene dune ridges. The OSL ages obtained indicated a rapid period of sedimentation (1,600 m within a few hundred years approximately 5,000 years ago) followed by a constant rate of progradation for the past 4,000 years of 0.39 m/yr. Based on these rates and the ages of the dune ridges, it is estimated that the average rate of dune development for the study site is one dune every 80 years.

In a similar study, Ballarini et al. (2003), explored using OSL dating for reconstructing coastal evolution on a timescale of decades to a few hundred years. Samples were collected from an accretionary barrier island in the northern Netherlands. The southwest part of the island is made up of a series of dune ridges. The island is growing in a southwesterly direction as a result of shoals merging with it. The ages of the deposits are known from historical sources. OSL ages of less than 10 years were obtained on the youngest samples. The study showed that the deposits on the island were formed over the last 300 years. This study illustrates the potential of using OSL dating for the high-resolution reconstruction of coastal evolution over the past few centuries.

1.4.2 Thermoluminescence studies

Several studies have attempted to use sediment characteristics to distinguish between nourishment sands and native sands. These include Pabich (1995) who used quartz staining and Foster et al. (1996) who used fluorescent tracers. Reed and Wells (2000) used grain size, shell color and sorting to define the distribution of native and nourishment sands of a renourished beach on the North Carolina coast.

Only two studies have looked at the residual TL signal and its use as a monitor of coastal processes. Rink and Pieper (2001) analysed the residual thermoluminescence in quartz collected from the surface and the subsurface of the beach at the St. Joseph Peninsula State Park. Subsurface samples were collected from within two berm structures that represent a hurricane deposit and a beach ridge produced by wave action during the seven-week period following Hurricane Georges in 1998. A higher residual signal was found in samples from the underwater zone than in those from the beach surface.

In another study, Pieper (2001) and Rink (2003) looked at the variation in the NRTL of quartz. They collected twenty-one underwater sand samples from a 200 km stretch of the Mediterranean Coast of Israel. Previous studies indicated that the sources of the sand along this coast were Nile River outlets at Rashid and Dymat. Sand is transported towards the coast by the littoral and shelf currents of the Nile littoral cell. The southeast portion of the Mediterranean coastline is densely populated. Sediment transport in these areas has been altered as a result of anthropogenic changes like sand quarrying and the erection of industrial and recreational structures. This study attempted

to correlate trends observed in NRTL signals with these human modifications. A series of natural TL curves were obtained, as well as TL curves measured after the administration of a beta dose. A mean value for the NRTL and a standard deviation were obtained for each sample. The resulting NRTL pattern showed a decreasing residual signal intensity with increasing distance from the sediment sources. From Ziqim to Jaffa the signal decreased. It rose sharply at Herzliyya and Shefayim and proceeded to decrease again with increasing distance northward along the coast. The decrease in signal intensity with increasing distance from the sediment source was attributed to successive cycles of subaerial exposure on beach surfaces followed by re-erosion and subaqueous transport in the littoral zone. The sharp peak in intensity seen at Herzliyya suggested the addition of sediment with a high NRTL into the bedload at the harbour at Tel Aviv. Conversely, it could be derived from the erosion of beach cliffs, river sediments, dredge sands or any sediment that has been accumulating a higher TL signal since burial. This study provided the basis for my current project.

CHAPTER 2- LOCATION

Location

The St. Joseph Peninsula is part of a barrier island chain that stretches across the northern Gulf of Mexico (Lamont et al., 1997). Figure 5 shows its location. The peninsula is 24 km in length and 1.4 km wide at its widest point (Rizk, 1991). At Eagle Harbor, its narrowest point, it is only 0.2 km wide (Rizk, 1991). It stretches from St. Joseph Point in the north to Cape San Blas in the south. The peninsula partially encloses St. Joseph Bay, which is the only sizeable body of water along the eastern gulf coast that isn't estuarine in origin or influenced by the influx of freshwater (Stewart and Gorsline, 1962). The bay is 18 km long and 6 km wide, with an area of 119 km^2 (Stewart and Gorsline, 1962). Its mean depth is 6 m. Near the northern end of the peninsula, it has a depth of 12 m (Stewart and Gorsline, 1962). Figure 6 is a bathymetric map of the study area.

The northern two-thirds of the peninsula is owned by the State of Florida while the southern end is federally owned and is part of the Eglin Airforce Base (FDEP, 1998). The land between these areas is privately owned. The T.H. Stone Memorial St. Joseph Peninsula State Park, which is on the northern end of the peninsula, is 14 km long and encompasses an area of approximately 2,516 acres (Benchley and Bense, 2000).

Climate

The climate of the peninsula is classified as humid subtropical. Rainfall averages 1.4 m per year (Stewart and Gorsline, 1962). The driest months are May, October and November (Benchley and Bense, 2000). The vegetation in the area includes scrub oak,

sand pine, lingual pine, palmetto, yaupon holly, sage, rosemary, grasses and sabal pine (Benchley and Bense, 2000).

Barrier Islands

Barrier islands are abundant along the Gulf of Mexico coast. Barrier island nuclei in the gulf were probably initiated by increased wave action resulting from a drop in sea level (Tanner, 1991). Increased wave action leads to the transport of both fine and coarse-grained sediment. These sediments will be deposited as a ridge at the shoreline. A rise in sea level will flood the landward side of the ridge and isolate it, turning it into a barrier island. Most barrier islands are initiated by a drop in sea level but develop during a sea level transgression. Nuclei that have been preserved represent the date of initiation of the barrier island (Tanner, 1991). The sea level history of the Gulf of Mexico has been reconstructed using beach ridges, cheniers, subdeltas and barrier island nuclei. There is evidence for several 1 to 3 m changes in sea level in the last 3,000 to 3,500 years (Tanner, 1991). Along the Florida Panhandle, sea level has risen 0.3 m over the past 125 years (Lamont et al., 1997). The formation and maintenance of barrier islands requires an abundant sand supply (Lamont et al., 1997). Since sea level stabilized 4,000 to 5,000 years ago, there has been little new sand added to the Gulf of Mexico barrier islands (Lamont et al., 1997). In addition to changing sea levels, the formation of Florida's barrier islands is also influenced by offshore geology. The area of continental shelf along which the peninsula lies, borders the entire west coast of Florida and is referred to as the Florida Platform or the West Florida Shelf (Lamont et al., 1997). This platform is divided into two sections; a large, smooth inner shelf and a small, gently sloping outer

shelf. The low relief slopes along the floor of the Gulf of Mexico result in low wave and tidal action (Lamont et al., 1997). Since the continental shelf is flat, most of the Gulf of Mexico is less than 180 m in depth (Lamont et al., 1997). As a result, sea surface circulation is mostly wind driven (Lamont et al., 1997). The area is dominated by "loop currents", which flow clockwise through the gulf and exit through the Florida Straits (Lamont et al., 1997). However, in the Florida Panhandle, the net movement of water is westward. This reversal of current is attributed to seasonal winds and tidal currents (Lamont et al., 1997). Barrier islands are best formed along coasts with small tidal ranges (Lamont et al., 1997). The St. Joseph peninsula experiences diurnal tides with a mean tidal range of 0.35 m (Foster and Cheng, 2001).

Several theories have been proposed to explain the formation of the peninsula. One theory suggests that the peninsula consists of at least two older islands joined where there was once a tidal inlet. It is argued that Eagle Harbor is the remnant of this inlet (Benchley and Bense, 2000). Each of the two islands started as a nucleus in open water and grew in three directions (towards both ends and seaward) (Tanner, 1987). The spit hook from one of these islands is still intact at the eastern side of Eagle Harbor. There are also relict channels between Richardson's Hammock and Cape San Blas. Cape San Blas itself may represent the remains of a former pre-holocene cape or headland (Rizk, 1991). Eventually both islands joined to form the modern peninsula.

Beach Ridges

Many of Florida's barrier islands are covered with beach ridges. These features are linear sand bodies deposited along the beach face in areas characterized by gentle

offshore slopes, low wave energy and an abundant sand supply (Fernald and Purdum, 1992). Since ridges form on the beach face, they indicate the orientation of the coastline and the approximate vertical position of sea level at the time of deposition (Fernald and Purdum, 1992; Donoghue and Tanner, 1992; Tanner, 1988). If beach ridges are covered by mangrove marsh vegetation, there was a sea level rise subsequent to ridge formation (Stapor et al., 1991). Ridges also reflect wave energy. Low ridges are produced by less energetic waves while high ones are produced by energetic waves (Stapor et al., 1991).

Several theories have been proposed to explain dune ridge formation. Shepard (1950) suggests that beach ridges form as a result of aggradation. They develop during neap tides and are pushed landward during spring tides. Doeglas (1955) showed that ridges are moved by both tidal and wind action. Doeglas also suggested that ridges are only built up to a level slightly above normal high tide. Von Drehle (1973) studied beach ridges in and around Port St. Joe, Florida. He suggested that they were coalesced sets of swash built ridges. According to Fernald and Purdum (1992), ridges are constructed by wave run-up in the swash zone. They grow upward and seaward as increasingly more material is deposited (Fernald and Purdum, 1992). A common feature of all models is that beach ridge development is a product of changing rates of sediment supply and water level change.

The sediment sources for beach ridge formation in the Panhandle region of Florida include the littoral transport of sand from the gulf shoreline and the Apalachicola River to the east (Benchley and Bense, 2000). The Chattahoochee and Flint Rivers join to form the Apalachicola River (Fernald and Purdum, 1992). This river is a major drainage

system that extends from the piedmont in Georgia to Alabama and then south to the gulf coast (Stewart and Gorsline, 1962). The Apalachicola River is 32 km east of Cape San Blas. In the past, it was one of the major sources of sand along the Florida Panhandle coast (Lamont et al., 1997). Sands transported by the Apalachicola River are reworked and redistributed by longshore drift and wave action (Lamont et al., 1997). The coarsest sands are dropped offshore, creating shoals (Lamont et al., 1997). Finer sands are carried in the current and deposited along beaches (Lamont et al., 1997). There are few areas in Florida where ridges are being deposited today because there is a shortage of sediment (Fernald and Purdum, 1992). With the development of barrier islands at the mouth of the Apalachicola River (i.e. St. Vincent Island, St. George Island), most of the sediment transported by the river is trapped. Along the northern gulf coast, recent beach sands are similar to Pleistocene sands in grain size and morphology. It is, therefore, likely that the sands in northwest Florida were derived from the reworking of older sediments and that the modern Apalachicola River is not a major sediment source to the beaches in the area (Hsu, 1960).

The surface of the peninsula consists of a series of north-south trending beach ridge and swale complexes. Many of these ridges are over 9 m high. According to Tanner (1988) at the core of these are relict beach ridges and dune systems that are likely associated with the Silver Bluff Sea Level stand near the end of the Pleistocene. At the north end of the peninsula, dunes and swales trend northeast to southwest (Benchley and Bense, 2000). The ridges closest to the mainland (furthest from the sea) are older than those adjacent to the beach (Tanner, 1988). As a result of fluctuating sea level and a

decrease in the abundance of sediment, the beach ridge history doesn't go beyond 3,500 years B.P. along the gulf coast (Tanner, 1991; Donoghue and Tanner, 1992).

Sediment transport and longshore drift

The St. Joseph Peninsula receives sediment from several sources. The Apalachicola River was the primary contributor of clastic sediment to the eastern Gulf of Mexico (Donoghue, 1993) and delivered sediment to the system at a rate greater than the coastal energy was able to handle (Tanner, 1963). The excess load accumulated in barrier islands, spits and shoals (Tanner, 1963). The shoals and barrier islands contain enough sand to account for the total sand load of the river for the last 5,000 years (Tanner, 1963).

The beaches along Florida's gulf coast are classified as low to moderate energy beaches (Gorsline, 1966). The wave conditions between Cape San Blas and Alabama are characterized by 0.3 m wave heights (Gorsline, 1966). Longshore current velocities range from 0.3 to 1.5 m/s (Gorsline, 1966). Net sediment transport in the gulf is to the west (Gorsline, 1966). In the northern Gulf of Mexico Cape San Blas acts as a divide. There are two distinct sedimentation cells to the left and right of it (Gorsline, 1966). The stretch of coast between Dog Island and Cape San Blas contains a minimum of 7 longshore transport cells and the stretch of coast between Cape San Blas and St. Joseph Point has 2 cells (Stone and Stapor, 1996).

Sediment migrates from the south end to the north end of the peninsula. This movement follows the prominent drift direction. Longshore drift can cause long-term changes in barrier islands. Prevailing winds and longshore currents scour the gulf side of the Peninsula and redeposit sediments along its tip, which is constantly growing towards

the north (Benchley and Bense, 2000). This method of deposition results in the movement of barrier islands (Davis, 1997). Barrier islands can also move landward as a result of storm waves overwashing the island and re-depositing sediment on the landward side. If washoever frequently occurs, peat is exposed at the beach surface. Unless more sand is available, the barrier island will be destroyed before it reaches the mainland (Davis, 1997). Most Holocene barrier islands are transgressive as a result of rising sea level. However, barriers that receive large amounts of sediment can build seaward (prograde). Evidence of barrier island transgression, or movement towards the mainland, includes peat, tree stumps and layers of fine-grained organic mud. These features represent a protected back barrier environment, marsh or mangrove swamp (Davis, 1997). With the exception of the mangrove swamps, the south end of the peninsula exhibits these characteristics. Accretion resulting from longshore sediment transport is also a mechanism for barrier island elongation (Aubrey and Gaines, 1982).

Although the St. Joseph Peninsula is a sand spit, its dynamics are similar to those of a barrier island. In the case of the St. Joseph Peninsula, transgression and progradation are occurring at the same time. This happens if sediment that reaches a barrier is not uniformly distributed (Davis, 1997). Most sediment is then trapped at the end of the island receiving the sediment, while the other end experiences a deficit (Davis, 1997). The result is progradation at the end of the island receiving the sediment and transgression at the sediment starved end.

Sedimentology

The beach sands from Apalachicola Bay, Florida to Mobile, Alabama have a fine- to medium-grained texture (Hsu, 1960). Sands west of the Apalachicola River, including the sands of the St. Joseph Peninsula, are well sorted (Hsu, 1960). The sands of the eastern gulf coast are predominantly quartz and contain little feldspar.

The beach sands of the gulf coast are comprised of quartz, heavy minerals and small amounts of feldspar. Heavy mineral sands are detrital particles with a density greater than 2.85 g/cm^3 (Donoghue and Greenfield, 1991). The heavy mineral suites of the Apalachicola river sands are almost exclusively opaque minerals and stable non-opaque minerals like zircon, tourmaline, staurolite and kyanite (Hsu, 1960). Hornblende and garnet are also present in small amounts (Hsu, 1960). Heavy minerals are usually found in high-energy environments where they are sorted by hydrodynamic processes due to the density contrast between these minerals and quartz (Donoghue and Greenfield, 1991). Heavy mineral sands are found to some extent on all beaches but are highly concentrated by reworking and winnowing resulting from waves generated as a result of the combined effect of daily tidal fluctuations, storm wave and wind action (Donoghue and Greenfield, 1991; Eichenholtz et al., 1989). Most heavy mineral concentration occurs during flooding (i.e. storm surges) when the current velocity and winnowing are at a maximum (Faulkner, 1986). Each time a flood occurs heavy minerals that were once scattered with other sediments end up resting on the new channel created by the scouring action of the flood (Faulkner, 1986). Wave action on the beaches winnows out the light minerals and leaves the heavy ones behind (Faulkner, 1986). As each wave retreats it

washes light minerals back towards the ocean. The heavy mineral lag deposits form a linear band that is usually parallel to the shoreline (Faulkner, 1986). Heavy mineral sands are usually concentrated into layers less than 0.1 m thick (Donoghue and Greenfield, 1991).

Heavy mineral sands of the region were likely derived from the southern Appalachians in the upper watershed of the Apalachicola River (Donoghue and Greenfield, 1991). Donoghue and Greenfield (1991) cite strong evidence that heavy mineral sands were transported to the Gulf of Mexico by the Apalachicola River during late quaternary low stands and deposited on the inner shelf of the northeastern Gulf of Mexico. During these low stands, there was increased wave activity. This high energy is needed to transport these high-density grains. Airborne gamma surveys have shown high concentrations of gamma activity (related to the presence of heavy minerals) in the floodplain of the modern river. According to Donoghue and Greenfield (1991), similar deposits were laid down on the inner shelf in the Quaternary period. These sands have been incorporated into barrier islands by storms, wave action and sea level rise (Donoghue and Greenfield, 1991).

Erosion

Most of Florida's barrier islands are eroding. The St. Joseph Peninsula is no exception. The northern 4.5 km of the peninsula has been accreting since the late 1860's, while erosion on the southern end has been increasing (Tanner, 1975). Approximately 370,809 m^3/yr of sand is eroding from the peninsula. 229,366 m^3/yr of this eroded material is transported to the north while the remaining 141,442 m^3/yr is transported to

the south. Figure 7 shows the distribution of the eroded sediment. Between 1875 and 1970, St. Joseph Point has migrated 1.2 km (FDEP, 1998). Despite this accretion, sections of the St. Joseph Peninsula experience the highest erosion rates in the state of Florida. Over the past 107 years, the southern 1.9 km of the peninsula has eroded 792 m at a rate of approximately 7.4 m/year (FDEP, 1998). From 1973 to 1997, the average erosion rate in the south was 9 m/year (FDEP, 1998). North along the peninsula this rate decreases to where the shoreline accretes at St. Joseph Point (FDEP, 1998). From 1973 to 1997, the state park experienced an average shoreline erosion rate of 0.09 m/year (FDEP, 1998). Figure 8 shows the zones of critical erosion along the peninsula.

Since barrier islands occur in regions with small tidal ranges and are dominated by wave action, they are often highly eroded during storms (Lamont et al., 1997). Much of the erosion in Gulf County is attributed to tropical storms and hurricanes (FDEP, 1998). Human impacts have also exacerbated the situation. Increased coastal development and numbers of tourists have contributed to the erosion problem. Both factors have lead to increased traffic along the beach (both vehicle and pedestrian). This has resulted in increased vegetation removal and subsequently a loss of dune stability.

CHAPTER 3- METHODS

3.1 Sample Collection

The dune ridge samples analysed in this study were collected from several locations on the St. Joseph Peninsula. Most samples were collected within the boundaries of the T.H. Stone Memorial St. Joseph Peninsula State Park. Sample locations are shown in Figure 9. Figures 10 to 12 are satellite images of three sample sites. They show the spatial relationship between each site and the gulf shoreline. These images were not available for all sites. Littoral samples were collected along the entire length of the peninsula. Sample intervals varied. Samples SJ003 to SJ019 were collected at a 0.3 km interval, SJ023 to SJ030 were collected at a 0.6 km interval and SJ049 to SJ059 were collected at a 1.6 km interval. Figure 13 shows each sample location with its corresponding latitude and longitude. All littoral samples were collected during a falling tide. Sample collection times in relation to tide levels are shown in Figure 14.

3.1.1 Dune Ridge Samples

OSL dating samples were collected from dune ridges on the peninsula using two methods. Samples from the 2001 field season were collected using a trenching technique. This method involved excavating a trench, 1 m in depth into the dune ridge, parallel to the strike of the ridge. All trench faces were cleaned off, sketched and photographed. Units targeted for sampling were those that displayed primary sedimentary structures. This was done to avoid collecting sediment that had experienced post-depositional mixing and, thus, avoid the complications associated with dating mixtures of well-bleached and partially-bleached sediment. Dating samples were collected by inserting a short length of

black PVC tube into the trench face after the outermost 0.02 m of the face had been cleared. The tube was then removed and both ends were sealed with duct tape.

In 2002, dune ridge samples were collected using a vibracoring technique. This technique was suggested as an alternative to trench excavation (T. Rittenour, personal communication). It maximizes the number of samples that can be collected within a given time period. Prior to collecting the samples, several 3 m and 6 m lengths of 3-inch diameter aluminum irrigation pipe were prepared. Brass core catchers were fitted to each pipe. Each aluminum tube was then thoroughly cleaned and both ends were sealed with duct tape. At each coring location, a vibrator was used to guide each length of aluminum tube into the ground. Figure 15 illustrates the process of vibracoring. For core extraction, a gin pole (Figure 16) constructed at McMaster University was used to guide the tube out of the ground. Each core was split into several smaller sections for transport.

OSL dating samples were collected from the four locations shown in Figure 9. Sample SJ14B was collected from within ridge set "na", which is believed to be one of the original barrier island nuclei (Rizk, 1991). This sample site is closest to the bay side of the peninsula and is therefore, believed to be the oldest sample. A 1.5 m deep trench was excavated at this site and a dating sample was collected from the east face of the trench at a depth of 1.1 m (see Figure 17). The uppermost 0.4 m of each trench face contained abundant roots and organic material. Between depths of 0.4 m and 1.0 m, there was also organic matter. Across the trench faces there were a series of thin, heavy mineral lamina. Several of these were continuous across all four trench faces. Sample SJ14B was collected from a clean quartz sand broken by four of these thin lamina. The

heavy mineral lamina in the trench, appear to dip seaward (westward) and towards the

A core sample designated SJ252 was collected approximately 4.2 m east of the SJ14 trench. Three dating samples were extracted from the core (see Figure 18). Sample A was collected from a depth of 1.0 m, approximately the same depth as sample SJ14B. This sample was collected from a clean quartz sand. Above this sample, there are two thin parallel heavy mineral lamina. Below it are a series of concave downwards curving lamina. Sample B was taken from a depth of 1.6 m. There is a set of three parallel heavy mineral lamina immediately above this sample and a single heavy mineral unit immediately below. Sample C was taken from a depth of 2.2 m in a clean quartz sand unit. Between 0.9 and 1.6 m depths in the core, there are heavy mineral units. These appear to be in groups of two to five parallel lamina that are either horizontal or concave downward. The heavy mineral layers are not well defined. They appear "smudged" grey lines, slightly darker in colour than the surrounding quartz sand.

One dating sample was collected from site SJ042. This site is the northernmost site, within ridge set "nd", along a jeep trail, which cuts transversely through and exposes a dune ridge at its crest. A trench was excavated into the crest of the dune ridge at this site and a dating sample was collected from a depth of 2.2 m in the west face of the trench (see Figure 19). The west face of the trench contained organic matter (i.e. roots) between 0.8 m and 1.3 m depths. There was little organic matter on the other faces. Each face had a series of irregular shaped areas of white quartz sand within the quartz rich units. These are either infilled burrows or iron staining from groundwater. Sampling was done

cautiously, to avoid these areas. The west and south faces had several thin heavy mineral lamina. Those on the west face dipped towards the north and those on the south face were predominantly horizontal. The lamina on the south face were continuous across the face while those on the west face were broken by the bioturbated areas.

Two samples were collected from SJ048. This site was within ridge set "nd" approximately 100 m from the Gulf of Mexico, where the west side of the ridge exhibited a sloping, unvegetated exposure (Figure 21). Two dating samples were collected from a vertical section of the ridge face that was cleaned back (Figure 20). Each exposed face shows abundant heavy mineral lamina. These are organized into sets of both landward dipping and seaward dipping lamina. Most of these are thin, with the exception of on at a 1 m depth and another at a 1.4 m depth. Sample B was taken from this lower one. Sample A was collected from a clean quartz sand wedge between two eastward dipping sets of heavy mineral lamina. The swale-like geometry of the groups of lamina exposed in and around the trench suggest a storm origin for this deposit. The heavy mineral lamina are continuous across all faces of the exposed section. However, there is an offset between the east face and the south face. The structures on the south face have been shifted downwards relative to those on the east face. This may be a result of post depositional slumping. Figure 20 shows the stratigraphy of this site and Figure 21 is a photograph of the exposure at this site.

In addition to the previous four sites, two samples were collected south of Eagle Harbour at SJ298. This site is located within ridge set "sh". It is not only the southernmost site, but it is also the closest to the Gulf of Mexico. A convex upward heavy

mineral unit extended more than 20 m north-south along the eroded dune exposure, in some locations as thick as 0.2 m (see Figure 23). Figure 22 shows that the dated location contained a 0.2 m thick heavy mineral unit overlain by thinner, equally spaced heavy mineral lamina and more widely spaced lamina extending down about 0.6 m. Below that, a shell rich sand about 0.1 m thick occurs. Below this, more heavy mineral lamina were present. The thickness of this unit and the presence of fragmented shells suggested the occurrence of a relatively recent, high magnitude storm. Based on historical data this deposit was believed to represent Hurricane Opal, which made landfall in Pensacola on October 4, 1995 and had a storm surge of 5 m. Sample 39 was collected from the heavy mineral band at a depth of 0.3 m and sample 40 was collected from the clean quartz sand beneath the heavy minerals at a depth of 0.45 m. Both samples were collected from a cleaned-off face in a pre-existing exposure. These were the only samples collected outside of the state park boundary. Appendix A contains additional photographs of the deposit at SJ298. Figure 24 is a beach profile showing the location of the SJ298 samples relative to sea level. The top of the dune ridge, which surmounts the dated location, was approximately 7 m above mean low water. The SJ298 samples were collected approximately 1 m above mean low water. Table 1 summarizes the depths from which each sample, from each sample site, was collected.

3.1.2 Littoral Samples

Thirty-three littoral samples and five sandbar samples were collected in August 2001. Samples were collected offshore at a water depth of approximately 1 m. At each sample location, an 800 g sample representing the uppermost 0.2 m of sediment was

collected. The sample was placed in a heavy duty Ziploc bag and transferred to a photo quality darkbag. The TL signal in quartz is most effectively zeroed by UV wavelengths (Spooner, 1987). Since these wavelengths are filtered by seawater, each sample was kept underwater until it was placed in a darkbag to prevent further zeroing of the TL signal.

3.2 Sample Preparation

Sample preparation was carried out under low intensity orange lighting. Two centimetres of sediment was removed from the ends of each dune ridge core sample to remove any material that may have been exposed to light during sample collection. For the vibracore samples collected in 2002, the cores were split using a rotary saw. One half of each core was archived for future study. From the working half of each core, dating samples were extracted. Samples were taken from undisturbed areas in the cores. Regions around the core catchers were highly disturbed and, therefore, avoided. The surface 0.01 m of material was removed. Approximately 100 g of material was then collected. A 0.01 m thickness of sediment was left adjacent to all core edges to avoid collecting material that had been disturbed during core extraction. Figure 25 shows the procedure followed to remove samples from the cores. Prior to any chemical treatment, the moisture content of each sample (with the exception of the littoral samples) was measured to provide an estimate of its present day water content. After a drying period of several days, a portion of each sample (1/2 for dune ridge and 2/3 for littoral) was removed and dry sieved to extract the 150-212 μm and 212-250 μm grain size fractions. The target fractions for the samples collected from site SJ298 were 125-250 μm and 250-

300 μm. An initial attempt was made to characterize the grain size distribution of each sample using a graphical technique. A cumulative plot was constructed for each sample that showed the cumulative percent versus the particle diameter. This method depends on being able to determine the 10, 25, 50, 75 and 90 percentiles from the cumulative plot. These values are then applied to a series of formulae outlined in Pettijohn (1949) to determine the sediment sorting, symmetry and peakedness of the grain size distribution. This technique is not applicable to this particular data set. The range of grain sizes within each size fraction was too large. The material in the largest and smallest fractions should have been further sieved to get a better idea of the distribution. Since the grain size data was clustered above the 50 percentile, it did not form a complete cumulative curve and it was not possible to interpolate at the required percentiles. An alternative is the method of moments. This is a method of calculating grain size statistical parameters directly without reference to graphical plots (Boggs, 1995). Folk (1974) suggests that this method gives a truer picture of grain size distributions than graphical techniques. There are, however, several disadvantages. One of the main ones is that in the top and bottom trays of the sieve stack there is a lot of material of unknown grain size. Therefore, it is necessary to make arbitrary assumptions about those particular ϕ–class intervals. The method of moments uses a series of calculations to determine the mean, standard deviation, skewness and kurtosis of a grain size distribution. All calculations are outlined in Boggs (1995). Grains within each target size range were treated with 10 % hydrochloric acid to remove carbonates and 30 % hydrogen peroxide to remove organic material. Lithium polytungstate heavy liquid separation was then used to isolate a quartz-

rich fraction (2.58 g/cm^3 < ρ < 2.65 g/cm^3). The quartz-rich fractions were etched with concentrated hydrofluoric acid for 40 minutes to remove the alpha-irradiated surfaces of the grains and to dissolve any feldspar that wasn't removed during the density separations (i.e. plagioclase feldspar with a density similar to that of quartz). After etching, each sample was treated with 10 % hydrochloric acid to remove any acid-soluble fluorides produced during the previous chemical treatments.

3.3 Dosimetry

For the dune ridge samples, gamma dose rates were measured in-situ at the time of sample collection using a Harwell gamma spectrometer calibrated in a scintillation triple point mode, which counts all U, Th and K in a single measurement. The gamma dose rates for the dune ridge samples were measured by inserting the probe into a 0.3 m deep hole in the face of the deposit at or near the sampling location. For the SJ298 dune ridge samples, the gamma dose was measured three times to verify the high radioactivity. The first estimates of the dose rate were obtained by holding the probe against the surface of the heavy mineral layer. Subsequent estimates were made by inserting the probe into a 0.30 m deep hole centred on the heavy mineral layer. The final estimates were obtained in the same manner as the first ones. The results of the second estimates were used for all calculations. Gamma dose rates were calculated using the following formula:

$$\text{Gamma Dose Rate (Gy/ka)} = \frac{\text{DISC count - CH3 count - 94 cpm}}{\text{1646 Gy/ka}}$$

where DISC= counts from the discriminator channel
CH3= counts obtained from Channel 3 on the gamma spectrometer.

The error in the gamma dose rate was estimated using:

$$\text{Error} = \frac{\sqrt{\text{total counts}}}{\text{total counts}} \times \text{gamma dose rate}$$

Gamma dose rates for the SJ252 samples were calculated using the ^{238}U, ^{232}Th, and ^{40}K contents since no in-situ measurements were made at the time of sample collection.

All dune ridge samples were collected from depths greater than 0.5 m below the modern surface (see Table 1). Cosmic dose rates were, therefore, calculated using the Anatol v.072B program, which was provided by N. Mercier. This program only takes into account hard cosmic rays. The contribution from soft cosmic rays (cosmic ray muons) at depths greater than 0.5 m is minor and can therefore be ignored (Berger, 1988). All calculations were based on the present day burial depth of each sample and on the model developed by Prescott and Hutton (1988). For all samples, a linear accumulation of overburden over the burial history of the sample was assumed. The geometry of each sample was also taken into account. To use standard tables for cosmic dose rate calculations, the overburden must have a sheet-like geometry to the horizon in all directions (2 pi geometry). Samples SJ14B and SJ252 (A, B and C) are closest to satisfying this assumption. To take into account both the geometry and the assumed accumulation rate, each present day depth was divided by two prior to the dose rate calculations. The remaining samples (SJ042A, SJ048A, SJ048B, SJ298-39 and SJ298-40) had large backing dunes, which reduced their geometry from 2 pi to 1 pi. Thus, in these cases, each present day depth value was divided again by two to take into account this geometry.

The uranium content of each sample was measured using delayed neutron counting. The thorium and potassium contents were determined using neutron activation analysis. The results of these analyses, were then used to calculate the beta dose rate to each sample, using the data of Adamiec and Aitken (1998).

Only gamma, cosmic and beta doses are considered in the dosimetry (Hutt and Raukus, 1995). Alpha dose consideration was eliminated by the hydrofluoric acid treatment during sample preparation. All dosimetry estimates are based on the assumption that the concentration of radioactivity in the sediment has remained relatively constant over time (Hutt and Raukus, 1995).

The dosimetry of the samples is summarized in Table 2. Dosimetry for the littoral samples is not included since they are not being used for dating.

3.4 Luminescence Measurements

3.4.1 Optically stimulated luminescence measurements

All measurements were made using an automated Risø TL-DA-15 reader. Blue light-emitting diodes, with an emission centred at 470 nm were used for OSL stimulation (Bøtter-Jensen et al., 2000). Stimulation must come from wavelengths longer than the wavelength of the observed luminescence (Wintle, 1993). Since the OSL emission of quartz is predominantly in the UV, visible light is used for stimulation (Aitken, 1994). An infrared laser diode unit with an emission centred at 830 nm was used for infrared stimulation. In luminescence dating, only photons of a higher energy than the incident photons are measured. Optical filters are used to ensure that the sample doesn't scatter or emit photons in the energy range being measured (Huntley and Lian, 1999). One 6 mm-

thick Hoya U-340 filter was used for UV detection (Bøtter-Jensen et al., 2000). This filter has a transmission range of 280 nm – 370 nm.

Measurements were based on a single-aliquot regenerative dose (SAR) protocol (Murray and Wintle, 2000). The SAR protocol has the advantage of using less sample than other methods (Huntley and Lian, 1999). This protocol is widely used because most sediment has had a variable bleaching history and is not homogenous in luminescence behaviour (Folz and Mercier, 1999). Therefore, identical aliquots are not available. SAR is a protocol in which many equivalent doses can be obtained with high precision from measurements on many individual aliquots. A regeneration method was used in this study because it doesn't require as many corrections as additive methods (Duller, 1998). The SAR protocol involves making repeated OSL measurements on a single aliquot of a sample. The first measurements are done to determine the aliquot's natural OSL. Subsequent measurements are used to determine the response of each aliquot to laboratory radiation. After each OSL measurement, a test dose is applied to monitor sensitivity changes during the measurement sequence.

Initial measurements were made to estimate the D_E's and to test for feldspar contamination. This was done by preparing three aliquots of each sample using 8 mm, 5 mm and 3 mm spray masks. The measurement protocol outlined in Table 3 was followed. The natural OSL and the OSL generated by a 6 Gy beta dose were measured. Prior to each OSL measurement, the sample was preheated to 220 °C at a rate of 10 °C/s and held at this temperature for 10 s. This was done to remove any unstable luminescence signal (Duller, 1998). The OSL signal was measured at 125 °C to prevent

the 110 °C TL trap from accumulating charge and, therefore, contributing to the OSL signal (Folz and Mercier, 1999). After each OSL measurement, a test dose was applied to monitor sensitivity changes during the measurement sequence (Murray and Wintle, 2002, in press). This is based on the assumption that the OSL response to the test dose provides an appropriate measure of the sensitivity changes during the measurement of the main OSL signal (Murray and Wintle, 2002, in press). For the response of the test dose to monitor the luminescence sensitivity, the assumption is made that the electron traps being sampled are the same as those responsible for the main OSL signal (Murray and Wintle, 2002, in press). The regenerated OSL growth curve and the natural OSL are sensitivity normalized before the unknown dose is calculated (Murray and Wintle, 2002, in press). A cut heat temperature of 160 °C was applied before each test dose measurement. The cut heat temperature is typically 20 °C lower than the preheat temperature (Murray and Wintle, 2002, in press). All measurements were carried out using a heating rate of 10 °C/s and 90 % power for the blue light emitting diodes. The D_E was estimated for each sample by comparing the ratio of the natural OSL signal to the OSL after a 6 Gy dose was administered. This was based on the assumption that the dose response curve was linear to 20 Gy. The estimated D_E's were then used to calculate the test dose and regeneration doses for each sample (see Table 4). The infrared stimulated luminescence of each aliquot was then measured to test for feldspar contamination. Any IRSL is inferred to correspond to feldspar contamination (Stokes, 1992). Samples were given a regeneration dose larger than the likely D_E so that any regenerated IR signal would be greater than that induced by the natural dose. This increases the sensitivity to feldspar content (Murray

and Wintle, 2000). A ratio of IRSL to OSL of less than 0.03 in the trial aliquots for each sample is taken as an indication of a sufficiently low level of feldspar contamination to begin use of the SAR protocol in D_E runs of 24 aliquots.

To test the dependence of the D_E on preheat temperature, preheat plateau tests were performed. Twenty-four aliquots of the 150-212 μm fraction (or the 125-250 μm fraction for the SJ298 samples) of each sample were prepared using an 8 mm mask. Aliquots were then measured in groups of four, with preheat temperatures ranging from 180 °C to 280 °C. The test and regeneration doses in Table 4 were used for these measurements. From the results of these measurements, a plot was constructed showing the D_E as a function of preheat temperature. A temperature within the plateau region of each plot was then selected as the preheat temperature for all subsequent measurements. Figure 26 shows the preheat plots obtained for each sample. Generally, low temperature preheats are used for young samples with low D_E's and higher temperature preheats are used for older samples with larger D_E's (Murray et al., 1997). With the exception of SJ14 and SJ252, which were measured using a preheat of 220 °C, all dune ridge samples were measured using a preheat of 200 °C.

Equivalent dose determinations were made on aliquots with 8 mm, 5 mm, 3 mm and 1 mm diameters. Twenty-four aliquots of each type were prepared. Each aliquot was measured following the sequence outlined in Table 5.

The results of the luminescence measurements were analysed using the Risø Luminescence Analyst v.2.22 program. The first several seconds of the OSL decay curve were integrated to obtain the dose dependent changes in the sample (1.2 s for SJ252A; 2 s

for SJ252B, SJ252C, SJ042A and SJ14B; 0.8 s for SJ298-39 and SJ298-40 and 0.4 s for SJ048A and SJ048B). This part of the signal is referred to as the fast component, which is believed to arise from the 325 °C TL trap (Murray and Wintle, 2000). Using this initial part of the signal has several advantages. The initial part of the luminescence signal is largest and, therefore, gives an enhanced signal to noise ratio. It is also the most likely part of the signal to have been removed by sunlight (Murray and Wintle, 2002, in press). The background integration limits were taken as the last 20 s of the decay curve. The final part of the signal defines the non-dose dependent part of the signal. The threshold recycling level was set at 10 % (based on Murray and Wintle, 2002, in press) to analyse measurement repeatability. The D_E's for all samples were determined using a linear fit.

All of the data collected had to meet a pre-defined set of criteria before being used to calculate ages. The recycling ratios had to be between 0.9 and 1.1. Errors on the D_E's had to be less than 20 %. Only data with a natural signal at least three times higher than the background was accepted. Each sample disc was visually inspected to ensure that it had an even coverage of grains.

Once all results had been analysed and the D_E distributions constructed, it was decided that additional aliquots needed to be measured to better characterize the 1mm D_E distributions and to improve sample statistics. Forty-eight additional 1 mm aliquots were prepared for both grain size fractions of SJ298-39 and for both grain size fractions of SJ252A. No changes were made to the measurement protocol.

For sample SJ298-39, 24 additional 8 mm aliquots were measured for each grain size fraction using a modified regeneration cycle. The regeneration doses were lowered.

The protocol in Table 5 was followed using regeneration doses of 0.3, 0.4 and 0.5 Gy. In many cases, the D_E's were well below the lowest regeneration dose. These additional measurements were made to test the effect of shifting the regeneration doses to lower doses on the distribution.

The ages of the samples were calculated using Anatol v.072B. All dose rate calculations were based on Aitken (1985). The systematic errors listed in Table 6 were applied to all calculations. ^{238}U and ^{232}Th values in grains were assumed to be the same as found by Rink and Odom (1991) and used to determine the internal alpha and beta dose rates. In cases where the gamma dose was measured in-situ, it was self-corrected for the estimated water content during measurement (Aitken, 1985). For cases where the gamma and beta dose rates were determined from sediment (i.e. for sample SJ252 A-C only) U, Th and K concentrations, I used the W and F functions provided by the Anatol program to determine the effective dose rate corrected for moisture. In the Anatol program "W" represents the "as-found" moisture content, which is obtained by taking the ratio of the weight of the water to the dry weight. "F" is the fraction of pore space occupied by moisture and is estimated by dividing the assumed average water content during burial by the moisture content (Aitken, 1985). An F-value of 0.8 +/- 0.2 was used for all calculations. The alpha dose attenuation factor was obtained by averaging the quartz values given in Rees-Jones' (1995) study of fine-grained quartz. Beta absorbed fractions (listed in Table 7) were from Mejdahl (1979). The external alpha dose was zero. Parameters relevant to etching were taken into account in all measurements. The etching coefficients shown in Table 8 were obtained from Brennan et al. (1991) and Brennan

(2003, in press). An etching depth of 9 μm was assumed based on the work of Mejdahl (1979). Three ages were calculated for each sample. A minimum age was calculated using the minimum D_E for each sample, a maximum age was calculated using the maximum D_E and a mean age was calculated using the average D_E.

3.4.2 Thermoluminescence measurements

All TL measurements were also made using an automated Risø TL-DA-15 reader. A series of three filters were used. A Corning 7-59 filter was used as a blue/violet filter and a Schott BG-39 filter was used to remove red fluorescence and to restrict the blue range detected (Stokes, 1992). An HA-3 heat-absorbing filter was also used.

The IRSL for the target grain size fractions of each sample was measured to test for feldspar contamination. Four aliquots of each sample were prepared using an 8 mm spray mask. Each aliquot was then measured following the protocol outlined in Table 3. A ratio of IRSL to OSL of less than 0.03 is taken as a general indication of a sufficiently low level of feldspar contamination to proceed with further measurements.

A series of preliminary measurements were made on samples SJ019 and SJ023 to determine the most appropriate heating rates, the need for a preheat prior to TL measurement, the best maximum temperature and whether or not there should be a time lapse between administration of the beta dose and measurement of the TL.

Initial measurements were made to test the effect of altering the heating rate and altering the maximum temperature. No preheat was applied. The maximum temperature was 400 °C and 250 data points were collected. Heating rates of 5 °C/s, 10 °C/s and 15 °C/s were used. Measurements were then repeated using maximum temperatures of

450 °C and 500 °C. This first set of measurements looked only at the natural TL signal. The second set of measurements was identical to the first, with the exception that the natural TL was not measured. Instead, a 20 Gy beta dose was administered and the TL response to this dose was measured.

The next set of measurements tested the effect of altering the number of data points being collected. Five aliquots of SJ019 and SJ023 (212-250 μm) were prepared. A preheat of 220 °C at a rate of 5 °C/s was used with a maximum temperature of 500 °C. Measurements were repeated twice, the first time collecting 250 data points and the second time collecting 500 data points.

The final set of preliminary measurements involved testing the effect of leaving the sample for 24 hours between measurement of the natural and administration of the beta dose and measurement of the TL.

Ten discs of each aliquot were then prepared using an 8 mm spray mask and Rusch Silkospray as an adhesive. For several samples more than one grain size fraction was measured, depending on the availability of material. The natural TL signal of each aliquot was measured. Following this, the TL response of each aliquot after receiving a 20 Gy beta dose was measured. Prior to each measurement, the sample was heated to 220 °C at a heating rate of 5 °C/s. Once this preheat temperature was reached it was maintained for 5 s. The TL was then recorded while the sample was heated from the preheat temperature to a maximum temperature of 500 °C at a heating rate of 5 °C/s. Background subtraction was used. The TL was performed twice, first recording the TL and the second time recording the background. The two were subtracted to give the

result. All measurements were conducted under nitrogen-rich conditions. Once all measurements were complete, each natural curve and each dose curve was shifted to line up the dominant peaks. To obtain NRTL values, the curves were then normalized using three techniques. In the first, both the natural and the dose curves were integrated between 315 °C and 335 °C to isolate the 325 °C peak. In the second method, the natural curves were integrated between 435 °C and 455 °C and the dose curves were integrated between 420 °C and 450 °C. This isolates the higher temperature, 445 °C peak. The third method involved integrating the natural curves between 250 °C and 455 °C and the dose curve between 250 °C and 450 °C. This analysed the effects of both the low and high temperature peaks. To obtain an NRTL value for each aliquot of each sample, the integration result for the natural was divided by the integration result for the dose curves. These values were averaged for each sample (depending on the number of aliquots of each sample) to obtain an average NRTL value. The standard deviations were used to determine which of the three methods should be used to analyse the TL data.

CHAPTER 4- RESULTS

4.1 Optically stimulated luminescence analysis of dune ridge samples

Figures 27 (a) and (b) show the grain size distribution for all dune ridge samples. SJ042A, SJ048A, SJ048B, SJ252A, SJ252B and SJ252C show similar trends. In all cases, the <90 and 90-150 μm fractions contain the least amount of sediment (<5 %) and >250 μm fraction contains the most. SJ14B is the exception to this. For this sample, the majority of the sediment is in the 150-212 μm fraction. For each sample, between 5 and 30 % of the material is in the 150-212 μm fraction (60 % for SJ14B) and between 5 and 15 % is in the 212-250 μm fraction. Samples SJ298-39 and SJ298-40 show different trends. For sample SJ298-40 the amount of material in each fraction increases as the grain size increases. The largest grain size fraction has the most material while the smallest fraction has the least. For the heavy mineral sample (SJ298-39), the 250-300 μm fraction has the most material. The grain size distribution of each sample was characterized using the method of moments. The results of these calculations are shown in Table 9.

Figure 28 shows the moisture content results for each dune ridge sample. With the exception of SJ252C, all moisture contents are below 6 %. For the SJ252 samples, the moisture content increases with depth in the core. Sample SJ252A has the lowest moisture content, while SJ252C has the highest moisture content. Samples SJ14B and SJ252A, which were collected at the same site from approximately the same depth have similar moisture contents.

The results of delayed neutron counting and neutron activation analysis are shown in Table 2. Potassium contents were less than 1.0 % for all samples. The deepest sample, SJ252C, had the lowest potassium content. The potassium contents for SJ14B and SJ252A agree within error. The uranium contents are low for all samples except SJ048B and SJ298-39. SJ048B had a higher uranium content than SJ048A despite the fact that the samples were collected approximately 0.3 m apart. Thorium contents were variable. Samples SJ14B, SJ048B and SJ298-39 had the highest contents. SJ298-39 had the highest content of all samples, at 101.5 ppm. The uranium and thorium contents are significantly different for the equivalent samples, SJ14B and SJ252A.

The results of feldspar contamination tests are shown in Table 10. Most of the IRSL/OSL ratios fall between 0.001 and 0.009. However, there are several exceptions to this. For sample SJ14B (150-212 μm and 212-250 μm), all results fall between 0.01 and 0.02. One aliquot has a ratio of 0.06. For SJ048A and SJ048B (150-212 μm and 212-250 μm) all results fall between 0.01 and 0.03, with the exception of two aliquots that have ratios of 0.04. Additional feldspar tests were performed on these samples during either the preheat plateau tests or the first set of D_E measurements for each grain size. All IRSL/OSL ratios are less than 0.03 with the exception of one aliquot from the 150-212 μm fraction of SJ048A, which has a ratio of 0.04. This aliquot also has an anomalously low OSL signal intensity compared to the others. These additional results are shown in Table 11. These samples were not used to calculate ages.

Table 12 lists the equivalent dose estimates for each of the dune ridge samples. The estimate for SJ14B, SJ252A and SJ252C is 0.5 Gy. The D_E's for SJ042A, SJ252B and SJ298-39 are estimated to be 0.3 Gy, 0.4 Gy and 0.2 Gy respectively. SJ048A, SJ048B and SJ298-40 have estimates of 0.05 Gy, 0.06 Gy and 0.07 Gy respectively. SJ14B and SJ252A have the same D_E estimates. All samples collected from the SJ252 core have similar estimates, as do the samples collected from the SJ048 trench. From the SJ298 trench, sample 39, which was stratigraphically highest, has a higher D_E estimate than sample 40.

Table 13 summarizes the D_E's obtained for each sample. In general, the results show that as the mask size, and thus the number of grains being measured, is reduced the amount of usable data is also reduced. With a few exceptions, the minimum, mean and maximum D_E's obtained for each mask size don't agree. For the 150- 212 μm fraction of sample SJ14B the 5 mm and 3 mm minimum D_E's agree, the 8 mm, 5 mm and 3 mm mean D_E's agree and with the exception of the 3 mm mask, all maximum D_E's agree. The 212-250 μm fraction has little usable data. Only the 5 mm and 1 mm mean D_E's agree. For the 150-212 μm fractions of SJ042A only the 8 mm, 5 mm and 3 mm and 8 mm and 1 mm mean D_E's agree within one standard deviation. For the 212-250 μm fraction the 8 mm and 5 mm and 5 mm and 3 mm minimum D_E's agree. All mean D_E's agree. The 8 mm and 3 mm maximum D_E's agree. For the 150-212 μm fraction of SJ048A, the 5 mm and 3 mm minimum D_E's agree, the 8 mm and 3 mm and 5 mm and 3 mm maximum D_E's agree and all mean D_E's agree. All minimum, mean and maximum D_E's agree for the

212-250 μm fraction. For the 150-212 μm fraction of SJ048B all minimum D_E's agree, the 8 mm, 5 mm and 3 mm mean D_E's agree and the 8 mm and 5 mm maximum D_E's agree. For the 212-250 μm fraction the minimum and mean D_E's agree. The 3 mm and 1 mm minimum D_E's agree, the 8 mm, 3 mm and 1 mm mean D_E's agree and the 8 mm and 3 mm D_E's agree for the 150- 212 μm fraction of SJ252A. For the 212-250 μm fraction, 8 mm and 1 mm and 3 mm and 1 mm minimum D_E's agree. For the 150-212 μm fraction of SJ252B the 5 mm and 3 mm minimum D_E's agree and the 8 mm, 5 mm and 3 mm mean D_E's agree. For the 212-250 μm fraction the 8 mm and 3 mm, 5 mm and 3 mm and 3 mm and 1 mm minimum D_E's agree. For the 150-212 μm fraction of sample SJ252C the 8 mm and 3 mm minimum D_E's agree and the 8 mm and 5 mm maximum D_E's agree. For the larger grain size fraction, the 5 mm, 3 mm and 1 mm and 8 mm and 1 mm minimum D_E's agree, the 8 mm, 5 mm and 3 mm mean D_E's agree and the 5 mm and 3 mm maximum D_E's agree. For both the 125-250 μm and 250-300 μm fractions of SJ298-39 all minimum D_E's agree. For the 125-250 μm fraction, all mean D_E's agree with the exception of the 1 mm mask. All maximum D_E's agree. For the larger grain size fraction all mean D_E's agree and the 8 mm and 5 mm maximum D_E's agree. The 125-250 μm fraction of SJ298-40 shows the same trends as the 125-250 μm fraction of SJ298-39 with the exception that only the 8 mm and 5 mm maximum D_E's agree. SJ298-39 and SJ298-40 show the most consistent D_E's. They have low errors and show little variation between the two grain size fractions and the four mask sizes.

Figures 29 to 37 show D_E distributions for each sample. For each sample, the distributions of the two grain size fractions of interest are similar. However, in several cases the smaller aliquots (i.e. 3 mm and 1 mm masks) show higher D_E's than the other mask sizes. Examples of this are seen in samples SJ252A, SJ252B, SJ252C, SJ048B and SJ298-39. Two of these samples (SJ048B and SJ298-39) were collected from heavy mineral rich units of very different character. SJ048B was a core sample centred on a thin heavy mineral lamina. As shown in Figure 20, half of this sample consisted of a clean quartz sand and half was a clean quartz sand that had undergone partial selective weathering. SJ298-39 was collected from the centre of a thick heavy mineral bed underlain by a series of closely spaced heavy mineral lamina. If the distribution plots are placed in order from oldest to youngest it becomes apparent that the older samples have much wider D_E distributions than the younger samples. As the sample gets younger, the distribution becomes narrower.

The D_E frequency distributions are characterized using skewness values. Skewness is a common test of normality. It describes the symmetry of the distribution relative to the mean and is calculated using the following formula:

$$\text{skewness} = [n/(n-1)(n-2)] * \Sigma [(x_i - X)/s]^3$$

where n= number of aliquots
x_i= individual D_E values
X= mean of D_E's
s= standard deviation

A positive skewness value indicates that the distribution is skewed to the right (has a long right "tail", which means a higher proportion of larger D_E's) while a negative value

indicates that the distribution is skewed to the left or has a long left "tail". This means that there is a larger proportion of D_E's that are small. A value of zero indicates that the distribution has perfect symmetry. Skewness values were calculated for each sample that had 10 or more usable aliquots. All values are listed in Table 13. For the purposes of this investigation values between

–0.5 and 0.5 are considered close to symmetric, values between –0.5 and –0.9 and 0.5 and 0.9 are considered skewed and values greater than 1.0 or less than –1.0 are considered strongly skewed. In terms of D_E's, a positive skewness indicates a distribution that is pulled towards higher D_E's and a negative skewness indicates a distribution pulled towards lower D_E's. For sample SJ14B, all results are skewed to the right with the exception of the 150-212 μm 8 mm distribution, which is skewed strongly to the left. Sample SJ042A shows the same trend. The most strongly skewed to the right were the 150-212 μm 3 mm results and the 212-250 μm 5 mm results. SJ252A results were skewed to the right with the exception of the 150-212 μm and 212-250 μm 5 mm results, which were skewed to the left. For SJ252B all results were skewed to the right. For SJ252C the 150-212 μm 8 mm and 3 mm and the 212-250 μm 3 mm results were skewed to the left. All other results were skewed to the right. For SJ048A all results were skewed to the right. For SJ048B all results were also shifted to the right. SJ298-39 results were skewed to the right with the exception of 125-250 μm 3 mm and 250-300 μm 8 mm and 5 mm results, which were skewed to the left. For SJ298-40, only the 125-250

μm 8 mm results were skewed to the left. All other results were skewed to the right. Several samples were close to having a symmetric or normal distribution. They are:

SJ14B 150-212 μm 5mm
SJ042A 212-250 μm 8mm
SJ252A 150-212 μm 5mm
SJ252B 212-250 μm 8mm
SJ252C 212-250 μm 5mm, 3mm
SJ298-39 125-250 μm 5mm, 3mm & 250-300 μm 3mm

The results for the additional 1 mm aliquot measurements are shown in Table 14. For the 125-250 μm fraction of SJ298-39, one aliquot had a usable OSL signal, but its recycling ratio was outside of the acceptable range. Therefore, no data was kept for processing. For the 250-300 μm fraction only 3 aliquots had a usable OSL signal. The three D_E's agreed within error. For sample SJ252A 5 and 6 aliquots were kept for the 150-212 μm and 212-250 μm grain size fractions respectively.

The results for the modified regeneration cycle measurement on SJ252A are listed in Table 15 and shown in Figure 38.

The results of all age calculations are shown in Table 16. The age of each sample is based on the average of the two largest mask sizes (8 mm and 5 mm). These were selected because they provided the most usable data and are most representative of the entire grain population. Table 17 summarizes these ages. For each of the SJ252 samples, the minimum, mean and maximum ages for the two grain sizes agree. Within each grain size fraction the minimum, mean and maximum ages are also indistinguishable. The minimum, mean and maximum ages agree between grain sizes for SJ14B. SJ14B is

equivalent to SJ252A. For the 150-212 μm fraction, the SJ252A ages are significantly higher than those for SJ14B. However, the 212-250 μm ages agree within error. SJ042 shows the same trends as SJ14B. Only the minimum ages for SJ048A agree between grain sizes. None of the ages for SJ048B agree between grain sizes. For samples A and B, the 150-212 μm ages don't agree and for the 212-250 μm mean and maximum ages don't agree. For sample SJ298-39, all ages agree between grain sizes. Within each grain size, the ages don't agree within error. The same is true for sample SJ298-40 with the exception that the 3 mm minimum ages and the 8 mm and 3 mm maximum ages don't agree between the two grain sizes.

4.2 Thermoluminescence analysis of littoral sands

Tables 18, 19 and 20 show the results of the feldspar contamination tests performed on quartz separates of the littoral samples. All samples (all grain size fractions) have IRSL/OSL ratios less than 0.007.

The first set of measurements showed that as the heating rate increased the peak intensity lowered and the peak itself was shifted to higher temperatures until, at a rate of 15 °C/sec the peak was no longer visible (Figure 40). At a maximum temperature of 500 °C, more of the TL peak was visible than at a temperature of 450 °C (Figure 41).

The second set of measurements, which involved measuring the TL response to a 20 Gy beta dose, showed the same trends. Therefore, all measurements were carried out using a heating rate of 5 °C/sec and a maximum temperature of 500 °C.

Results for the third set of measurements were similar. However, it was decided that collecting 500 datapoints as opposed to 250 would lead to a better definition of the TL glow curves (Figure 42).

The fourth set of measurements showed that the natural obtained without a preheat had a higher standard deviation then when a preheat was used (Figure 43). Therefore, it was decided that a preheat would be used for all measurements.

The final set of measurements showed no significant differences. A time lapse of 24 hours between measurements was not used in subsequent measurements (Figure 44).

Natural and dosed TL curves for each sample and each grain size fraction are shown in Appendix B. All natural curves show peaks in signal intensity at approximately 325 °C and 445 °C. All dose curves show peaks at approximately 150 °C and 350 °C. In all cases, the 150 °C peak is less dominant than the high temperature feature. This is not the case for the natural glowcurves. In some cases, the low temperature feature is dominant and in other cases, the high temperature peak is the dominant feature. Figure 45 shows the relationship between the type of dominant peak and its location along the peninsula for each grain size fraction. All grain size fractions show similar trends. As one moves from south to north, there is a decrease in the abundance of dominant low temperature features and a corresponding increase in the number of aliquots with a dominant high temperature feature. The strength of this relationship varies with grain size. For the 90-150 μm fraction, 19 samples were plotted and the data was fitted with a second order polynomial. The R^2 value of 0.59 indicates a moderate positive correlation between the type of dominant peak and location on the peninsula. The data set, however,

has several anomalous points. When two of these outliers are removed (SJ023 and SJ070) the R^2 value increases to 0.74, thus, showing the effects of outlying points on the apparent trend. For the 150-212 μm fraction, 32 samples were plotted and a linear trend was fitted to the data. The R^2 value was 0.22, indicating a much weaker trend than what was seen in the smaller grain size fraction. The 150-212 μm fraction shows more scatter. For the 212-250 μm fraction 36 data points were plotted and fitted with a second order polynomial trend. The scatter is high and the R^2 value is 0.41.

All data (both natural and dose curves) was shifted to the dominant peak location to line up the peaks. All shifted curves for each grain size are presented in Appendix C. The data was processed using the three integration methods outlined in the methods section of this thesis. The results of the integrations are shown in Tables 21-23. Figures 46 to 48 are plots of NRTL versus distance northwards along the peninsula. The points on the graphs represent the mean of a maximum of 10 aliquots. Each point is plotted with an error of one standard deviation. These plots include all sandbar samples. With the exception of SJ055 (methods 1 and 3, 212-250 μm), the sandbar samples have higher NRTL values than their corresponding littoral samples. On these plots, it was evident that the normalization methods 1 and 3 give lower standard deviations than method 2. Method 2 was therefore discarded. All data was then re-plotted excluding the sandbar samples and two methods were used to fit a trend line to each dataset. Figures 49 to 51 show the data fitted with a linear trend and Figures 52 to 54 show the same data fitted with a sixth order polynomial trend. Table 24 summarizes the R^2 values for each plot.

The results show a positive correlation between NRTL and distance north along the peninsula. NRTL decreases with increasing distance northwards. The slope of the linear trend decreases with increasing grain size. The plots also show that in the south the NRTL decreases with increasing grain size (i.e. in the south the larger grain size has a lower NRTL). In the north, the NRTL is constant and doesn't change with grain size.

Figure 55 shows the percent standard deviation versus location for each sample. There are no trends with distance. Most data falls between 2 % and 8 %. There is an increase in the standard deviation between N29°48.0000 and N29°49.0000. Figures 56 to 58 show the relationship between grain size and NRTL. Again, there does not appear to be a trend. Figures 59 to 61 have tide curves superimposed on the NRTL plots. There does not appear to be a trend.

In three cases, sample sites were revisited several days after the initial sample collection and new samples were collected. Table 25 summarizes the NRTL values obtained for each set of samples. With the exception of the SJ029/073 (150-212 μm, methods 1 and 3) and the SJ024/071 (212-250 μm, method 3) pairs, measurements made on samples collected during the first day agree with those made on samples collected at equivalent locations several days later. All results agree within two standard deviations except SJ024/071 (method 3).

Sample abundance limited the number of aliquots measured for each sample. A maximum of 10 aliquots were measured. In some cases, only 5 aliquots were measured because of sample availability. To test if the sample statistics could be improved 48 discs of each grain size for sample SJ051 were measured. This was the only sample that had an

abundance of material in the desired grain size fractions. The results of these measurements are shown in Table 26. There is an improvement in sample statistics. For method 1, the 90-150 μm fractions showed an improvement in standard deviation of 44 %. The 150-212 μm fraction showed an improvement of 67 %. The 90-150 μm and 150-212 μm fractions for the third method show improvements of 52 % and 67 %. There was no improvement in standard deviation with increasing the number of aliquots for method 1 and 3 for the 212-250 μm fractions.

CHAPTER 5- DISCUSSION

5.1 Optically stimulated luminescence analysis of dune ridge samples

Samples SJ298 and SJ048 have the greatest amount of material in the >250 μm fraction. Both sites are suspected storm deposits. This grain size trend may be a characteristic of storm deposits. The fact that SJ252 also shows these trends could indicate that site SJ14 is aeolian decoration on top of an ancient storm deposit.

The grain size distribution of each dating sample was characterized using the method of moments. The standard deviation represents the degree of sorting (Folk, 1974). With the exception of SJ14B and SJ298-39, all results for all samples fall between 0.71 and 1.00 ϕ, which indicates that all of the samples are moderately sorted. SJ14B and SJ298-39 have standard deviations between 0.50 and 0.71 ϕ and are therefore classified as moderately well sorted. Samples collected from the heavy mineral layers (SJ048B and SJ298-39) have lower standard deviations than samples collected from the same site within a clean quartz sand. This lower degree of sorting is likely related to their storm origin. Storms are high-energy events and have the potential to transport both fine and coarse-grained sediments. Skewness is a measure of the degree of symmetry of a grain size distribution (Folk, 1974). All samples, except SJ298-40, are within the –0.3 to –1.0 range and are therefore considered coarsely skewed. All samples have more material in the coarser grain size fractions. Kurtosis is the ratio between the sorting in the tails of the distribution and the sorting in the central portion of the normal curves. All samples have kurtosis values greater than 1.00, which indicates that the central grain size fractions are

better sorted than the tails (the finer and coarser grain size fractions). SJ298-39 shows this strongly. The significance of kurtosis is still not fully understood (Boggs, 1995).

The dosimetry results for the samples met expectations. Low potassium results were expected since there is little feldspar in the samples. Heavy mineral rich sands that are concentrated by wave and wind action contain significant alpha, beta and gamma radioactivity due to trace amounts of uranium and thorium found in monazite and zircon (Donoghue and Greenfield, 1991). Monazite can contain up to 12 % thorium oxide and 1% uranium trioxide (Donoghue and Greenfield, 1991). The uranium and thorium results were expected to be highest for SJ048B and SJ298-39 since these samples were collected from heavy mineral layers, which are known to contain zircon and monazite.

Normally when creating a regeneration cycle, the beta doses are selected to bracket the equivalent dose (based on an estimate of the equivalent dose). However, because of the low estimated equivalent doses and the limits imposed by the Risø reader, this was not possible for many of the samples. To test the effect of the regeneration cycle on the results a new regeneration cycle was applied to one of the problematic samples. The new regeneration cycle had a smaller range of beta doses that clustered around the estimated equivalent dose. The distributions obtained using both regeneration cycles were identical. The regeneration cycle doesn't appear to have an effect on the equivalent dose distributions.

Similarly, increasing the number of aliquots from 24 to 48 for the 1 mm masks, which were problematic, did not improve sample statistics or help characterize the D_E distribution. The sample is too young and therefore has a very low OSL signal. The

detection limit of the current Risø reader is not low enough to obtain meaningful results on small aliquots. Since it is not possible with the current equipment to be able to get good sample statistics on 1 mm mask aliquots or, therefore, to adequately characterize and understand these distributions, the 1mm aliquot results should not be used.

Despite the lack of data for the 1 mm mask aliquots, some samples show large D_E's that are far outside of the distribution of larger mask sizes. As the size of the aliquot is decreased from 8 mm to 1 mm, the number of grains is decreased. The 8 mm aliquots show the contribution to the luminescence signal from numerous grains (although most of the signal comes from only a few of those grains). The 1 mm aliquots are showing the contribution to the signal from single grains that may not be representative of the entire population of grains. Since the larger aliquots are more representative of the entire population, only these should be used for age calculations.

The extremely high doses seen in the small mask sizes could represent single grains of quartz in close proximity to heavy mineral grains, as opposed to the classical interpretation that the high doses are due to incomplete zeroing at burial. These quartz grains would therefore have received a high radiation dose during burial. Zircon and monazite are common heavy minerals on the peninsula. To test the feasibility of this explanation for the high D_E's, the dose variation near single monazite and zircon grains was calculated. The model upon which all calculations were based, was created by B. Brennan and will be discussed in depth in future publications. The results shown in Table 27 are the ratios of the dose of an etched quartz grain to the dose delivered to that grain from the matrix. For the matrix, 30 % porosity and 80 % saturation were assumed. A

moisture content of 7 % was assumed. This value is slightly higher than the average moisture content of 5 % for all dune ridge samples. A mean density of 2.10 g/cm^3 for the matrix was also assumed. Three size combinations were considered. The first combination was a small quartz grain and a larger zircon or monazite grain (110 μm quartz and 150 μm heavy mineral grain). The second case involved a large quartz grain and a smaller heavy mineral grain (110 μm quartz and 70 μm heavy mineral grain). The third scenario was where the quartz and heavy mineral grains were the same size (70 μm). The model considered four separation distances between the quartz and heavy mineral grains. It considered distances of 0 (touching), 100, 200 and 300 microns. In all cases, as the separation between the grains increases, the contribution to the dose by the heavy mineral grain decreases. Using published average concentrations of uranium and thorium, monazite clearly has a greater contribution to the dose than zircon. Each dose ratio for zircon and monazite was multiplied by each mean D_E. The results are shown in Table 28. All maximum D_E's are accounted for by proximity to a zircon or monazite grain. The separation distance between the quartz and heavy mineral grain is a maximum of 300 μm.

The broadening of the D_E distributions with age may reflect a post depositional even. During the 2001 field season, it was observed that in older deposits the sedimentary structures (particularly heavy mineral lamina) were not as well defined as the same structures present in younger deposits. This could be related to pore water movement in the sediment after deposition. As water moves through the deposit, it

moves finer grain sizes and "smears" out the deposit. What is being seen in the D_E distributions could be reflecting this post depositional "smearing".

Only nine of the forty-eight D_E distributions that had enough data to calculate skewness values, were close to normal distributions. This means that only 19 % of the data gives a normal distribution. Symmetric D_E distributions are expected when dealing with deposits that have experienced extensive bleaching. Full zeroing of the luminescence signal would be expected for coastal deposits experiencing lots of sunlight exposure. The two potential storm deposits (SJ048 and SJ298) don't have a normal distribution. This could be related to unbleached or partially bleached material being incorporated into the deposit as a result of the storm event. These distributions could also be related to the presence of heavy minerals. Samples that have been in close proximity to heavy mineral grains should have higher D_E's than samples that have not been near heavy minerals. The D_E distributions would therefore be expected to be right skewed.

Ages can be estimated based on the geometry of the peninsula. The youngest sets of dune ridges should be closest to the Gulf of Mexico, while the oldest should be located closest to the St. Joseph Bay (Rizk, 1991). Since sites SJ14 and SJ252 were closest to the bay side of the peninsula, it was expected that the samples from these sites would be the oldest. Samples collected at SJ298 were expected to give the youngest ages since they were collected from a deposit on the Gulf of Mexico shoreline. Sample SJ042A was expected to give an age between SJ14 and SJ048 since it was collected from the middle of the peninsula. All samples met these expectations. Table 17 summarizes the ages obtained for the samples. The oldest sites, with mean ages of approximately 1,000 years

B.P and 1,300-1,800 years B.P. were SJ14 and SJ252 respectively. The youngest were SJ298-39 and SJ298-40 with ages of approximately 8 and 21 years B.P. and SJ048 with an age of approximately 90 years B.P. Site SJ042 gave an age of approximately 600 years B.P.

Rizk (1991) divided the peninsula up into a series of dune ridge sets (shown in Figure 7) and developed a model to explain the development of the peninsula. This study focuses only on Rizk's northern dune ridge sets. Samples SJ042 and SJ048 were collected from set "nd" and SJ14 and SJ252 were collected from set "na". Ridge set "na" is one of the nuclei from which the northern half of the peninsula is believed to have formed. Ridge set "na" is believed to have emerged by 1,500 years B.P. (Rizk, 1991). SJ14 and SJ252, which were collected from this set, are in agreement with this 1,500 year maximum age. These two samples gave ages of approximately 1,000 and 900-2,200 years B.P. respectively. There are few other dates on the peninsula that can be used to confirm the results of this study. A dated peat just south of Richardson's Hammock gives an age of 745 years B.P. (Rizk, 1991). Other dates on the Peninsula are from archaeological work on shell middens in Richardson's Hammock and at the Old Cedar Site (set "sf", which is east of the State Park entrance). The Richardson's Hammock archaeological sites are assigned an age of 500-1,500 A.D. while the Old Cedar Site is assigned a date of 500-1,000 A.D. On the northern end of the peninsula, within set "ne" there is a pile of red bricks. One interpretation is that they are from a Spanish homestead circa 1650-1750 A.D. A more widely accepted interpretation is that the bricks are from an abandoned lighthouse from 1838 A.D. These are the only dates available for sites on the peninsula.

Based on the presence of fragmented shell material and on the presence of heavy minerals and their position on the beach, samples SJ048B and SJ298-39 are hurricane deposits. The mean age of approximately 80 years B.P. (see Table 17) for SJ048B suggests that the hurricane responsible for creating the deposit made landfall in the area between 1911 and 1933. Several hurricanes made landfall in the region during this period. The peak period for gulf hurricanes was 1916 to 1925 (Williams and Duedall, 1997). During this period, 14 storms made landfall and 6 of these were severe hurricanes. Three of these hurricanes made landfall in the Panhandle region. A category 2 hit Panama City on August 31, 1915. A category 3 storm, with a track similar to Hurricane Opal, made landfall just west of Pensacola on October 12, 1916. On September 21, 1917, another category 3 hurricane made landfall at Fort Walton Beach, just east of Pensacola. A category 1 hurricane hit Port Saint Joe on the morning of September 15, 1924 and caused extensive damage. A category 3 storm hit Panama City on September 22, 1929. This hurricane had a tidal surge of over 2.7 m and caused extensive damage (Williams and Duedall, 1997). The deposit at SJ048 likely represents the 1929 unnamed hurricane based on the track of the storm and the magnitude of the storm.

Sample SJ298-39 is believed to represent Hurricane Opal. This is based on the presence of numerous thick heavy mineral layers and the presence of a fragmented shell deposit approximately 0.70 m below the heavy mineral layer that was sampled. Storm waves from Hurricane Opal impacted over 2,000 km of coastline from southwest Florida to Louisiana on October 4, 1995 (Stone et al., 1996). The storm made landfall at Pensacola. Prior to landfall, Hurricane Opal was classified as a category 5 storm (Stone

et al., 1996). Storm surge levels of greater than 5 m were reported (Stone et al., 1996). Opal was one of the strongest of the 18 hurricanes that have hit Pensacola since 1900.

The time lapse between the landfall date of the hurricane and the date that the sample was collected was 6 years and 11 months. The age of the samples at site SJ298 should, therefore, match this age. The mean ages for samples SJ298-39 and SJ298-40 disagree and overestimate the expected age, despite the fact that they were collected approximately 0.20 m apart. The 125-250 μm grain size fraction of sample 39 gives an age of 8.4 +/- 0.5 years B.P. while sample 40 gives an age of 21 +/- 1 year B.P. R.G. Dean's model of storm surge sediment transport can be used to explain these overestimates (Hellegaard, 1995). This model explains how sand from an older deposit can be reworked and deposited with material that is more recent. During a storm, the storm surge will break up existing dune fields and use some of the material to create an offshore deposit (Hellegaard, 1995). If the slope of the shore is low, waves will carry sand back onto the beach surface (Hellegaard, 1995). This is one way of bringing older material that already has a dose into the system. This overestimate could also be related to the nature of the storm. There may have been erosion prior to the deposition of the heavy mineral deposit.

5.2 Thermoluminescence analysis of littoral sands

Several trends are evident in the TL results. The high temperature feature becomes dominant and the low temperature feature disappears with increasing distance northwards along the peninsula. Figure 62 shows the gradual disappearance of the low temperature feature and the increasing dominance of the high temperature one. In TL

when a certain temperature is reached, the eviction of electrons takes place quickly from all traps of a specific type (Aitken, 1998). On TL glow curves, the temperature of the peak emission is characteristic of the type of trap (Aitken, 1998). For example, if a maximum emission occurs at 325 °C on a TL glow curve this indicates that sets of traps whose electrons are evicted at 325 °C were emptied. The bleachability of a trap is dependent on its depth below the conduction band (the energy level representation of luminescence is discussed in the introduction). The deeper the trap, the harder it is to bleach by sunlight or heat (Aitken, 1998). In many quartz samples, only the trap type associated with the 325 °C TL peak is easily bleached (Aitken, 1998). Generally, low temperature peaks are more easily bleached than high temperature ones. Sand found in the north has been transported a greater distance than sand found in the south. As a result of this, sand in the north has had more exposure to UV light and has therefore experienced more bleaching. Since the low temperature peak is most easily bleached, by the time sand has reached the north end of the peninsula this peak is no longer the dominant feature. The high temperature peaks are also being bleached, but at a slower rate than the low temperature ones. This was shown by Keizars (2003) who used bleaching experiments to demonstrate the loss of the high temperature peak with increasing solar exposure. Figure 63 shows the results of some of these exposure experiments.

Another trend seen in the data is that the NRTL of the sandbar samples is higher than the NRTL of the corresponding littoral samples. There were few sandbar samples collected during the August 2001 field season. The sandbar at the south end of the

peninsula was close to shore so 5 samples were collected along the length of the bar. In the north, the bar was further offshore and inaccessible. The beach is a dynamic system. A typical beach profile is shown in Figure 64. Its profile and characteristics are altered by several factors, including seasonality. A beach has a summer and winter profile. Where storms are common, large waves destroy or limit the extent of the berm. The beach is eroded and the eroded material is carried offshore where it is temporarily stored in longshore sandbars (van Rijn et al., 2003). Where storm waves are unusual, the movement of beach sand is shoreward. Offshore bars are destroyed and sediment is transported to the upper part of the beach where it rebuilds a broad, flat berm. Summer swells build the beach by pushing offshore sandbars onto the shoreline (van Rijn et al., 2003). A summer profile, when storms are unusual, has no longshore bars (Ritter, 1986). A winter profile is characterized by no berm but a series of longshore bars (Ritter, 1986). All samples in this study were collected during the summer. Sandbar samples would be expected to have a higher NRTL than samples closer to shore, like the ones collected at a 1 m water depth, between the sandbar and the berm. Sediment stored in an offshore sandbar is less likely to experience the exposure cycles that nearshore sediment will experience.

With increasing distance northwards along the peninsula, the NRTL progressively decreases for each of the three grain size fractions. Figures 58 to 59 show this trend. This phenomenon is related to the amount of UV exposure that the grains have received during transport. As sand is transported in the nearshore zone, it follows a "zigzag" path (refer to Figure 65). The grain is transported onshore during wave run-up in the swash

zone and carried back into the water during rundown. During the period when sediment is on the beach face, it is exposed to UV light, which as previously discussed, is the most effective wavelength for bleaching the luminescence signal. Sediment is also exposed to light when submerged under a few hundred microns of water (Forrest, 2001). While the grain is under deeper water, it is being exposed to less UV light since UV light is strongly filtered by seawater. Quartz grains at the north end of the peninsula have undergone several of these exposure cycles since they have been transported a greater distance than grains in the south. Therefore, grains that have travelled further along the peninsula have had their TL signal bleached to a lower level than those grains that are closer to the source. The residual TL is therefore lower for samples in the north. The same trend was seen by Pieper (2001) and Rink (2003) along a stretch of the Mediterranean coastline.

An alternative explanation is that the NRTL intensity is related to the offshore bathymetry of the St. Joseph Peninsula. The NRTL appears to be highest along areas of the peninsula where the increase in water depth offshore is rapid. The NRTL is highest at the south end of the peninsula and lowest at the north end. Based on the bathymetric map shown in Figure 6, the shelf break is closer to shore at the southern end of the peninsula than at the northern end. During storms, material stored in this deeper water may be transported into the nearshore zone or onto the beach surface. However, this would mainly be a source for the TL-rich smaller grain sizes (90-150μm). This material would have a high NRTL because it has been sheltered from sunlight. Alternatively, the channel structures seen in the bathymetry might be scoured exposures of much older buried river

channels, providing a local source for the TL–rich larger grains sizes south of the study area.

The slope of this linear trend decreases with increasing grain size. This is happening because in the north the NRTL values are remaining relatively constant while in the south the NRTL values are decreasing with increasing grain size.

Although the linear trend is the dominant trend, there are also small-scale fluctuations along the length of the peninsula. In earlier studies (Pieper, 2001 and Rink, 2003) along the Mediterranean coast, a rapid increase in NRTL over a short distance indicated the introduction of new material into the system. The new material had a high NRTL because it has been exposed to little light and its closer to the source. Small fluctuations in this current study could represent the introduction of new material into the system at several locations along the peninsula. This introduction of material could be accomplished through small-scale beach nourishment projects. Erosion is a major source of concern along the peninsula. Many homeowners privately bring in sand to renourish their property and protect their homes. These small-scale nourishment projects are not endorsed by the FDEP and are not included in their records. Older material with a higher residual could also be a result of offshore sand being transported towards shore. The fluctuations could also be a result of old tidal inlets being scoured during storms. For this to happen the storm wave base must be deep enough to scour the sea floor. Much fine-grained material (i.e. 90-150 μm) is stored offshore. This material can be brought closer to shore during large storms. The trends could also be a result of the introduction of sand from official nourishment projects. For example, sediment was brought in when the rock

wall at Stump hole was constructed after Hurricane Opal in1995. This nourishment sand is stored offshore in the bar. During the summer, it is transported onshore and leads to a high NRTL signal in the littoral samples. The small fluctuations in NRTL may also be related to bathymetry. NRTL in the north shows greater fluctuations than NRTL in the south. This could be a result of changes in the bathymetry along the northern part of the peninsula. In the north, at approximately SJ011, there is a deep pool offshore. There is another at St. Joseph Point, at the northernmost end of the peninsula. In areas such as these, material is being sourced from deeper water. It has, therefore, had little sunlight exposure and as a result has a higher NRTL signal than adjacent shallow areas. Fluctuations could also be related to the location of the shelf break. The shelf break is closer to shore at the southern end of the peninsula than at the northern end. This also happens to be where the most fluctuation in NRTL is. When the shelf break is close to shore, material brought into the system is easily lost. New material with a high NRTL is added to the system. This material travels a short distance before being lost beyond the shelf break. It is too deep for this material to be brought back into the system. The fluctuations seen in the south in the NRTL signal could be a result of material being added to the system at several locations along the peninsula, undergoing few subaerial exposure cycles and then being removed from the system. Where the shelf is wide, and the break is further offshore, the material spends more time in the system and experiences more subaerial exposure cycles. There should, therefore, be less fluctuation in the NRTL. At the south end of the peninsula, there are also several east-west trending troughs approximately 10 to 11 m in depth. These are possibly ancient tidal or alluvial channels.

If these channels are scoured during large storm events, they may provide coarse grained (i.e. 150-250 μm size) material with a high TL signal to the system.

The NRTL in the south decreases with increasing grain size. The larger grain size has a lower NRTL. To understand this trend it is important to understand the dynamics of the swash zone. Wave run-up is characterized by decreasing flow and rundown is characterized by accelerating flow (Elfrink and Baldock, 2002). The fluid acceleration during run up and rundown is capable of moving coarse-grained material as well as fine-grained material (Elfrink and Baldock, 2002). In most natural beaches, the coarsest material is found at the seaward edge of the swash zone (Elfrink and Baldock, 2002). The coarsest material is found at the lowest down rush level. Finer material is easier to transport and is therefore carried off the beach surface. Since fine-grained sand is easier to entrain and transport it should, therefore, travel further and remain suspended in the water column for a longer period. On the other hand, the larger grain size, which is more difficult to entrain and to keep in motion, will spend more time on the beach surface. Fine grains will be winnowed out while coarser grained material will remain on the beach surface. The UV component of sunlight is strongly filtered by seawater. The fine material that remains in suspension in the water column will be exposed to less UV light than the coarse material that is exposed nearshore and on the beach surface. It would, therefore, be expected that the larger grain sizes would have the lowest residual signal because of longer subaerial exposure in the swash and oceanward parts of the berm. This trend can also be explained by beach drifting (Figure 66). Wavefronts approach the shore obliquely. Swash is therefore directed obliquely up the beach. Sand is therefore also

moved obliquely up the beach. When backwash flows down the slope of the beach, it is controlled by the flow of gravity. It, therefore, moves directly downslope instead of obliquely. Particles are pulled seaward and come to rest on one side of their starting position (i.e. in Figure 66 the sand grain has moved from 1 to 2 to 3). On a particular day wavefronts usually approach from the same direction. Therefore, this movement is repeated many times. An individual grain can travel a great distance along a beach in this way. The heavier and larger grains will spend more time on the beach surface.

The NRTL in the north remains relatively consistent. There is no change with increasing grain size as was seen in the southern samples. There are two possible explanations for this. The first is that the residual in the northern samples has reached its lowest level. All grain sizes have been in transport for an extended period and been exposed to sufficient light to reduce their NRTL to its lowest level. Another possibility is that during wave runup and rundown in the swash zone the larger grain size fraction (212-250 μm) was broken up. Therefore, the smaller grain size fractions are composed of fragments of what was originally 212-250 μm fraction. The smaller grain sizes would then show similar NRTL results as the larger grain size fraction.

There is an increase in standard deviation between N29°48.000 and N29°49.000. This location corresponds to the Hurricane Georges (1994) deposit studied by Rink and Pieper (2001). With the exception of the 90-150 μm fraction, each grain size fraction shows this. The high standard deviation indicates a mixture of grains with different NRTL values. This mixture could be accomplished by storm waves during a hurricane.

It could represent a mix of sediment sourced from further offshore (higher NRTL because deep, therefore. less subaerial exposure and less bleaching). It could also be a mix of sediment from onshore, which has been exposed to light for long periods or the interaction of grains with sufficient burial times to build up the TL signal. The storm may also have brought in different types of quartz showing different bleaching characteristics (Godfrey-Smith et al., 1988, Rink et al., 1994). The NRTL results obtained on samples collected at the same locations but on different days agree within error. Therefore, there do not appear to be daily fluctuations in NRTL during storm free periods.

There is an improvement in statistics when comparing the results from 10 aliquots versus those from 48 aliquots. In some cases, standard deviations were not significantly improved by increasing the number of aliquots measured (i.e. method 1 212-250 μm and method 3 212-250 μm). Normally this would indicate that any inhomogeneity or variation between aliquots of the same sample is real and not a result of sample statistics. However, in most cases the standard deviation was significantly improved by increasing the number of aliquots. This would suggest that at least some of the variability being seen is a result of sample statistics.

5.3 Future Study

One of the main problems with the OSL portion of this project was the inability to obtain an adequate signal from small amounts of the young samples. A solution to this would be to perform single grain measurements on each sample. This would not only further characterize the distributions of D_E's but also improve the signal intensity. The laser on the single grain attachment is more powerful then the one on the standard Risø

unit. It should therefore be able to measure smaller D_E's. For the samples that had high D_E's relative to the distributions, it would be useful to determine the proportions of zircon and monazite in the samples. It would then be possible to calculate the probability of finding a quartz grain next to a zircon or monazite grain.

There are few dates available along the length of the peninsula. This makes it difficult to resolve the chronological order of the development of the peninsula. Future studies need to focus on collecting multiple samples from each dune ridge set. It would also be useful to sample at the boundaries of each ridge set.

To better define the trends in the TL data it would be useful to resample the entire length of the peninsula using a small sample interval and using this same interval along the length of the peninsula. Sampling should be conducted during the winter season when the longshore bars are close to shore. This would allow for an extensive dataset including not only 1 m water depth samples, but also samples from the longshore bars along the length of the peninsula. This was actually started in October 2002. It would also be useful to obtain samples of nourishment sand that was used at various locations when possible (or, when possible, obtain a sample from the source of the nourishment sand). It would then be possible to characterize the TL signature of this sand and use this knowledge to recognize this sand and its contribution to the trends. It would also be interesting to further investigate changes in NRTL on a daily, weekly and monthly basis during both calm and stormy periods. It would be advisable to measure an increased number of aliquots (preferably > 48) to improve sample statistics.

CHAPTER 6- CONCLUSIONS

6.1 Optically stimulated luminescence analysis of dune ridge samples

Several samples have large D_E's relative to the D_E distributions. There are two ways of getting grains with large doses. The first is from proximity to other grains that are delivering high doses. The second is by incomplete zeroing. This is possible for the storm deposits from SJ048 and SJ298. However, in dune environments this scenario is less likely. Therefore, I believe that the high D_E's are accounted for proximity of quartz to a zircon or a monazite grain.

Based on the geometry of the ridges on the peninsula, the youngest dune ridges should be closest to the Gulf side of the peninsula. The oldest ridges should be on the bay side of the peninsula. The ages obtained for the samples collected within the northern portion of the peninsula are in agreement with the proposed development of the peninsula. Samples SJ14B and SJ252 were collected from ridge "na" and are in agreement with the belief that this set emerged by 1500 years B.P. Based on the ages obtained in this study, the part of the peninsula north of Eagle Harbour has a 600-700 year progradation history.

Two hurricane deposits were analysed in this study. Sample SJ048 gave an age in agreement with a category three storm that hit Panama City on September 22, 1929. Sample SJ298 is believed to represent Hurricane Opal, which made landfall at Pensacola on October 4, 1995. The ages obtained are in agreement with this. However, the ages obtained for samples 39 and 40 disagree. This could be related to the dynamics of

sediment transport during the storm. This study has shown that it is possible to date young samples by using quartz collected from heavy mineral layers.

6.2 Thermoluminescence analysis of littoral sands

Several trends were visible in the TL data. The low temperature feature present in the natural glow curves disappears with increasing distance northwards and the higher temperature feature becomes more dominant. This is a result of increasing solar exposure with increasing distance in the direction of longshore drift. Sandbar samples have a higher residual signal than their corresponding littoral samples. This is related to the amount of time the samples spend on the beach surface being exposed to solar radiation. Since sand stored in offshore sand bars spends little time on the beach surface being exposed to sunlight, the NRTL is experiencing little reduction. The NRTL decreases progressively with increasing distance northwards along the peninsula. This is also related to increasing solar exposure. Although the dominant trend is that of decreasing NRTL, there are also small-scale variations. These could be related to the introduction of material with a higher NRTL. Possible sources of this material could include nourishment sands, sands stored offshore that are transported onshore during storms or sands scoured from tidal inlets during storm events. This material could be nourishment sands or offshore sands that are transported onshore during storms. This study shows that NRTL is a useful tool in studies of sediment transport in the nearshore and with further study, this method has the potential to be used as an alternative to other sediment tracing methods.

CHAPTER 7- FIGURES AND TABLES

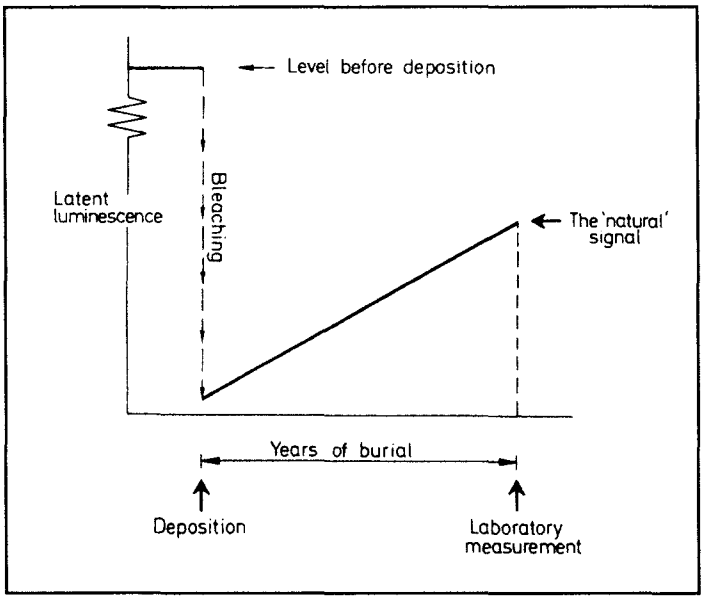

Figure 1- The basis of luminescence dating. The event being dated is the setting to zero of the luminescence signal that was aquired at some point in the past. The zeroing of this signal occurs through exposure to daylight or sunlight during erosion, transport and deposition. Once the material is buried the signal begins to build again. (Aitken, 1998).

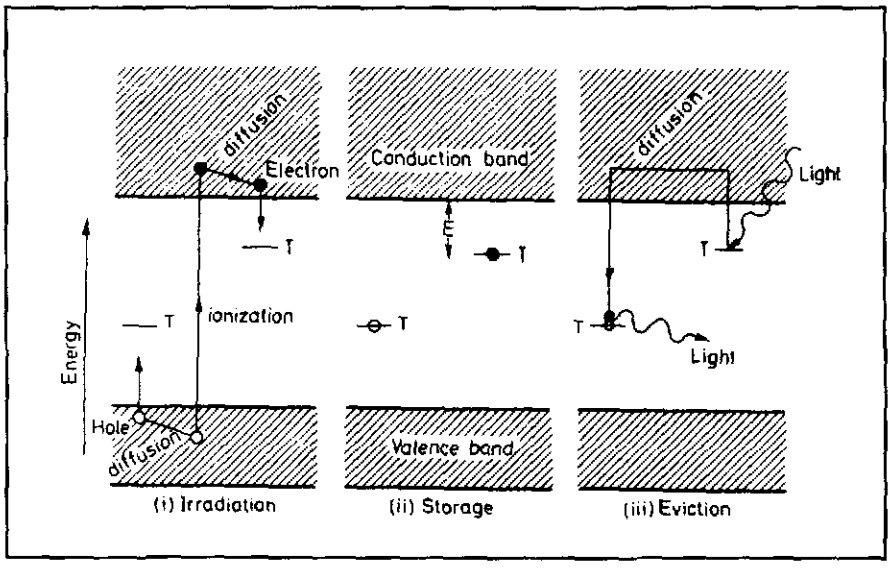

Figure 2- OSL processes represented by the conduction band model. i) The mineral is exposed to nuclear radiation. The mineral's binding electrons are excited above their ground states. ii) As the electrons return to their ground states, some become trapped in defects in the crystal lattice (represented by "T"). iii) When the mineral is exposed to light the defects are emptied and light is emitted. (Aitken, 1998).

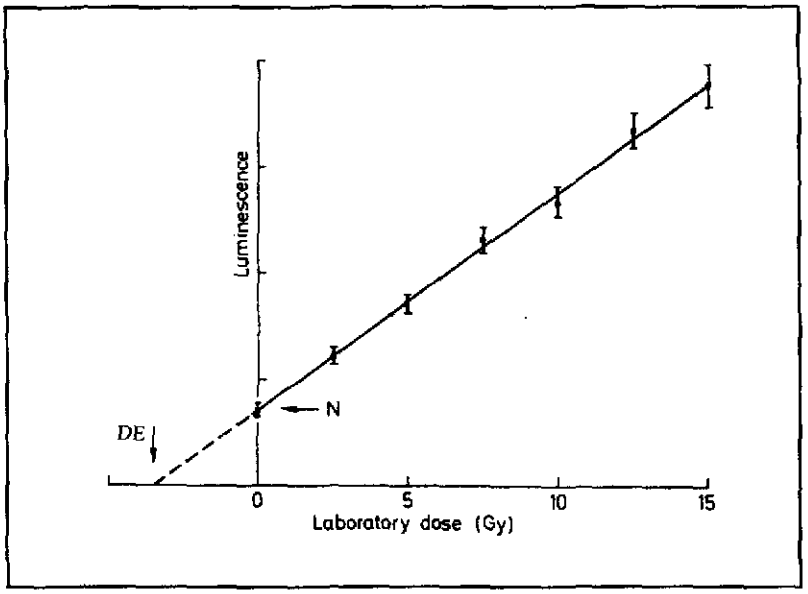

Figure 3- The additive dose method of evaluating equivalent doses. Each point on the graph is the average OSL from a group of aliquots. All members of a specific group were given the same laboratory dose. The equivalent dose is the intercept on the dose axis. DE represents the equivalent dose and N N represents the natural signal intensity (Aitken, 1998)

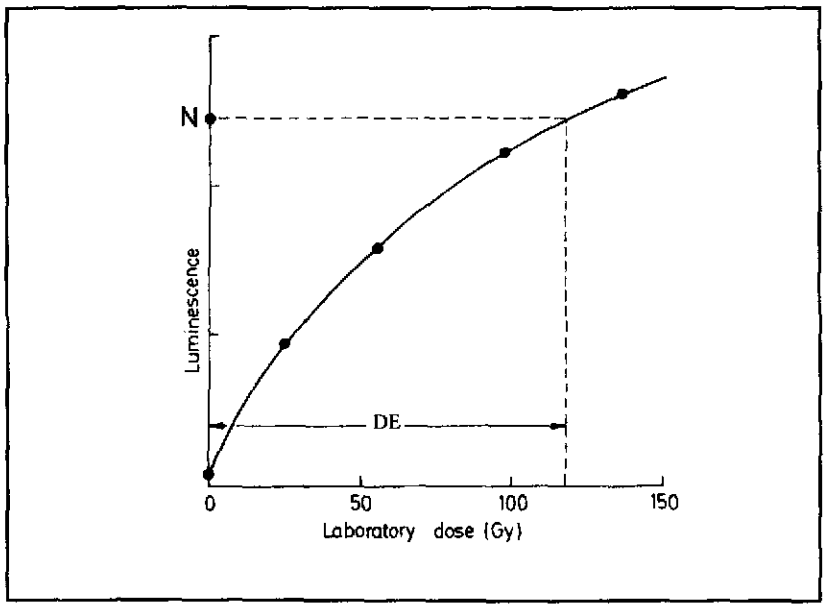

Figure 4- The regeneration method of determining equivalent dose. The natural OSL (shown as N) is compared to the OSL resulting from aliquots that have been bleached down to a low level and then dosed. DE represents the equivalent dose. (Aitken, 1998)

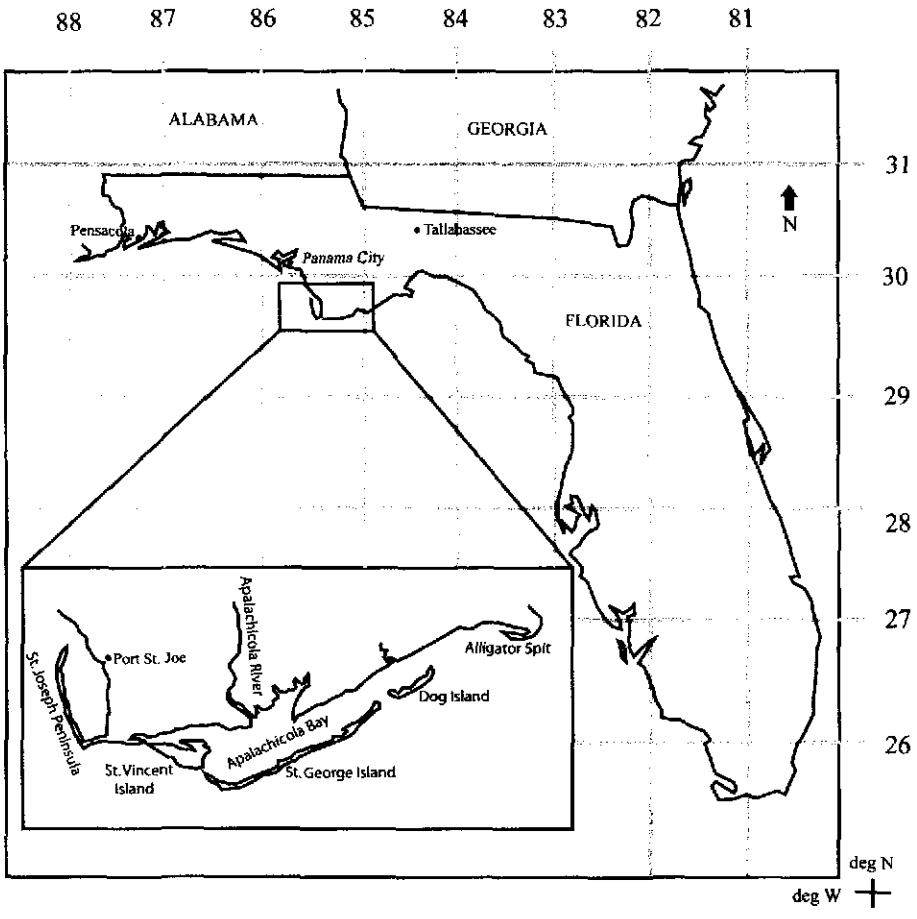

Figure 5- Location map. The St. Joseph Peninsula is located in northwestern Florida.

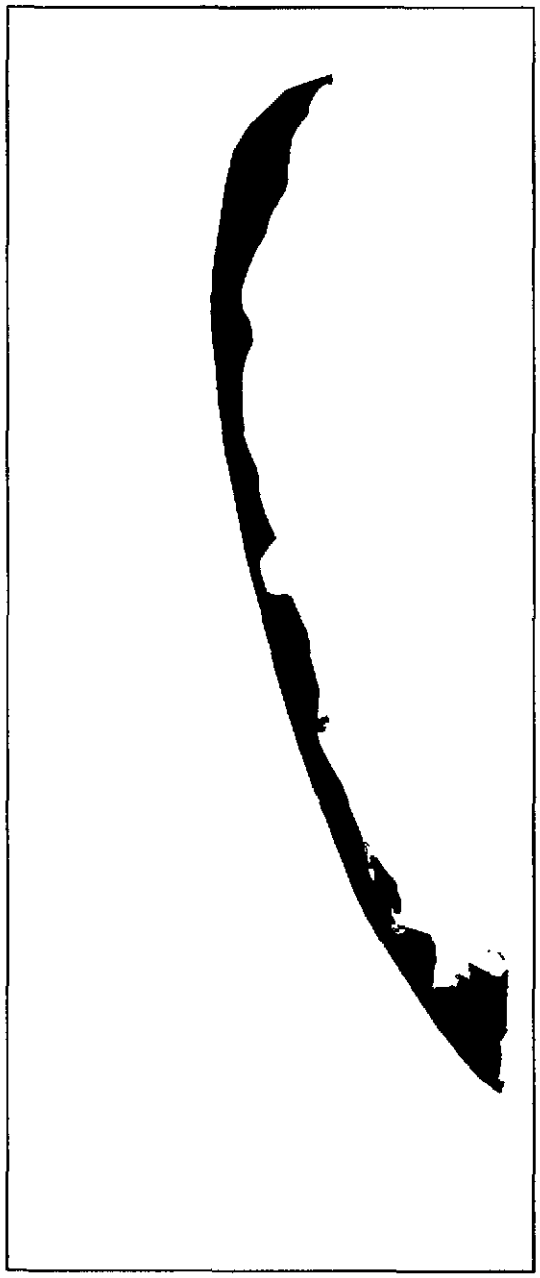

Figure 6- Bathymetric map of the area surrounding the St. Joseph Peninsula. The contour interval is 1.5 m (Hatchett, 1998).

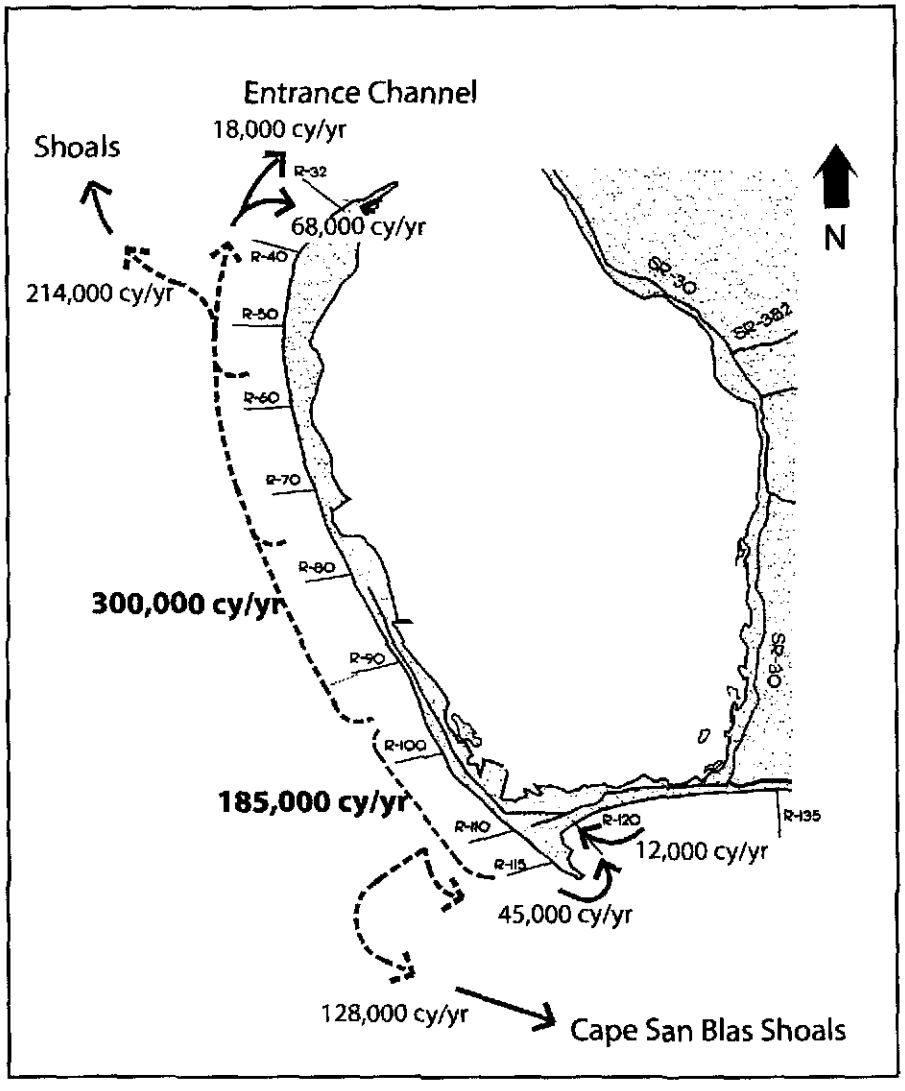

Figure 7- Approximately 485,000 cy/yr of sand is eroded from the peninsula. Of this 300,000 cy/yr is transported north and 185,000 cy/yr is transported south. Of the material transported north, 214,000 cy/yr is deposited in shoals northwest of the peninsula, 18,000 cy/yr is deposited at the St. Joseph Bay entrance channel and is dredged and deposited offshore and 68,000 cy/yr accumulates at the north end of the peninsula. Of the material transported south, 45,000 cy/yr accumulates at Cape San Blas, 12,000 cy/yr is deposited on the east side of Cape San Blas and 128,000 cy/yr is deposited on the Cape San Blas shoal. Solid lines represent deposition while dashed lines represent erosion. (FDEP. 1998)

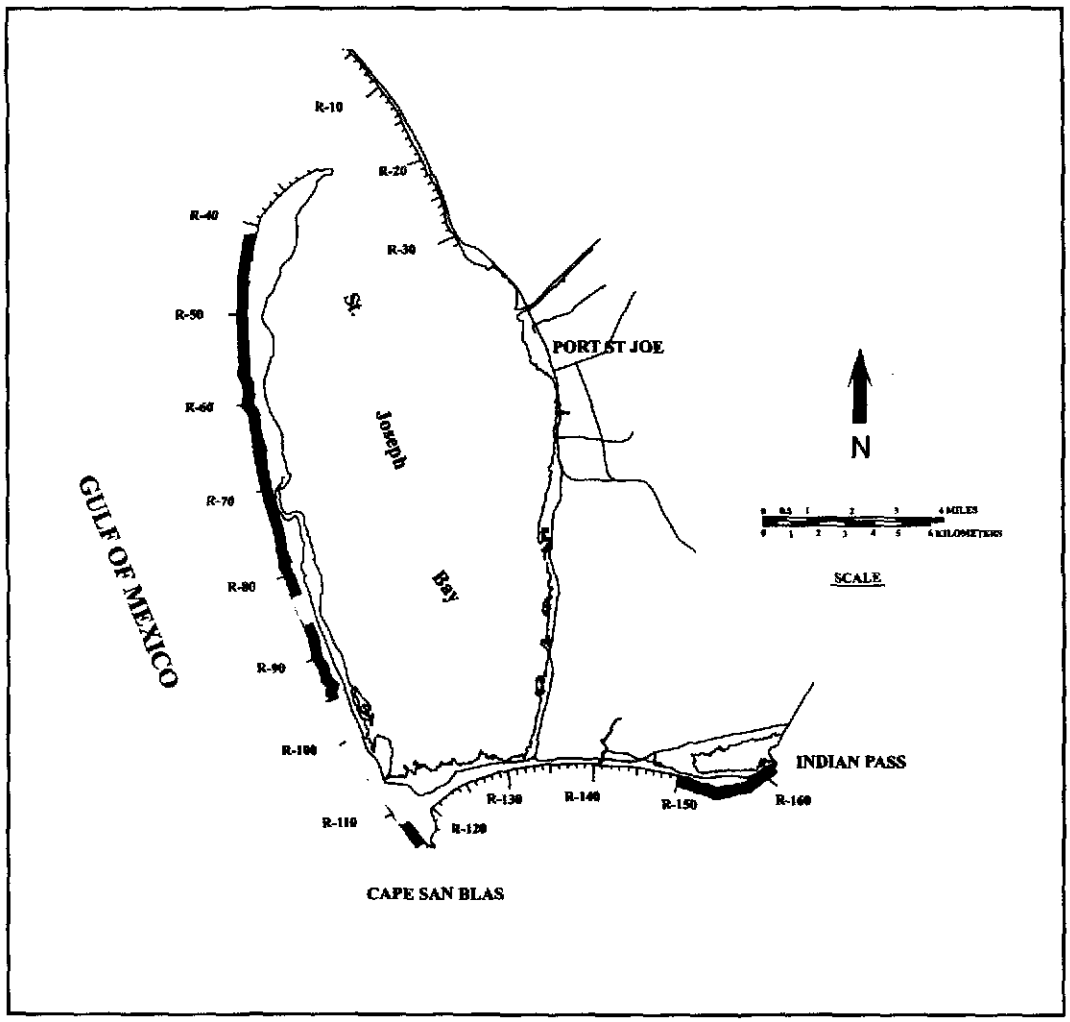

Figure 8-Erosion along the St. Joseph Peninsula. Areas of critical erosion are shown in gray while areas of non critical erosion are shown in black. R-values refer to range monument locations along the peninsula (FDEP, 2001).

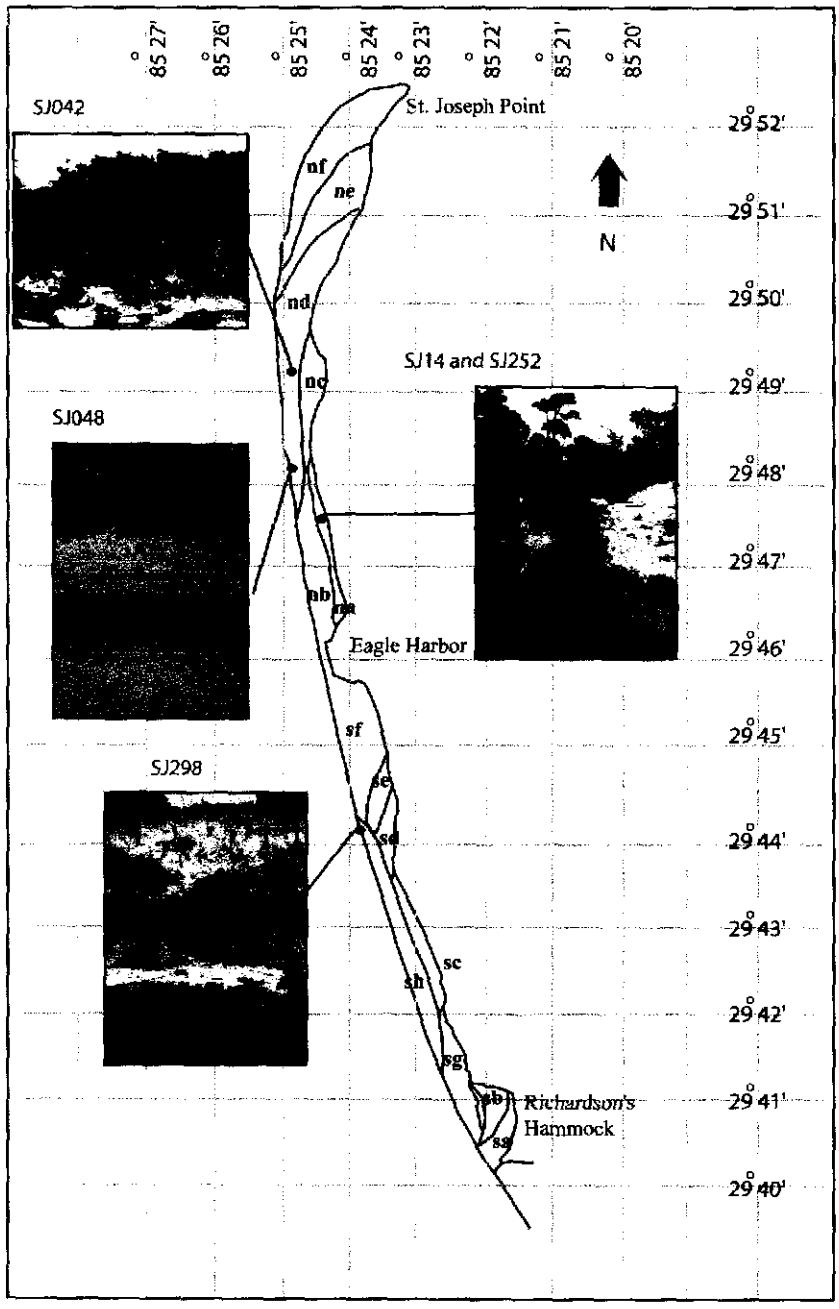

Figure 9- Sample locations. Beach ridge set boundaries were determined by Rizk (1991). Photos SJ048 and SJ298 were taken looking east. Photos SJ042 and SJ14/252 were taken looking south and north respectively.

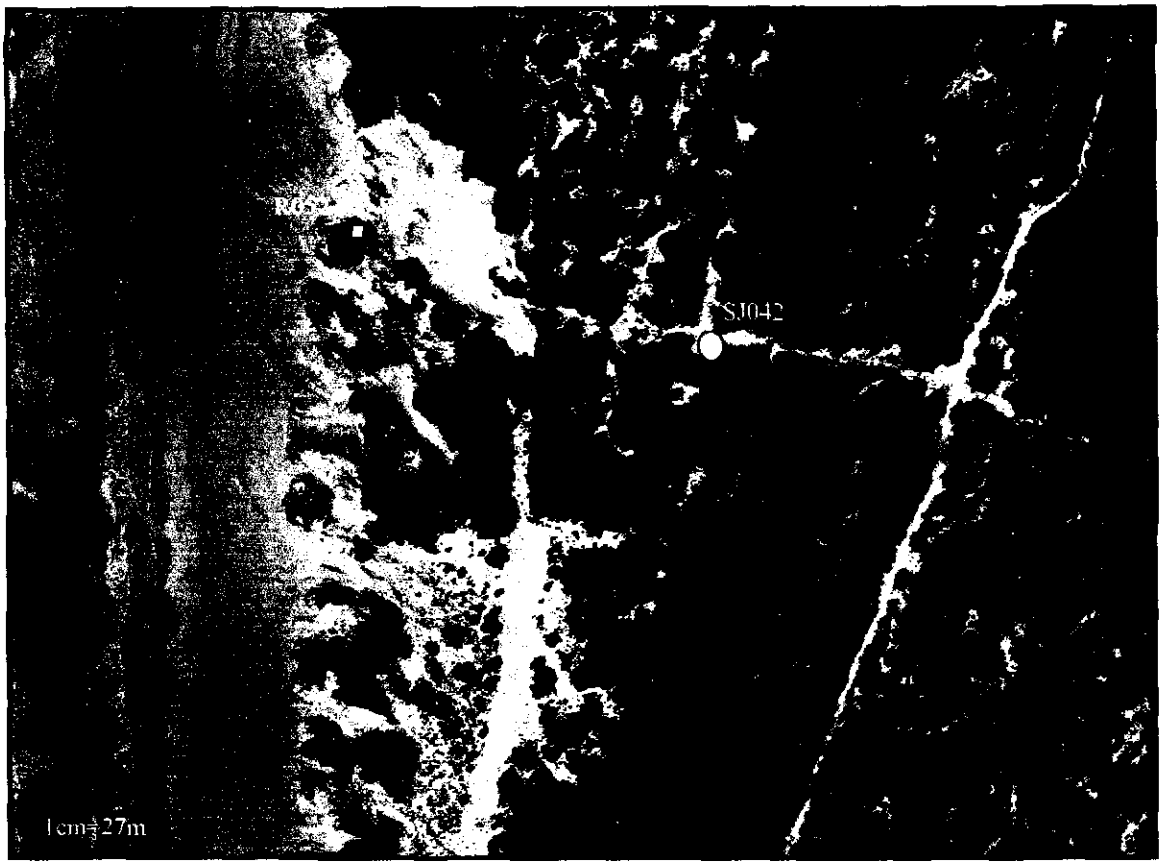

Figure 10- Location of the SJ042 trench. The solid white square shows the location of range monument R052GU83. (Florida Department of Natural Resources, 1998)

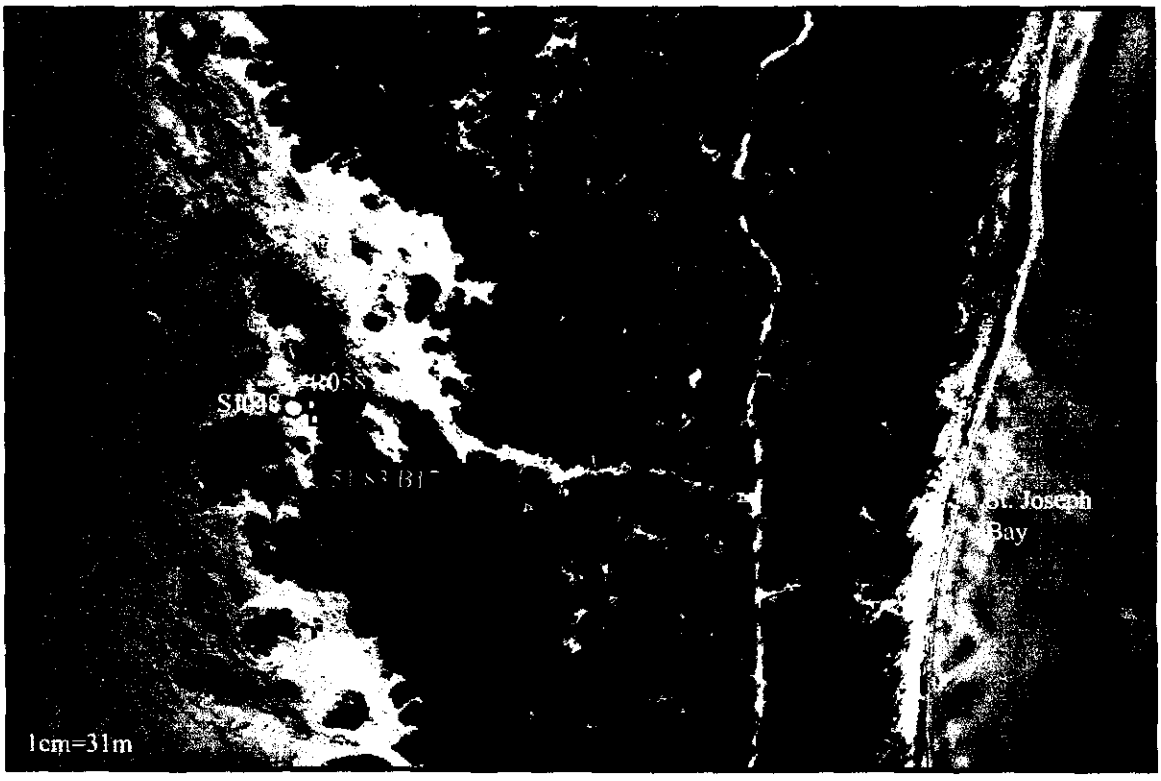

Figure 11- Location of the SJ048A and SJ048B trench. The solid white squares show the locations of range monuments R058GU83 and 5183B17. (Florida Department of Natural Resources, 1998)

Figure 12- Location of SJ298 trench. The solid white square shows the location of range monument R084GU83. (Florida Department of Natural Resources)

sample	N		W	
	°	'	°	'
SJ019	29	51.125	85	24.852
SJ018	29	50.954	85	24.888
SJ016	29	50.609	85	24.966
SJ015	29	50.436	85	25.002
SJ014	29	50.256	85	25.023
SJ013	29	50.086	85	25.037
SJ012	29	49.908	85	25.042
SJ011	29	49.724	85	25.047
SJ010	29	49.544	85	25.032
SJ009	29	49.372	85	25.031
SJ006	29	49.206	85	25.000
SJ007	29	49.048	85	24.980
SJ008	29	48.888	85	24.979
SJ005	29	48.714	85	24.943
SJ004	29	48.557	85	24.924
SJ003	29	48.367	85	24.904
SJ070	29	48.366	85	24.911
SJ023	29	48.027	85	24.833
SJ024	29	47.879	85	24.757
SJ071	29	47.684	85	24.758
SJ025	29	47.336	85	24.693
SJ026	29	47.006	85	24.609
SJ027	29	46.671	85	24.536
SJ029	29	46.016	85	24.350
SJ072	29	46.010	85	24.364
SJ073	29	46.014	85	24.353
SJ030	29	45.686	85	24.281
SJ049	29	44.886	85	24.006
SJ050	29	44.088	85	23.704
SJ051	29	43.338	85	23.393
SJ052A	29	42.560	85	23.060
SJ052B	29	42.548	85	23.074
SJ054	29	41.798	85	22.879
SJ055	29	41.788	85	22.894
SJ056	29	41.070	85	22.213
SJ057	29	41.063	85	22.232
SJ058	29	40.780	85	21.995
SJ059	29	40.768	85	22.011

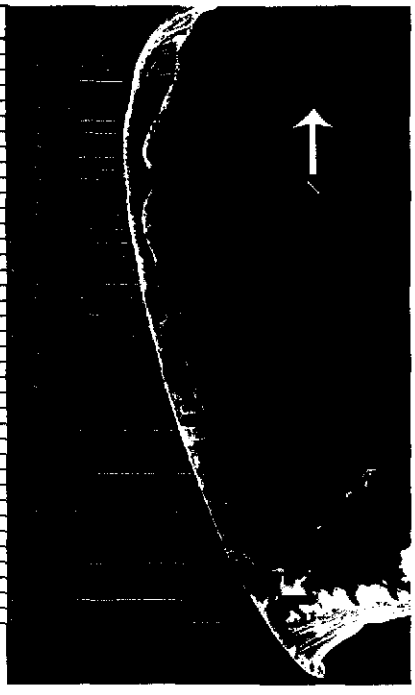

Figure 13- Latitude, longitude and map location of littoral samples (modified from USGS, 1999)

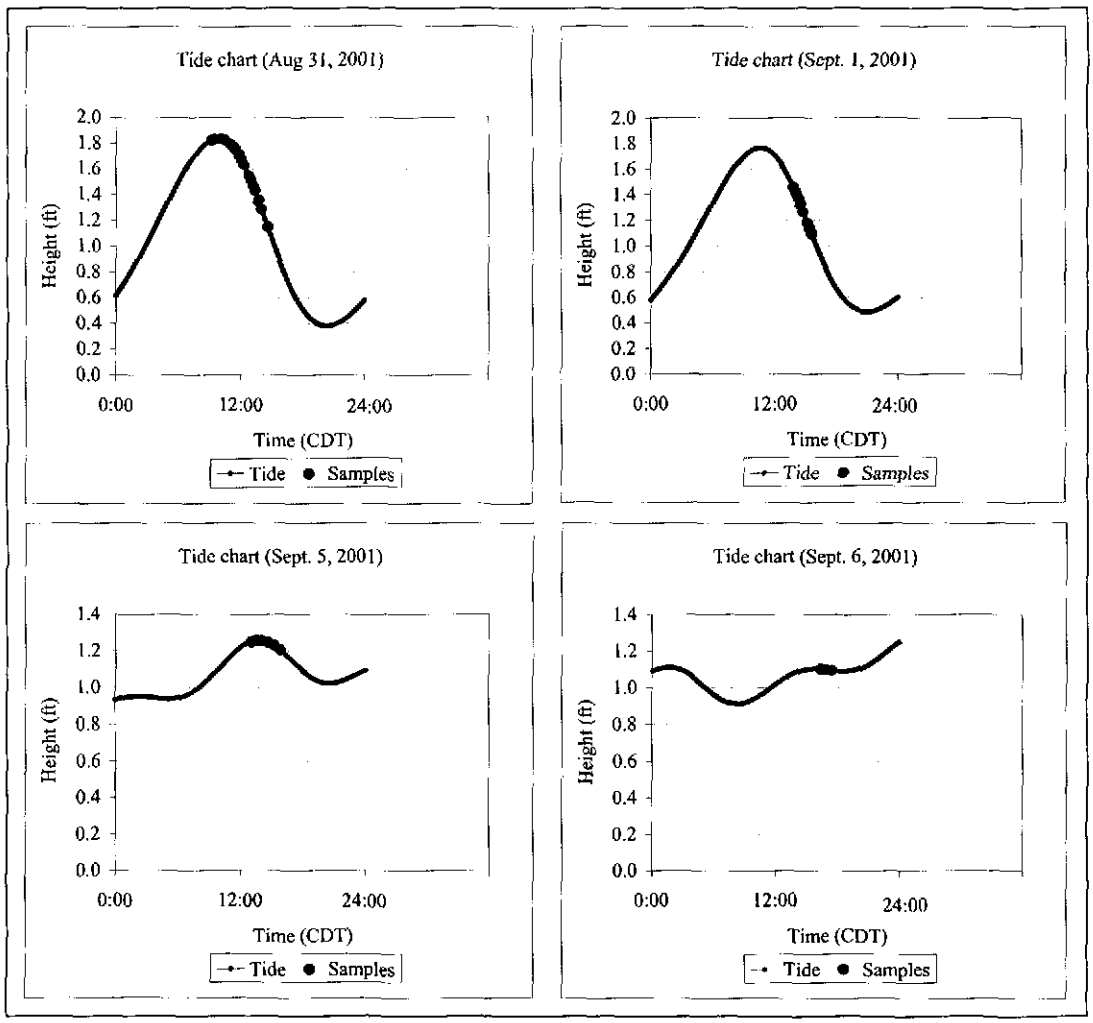

Figure 14- Littoral sample collection times and corresponding tide level. All littoral samples were collected during a falling tide. CDT refers to central time.

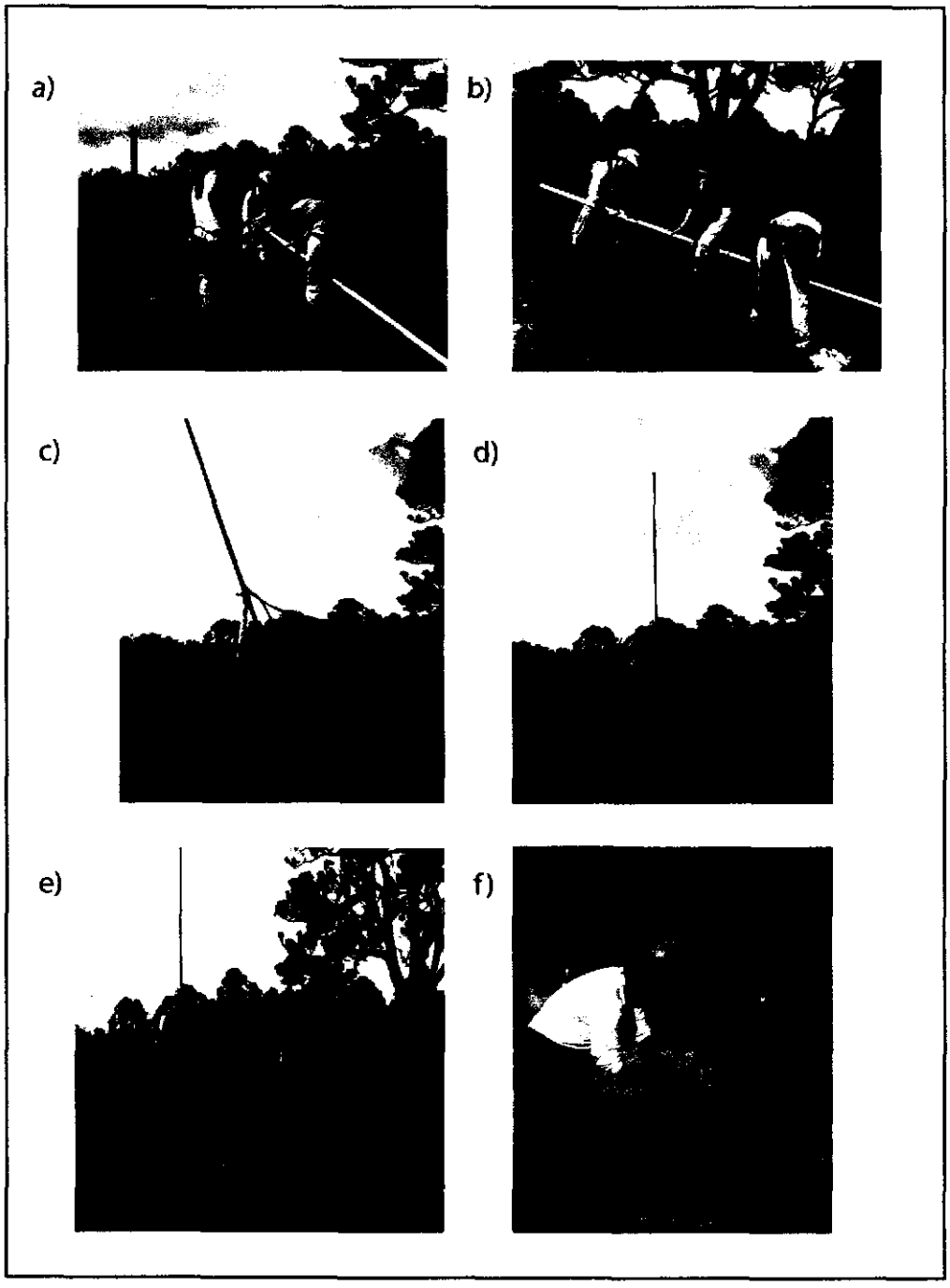

Figure 15- Vibracoring methods. (a) and (b) show the vibrator being fitted onto the aluminum irrigation pipe. (c) shows the irrigation pipe being put into position. (d), (e) and (f) show the pipe being driven into the ground

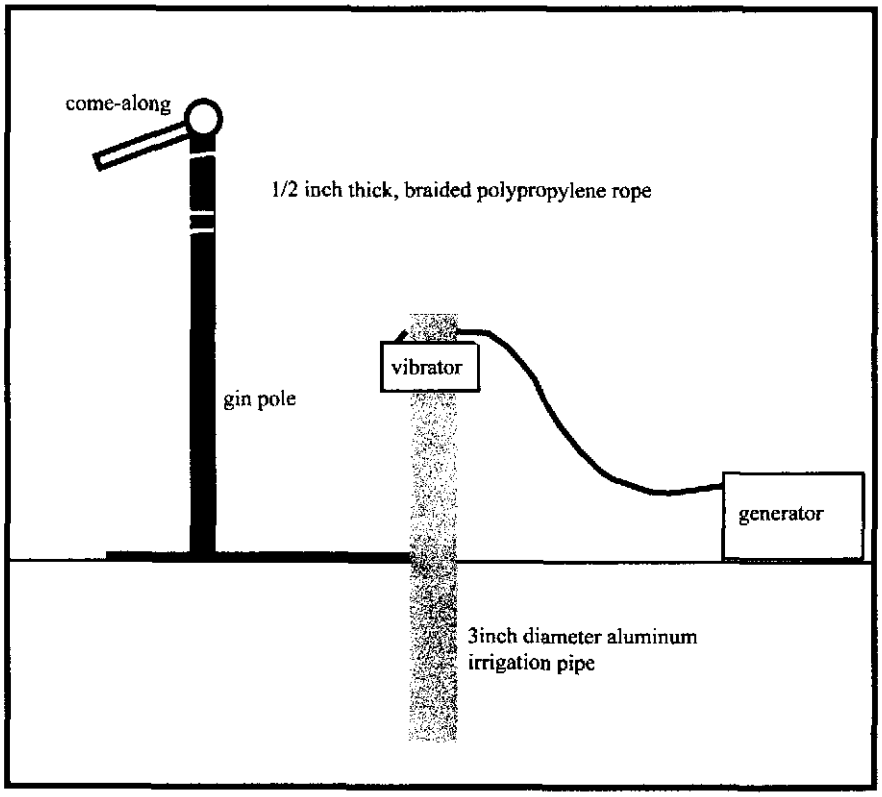

Figure 16- Core extraction using a gin pole constructed at McMaster University.

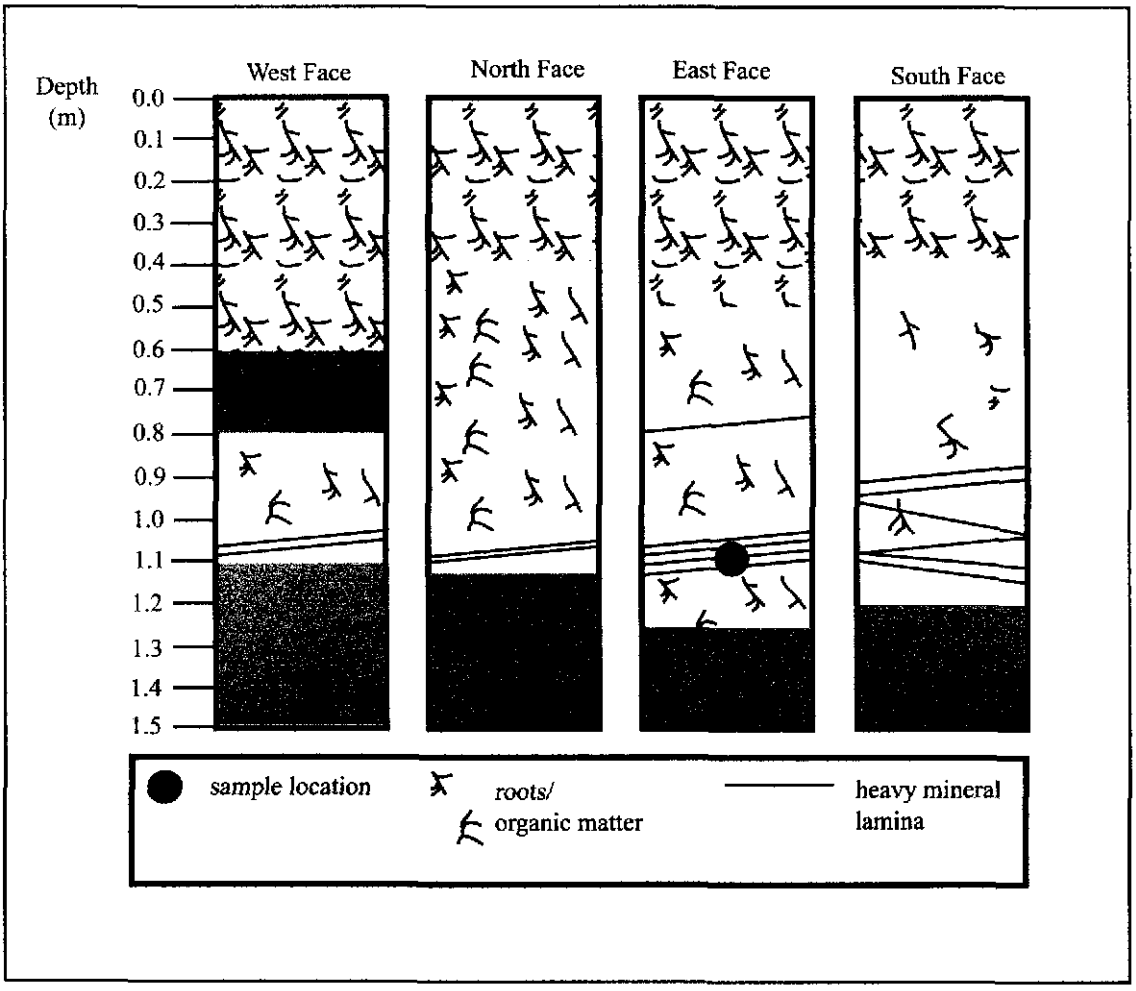

Figure 17- SJ14B sample location. Grey areas represent unexposed areas

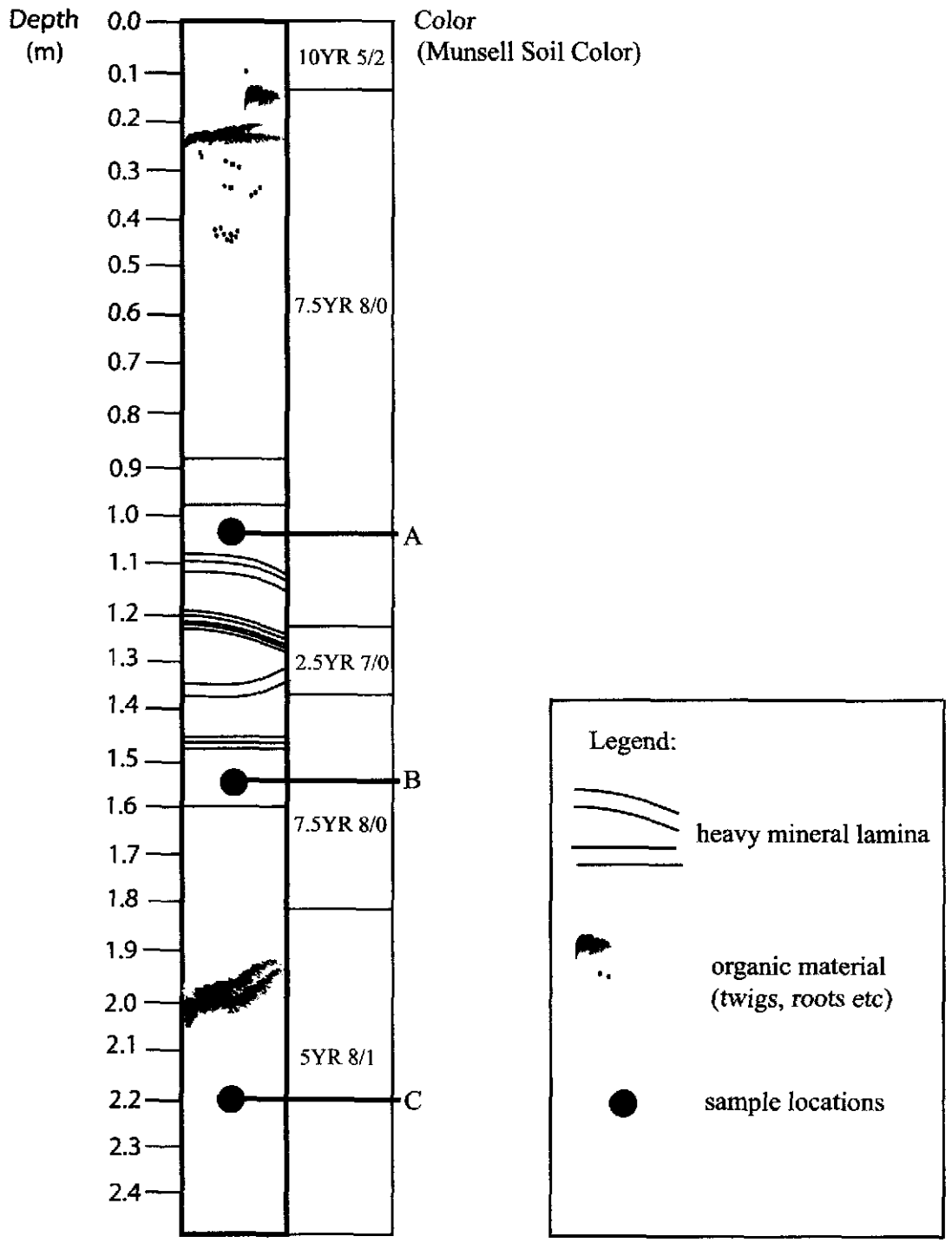

Figure 18- Sample locations in core SJ252. The solid circles represent the sampling locations. Solid black lines indicate heavy mineral lamina.

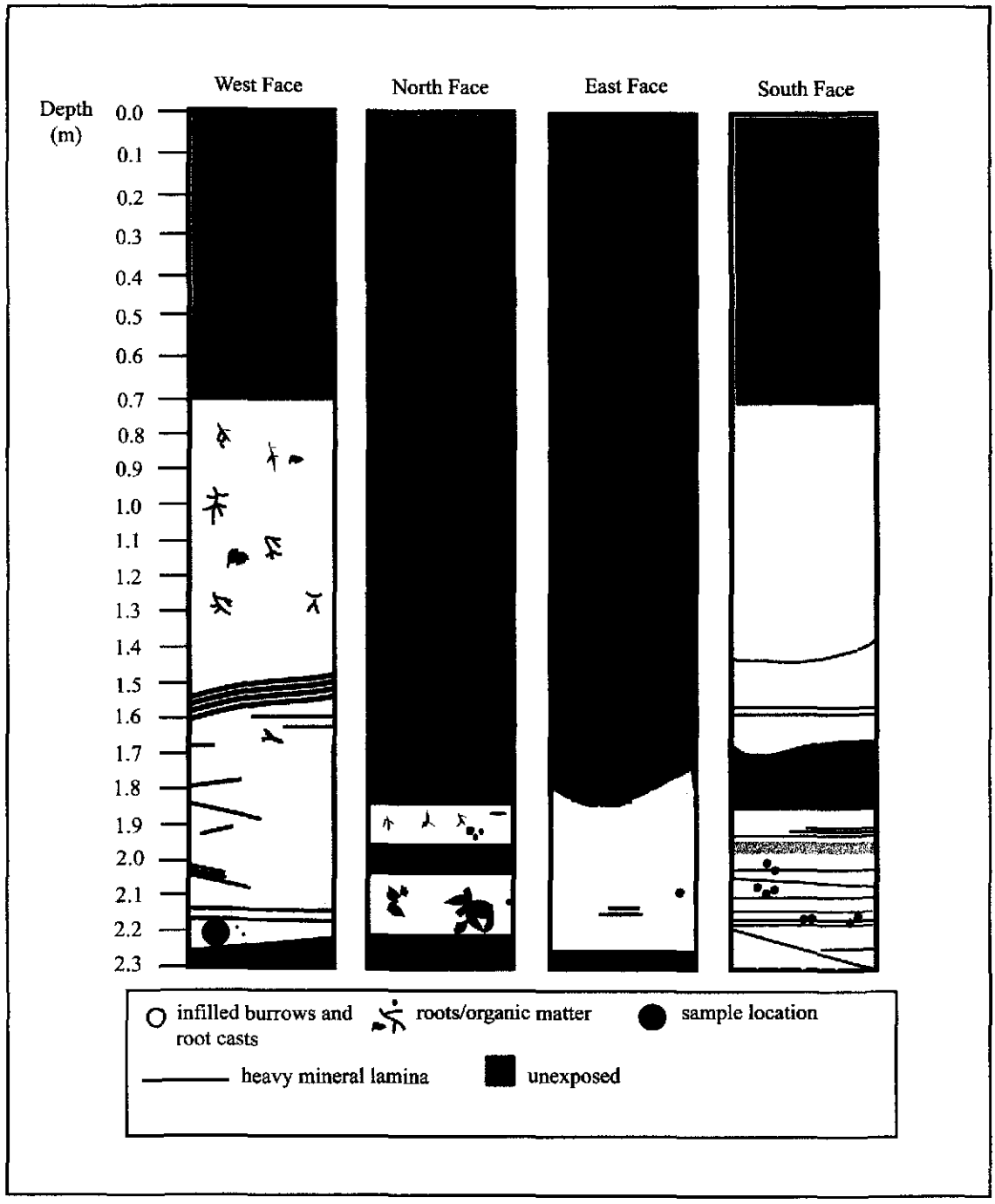

Figure 19- SJ042A sample location. Variations in the shades of grey indicate the variations in color of the quartz sand units. Black lines and grey lines represent heavy mineral lamina. White regions represent areas of post depositional bioturbation

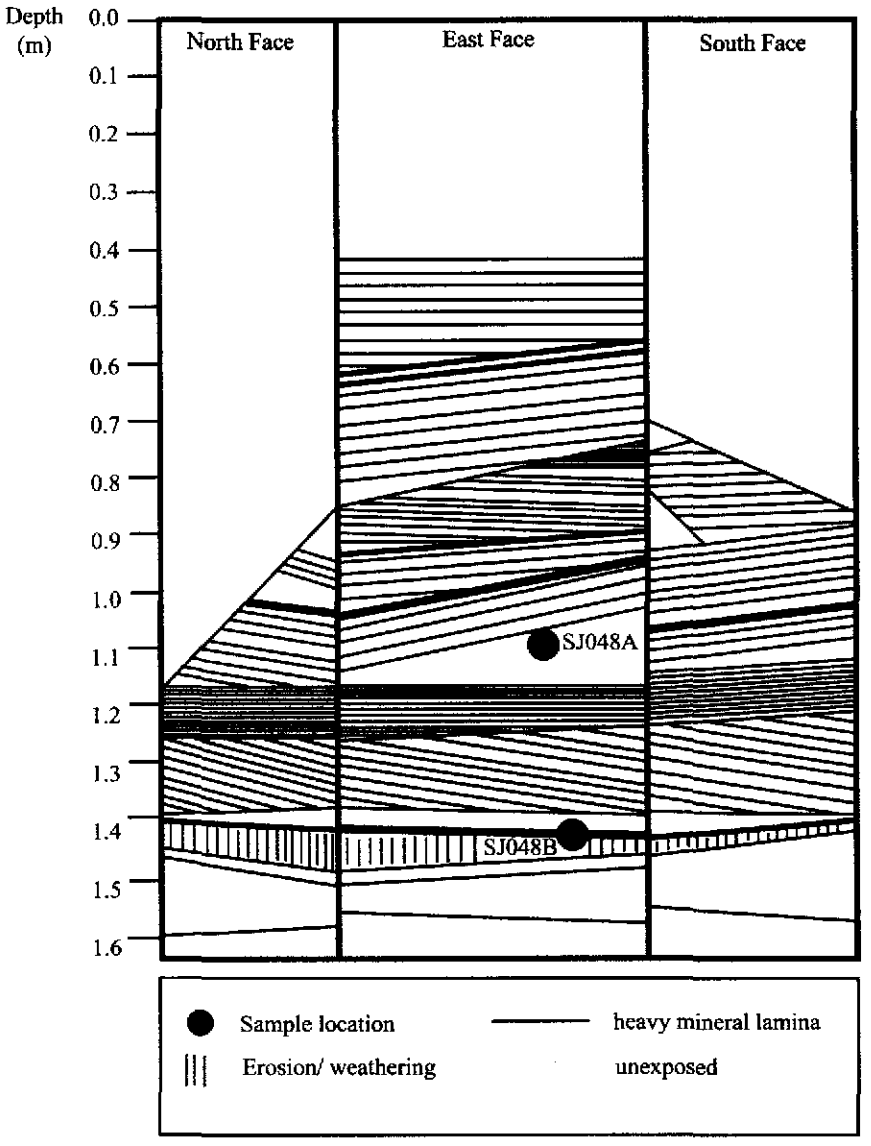

Figure 20- SJ048 sample locations. Bulk dating samples were collected from the east face of this exposure. There is 4 m of unexposed overburden above the 0 m depth mark on this figure. The units showing "erosion/weathering" are units with loosely packed grains that have undergone selective weathering.

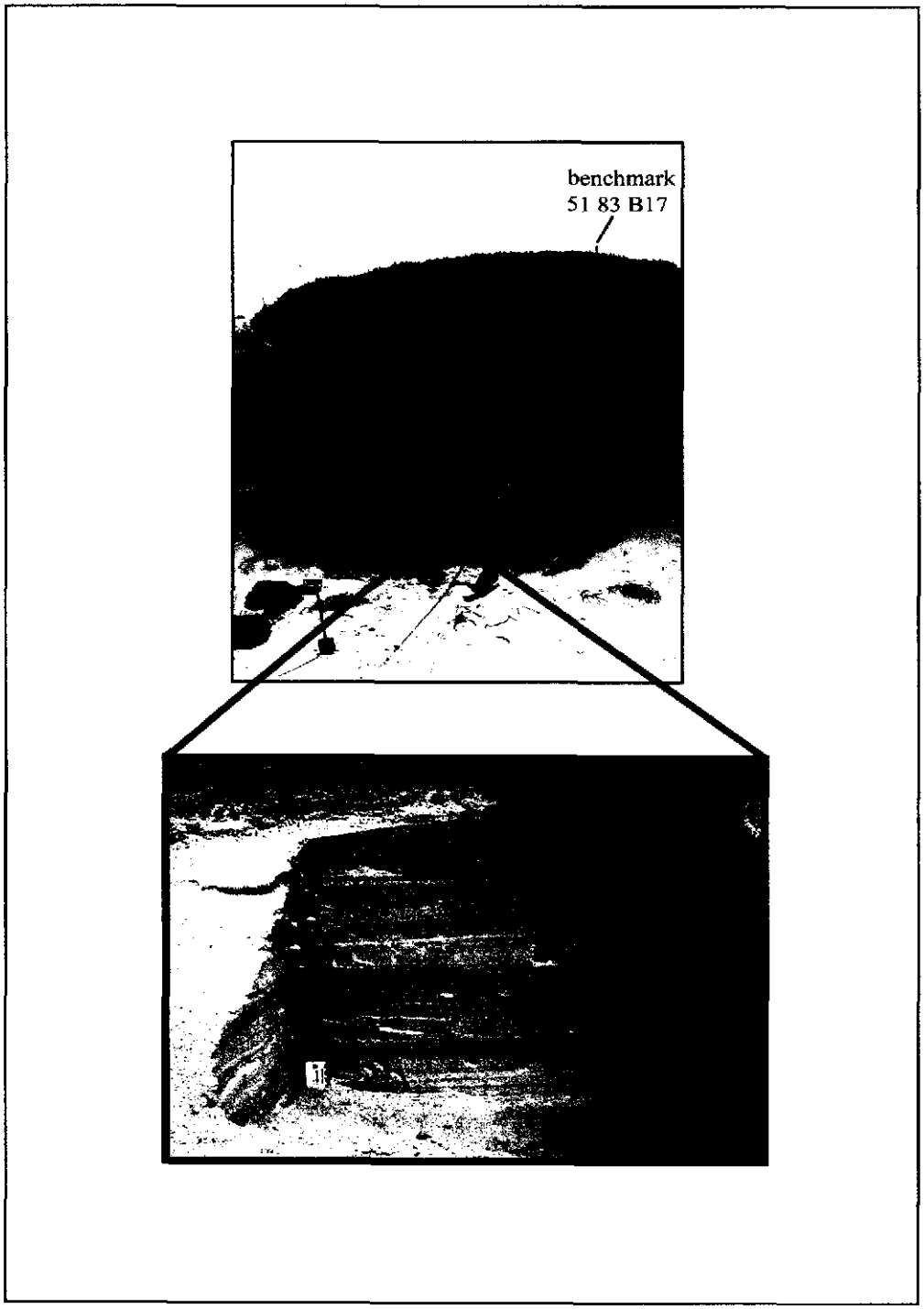

Figure 21- Trench at SJ048. Approximate SJ048A and SJ048B sample locations are shown by solid black circles.

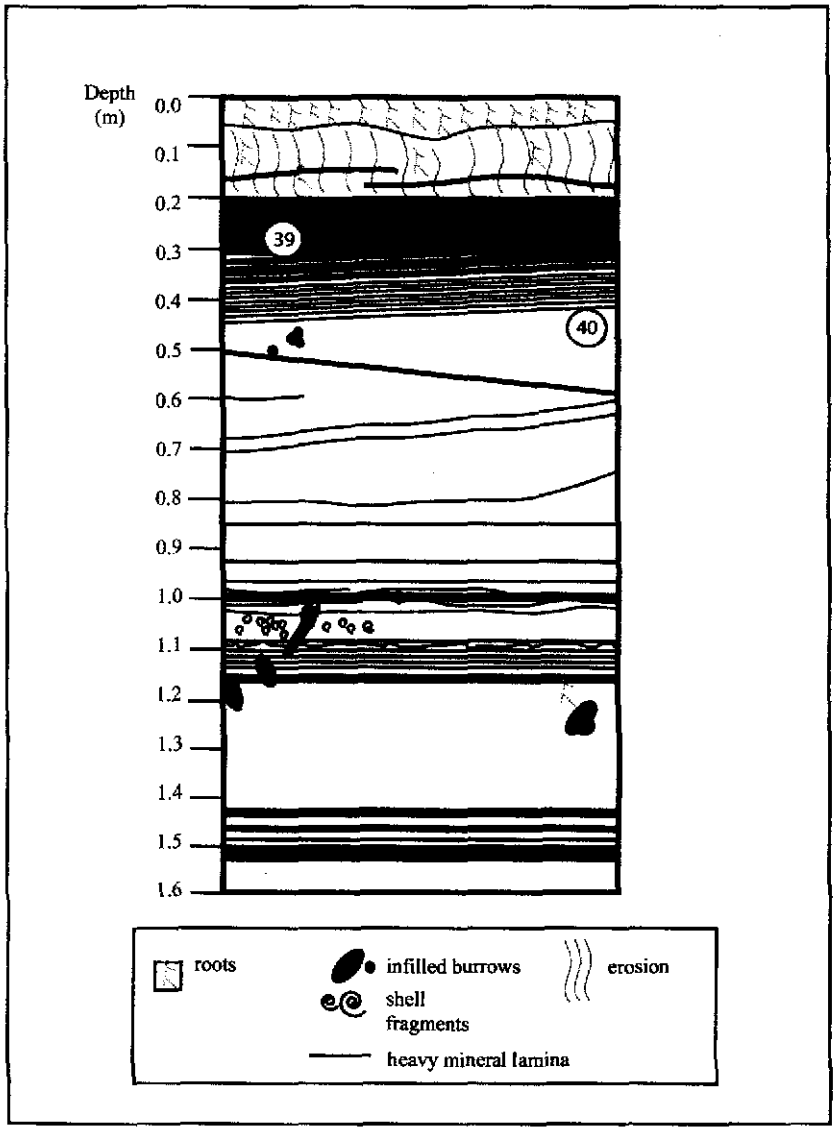

Figure 22- Location of the SJ298 samples. Bulk samples were collected from a storm Deposit on White Sands Dr., St. Joseph Peninsula, Florida. There is 3 m of overburden above the 0 m depth mark on this figure. Areas that show "erosion" are units with loosely packed grains that have experienced selective weathering.

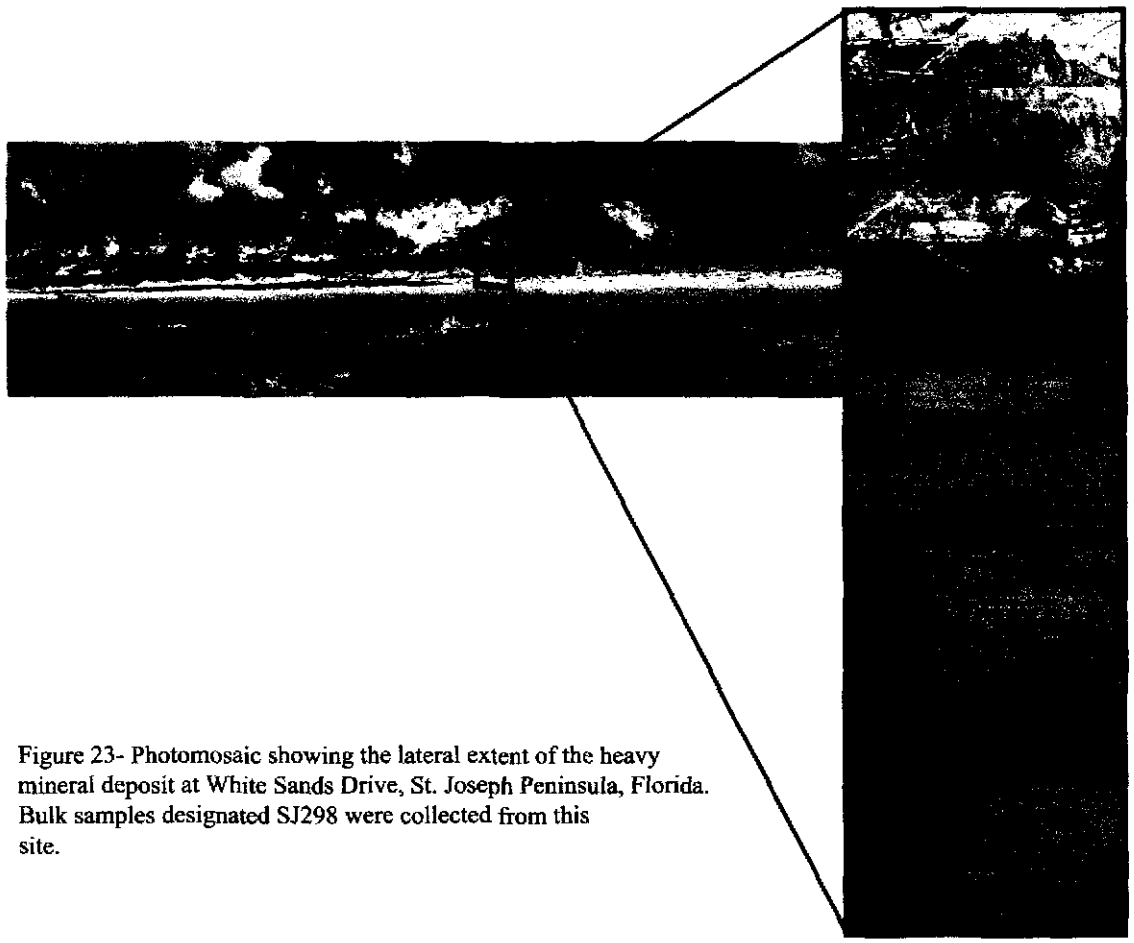

Figure 23- Photomosaic showing the lateral extent of the heavy mineral deposit at White Sands Drive, St. Joseph Peninsula, Florida. Bulk samples designated SJ298 were collected from this site.

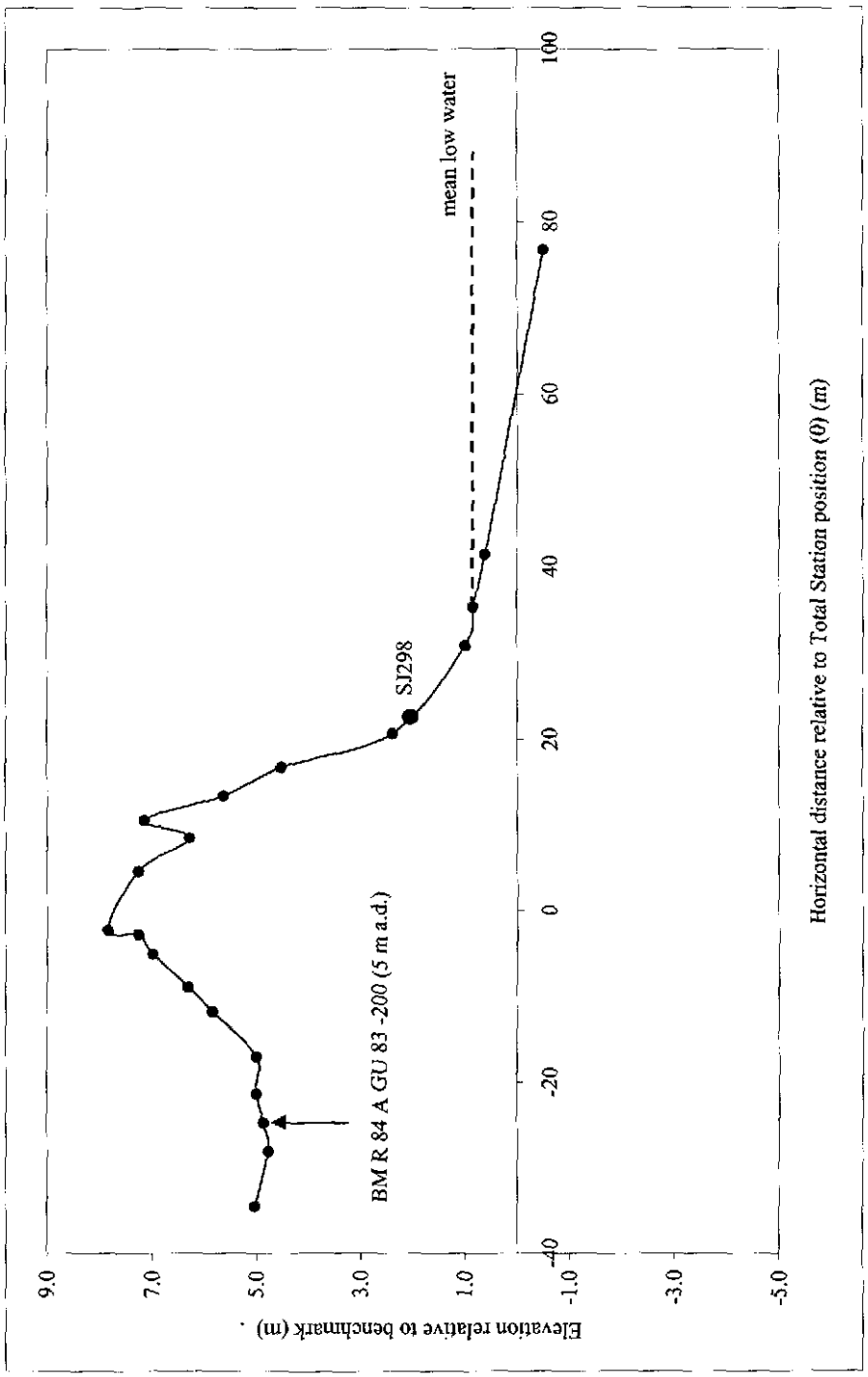

Figure 24- Beach profile at SJ298 sample location.

Table 1- Dune ridge sample depths

sample	sample depth in trench (m)	Overburden * (m)	Actual sample depth (m)
SJ14B	1.10	0.00	1.10
SJ042A	1.49	0.73	2.22
SJ048A	0.70	4.08	4.78
SJ048B	1.04	4.08	5.12
SJ252A	1.10	0.00	1.10
SJ252B	1.59	0.00	1.59
SJ252C	2.24	0.00	2.24
SJ298-39	0.28	3.30	3.58
SJ298-40	0.43	3.30	3.73

* estimated from photos taken at the time of sample collection

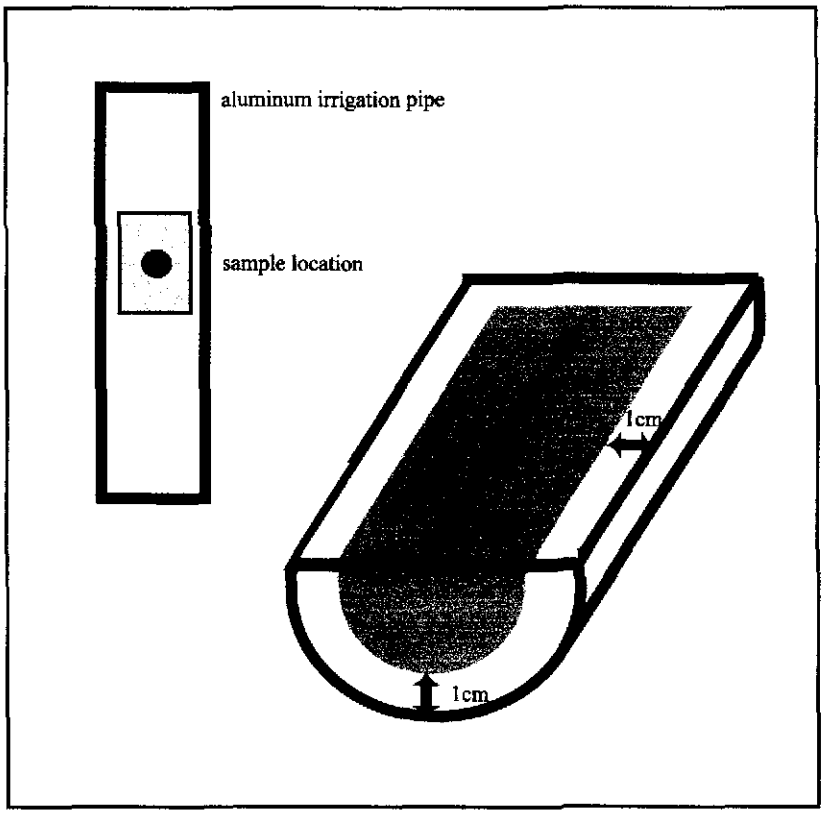

Figure 25- Sample removed from large core samples. The shaded area represents the 100 grams collected as a dating sample.

Table 2 - Dosimetry for the dune ridge samples

150-212μm		NAA Results			Internal Dose Rates	External Dose Rates			
sample	moisture content	U (ppm)	Th (ppm)	K (%)	beta dose rate	gamma dose rate (μGy/a)	cosmic dose (μGy/a)	beta dose rate (μGy/a)	Total dose rate (μGy/a)
SJ14B	0.0192	0.49 +/- 0.1	2.1 +/- 0.2	0.0054 +/- 0.0009	3.5 +/- 0	50 +/- 1.1	196.67	93.7 +/- 11.3	352.7 +/- 11.4
SJ042A	0.0423	0.19 +/- 0.1	0.6 +/- 0.1	0.0027 +/- 0.0008	3.5 +/- 0	23.5 +/- 0.4	196.18	32.2 +/- 10.6	264.3 +/- 10.7
SJ048A	0.0532	0.12 +/- 0.1	0.6 +/- 0.1	0.0088 +/- 0.0011	3.5 +/- 0	109 +/- 1.4	178.03	28.8 +/- 10.5	328.3 +/- 10.6
SJ048B	0.0167	1.31 +/- 0.1	6.1 +/- 0.4	0.0045 +/- 0.0012	3.5 +/- 0	132 +/- 2.3	176.12	252.6 +/- 12.9	573.1 +/- 13.1
SJ252A	0.0222	0.29 +/- 0.1	0.7 +/- 0.1	0.0044 +/- 0.0720	3.5 +/- 0	65.8 +/- 20.9	196.67	46.5 +/- 52.7	321.4 +/- 56.7
SJ252B	0.0377	0.21 +/- 0.1	0.3 +/- 0.0	0.0056 +/- 0.0720	3.5 +/- 0	38 +/- 20.1	187.98	31.3 +/- 51.9	269.7 +/- 55.6
SJ252C	0.1163	0.07 +/- 0.1	0.3 +/- 0.0	0.0008 +/- 0.0720	3.5 +/- 0	20.2 +/- 18.8	179.97	12.2 +/- 48.2	224.8 +/- 51.8

212-250μm		NAA Results			Internal Dose Rates	External Dose Rates			
sample	moisture content	U (ppm)	Th (ppm)	K (%)	beta dose rate (μGy/a)	gamma dose rate (μGy/a)	cosmic dose (μGy/a)	beta dose rate (μGy/a)	Total dose rate (μGy/a)
SJ14B	0.0192	0.49 +/- 0.1	2.1 +/- 0.2	0.0054 +/- 0.0009	4.2 +/- 0	50 +/- 1.1	196.67	87.1 +/- 10.6	364.4 +/- 12.8
SJ042A	0.0423	0.19 +/- 0.1	0.6 +/- 0.1	0.0027 +/- 0.0008	4.2 +/- 0	23.5 +/- 0.4	196.18	30 +/- 10	262.8 +/- 10
SJ048A	0.0532	0.12 +/- 0.1	0.6 +/- 0.1	0.0088 +/- 0.0011	4.2 +/- 0	109 +/- 1.4	178.03	27 +/- 9.9	327.1 +/- 10
SJ048B	0.0167	1.31 +/- 0.1	6.1 +/- 0.4	0.0045 +/- 0.0012	4.2 +/- 0	132 +/- 2.3	176.12	234.2 +/- 12	555.4 +/- 12.2
SJ252A	0.0222	0.29 +/- 0.1	0.7 +/- 0.1	0.0044 +/- 0.0720	4.2 +/- 0	65.8 +/- 20.9	196.67	43.5 +/- 51.6	319 +/- 55.7
SJ252B	0.0377	0.21 +/- 0.1	0.3 +/- 0.0	0.0056 +/- 0.0720	4.2 +/- 0	38 +/- 20.1	187.98	29.4 +/- 50.8	268.5 +/- 54.7
SJ252C	0.1163	0.07 +/- 0.1	0.3 +/- 0.0	0.0008 +/- 0.0720	4.2 +/- 0	20.2 +/- 18.8	179.97	11.3 +/- 47.3	224.6 +/- 50.9

125-250μm		NAA Results			Internal Dose Rates	External Dose Rates			
sample	moisture content	U (ppm)	Th (ppm)	K (%)	beta dose rate (μGy/a)	gamma dose rate (μGy/a)	cosmic dose (μGy/a)	beta dose rate (μGy/a)	Total dose rate (μGy/a)
SJ298-39	0.0500	35.9 +/- 0.1	101.5 +/- 1.6	0.0178 +/- 0.0031	3.7 +/- 0	6882.14 +/- 20.33	185.43	5413.1 +/- 28.9	12493.2 +/- 35.3
SJ298-40	0.0456	0.06 +/- 0.01	0.33 +/- 0.03	0.0071 +/- 0.0007	3.7 +/- 0	1690.16 +/- 9.92	184.68	16.7 +/- 10.3	1891.5 +/- 14.3

250-300μm		NAA Results			Internal Dose Rates	External Dose Rates			
sample	moisture content	U (ppm)	Th (ppm)	K (%)	beta dose rate (μGy/a)	gamma dose rate (μGy/a)	cosmic dose (μGy/a)	beta dose rate (μGy/a)	Total dose rate (μGy/a)
SJ298-39	0.0500	35.9 +/- 0.1	101.5 +/- 1.6	0.0178 +/- 0.0031	4.5 +/- 0	6882.14 +/- 20.33	185.43	4935.3 +/- 25.9	12016.2 +/- 32.9
SJ298-40	0.0456	0.06 +/- 0.01	0.33 +/- 0.03	0.0071 +/- 0.0007	4.5 +/- 0	1690.16 +/- 9.92	184.68	15.4 +/- 9.5	1890.3 +/- 13.7

notes:
cosmic dose rate calculations include only hard cosmic rays
gamma dose rates for SJ14B, SJ042A, SJ048A, SJ048B, SJ298-39 and SJ298-40 were measured in situ
gamma dose rates for SJ252A, SJ252B and SJ252C were calculated using the U, Th, and K contents
cosmic dose rates were calculated assuming a 1pi geometry for all samples except SJ14B and SJ252A,B&C
In all cases the internal alpha dose rate is 8.8 +/- 0.6 mGy/a and the external alpha dose rate is 0 mGy/a

Table 3- Protocol for estimating equivalent doses and testing for feldspar contamination

1) Preheat (220 °C) at a rate of 10 °C/s for 10 s
2) Natural OSL- stimulate for 100 s at 125 °C
3) Beta Dose (6 Gy)
4) Preheat (220 °C) at a rate of 10 °C/s for 10 s
5) OSL- stimulate for 100 s at 125 °C
6) Beta Dose (6 Gy)
7) Preheat (220 °C) at a rate of 10 °C/s for 10 s
8) IRSL

Table 4 - Test and regeneration doses for dune ridge samples

sample	test dose	r1	r2	r3	r4	r5	r6
SJ14B	0.5	0.3	0.5	1.0	1.5	0	0.3
SJ042A	0.5	0.4	0.6	0.8	-	0	0.4
SJ048A	0.3	0.4	0.6	0.8	-	0	0.4
SJ048B	0.3	0.4	0.6	0.8	-	0	0.4
SJ252A	0.5	0.3	0.5	1.0	-	0	0.3
SJ252B	0.5	0.3	0.5	1.0	-	0	0.3
SJ252C	0.5	0.3	0.5	1.0	-	0	0.3
SJ298-39	0.3	0.4	0.6	0.8	-	0	0.4
SJ298-40	0.3	0.4	0.6	1.0	-	0	0.4

note: all doses are expressed in Gy (1Gy=10s)

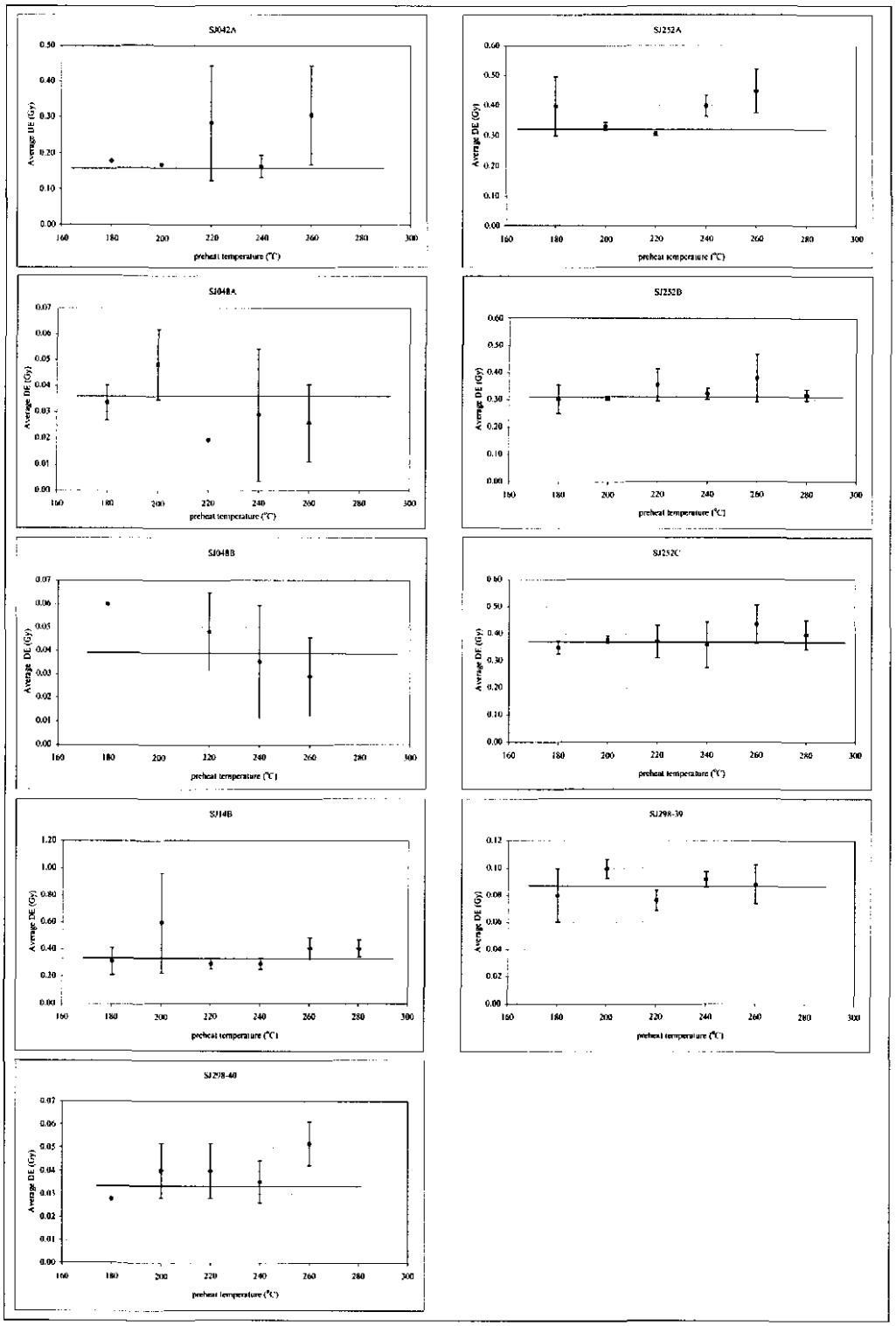

Figure 26- Preheat plateau test results for the dune ridge samples. The black lines represent the plateau region. All measurements were done using a 5mm mask and the 150-212μm fraction of each sample, with the exception of SJ298-39 and SJ298-40 where the 125-250μm grain size fraction was used.

Table 5- SAR protocol

1) Preheat (220°C) at rate of 10°C/s for 10s
2) Natural OSL- stimulate for 100s at 125°C
3) Test dose
4) Heat to 160°C at rate of 10°C/s
5) OSL-stimulate for 100s at 125°C
6) Dose (R1)
7) Preheat (220°C) at rate of 10°C/s for 10s
8) OSL-stimulate for 100s at 125°C
9) Repeat steps 3-8 using R2, R3, R4, R5, R6

Table 6- Systematic errors applied to age calculations in Anatol v.072B

parameter	error (%)
paleodose measurement	1.5
U, Th, K (grain and environment)	5
alpha efficiency	2
internal beta dose rate (beta counting)	3
alpha counting	7.7
external beta dose rate (beta counting)	4
external alpha dose rate (alpha counting)	7.7
gamma dose rate (in situ)	2
etching coefficients	5
F value	0.2

Table 7- Beta Absorbed Fractions

		beta absorbed fractions		
grain size fraction (μm)	mean grain size (μm)	U-238	Th-232	K-40
150-212	181	0.1370	0.1950	0.0633
212-250	231	0.1600	0.2200	0.0800
125-250	188	0.1406	0.1994	0.0661
250-300	275	0.1790	0.2400	0.0965

(source: Mejdahl, 1979)

Table 8- Etching Coefficients

grain size fraction (μm)	mean grain size (μm)		U-238	Th-232
150-212	181	alpha	0.0800	0.1000
		beta	0.8700	0.8200
212-250	231	alpha	0.0600	0.0700
		beta	0.8400	0.7700
125-250	188	alpha	0.0700	0.0900
		beta	0.8600	0.8100
250-300	275	alpha	0.0500	0.0600
		beta	0.8300	0.7600

etching depth = 9μm (40 minute HF treatment) (Mejdahl, 1979)
beta values from Brennan, 2003
alpha values from Brennan et al, 1991

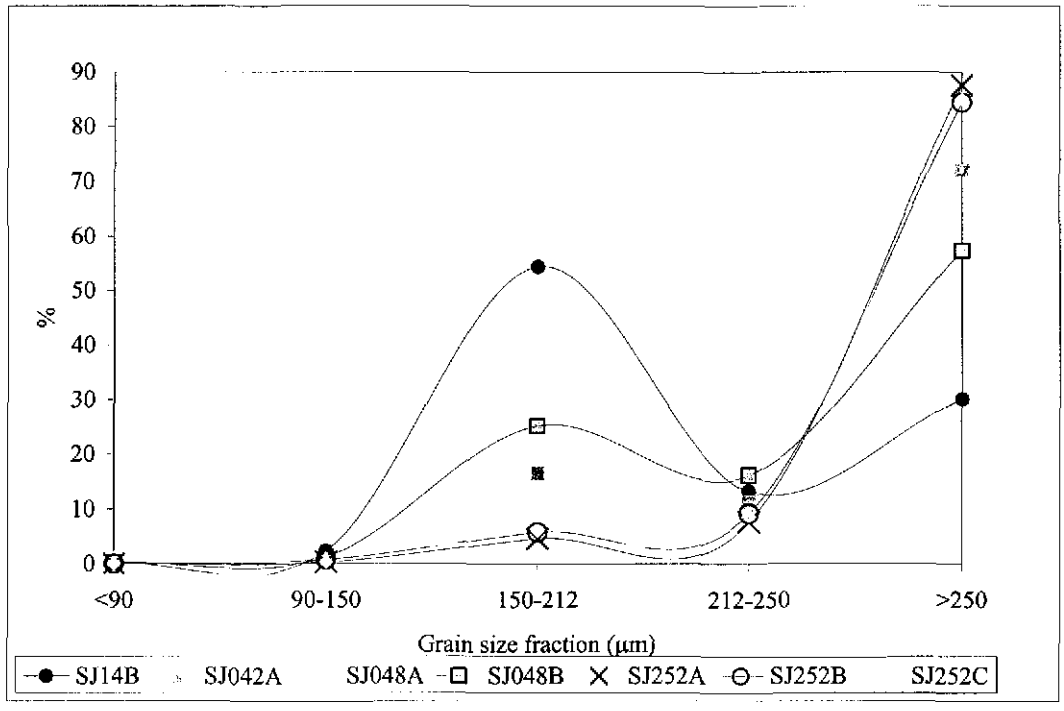

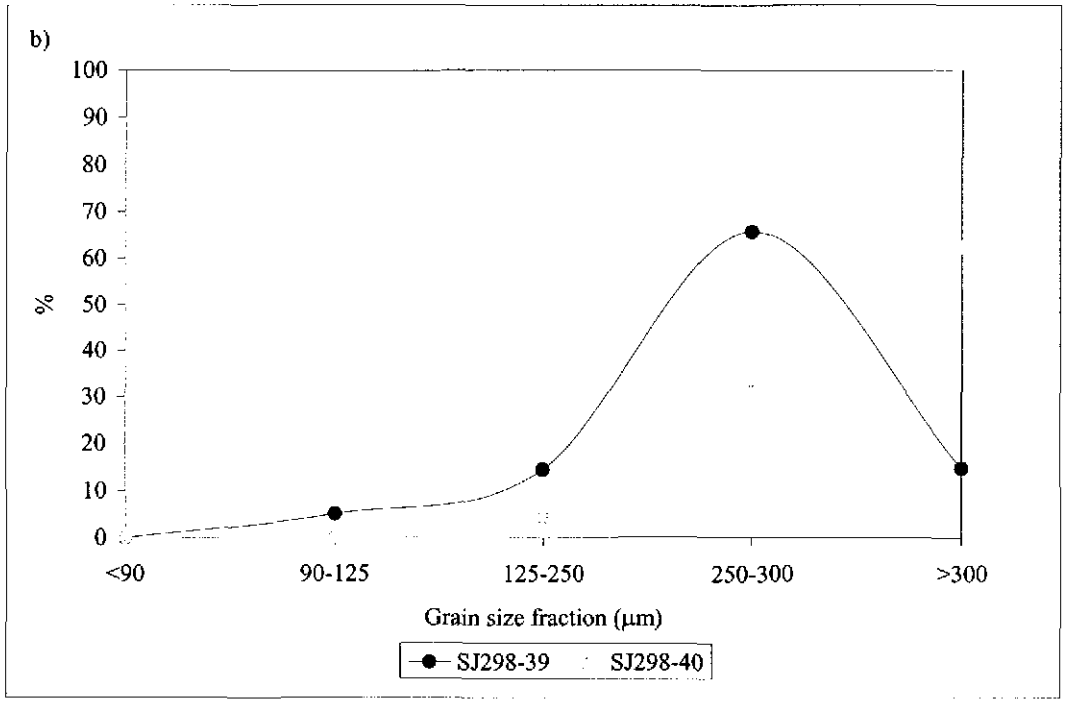

Figure 27 (a) & (b)- Grain Size distributions for the dune ridge samples.

Table 9-Grain size statistical parameters calculated using the "Method of Moments"

Sample	Mean (1st moment)	Standard Deviation (2nd moment)	Skewness (3rd moment)	Kurtosis (4th moment)
SJ14B	2.0075	0.6809	-0.6763	1.7588
SJ042A	1.3771	0.8809	-1.0425	1.2618
SJ048A	1.5981	0.8329	-0.8054	1.6307
SJ048B	1.5867	0.8157	-0.9714	1.4700
SJ252A	1.1585	0.9508	-1.0320	1.1126
SJ252B	1.2038	0.9389	-1.0207	1.1418
SJ252C	1.1932	0.9389	-1.0370	1.1383
SJ298-39	1.8934	0.5588	-0.5429	3.8132
SJ298-40	1.2832	0.9001	-1.2151	1.5477

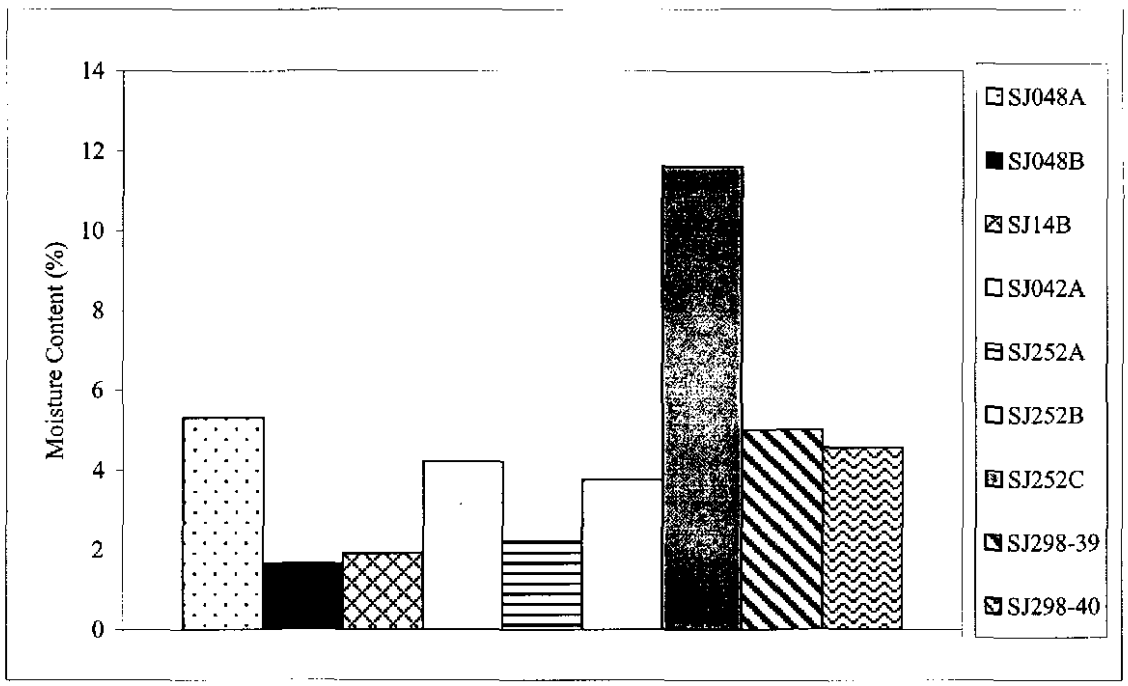

Figure 28- Moisture content of the dune ridge samples. Moisture contents were calculated based on Aitken (1985).

Table 10- Feldspar contamination in quartz separates from the dune ridge samples

sample	grain size (μm)	IRSL intensity	OSL intensity	IRSL/OSL
SJ252A	150-212	131	52362	0.003
		95	85399	0.001
		224	90618	0.002
		26	25634	0.001
		140	69433	0.002
		21	28230	0.001
		8	10958	0.001
		28	15358	0.002
		13	11301	0.001
SJ252A	212-250	55	82206	0.001
		72	52952	0.001
		178	56355	0.003
		126	41406	0.003
		30	19116	0.002
		66	30118	0.002
		12	5976	0.002
		24	8484	0.003
		25	6352	0.004
SJ252B	150-212	110	50177	0.002
		154	46875	0.003
		120	61039	0.002
		24	30311	0.001
		28	31131	0.001
		45	21570	0.002
		14	17079	0.001
		34	16320	0.002
		16	19730	0.001
SJ252B	212-250	93	36467	0.003
		279	39028	0.007
		144	37169	0.004
		23	21876	0.001
		29	22773	0.001
		16	29000	0.001
		20	16566	0.001
		14	7020	0.002
		19	6616	0.003
SJ252C	150-212	53	63216	0.001
		233	71422	0.003
		82	87391	0.001
		54	48685	0.001
		42	43036	0.001
		53	31387	0.002
		19	9044	0.002
		22	18757	0.001
		19	13620	0.001
SJ252C	212-250	131	65351	0.002
		48	48018	0.001
		66	73007	0.001
		22	25813	0.001
		54	25789	0.002
		37	25456	0.001
		19	9888	0.002
		11	12168	0.001
		26	11310	0.002
SJ298	125-250	86	33298	0.003
39		79	29904	0.003
		36	29620	0.001
		41	30528	0.001
		58	15566	0.004
		95	24567	0.004
SJ298	250-300	24	6106	0.004
39		19	6176	0.003
		22	7930	0.003
		18	6372	0.003
		13	4373	0.003
		29	8727	0.003
SJ298	125-250	76	95223	0.001
40		207	93045	0.002
		138	82289	0.002
		88	85359	0.001
		125	91996	0.001
		171	85324	0.002
SJ298	250-300	29	8109	0.004
40		18	4438	0.004
		17	5383	0.003
		23	5266	0.004
		8	4078	0.002
		22	4202	0.005

sample	grain size (μm)	IRSL intensity	OSL intensity	IRSL/OSL
SJ14B	150-212	341	52521	0.006
		200	45193	0.004
		152	56683	0.003
		237	31587	0.008
		342	37115	0.009
		76	36026	0.002
		59	20190	0.003
		174	17188	0.010
		39	12288	0.003
SJ14B	212-250	282	61711	0.005
		15	249	0.060
		206	19141	0.011
		81	6240	0.013
		426	18797	0.023
		75	4655	0.016
		95	12855	0.007
		176	14475	0.012
		49	19932	0.002
SJ042A	150-212	168	44720	0.004
		389	88500	0.004
		184	65293	0.003
		114	29003	0.004
		52	26556	0.002
		188	25656	0.007
		50	7640	0.007
		81	9826	0.008
		98	40239	0.002
SJ042A	212-250	118	55726	0.002
		149	28827	0.005
		62	7409	0.008
		69	26058	0.003
		52	10557	0.005
		95	21335	0.004
		42	18026	0.002
		178	38686	0.005
		72	12363	0.006
SJ048A	150-212	139	66490	0.002
		387	50029	0.008
		351	46974	0.007
		165	25429	0.006
		125	34705	0.004
		125	48462	0.003
		54	18822	0.003
		70	7887	0.009
		123	25463	0.005
SJ048A	212-250	37	16850	0.002
		84	5122	0.016
		36	7351	0.005
		113	10399	0.011
		149	14851	0.010
		67	16298	0.004
		89	3709	0.024
		122	4330	0.028
		311	8547	0.036
SJ048B	150-212	255	77945	0.003
		110	23907	0.005
		166	46820	0.004
		182	36607	0.005
		180	48692	0.004
		1421	33128	0.043
		141	16433	0.009
		312	14076	0.022
		75	28206	0.003
SJ048B	212-250	20	1078	0.019
		14	1661	0.008
		16	1796	0.009
		8	1145	0.007
		15	959	0.016
		8	1058	0.008
		5	788	0.006
		23	829	0.028
		8	668	0.012

Table 11- Additional feldspar contamination tests.

	grain size (μm)	OSL	IRSL	IRSL/OSL
SJ14B	150-212	10000	32	0.003
		1779	7	0.004
		3045	34	0.011
		3067	12	0.004
		6821	26	0.004
		5254	30	0.006
		2926	22	0.008
		4950	26	0.005
		6657	31	0.005
		4462	26	0.006
		4819	14	0.003
		2743	15	0.005
		3094	15	0.005
		1450	9	0.006
		2925	20	0.007
		3179	21	0.007
		3928	16	0.004
		3080	22	0.007
		3355	21	0.006
		6898	24	0.003
		3577	33	0.009
		3438	16	0.005
		3065	17	0.006
		1504	18	0.012
SJ14B	212-250	4313	17	0.004
		2104	10	0.005
		2578	8	0.003
		2668	13	0.005
		1539	18	0.012
		1558	18	0.012
		2594	28	0.011
		2805	21	0.007
		2978	15	0.005
		1720	14	0.008
		2292	20	0.009
		3332	10	0.003
		3738	26	0.007
		3723	14	0.004
		5023	45	0.009
		4477	25	0.006
		4189	23	0.005
		4519	26	0.006
		3397	25	0.007
		2934	13	0.004
		1859	9	0.005
		3381	20	0.006

	grain size (μm)	OSL	IRSL	IRSL/OSL
SJ048A	150-212	1686	17	0.010
		1224	16	0.013
		481	18	0.037
		766	16	0.021
		1018	10	0.010
		1458	14	0.010
		1266	19	0.015
		987	13	0.013
		1286	15	0.012
		797	10	0.013
		1172	7	0.006
		1091	7	0.006
		1176	10	0.009
		1355	19	0.014
		1086	19	0.017
		728	8	0.011
		1347	15	0.011
		2265	9	0.004
		2030	12	0.006
		2155	11	0.005
SJ048A	212-250	1422	11	0.008
		920	8	0.009
		732	11	0.015
		1156	5	0.004
		1433	5	0.003
		704	13	0.018
		660	16	0.024
		770	13	0.017
		622	16	0.026
		1004	12	0.012
		497	11	0.022
		723	16	0.022
		477	12	0.025
		569	12	0.021
		512	6	0.012
		649	8	0.012
		994	11	0.011
		1180	9	0.008
		844	16	0.019
		1084	8	0.007
		693	11	0.016
		762	9	0.012
		962	14	0.015
		533	6	0.011

	grain size (μm)	OSL	IRSL	IRSL/OSL
SJ048B	150-212	10000	32	0.003
		1779	7	0.004
		3045	34	0.011
		3067	12	0.004
		6821	26	0.004
		5254	30	0.006
		2926	22	0.008
		4950	26	0.005
		6657	31	0.005
		4462	26	0.006
		4819	14	0.003
		2743	15	0.005
		3094	15	0.005
		1450	9	0.006
		2925	20	0.007
		3179	21	0.007
		3928	16	0.004
		3080	22	0.007
		3355	21	0.006
		6898	24	0.003
		3577	33	0.009
		3438	16	0.005
		3065	17	0.006
		1504	18	0.012

Table 12- *Equivalent dose estimates for the dune ridge samples*

sample	grain size (μm)	mask size (mm)	natural intensity	OSL intensity	Est. D_E (s)	Ave. Est. D_E (s)
SJ14B	150-212	8	4855	52521	5.5	4.9
		8	3197	45193	4.2	
		8	4719	56683	5.0	
		5	2338	31587	4.4	4.1
		5	2694	37115	4.4	
		5	2166	36026	3.6	
		3	95586	20190	284.1	97.7
		3	1247	17188	4.4	
		3	971	12288	4.7	
SJ14B	212-250	8	4509	61711	4.4	9.9
		8	86	249	20.7	
		8	*1493*	*19141*	4.7	
		5	391	6240	3.8	5.5
		5	2703	18797	8.6	
		5	323	4655	4.2	
		3	936	12855	4.4	4.9
		3	*1197*	*14475*	*5.0*	
		3	1762	19932	5.3	
SJ042A	150-212	8	1669	44720	2.2	2.2
		8	3150	88500	2.1	
		8	2364	65293	2.2	
		5	1130	29003	2.3	2.3
		5	961	26556	2.2	
		5	993	25656	2.3	
		3	327	7640	2.6	2.2
		3	366	9826	2.2	
		3	1305	40239	1.9	
SJ042A	212-250	8	2362	55726	2.5	2.7
		8	1531	28827	3.2	
		8	294	7409	2.4	
		5	886	26058	2.0	2.2
		5	418	10557	2.4	
		5	827	21335	2.3	
		3	754	18026	2.5	2.7
		3	1359	38686	2.1	
		3	704	12363	3.4	
SJ048A	150-212	8	413	66490	0.4	0.4
		8	361	50029	0.4	
		8	412	46974	0.5	
		5	171	25429	0.4	0.4
		5	213	34705	0.4	
		5	341	48462	0.4	
		3	135	18822	0.4	0.8
		3	165	7887	1.3	
		3	309	25463	0.7	
SJ048A	212-250	8	143	16850	0.5	0.7
		8	78	5122	0.9	
		8	*77*	*7351*	0.6	
		5	139	10399	0.8	0.9
		5	153	14851	0.6	
		5	315	16298	1.2	
		3	192	3709	3.1	2.1
		3	*102*	*4330*	*1.4*	
		3	234	8547	1.6	
SJ048B	150-212	8	896	77945	0.7	0.7
		8	268	23907	0.7	
		8	511	46820	0.7	
		5	309	36607	0.5	0.6
		5	603	48692	0.7	
		5	377	33128	0.7	
		3	148	16433	0.5	0.6
		3	133	14076	0.6	
		3	334	28206	0.7	
SJ048B	212-250	5	275	1078	0.5	0.6
		5	446	1661	0.5	
		5	638	1796	0.7	
		5	323	1145	0.6	
		5	269	959	0.6	
		5	231	1058	0.4	
		5	209	788	0.5	
		5	228	829	0.6	
		5	225	668	0.7	

Note: 1Gy = 10 seconds

sample	grain size (μm)	mask size (mm)	natural intensity	OSL intensity	Est. D_E (s)	Ave. Est. D_E (s)
SJ252A	150-212	8	3994	52362	4.6	4.7
		8	6609	*85399*	4.6	
		8	7555	90618	5.0	
		5	1923	25634	4.5	4.8
		5	6540	69433	5.7	
		5	1994	28230	4.2	
		3	*834*	*10958*	*4.6*	*5.3*
		3	1451	15358	5.7	
		3	1048	11301	5.6	
SJ252A	212-250	8	6484	82206	4.7	4.8
		8	4153	52952	4.7	
		8	4599	*56355*	4.9	
		5	3090	41406	4.5	4.9
		5	1603	19116	5.0	
		5	2563	30118	5.1	
		3	539	5976	5.4	5.9
		3	1182	8484	8.4	
		3	418	6352	3.9	
SJ252B	150-212	8	3443	50177	4.1	4.3
		8	3723	46875	4.8	
		8	4097	61039	4.0	
		5	2062	30311	4.1	4.1
		5	2060	31131	4.0	
		5	1481	21570	4.1	
		3	2250	17079	7.9	5.4
		3	1101	16320	4.0	
		3	1397	19730	4.2	
SJ252B	212-250	8	2564	36467	4.2	4.3
		8	2611	39028	4.0	
		8	2899	37169	4.7	
		5	1337	21876	3.7	4.1
		5	1747	22773	4.6	
		5	1947	29000	4.0	
		3	1062	16566	3.8	4.4
		3	602	7020	5.1	
		3	466	6616	4.2	
SJ252C	150-212	8	4792	63216	4.5	4.9
		8	5989	71422	5.0	
		8	7591	87391	5.2	
		5	3820	48685	4.7	4.8
		5	3683	43036	5.1	
		5	2433	31387	4.7	
		3	*853*	*9044*	*5.7*	*5.2*
		3	1453	18757	4.6	
		3	1170	13620	5.2	
SJ252C	212-250	8	6569	65351	6.0	5.9
		8	4037	48018	5.0	
		8	*8020*	*73007*	*6.6*	
		5	1983	25813	4.6	4.6
		5	1905	25789	4.4	
		5	1999	25456	4.7	
		3	739	9888	4.5	4.4
		3	949	12168	4.7	
		3	734	11310	3.9	
SJ298 40	125-250	8	1125	95223	0.7	0.7
		8	1023	93045	0.7	
		8	914	82289	0.7	
		8	945	85359	0.7	
		8	1092	91996	0.7	
		8	954	85324	0.7	
SJ298 40	250-300	8	764	8109	0.6	0.6
		8	378	4438	0.5	
		8	499	5383	0.6	
		8	528	5266	0.6	
		8	353	4078	0.5	
		8	385	4202	0.5	
SJ298 39	125-250	5	636	33298	1.1	1.9
		5	677	29904	1.4	
		5	642	29620	1.3	
		5	632	30528	1.2	
		5	1360	15566	5.2	
		5	567	24567	1.4	
SJ298 39	250-300	8	1384	6106	1.4	1.2
		8	1122	6176	1.1	
		8	1774	7930	1.3	
		8	1262	6372	1.2	
		8	776	4373	1.1	
		8	1642	8727	1.1	

Table 13- Summary of equivalent doses (DE) obtained for the dune ridge samples and skewness values for the frequency distributions

sample	grain size (μm)	mask size (mm)	min DE (Gy)	mean DE (Gy)	max DE (Gy)	number of aliquots used	number of aliquots *measured*	usable data (%)	Skewness
SJ14B	150-212	8	0.00 +/- 0.00	0.34 +/- 0.02	0.43 +/- 0.01	19	24	79.17	-3.04
		5	0.28 +/- 0.01	0.36 +/- 0.01	0.45 +/- 0.01	17	23	73.91	0.05
		3	0.25 +/- 0.02	0.37 +/- 0.03	0.62 +/- 0.02	15	22	68.18	0.99
		1	-	0.21 +/- 0.03	-	1	24	4.17	not enough data
	212-250	8	-	-	-	0	24	0.00	not enough data
		5	0.29 +/- 0.01	0.35 +/- 0.02	0.43 +/- 0.01	7	24	29.17	0.87
		3	-	-	-	0	12	0.00	not enough data
		1	-	0.40 +/- 0.03	-	1	24	4.17	not enough data
SJ042A	150-212	8	0.00 +/- 0.00	0.17 +/- 0.01	0.23 +/- 0.00	24	24	100.00	-3
		5	0.11 +/- 0.01	0.16 +/- 0.01	0.41 +/- 0.01	22	23	95.65	3.72
		3	0.09 +/- 0.00	0.15 +/- 0.01	0.34 +/- 0.01	23	24	95.83	2.65
		1	-	0.20 +/- 0.02	-	1	24	4.17	not enough data
	212-250	8	0.12 +/- 0.01	0.17 +/- 0.01	0.24 +/- 0.01	21	24	87.50	0.32
		5	0.10 +/- 0.01	0.15 +/- 0.01	0.33 +/- 0.01	20	24	83.33	3.12
		3	0.09 +/- 0.01	0.15 +/- 0.01	0.24 +/- 0.01	18	24	75.00	0.78
		1	-	-	-	0	23	0.00	not enough data
SJ048A	150-212	8	0.03 +/- 0.00	0.03 +/- 0.001	0.04 +/- 0.00	23	24	95.83	1.46
		5	0.02 +/- 0.00	0.03 +/- 0.001	0.05 +/- 0.00	22	24	91.67	0.67
		3	0.02 +/- 0.00	0.03 +/- 0.003	0.04 +/- 0.01	5	23	21.74	not enough data
		1	-	-	-	0	23	0.00	not enough data
	212-250	8	0.02 +/- 0.00	0.04 +/- 0.01	0.17 +/- 0.01	24	24	100.00	4.48
		5	0.03 +/- 0.01	0.07 +/- 0.03	0.35 +/- 0.02	10	24	*41.67*	*3.03*
		3	-	-	-	0	24	0.00	not enough data
		1	-	-	-	0	24	0.00	not enough data
SJ048B	150-212	8	0.04 +/- 0.00	0.05 +/- 0.002	0.08 +/- 0.00	24	24	100.00	1.03
		5	0.04 +/- 0.00	0.05 +/- 0.002	0.08 +/- 0.00	24	24	100.00	1.15
		3	0.03 +/- 0.01	0.05 +/- 0.01	0.11 +/- 0.01	12	24	50.00	1.59
		1	0.04 +/- 0.01	0.12 +/- 0.05	0.31 +/- 0.05	5	24	20.83	not enough data
	212-250	8	*0.03 +/- 0.00*	*0.05 +/- 0.002*	*0.06 +/- 0.01*	24	24	100.00	0.45
		5	0.03 +/- 0.01	0.04 +/- 0.01	0.11 +/- 0.01	15	23	65.22	3.18
		3	0.02 +/- 0.01	0.05 +/- 0.01	0.08 +/- 0.01	8	23	34.78	not enough data
		1	-	-	-	0	24	0.00	not enough data
SJ252A	150-212	8	0.38 +/- 0.01	0.44 +/- 0.02	0.86 +/- 0.01	23	24	95.83	3.95
		5	0.35 +/- 0.01	0.39 +/- 0.01	0.43 +/- 0.01	24	24	100.00	-0.32
		3	0.29 +/- 0.02	0.46 +/- 0.03	0.89 +/- 0.02	24	24	100.00	1.92
		1	0.27 +/- 0.04	0.48 +/- 0.07	1.17 +/- 0.08	13	24	54.17	not enough data
	212-250	8	0.35 +/- 0.01	0.41 +/- 0.01	0.58 +/- 0.01	24	24	100.00	2.24
		5	0.21 +/- 0.01	0.35 +/- 0.01	0.39 +/- 0.01	23	24	95.83	-0.56
		3	0.30 +/- 0.02	0.38 +/- 0.01	0.50 +/- 0.03	21	24	87.50	0.61
		1	0.34 +/- 0.03	0.66 +/- 0.27	1.48 +/- 0.23	4	24	16.67	not enough data
SJ252B	150-212	8	0.33 +/- 0.01	0.36 +/- 0.01	0.42 +/- 0.01	21	24	87.50	0.71
		5	0.29 +/- 0.01	0.36 +/- 0.01	0.53 +/- 0.01	21	24	87.50	1.15
		3	0.27 +/- 0.01	0.39 +/- 0.02	0.58 +/- 0.02	19	24	79.17	1.07
		1	0.45 +/- 0.04	0.61 +/- 0.16	0.77 +/- 0.08	2	24	*8.33*	not enough data
	212-250	8	0.29 +/- 0.01	0.38 +/- 0.01	0.46 +/- 0.01	24	24	100.00	0.1
		5	0.25 +/- 0.01	0.37 +/- 0.02	0.61 +/- 0.02	23	24	95.83	1.94
		3	0.29 +/- 0.03	0.36 +/- 0.03	0.70 +/- 0.08	12	24	50.00	2.84
		1	0.33 +/- 0.01	0.44 +/- 0.11	0.54 +/- 0.05	2	24	8.33	not enough data
SJ252C	150-212	8	0.28 +/- 0.01	0.41 +/- 0.01	0.49 +/- 0.01	23	23	100.00	-1.5
		5	0.33 +/- 0.01	0.39 +/- 0.01	0.50 +/- 0.01	24	24	100.00	0.77
		3	*0.30 +/- 0.01*	*0.36 +/- 0.01*	*0.42 +/- 0.02*	23	24	95.83	-0.14
		1	0.40 +/- 0.02	0.56 +/- 0.07	0.70 +/- 0.02	4	23	17.39	not enough data
	212-250	8	0.35 +/- 0.01	0.41 +/- 0.01	0.56 +/- 0.01	23	24	95.83	2.04
		5	0.30 +/- 0.02	0.39 +/- 0.01	0.46 +/- 0.02	21	24	87.50	0.06
		3	0.26 +/- 0.03	0.38 +/- 0.01	0.47 +/- 0.01	19	24	79.17	-0.32
		1	0.32 +/- 0.04	0.73 +/- 0.22	1.34 +/- 0.10	4	24	16.67	not enough data
SJ298 39	125-250	8	0.08 +/- 0.01	0.11 +/- 0.005	0.12 +/- 0.01	22	24	91.67	1.2
		5	0.07 +/- 0.01	0.10 +/- 0.004	0.13 +/- 0.01	20	24	83.33	0.15
		3	0.08 +/- 0.01	0.10 +/- 0.003	0.12 +/- 0.01	17	24	70.83	-0.4
		1	-	1.1 +/- 0.2	-	1	24	4.17	not enough data
	250-300	8	0.08 +/- 0.00	0.12 +/- 0.002	0.13 +/- 0.01	24	24	100.00	-0.9
		5	0.08 +/- 0.01	0.11 +/- 0.003	0.13 +/- 0.01	20	24	83.33	-0.89
		3	0.08 +/- 0.01	0.12 +/- 0.007	0.17 +/- 0.01	16	24	66.67	0.16
		1	-	-	-	0	24	0.00	not enough data
SJ298 40	125-250	8	0.03 +/- 0.00	0.04 +/- 0.002	0.06 +/- 0.00	23	24	95.83	-0.63
		5	0.03 +/- 0.00	0.04 +/- 0.002	0.07 +/- 0.01	23	24	*95.83*	1.27
		3	0.03 +/- 0.00	0.05 +/- 0.005	0.11 +/- 0.01	14	24	58.33	2.19
		1	-	0.08 +/- 0.01	-	1	24	4.17	not enough data
	250-300	8	0.03 +/- 0.00	0.04 +/- 0.002	0.10 +/- 0.00	24	24	100.00	3.19
		5	0.03 +/- 0.01	0.04 +/- 0.004	0.07 +/- 0.01	12	24	50.00	0.57
		3	0.04 +/- 0.01	0.15 +/- 0.10	0.45 +/- 0.03	4	24	16.67	not enough data
		1	-	-	-	0	24	0.00	not enough data

note: error on the mean DE = Standard deviation/ SQRT(n)

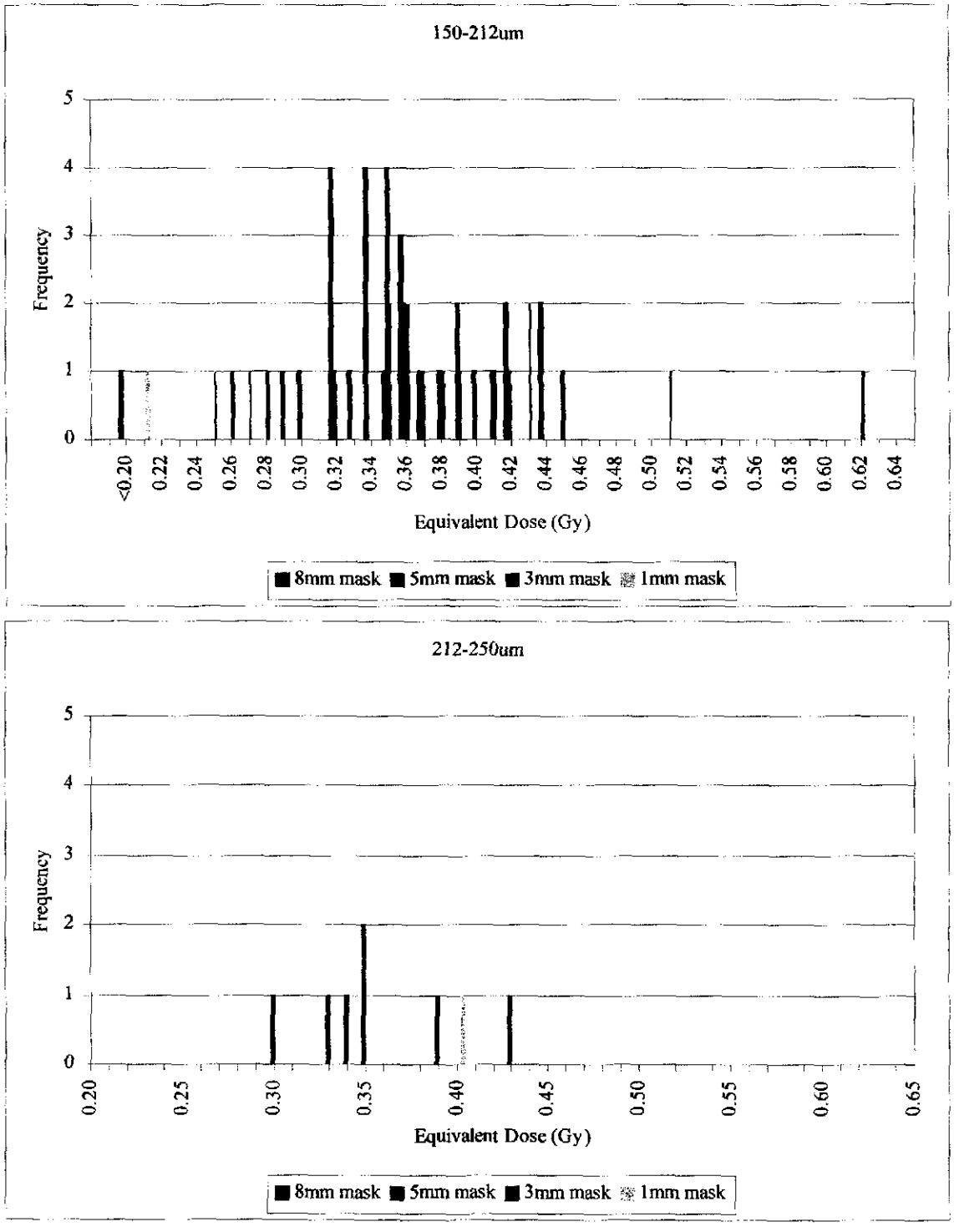

Figure 29- Frequency histograms for dune ridge sample SJ14B. Bin Size= 0.01 Gy

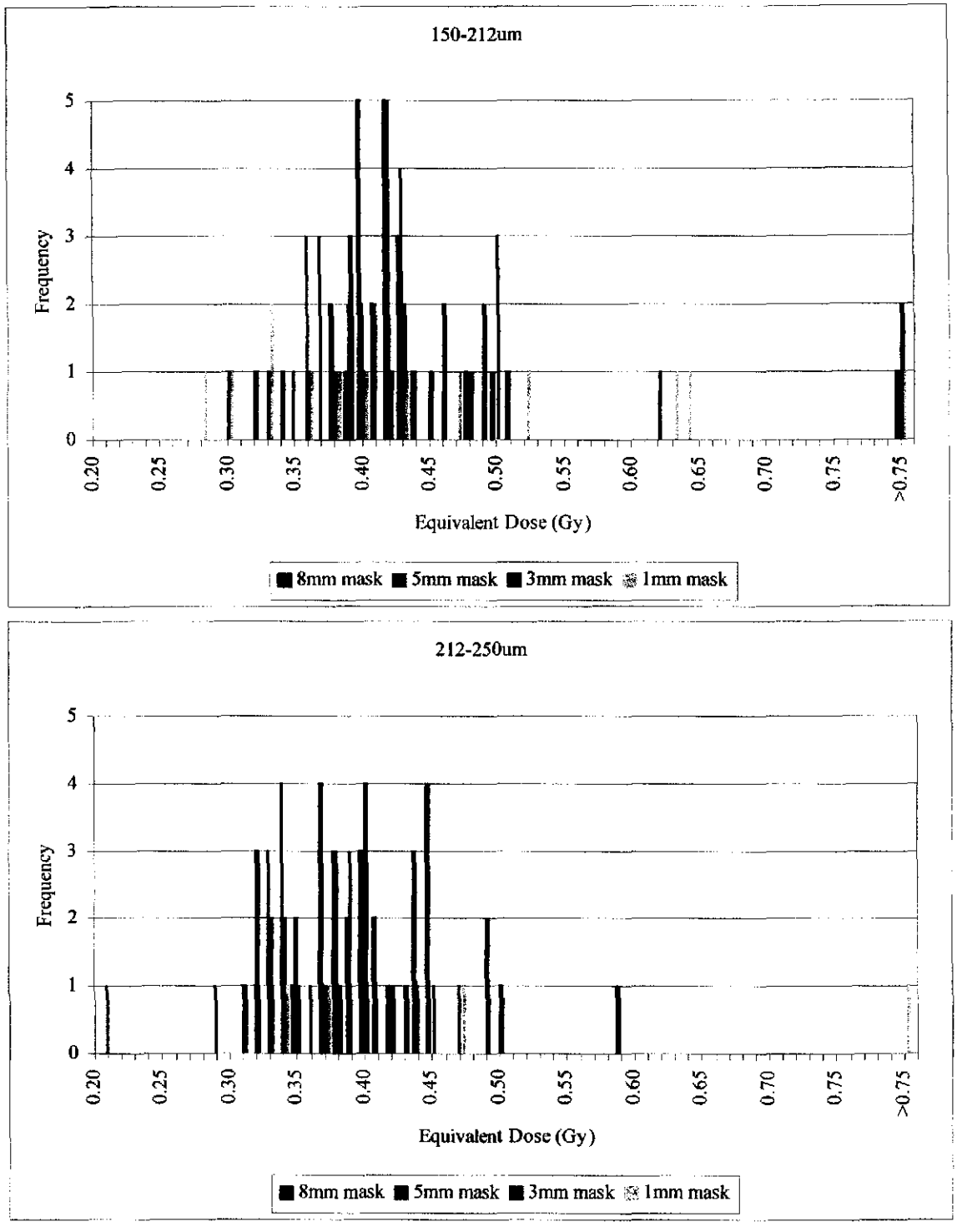

Figure 30- Frequency histograms for dune ridge sample SJ252A. Bin Size= 0.01 Gy

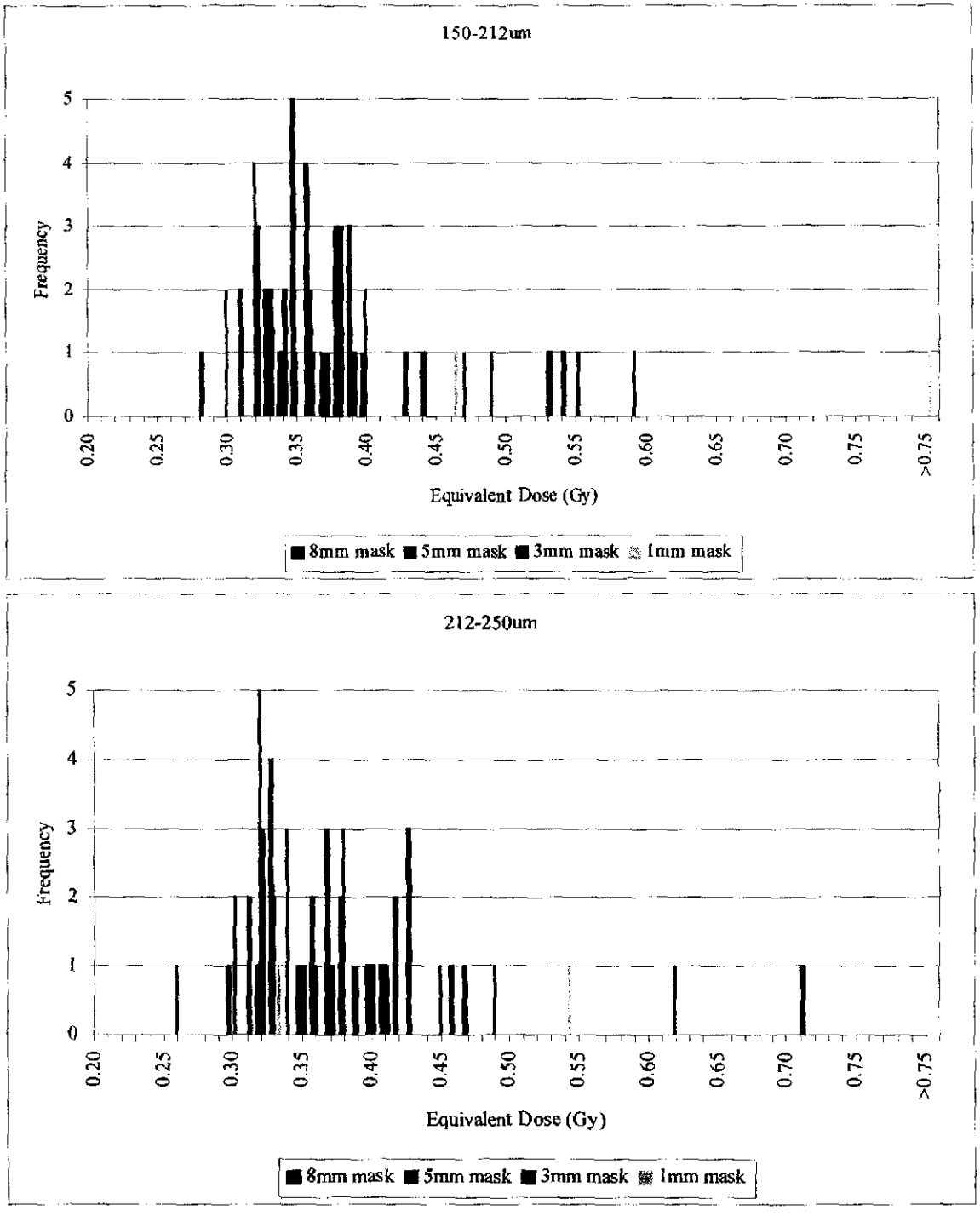

Figure 31- Frequency histograms for dune ridge sample SJ252B. Bin size= 0.01 Gy

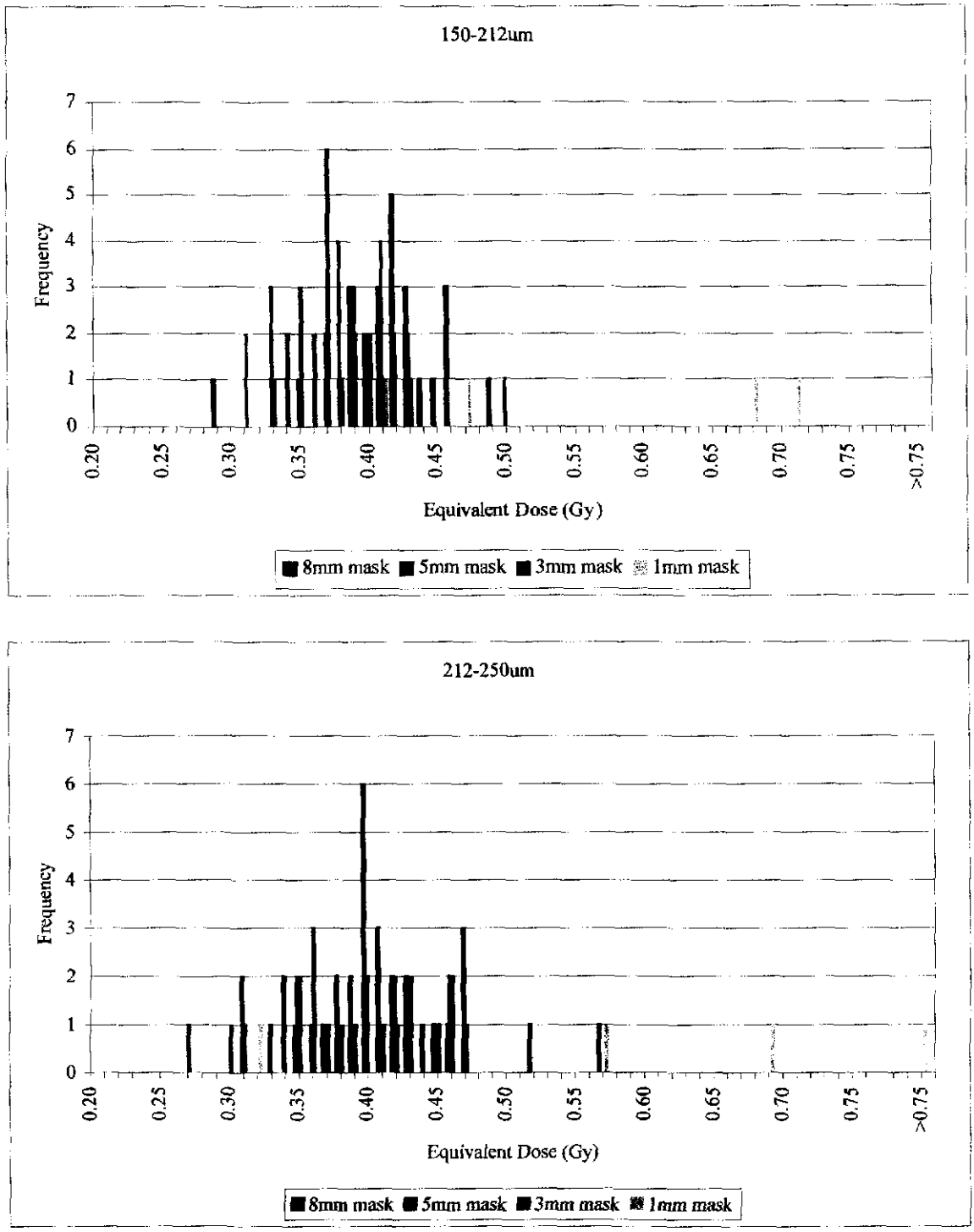

Figure 32- Frequency histograms for dune ridge sample SJ252C. Bin size= 0.01 Gy

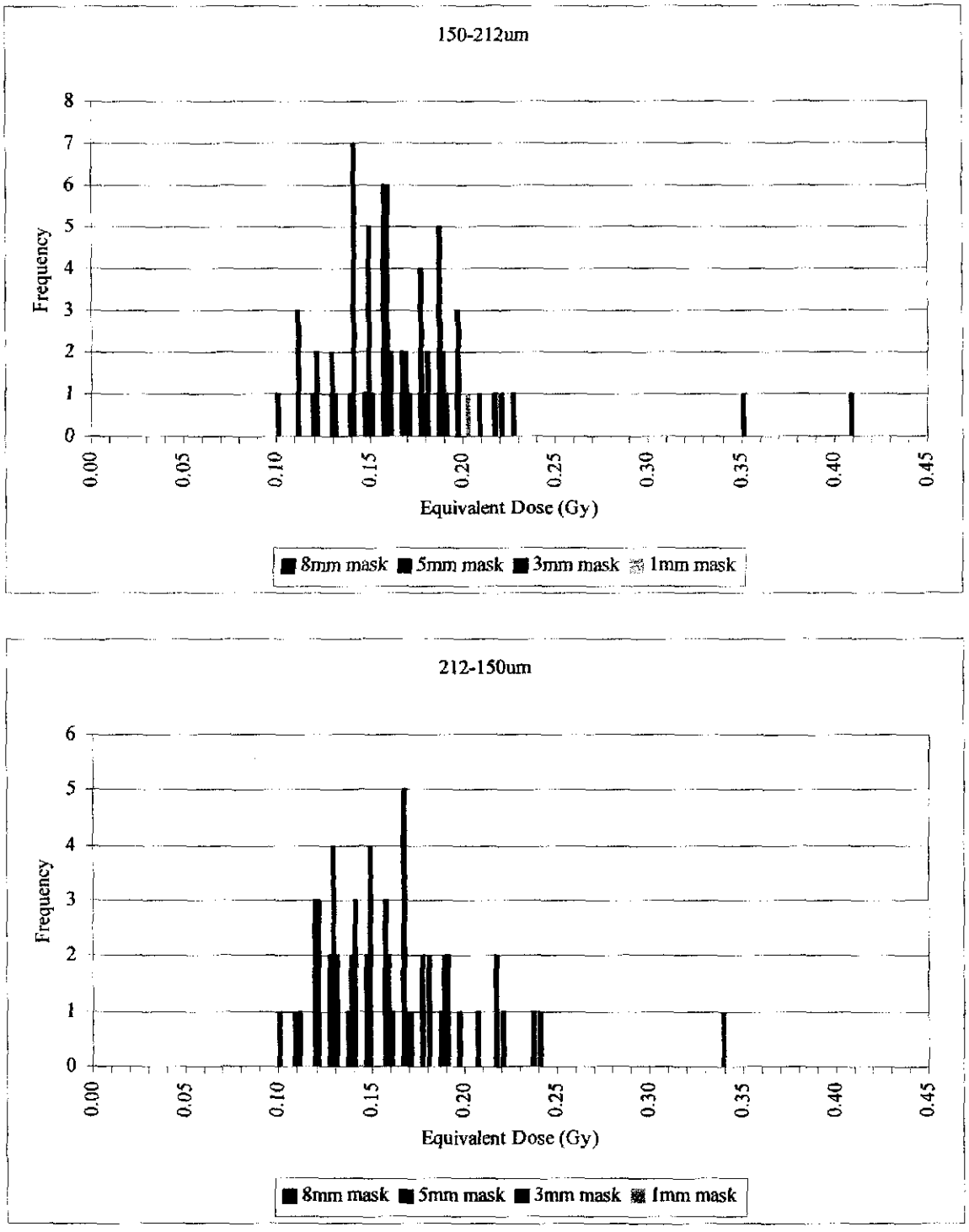

Figure 33- Frequency histograms for dune ridge sample SJ042A. Bin size= 0.01 Gy

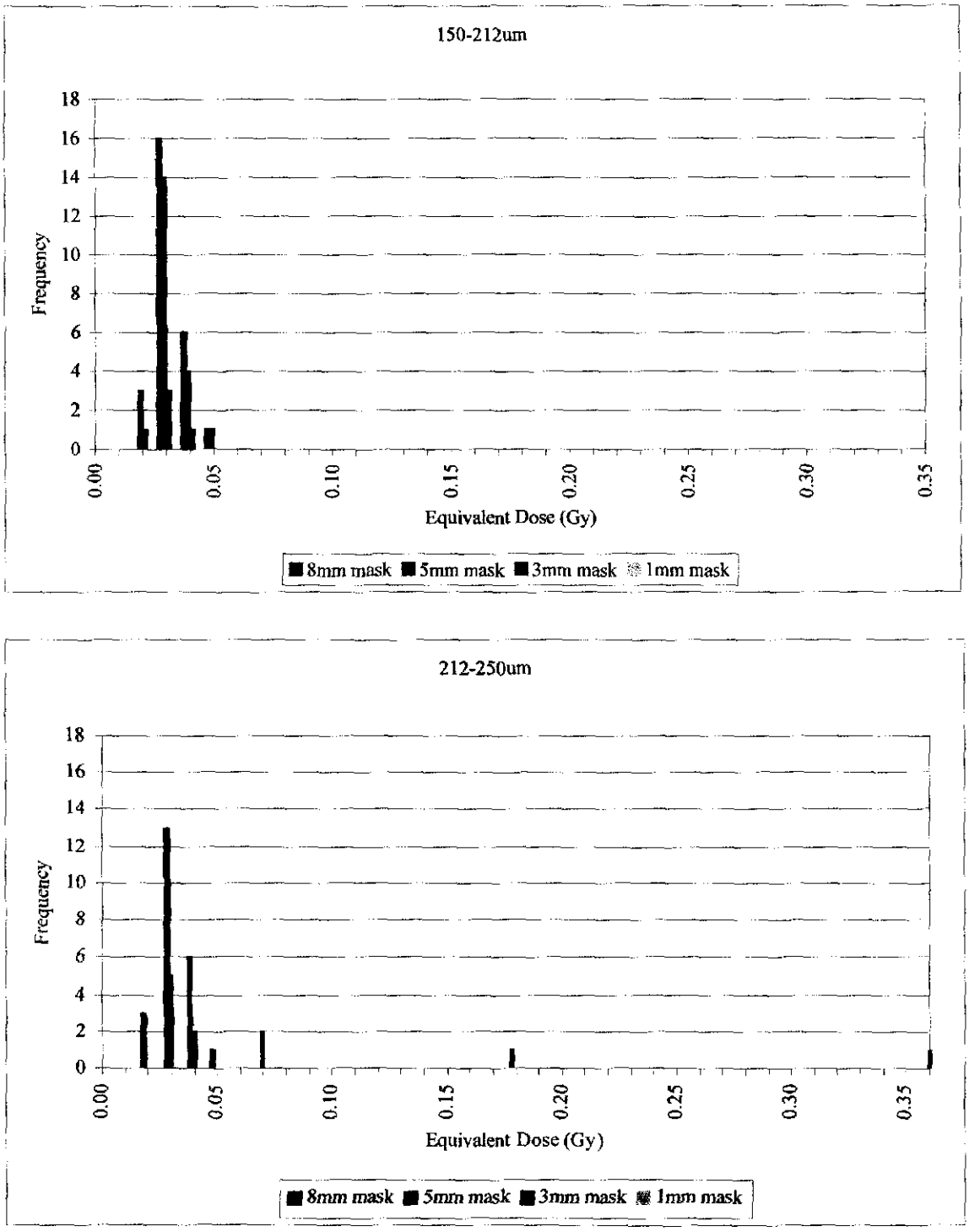

Figure 34- Frequency histograms for dune ridge sample SJ048A. Bin size= 0.01 Gy

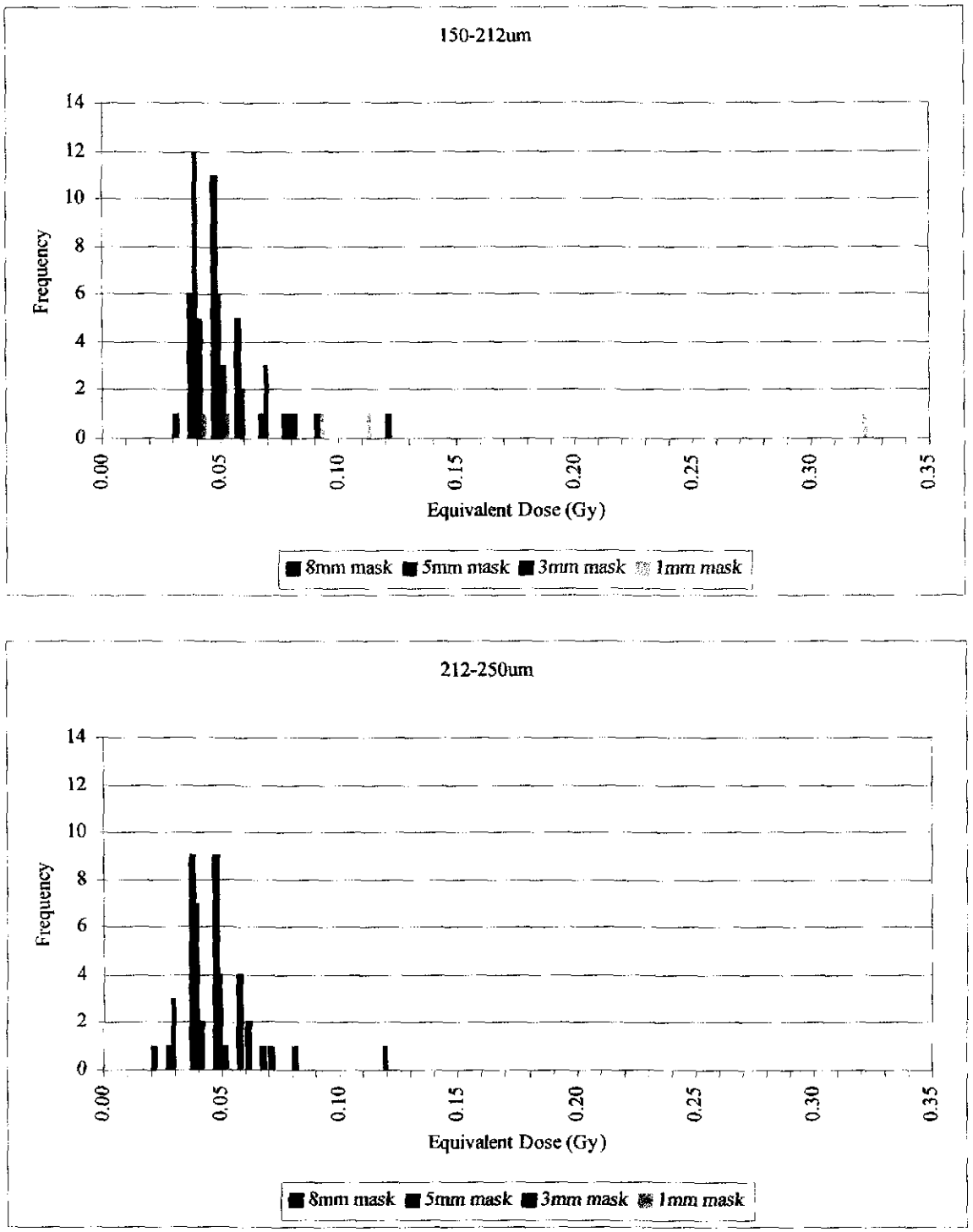

Figure 35- Frequency histograms for dune ridge sample SJ048B. Bin size= 0.01 Gy

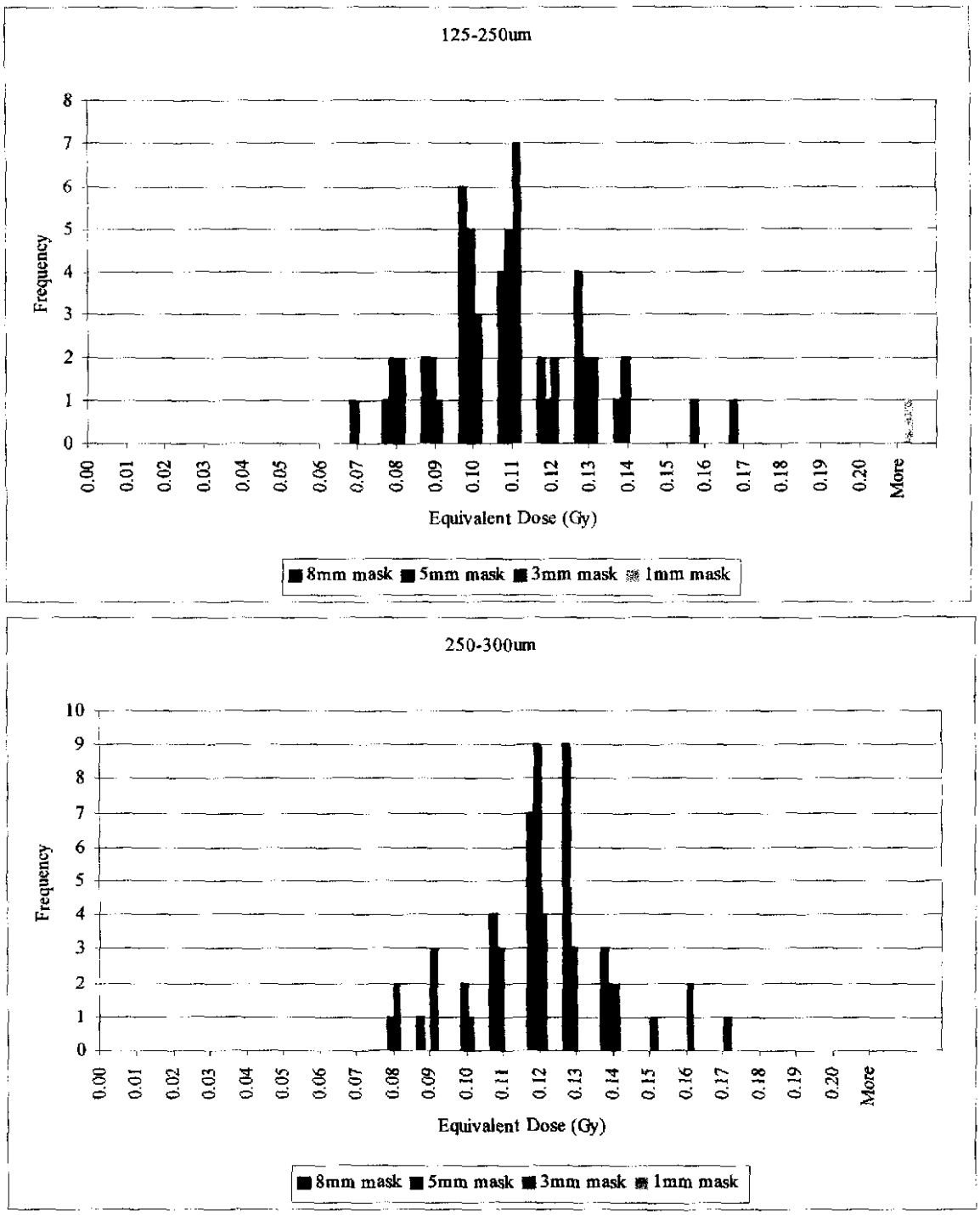

Figure 36- Frequency histograms for dune ridge sample SJ298-39. Bin size= 0.01 Gy

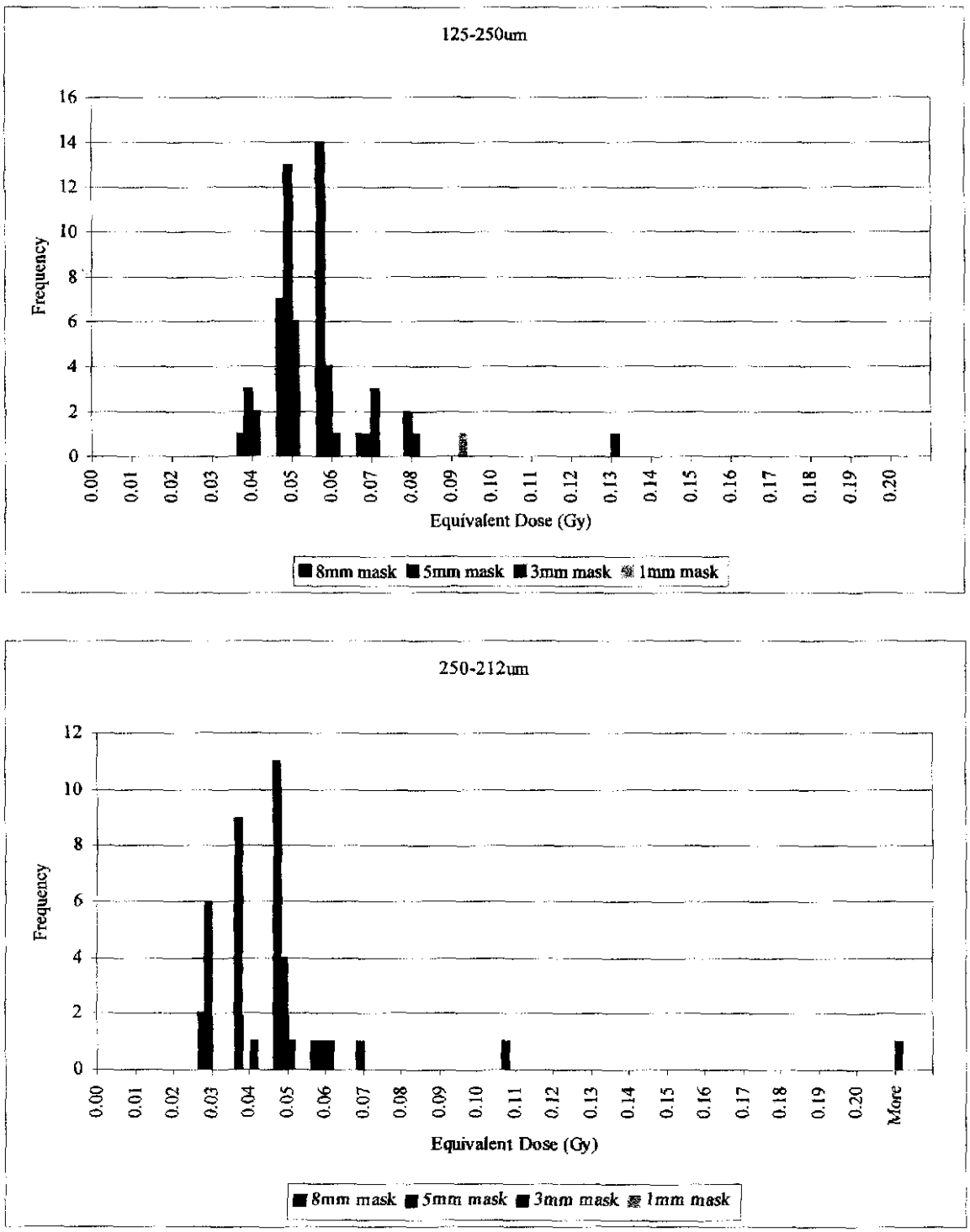

Figure 37- Frequency histograms for dune ridge sample SJ298-40. Bin size= 0.01 Gy

Table 14- Summary of 48 disc measurements

sample	grain size (μm)	mask size (mm)	min DE (Gy)	mean DE (Gy)	max DE (Gy)	number of aliquots used	number of aliquots measured	usable data (%)	Skewness
SJ298-39	125-250	1	-	-	-	0	48	0.00	-
	250-300	1	0.13 +/- 0.02	0.16 +/- 0.01	0.17 +/- 0.03	3	47	6.38	not enough data
SJ252A	150-212	1	0.24 +/- 0.04	0.33 +/- 0.02	0.40 +/- 0.05	6	48	12.50	not enough data
	212-250	1	0.30 +/- 0.02	0.49 +/- 0.15	1.09 +/- 0.10	5	48	10.42	not enough data

Table 15- Results obtained using a modified regeneration cycle

sample	grain size (μm)	mask size (mm)	min DE (Gy)	mean DE (Gy)	max DE (Gy)	number of aliquots used	number of aliquots measured	usable data (%)	Skewness
SJ298-39	125-250	8	0.00 +/- 0.00	0.10 +/- 0.006	0.13 +/- 0.01	22	24	91.67	-2.47
	250-300	8	0.08 +/- 0.00	0.11 +/- 0.002	0.14 +/- 0.00	23	24	95.83	-0.07

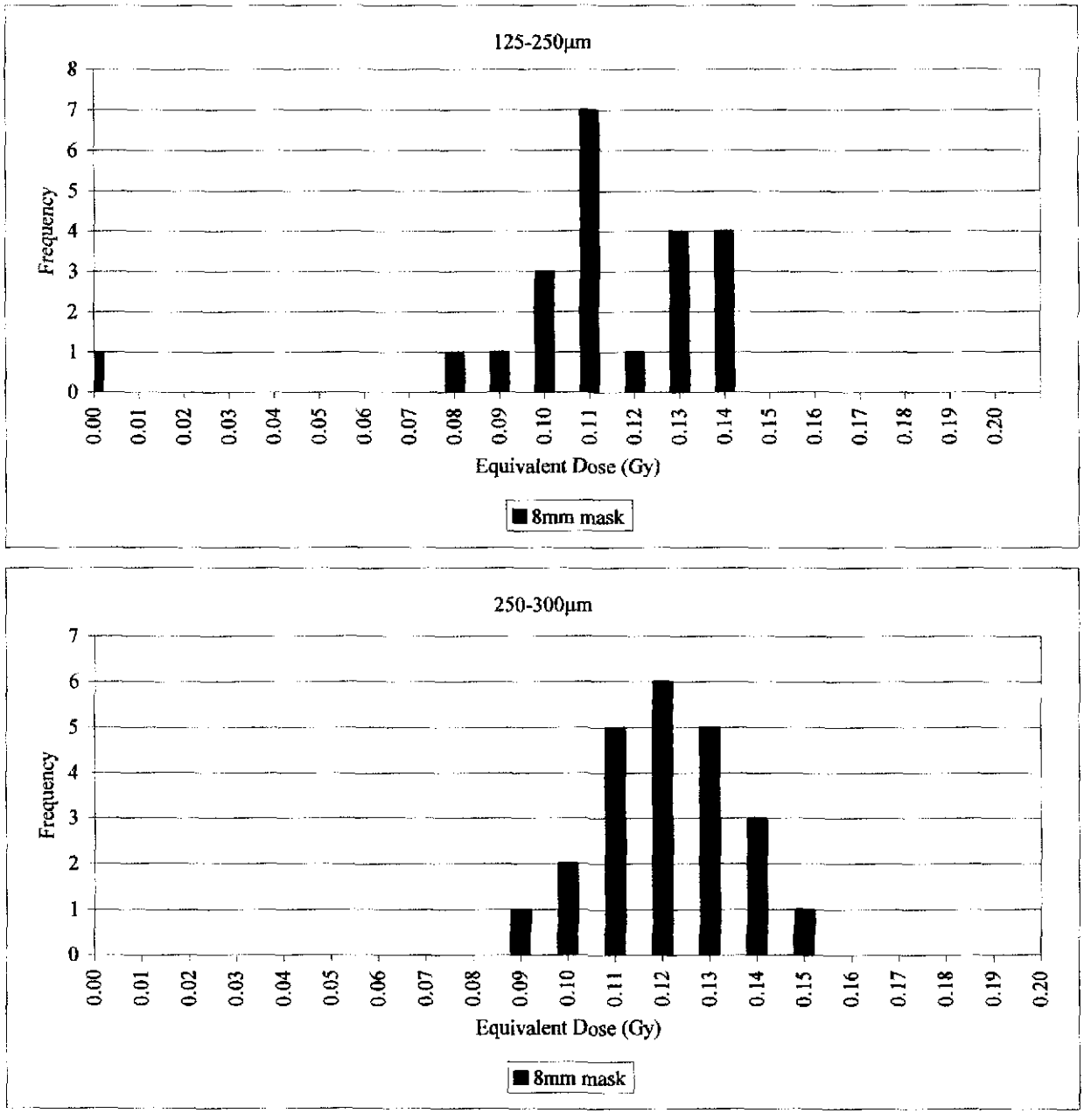

Figure 38- Results obtained using a modified regeneration cycle results. Measurements were made on 8mm aliquots of SJ298-39.

Table 16- Age calculations

sample	grain size (μm)	mask size (mm)	min age	stat error	total error	mean age	stat error	total error	max age	stat error	total error	n
SJ14B	150-212	8	0	0	0	963	63	68	1218	48	57	19
		5	793	37	42	1020	43	50	1275	49	59	17
		3	708	59	62	1048	89	93	1757	79	91	15
		1	-	-	-	595	85	86	-	-	-	1
	212-250	8	-	-	-	-	-	-	-	-	-	0
		5	836	38	43	1009	64	68	1239	47	56	7
		3	-	-	-	-	-	-	-	-	-	0
		1	-	-	-	1153	91	95	-	-	-	1
SJ042A	150-212	8	0	0	0	643	44	46	870	35	38	24
		5	416	40	41	605	44	45	1551	72	78	22
		3	340	13	15	567	43	44	1286	63	68	23
		1	-	-	-	756	79	80	-	-	-	1
	212-250	8	456	40	41	646	44	45	913	50	53	21
		5	380	39	40	570	42	44	1255	60	64	20
		3	342	39	39	570	42	44	913	50	53	18
		1	-	-	-	-	-	-	-	-	-	0
SJ048A	150-212	8	91	2	3	91	4	4	121	3	4	23
		5	60	1	2	91	4	4	152	4	5	22
		3	60	1	2	91	9	9	121	29	29	5
		1	-	-	-	-	-	-	-	-	-	0
	212-250	8	61	1	2	122	29	30	519	33	35	24
		5	91	29	29	213	89	89	1069	68	70	10
		3	-	-	-	-	-	-	-	-	-	0
		1	-	-	-	-	-	-	-	-	-	0
SJ048B	150-212	8	69	1	2	87	3	5	139	3	5	24
		5	69	1	2	87	3	5	139	3	5	24
		3	52	17	17	87	17	17	191	17	19	12
		1	69	17	17	209	86	86	540	86	88	5
	212-250	8	54	1	2	90	4	5	108	17	18	24
		5	54	17	17	72	17	17	198	18	19	15
		3	36	17	17	90	17	18	144	18	18	8
		1	-	-	-	-	-	-	-	-	-	0
SJ298-39	125-250	8	6.4	0.80	0.83	8.80	0.40	0.52	9.60	0.80	0.87	22
		5	5.6	0.80	0.82	8.00	0.32	0.44	10.40	0.80	0.89	20
		3	6.4	0.80	0.83	8.00	0.24	0.39	9.60	0.80	0.87	17
		1	-	-	-	88.00	15.90	16.30	-	-	-	1
	250-300	8	6.00	1.00	0.00	9.99	0.17	0.40	10.80	0.83	0.92	24
		5	6.65	0.83	0.86	9.15	0.25	0.42	10.80	0.83	0.92	20
		3	6.65	0.83	0.86	9.99	0.58	0.69	14.10	0.83	0.98	16
		1	-	-	-	-	-	-	-	-	-	0
SJ298-40	125-250	8	15.00	0.00	0.00	21.00	1.00	1.00	31.00	0.00	0.00	23.00
		5	15.00	0.00	0.00	21.00	1.00	1.00	36.00	5.00	5.00	23.00
		3	15.00	0.00	0.00	26.00	2.00	2.00	57.00	5.00	5.00	14.00
		1	-	-	-	42.00	5.00	5.00	-	-	-	1.00
	250-300	8	15.00	0.00	0.00	21.00	1.00	1.00	52.00	1.00	0.00	24.00
		5	15.00	5.00	5.00	21.00	2.00	2.00	36.00	5.00	5.00	12.00
		3	21.00	5.00	5.00	78.00	52.00	52.00	236.00	15.00	16.00	4.00
		1	-	-	-	-	-	-	-	-	-	-
SJ252A	150-212	8	1181	210	212	1368	249	250	2674	473	476	23
		5	1088	194	195	1213	216	217	1337	237	239	24
		3	902	170	171	1430	268	270	2768	492	495	24
		1	839	191	192	1493	338	339	3639	686	690	13
	212-250	8	1096	194	195	1284	226	228	1817	319	321	24
		5	658	119	119	1096	194	195	1222	215	217	23
		3	940	175	176	1190	210	211	1566	288	290	21
		1	1065	207	208	2068	898	899	4638	1071	1076	4
SJ252B	150-212	8	1223	255	256	1334	277	278	1556	323	324	21
		5	1074	224	225	1334	277	278	1964	407	408	21
		3	1000	209	210	1445	306	308	2149	449	451	19
		1	1667	372	374	2260	739	740	2853	655	657	2
	212-250	8	1079	223	224	1414	290	291	1712	351	352	24
		5	930	193	193	1377	289	291	2271	468	470	23
		3	1079	245	246	1340	293	294	2606	604	606	12
		1	1228	253	254	1638	518	519	2010	447	449	2
SJ252C	150-212	8	1245	290	290	1823	422	423	2179	503	505	23
		5	1467	340	341	1734	401	403	2223	514	515	24
		3	1334	310	311	1601	371	372	1867	438	439	23
		1	1778	418	419	2490	647	648	3113	722	724	4
	212-250	8	1558	355	356	1825	416	417	2492	566	568	23
		5	1335	314	315	1736	395	397	2047	472	473	21
		3	1157	292	292	1691	385	387	2092	476	477	19
		1	1424	365	366	3249	1194	1196	5965	1418	1422	4

n= number of aliquots used to determine mean ages

Table 17- Summary of ages for the dune ridge samples

sample	grain size (μm)	minimum age	mean age	maximum age
SJ14B	150-212	793 +/- 42	992 +/- 59	1247 +/- 58
	212-250	836 +/- 43	1009 +/- 68	1239 +/- 56
SJ042A	150-212	416 +/- 41	624 +/- 46	1211 +/- 58
	212-250	418 +/- 41	608 +/- 45	1084 +/- 59
SJ048A	150-212	76 +/- 3	91 +/- 4	137 +/- 5
	212-250	76 +/- 16	168 +/- 60	794 +/- 53
SJ048B	150-212	69 +/- 2	87 +/- 5	139 +/- 5
	212-250	54 +/- 10	81 +/- 11	153 +/- 19
SJ298-39	125-250	6.0 +/- 0.8	8.4 +/- 0.5	10.0 +/- 0.9
	250-300	6.3 +/- 0.4	9.6 +/- 0.4	10.8 +/- 0.9
SJ298-40	125-250	15 +/- 0	21 +/- 1	34 +/- 3
	250-300	15 +/- 3	21 +/- 2	44 +/- 3
SJ252A	150-212	1135 +/- 204	1291 +/- 234	2006 +/- 358
	212-250	877 +/- 157	1190 +/- 212	1520 +/- 269
SJ252B	150-212	1149 +/- 241	1334 +/- 278	1760 +/- 366
	212-250	1005 +/- 209	1396 +/- 291	1992 +/- 411
SJ252C	150-212	1356 +/- 316	1779 +/- 413	2201 +/- 510
	212-250	1447 +/- 336	1781 +/- 407	2270 +/- 521

All ages represent the average of the 8 mm and 5 mm mask sizes

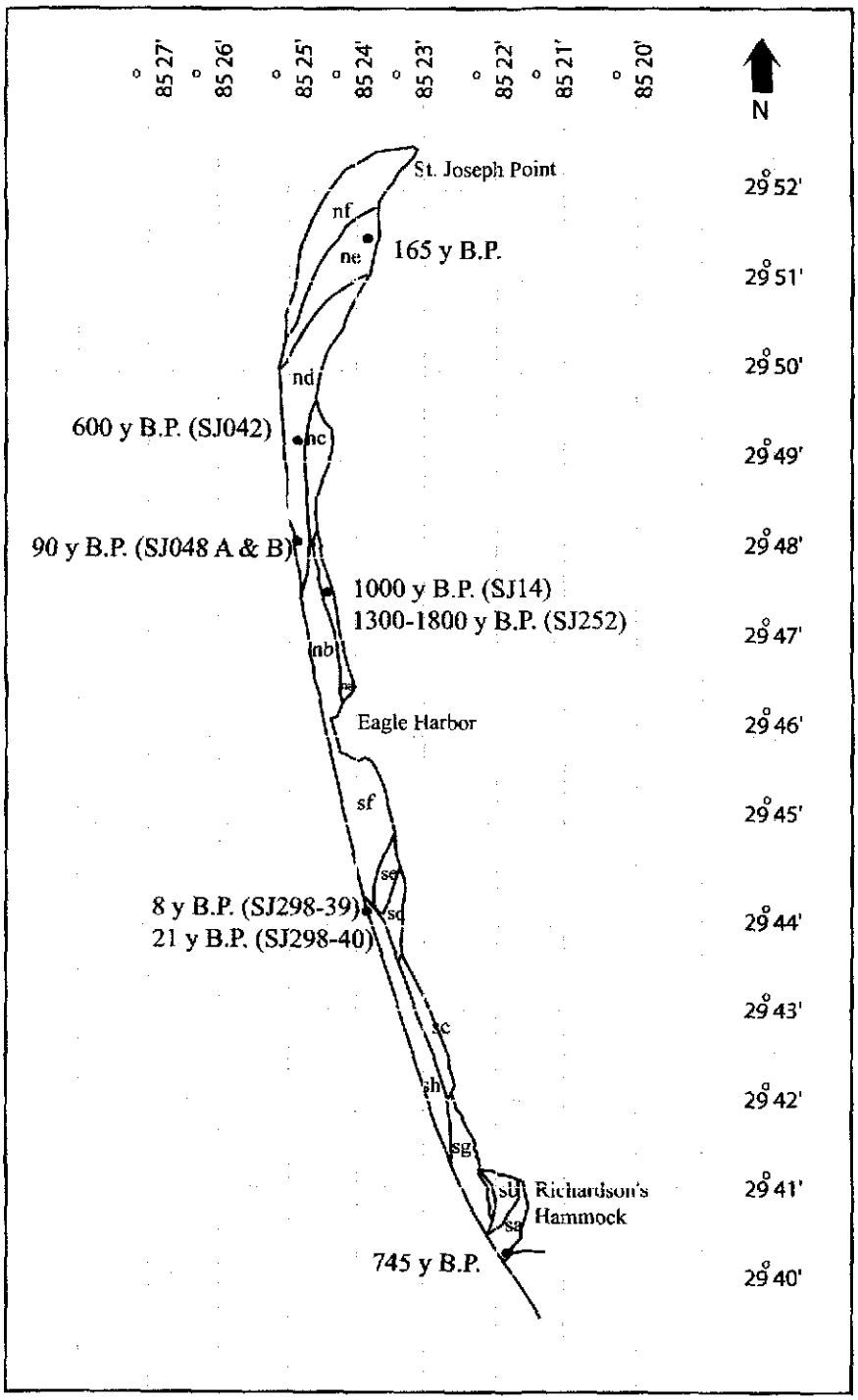

Figure 39- Ages on the peninsula. The 745 year B.P. age comes from a dated peat (Stapor, 1975) and the 165 year B.P. age comes from a spanish mission site (Benchley and Bense, 2000)

Table 18- Feldspar contamination for the 90-150μm fractions

Sample	IRSL	OSL	IRSL/OSL
SJ059	115	117462	0.0010
	91	100054	0.0009
	128	95339	0.0013
	77	120239	0.0006
SJ058	78	153023	0.0005
	189	142308	0.0013
	87	160132	0.0005
	146	52491	0.0028
SJ057	144	238605	0.0006
	133	179143	0.0007
	104	133664	0.0008
	126	188595	0.0007
SJ056	136	117988	0.0012
	95	173801	0.0005
	74	143210	0.0005
	135	155898	0.0009
SJ052B	153	133834	0.0011
	128	251908	0.0005
	113	180265	0.0006
	135	244762	0.0006
SJ052A	305	122770	0.0025
	108	75512	0.0014
	55	76513	0.0007
	89	93983	0.0009
SJ051	169	247005	0.0007
	39	70586	0.0006
	429	220288	0.0019
	27	93262	0.0003
SJ049	159	239566	0.0007
	153	188309	0.0008
	229	177784	0.0013
	116	157807	0.0007
SJ029	54	64084	0.0008
	113	52890	0.0021
	63	55367	0.0011
	218	72455	0.0030
SJ026	119	133503	0.0009
	137	177620	0.0008
	156	115959	0.0013
	80	163017	0.0005
SJ023	136	41544	0.0033
	87	*57098*	*0.0015*
	75	40055	0.0019
	139	59738	0.0023
SJ070	134	121168	0.0011
	91	153075	0.0006
	62	140340	0.0004
	97	156372	0.0006
SJ007	156	119774	0.0013
	324	90114	0.0036
	101	77854	0.0013
	65	76965	0.0008
SJ008	267	68255	0.0039
	91	78384	0.0012
	139	89963	0.0015
	61	92436	0.0007
SJ012	90	70298	0.0013
	191	111260	0.0017
	103	*105050*	*0.0010*
	115	92173	0.0012
SJ019	64	36256	0.0018
	22	19220	0.0011
	116	28378	0.0041
	270	37381	0.0072

Table 19- Feldspar contamination test results for the 150-212μm grain size quartz separates of the littoral samples

Sample	IRSL	OSL	IRSL/OSL
SJ058	115	75351	0.0015
	143	121492	0.0012
	160	86124	0.0019
	83	143684	0.0006
SJ057	60	141314	0.0004
	160	138110	0.0012
	55	124607	0.0004
	69	69396	0.0010
SJ056	101	71361	0.0014
	423	125676	0.0034
	47	69907	0.0007
	117	83971	0.0014
SJ054	149	74600	0.0020
	70	80180	0.0009
	68	57478	0.0012
	38	88305	0.0004
SJ055	67	61286	0.0011
	162	82180	0.0020
	103	76281	0.0014
	53	102844	0.0005
SJ052B	239	80702	0.0030
	73	79824	0.0009
	100	113363	0.0009
	62	78832	0.0008
SJ052A	142	108518	0.0013
	249	137116	0.0018
	119	171372	0.0007
	98	142983	0.0007
SJ051	29	44189	0.0007
	147	134348	0.0011
	57	95768	0.0006
	110	68779	0.0016
SJ049	242	96996	0.0025
	95	87208	0.0011
	91	106061	0.0009
	116	78025	0.0015
SJ030	125	139403	0.0009
	99	96298	0.0010
	98	102432	0.0010
	65	101480	0.0006
SJ073	58	98788	0.0006
	202	168044	0.0012
	73	70103	0.0010
	114	126856	0.0009
SJ029	104	74533	0.0014
	111	91400	0.0012
	120	81585	0.0015
	222	107161	0.0021
SJ026	42	53987	0.0008
	60	50958	0.0012
	239	79647	0.0030
	196	96149	0.0020
SJ024	59	81096	0.0007
	175	119550	0.0015
	75	85026	0.0009
	86	137361	0.0006
SJ071	90	83845	0.0011
	63	63694	0.0010
	51	72714	0.0007
	114	96128	0.0012
SJ070	87	69839	0.0012
	70	95814	0.0007
	101	91392	0.0011
	149	68463	0.0022

Sample	IRSL	OSL	IRSL/OSL
SJ023	63	87990	0.0007
	75	71682	0.0010
	88	59979	0.0015
	100	89467	0.0011
SJ003	90	54196	0.0017
	106	129975	0.0008
	121	93032	0.0013
	176	71178	0.0025
SJ004	102	66309	0.0015
	287	150096	0.0019
	123	112797	0.0011
	57	78894	0.0007
SJ005	82	133551	0.0006
	146	99540	0.0015
	112	77488	0.0014
	205	90454	0.0023
SJ006	65	66500	0.0010
	70	63585	0.0011
	115	95821	0.0012
	182	95340	0.0019
SJ007	127	57026	0.0022
	66	69812	0.0009
	98	79660	0.0012
	83	84354	0.0010
SJ008	103	121674	0.0008
	90	69406	0.0013
	130	80422	0.0016
	87	75681	0.0011
SJ009	168	91787	0.0018
	134	104760	0.0013
	105	97774	0.0011
	83	105940	0.0008
SJ010	70	72796	0.0010
	80	74428	0.0011
SJ011	88	89354	0.0010
	134	125694	0.0011
	122	122398	0.0010
	169	161749	0.0010
SJ012	187	109581	0.0017
	263	108593	0.0024
	122	122859	0.0010
	91	97105	0.0009
SJ013	52	61465	0.0008
	375	79428	0.0047
	66	83653	0.0008
	85	46899	0.0018
SJ014	72	104208	0.0007
	111	82045	0.0014
	129	92295	0.0014
	119	69443	0.0017
SJ015	96	51003	0.0019
	84	43611	0.0019
	118	74900	0.0016
	208	61305	0.0034
SJ016	67	56834	0.0012
	72	61242	0.0012
	83	62859	0.0013
	58	80327	0.0007
SJ018	131	60431	0.0022
	57	71861	0.0008
	200	66775	0.0030
	80	71598	0.0011
SJ019	65	58722	0.0011
	183	77355	0.0024
	119	110837	0.0011
	91	60685	0.0015

Table 20- Feldspar contamination test results for the 212-250μm grain size quartz separates of the littoral samples

Sample	IRSL	OSL	IRSL/OSL
SJ059	109	69733	0.0016
	203	75040	0.0027
	173	*88975*	*0.0019*
	70	60061	0.0012
SJ058	79	40596	0.0019
	136	48485	0.0028
	101	58494	0.0017
	73	40049	0.0018
SJ057	65	78036	0.0008
	105	66280	0.0016
	104	57211	0.0018
	185	44375	0.0042
SJ056	139	50454	0.0028
	69	44349	0.0016
	105	58882	0.0018
	141	57421	0.0025
SJ055	69	122821	0.0006
	85	56987	0.0015
	125	77270	0.0016
	100	87909	0.0011
SJ054	23	42745	0.0005
	313	34444	0.0091
	93	44017	0.0021
	75	65118	0.0012
SJ052B	81	65284	0.0012
	198	75320	0.0026
	72	68593	0.0010
	209	*63687*	*0.0033*
SJ052A	101	45306	0.0022
	132	87115	0.0015
	67	59692	0.0011
	207	73601	0.0028
SJ051	81	55991	0.0014
	62	55630	0.0011
	143	51884	0.0028
	119	51092	0.0023
SJ050	140	71735	0.0020
	145	78739	0.0018
	32	63432	0.0005
	80	58380	0.0014
SJ049	132	54412	0.0024
	144	72240	0.0020
	78	51863	0.0015
	73	33980	0.0021
SJ030	52	45577	0.0011
	56	33966	0.0016
	77	46770	0.0016
	100	37298	0.0027
SJ072	99	86654	0.0011
	50	52273	0.0010
	131	85810	0.0015
	127	74634	0.0017
SJ073	94	75763	0.0012
	163	101135	0.0016
	199	104783	0.0019
	139	110837	0.0013
SJ029	55	45905	0.0012
	72	48010	0.0015
	149	46860	0.0032
	78	56580	0.0014
SJ027	153	76448	0.0020
	98	88043	0.0011
	183	78971	0.0023
	43	40904	0.0011
SJ026	128	38468	0.0033
	135	53727	0.0025
	24	30257	0.0008
	71	58498	0.0012
SJ025	325	60622	0.0054
	77	53353	*0.0014*
	39	45063	0.0009
	123	55321	0.0022

Sample	IRSL	OSL	IRSL/OSL
SJ024	126	95777	0.0013
	52	48116	0.0011
	50	*57842*	*0.0009*
	431	108418	0.0040
SJ071	82	109841	0.0007
	173	97773	0.0018
	76	87210	0.0009
	144	99213	0.0015
SJ070	220	34057	0.0065
	33	30671	0.0011
	106	47385	0.0022
	51	45841	0.0011
SJ003	157	63747	0.0025
	198	82258	0.0024
	107	54693	0.0020
	64	74815	0.0009
SJ004	41	40715	0.0010
	104	30121	0.0035
	56	47425	0.0012
	39	37542	0.0010
SJ005	35	37488	0.0009
	99	19892	0.0050
	64	42976	0.0015
	95	40410	0.0024
SJ006	97	49122	0.0020
	181	75350	0.0024
	140	77519	0.0018
	369	*65604*	*0.0056*
SJ007	119	54534	0.0022
	133	66341	0.0020
	82	65877	0.0012
	84	61206	0.0014
SJ008	86	30958	0.0028
	62	58192	0.0011
	94	55613	0.0017
	111	40906	0.0027
SJ009	46	45449	0.0010
	105	37437	0.0028
	117	52009	0.0022
	103	57456	0.0018
SJ010	50	72742	0.0007
	148	73839	0.0020
	127	61683	0.0021
	204	85425	0.0024
SJ011	191	65610	0.0029
	136	64576	0.0021
	149	85037	0.0018
	68	15907	0.0043
SJ013	142	45330	0.0031
	106	57492	0.0018
	76	56046	0.0014
	88	54339	0.0016
SJ014	83	53830	0.0015
	84	43342	0.0019
	70	51114	0.0014
	68	55888	0.0012
SJ015	96	87818	0.0011
	63	74835	0.0008
	103	71228	0.0014
	130	100150	0.0013
SJ016	52	49642	0.0010
	142	57710	0.0025
	55	48068	0.0011
	197	42614	0.0046
SJ018	115	56650	0.0020
	49	43416	0.0011
	64	75071	0.0009
	71	48120	0.0015
SJ019	234	54783	0.0043
	80	*62245*	*0.0013*
	240	65659	0.0037
	70	88275	0.0008

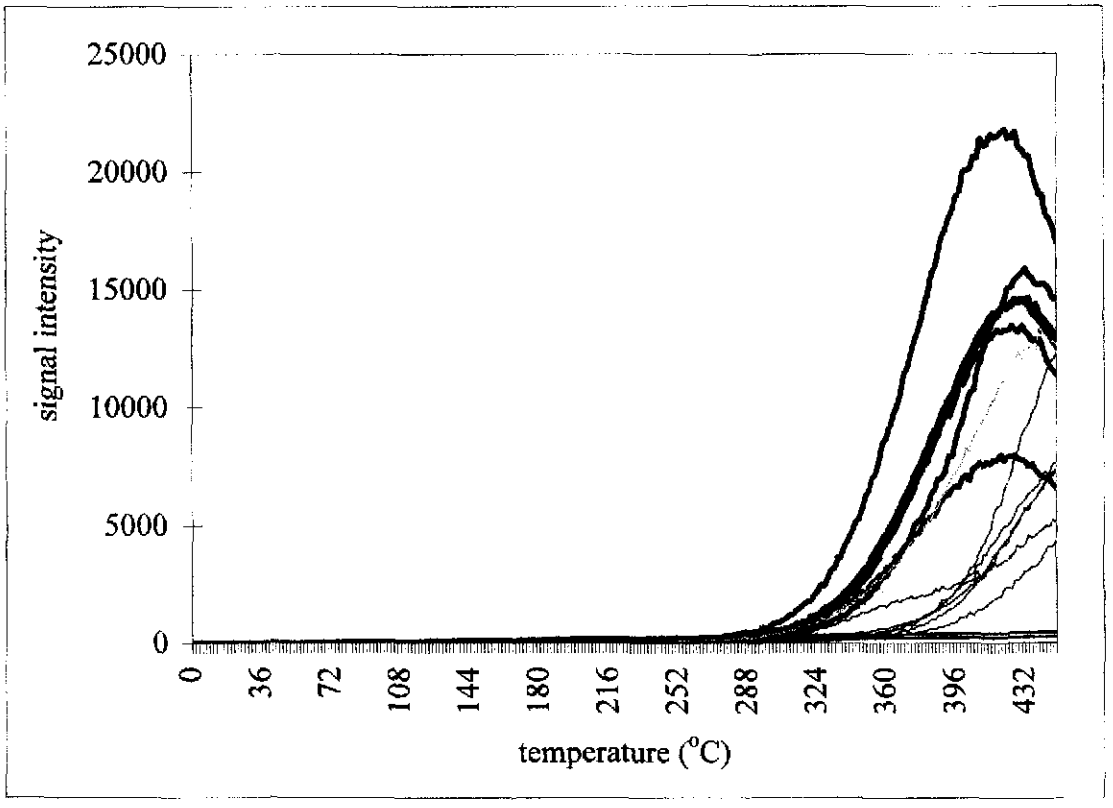

Figure 40- Effect of altering the heating rate. The glowcurves shown are from the 212-250 μm grain size fraction of sample SJ019. The thick black lines represent a heating rate of 5 °C/sec, the light grey lines represent a rate of 10 °C/sec and the dark grey lines represent a rate of 15 °C/sec. No beta dose was administered.

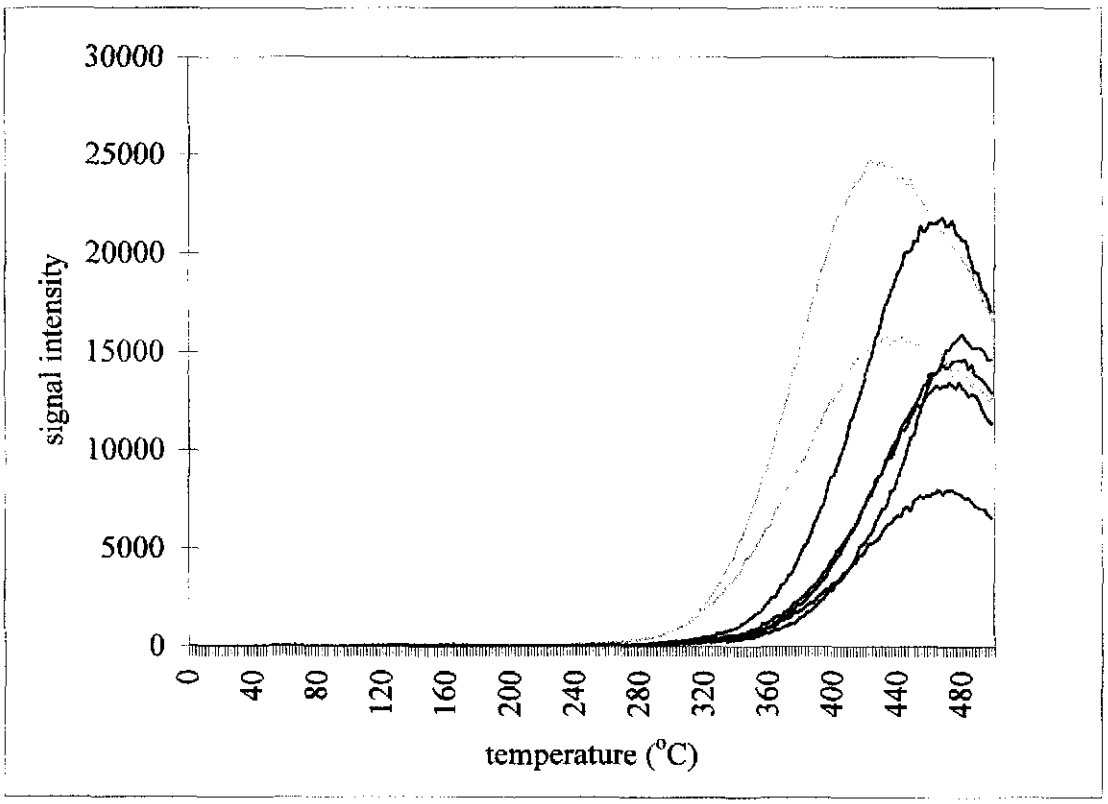

Figure 41- Effect of altering the maximum temperature. The curves shown are from the 212-250 μm grain size fraction of sample SJ019. The grey lines represent a maximum temperature of 500 °C while the black lines represent a maximum temperature of 450 °C. TL was recorded while the sample was heated from its preheat temperature to a maximum temperature of either 450 °C or 500 °C.

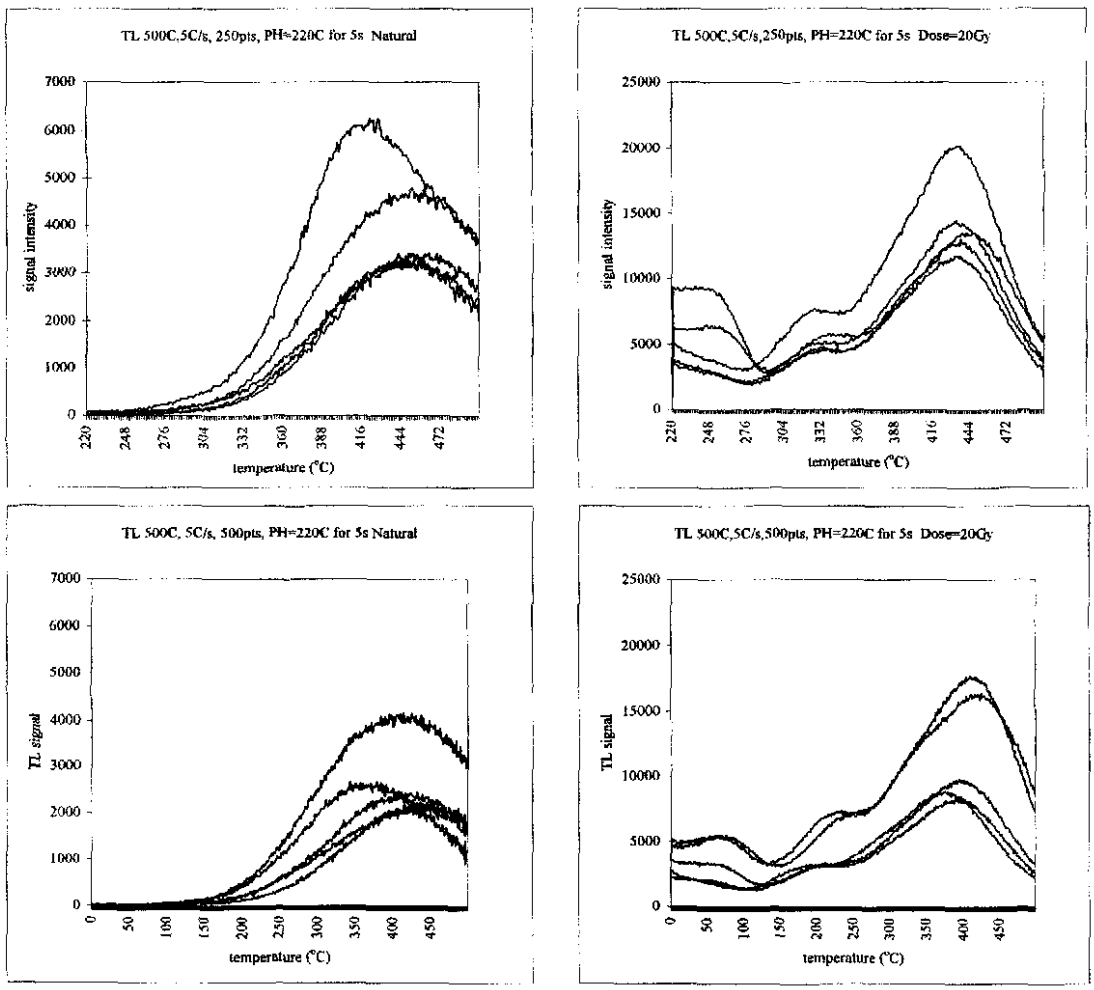

Figure 42- Effect of increasing the number of datapoints collected.

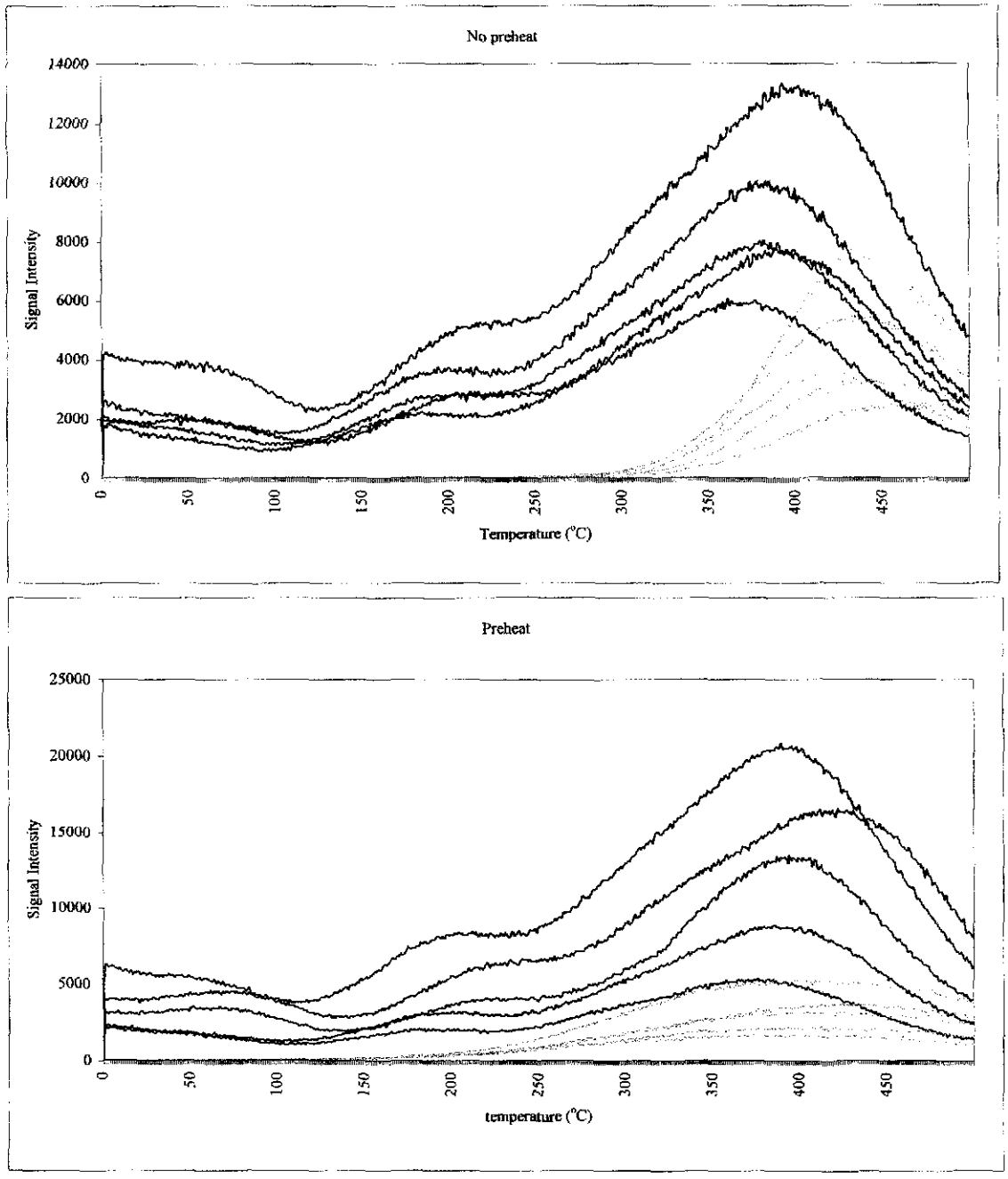

Figure 43- Comparison of preheat vs. no preheat. Measurements were made on the 212-250μm fraction of SJ019 (TL 500C, 5C/s, 500pts, PH=0C for 0s or 220C for 5s). Grey lines represent the natural glowcurves and black lines represent glowcurves obtained after administering a 20Gy beta dose.

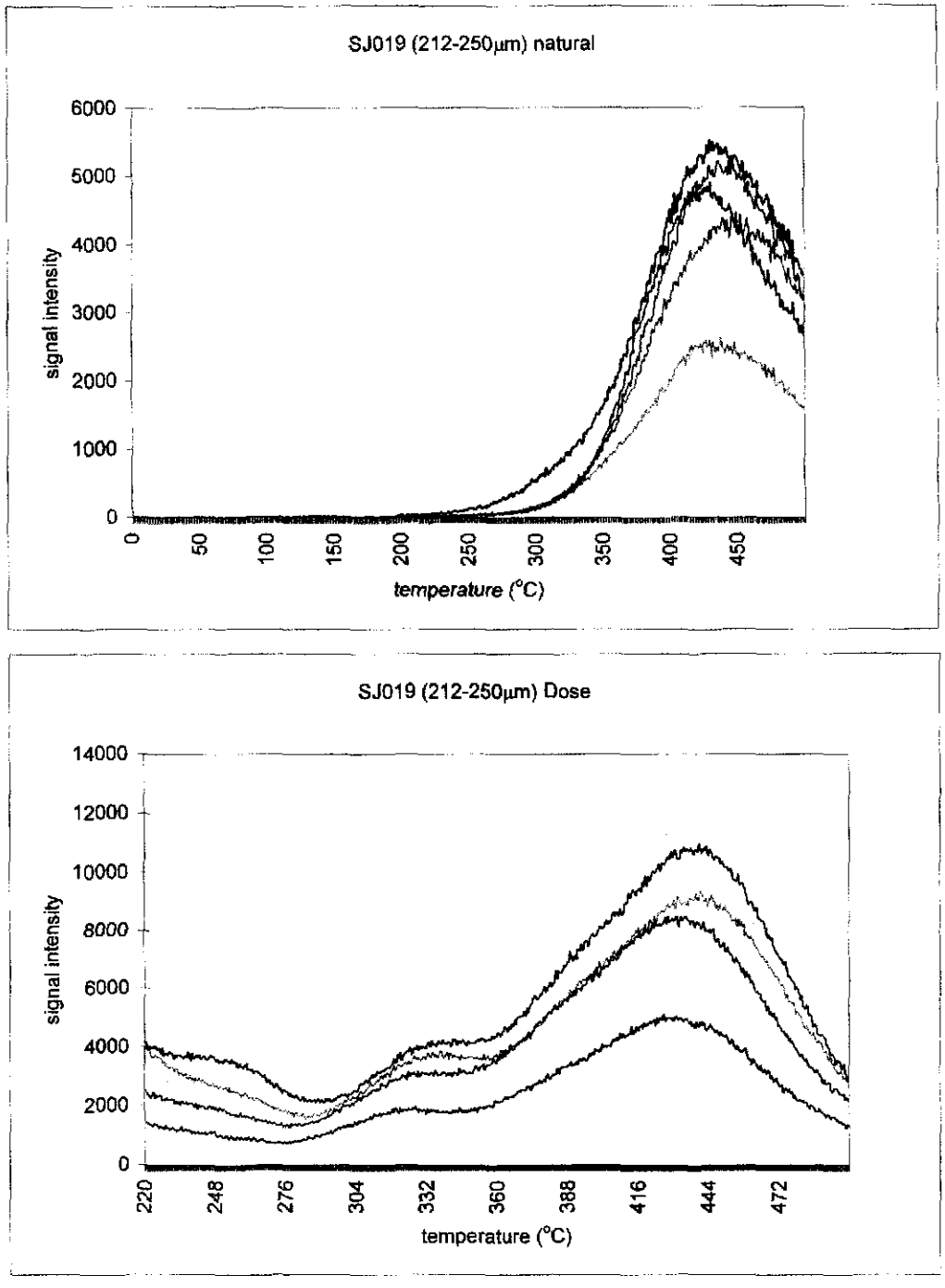

Figure 44- Results of waiting 24 hours between administration of the beta dose and measurement. The top graph shows the natural (measured on January 31, 2002). A beta dose was administered on January 31, 2002 and the response to this beta dose was measured on February 1, 2002.

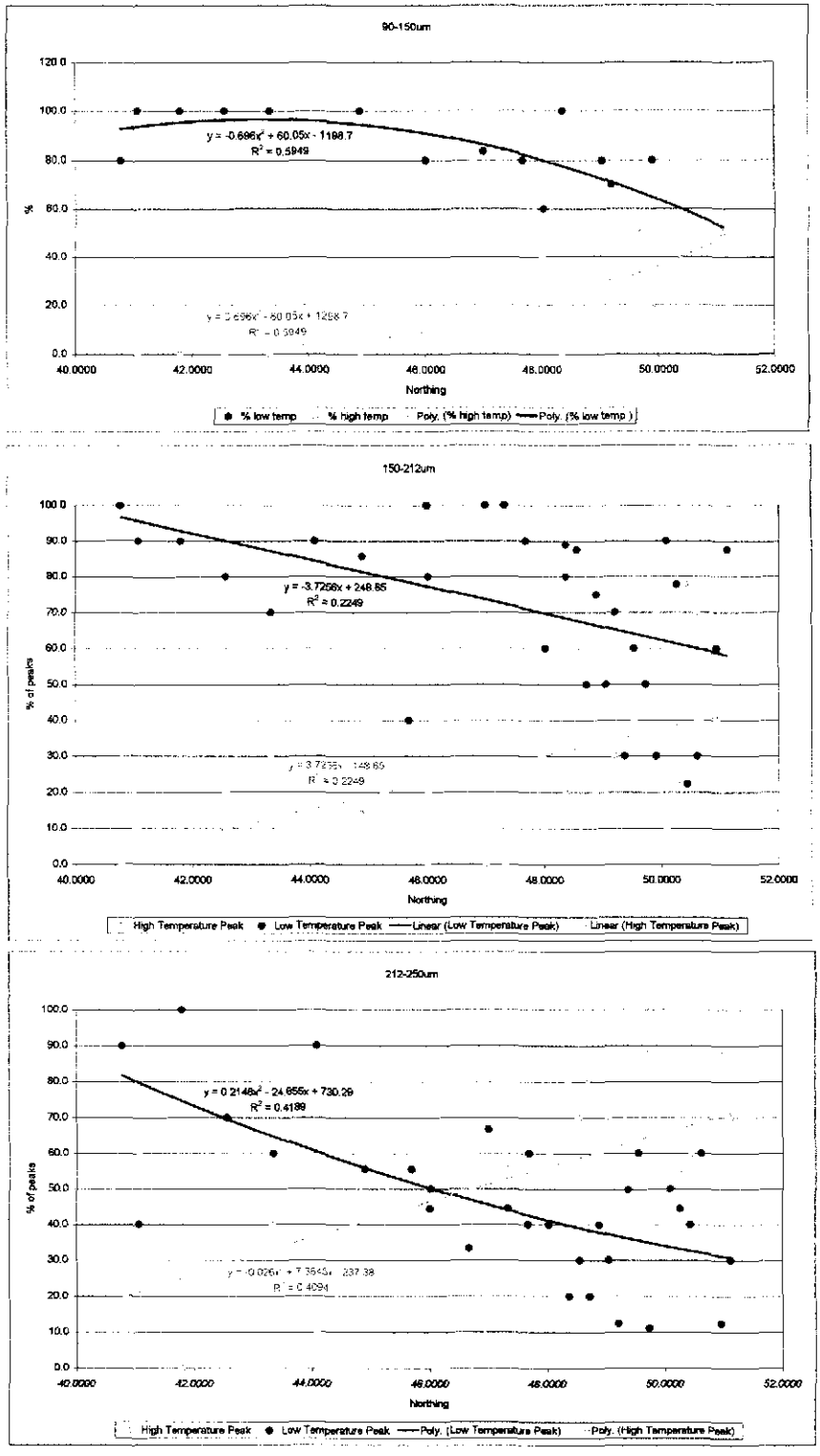

Figure 45- Relationship between dominant peak and location along the peninsula.

Table 21- NRTL values for the 90-150μm fractions of the littoral samples.

	INTEGRATION METHOD 1				INTEGRATION METHOD 2				INTEGRATION METHOD 3			
sample	n	NRTL	STDEV	% STDEV	n	NRTL	STDEV	% STDEV	n	NRTL	STDEV	% STDEV
*SJ059	10	0.63	0.02	2.51	10	0.49	0.02	3.23	10	0.66	0.02	2.40
SJ058	5	0.43	0.06	13.52	3	0.41	0.02	4.22	3	0.47	0.05	9.83
*SJ057	10	0.78	0.01	1.62	10	0.70	0.01	1.36	10	0.84	0.01	1.51
SJ056	10	0.75	0.03	4.01	9	0.57	0.02	4.09	9	0.78	0.03	3.42
SJ054	10	0.67	0.02	3.30	10	0.56	0.03	4.52	10	0.72	0.02	3.07
*SJ052B	10	0.77	0.03	3.29	10	0.59	0.04	7.50	10	0.81	0.03	3.51
SJ052A	9	0.43	0.01	3.10	7	0.66	0.00	0.57	7	0.47	0.01	2.41
SJ051	9	0.63	0.02	3.17	8	0.56	0.01	1.89	8	0.69	0.02	3.07
SJ049	10	0.58	0.01	2.18	10	0.49	0.03	6.45	10	0.62	0.02	2.55
SJ029	8	0.30	0.01	4.71	7	0.36	0.01	3.15	7	0.36	0.02	4.20
SJ026	6	0.47	0.02	3.47	6	0.54	0.02	3.78	6	0.55	0.02	2.97
SJ024	5	0.35	0.01	2.56	4	0.39	0.03	7.69	4	0.40	0.01	2.50
SJ023	9	0.28	0.03	9.52	6	0.36	0.02	4.54	6	0.34	0.02	7.20
SJ070	5	0.59	0.03	4.55	4	0.48	0.04	7.29	4	0.58	0.03	5.17
SJ007	5	0.32	0.02	6.99	5	0.36	0.01	3.73	5	0.38	0.02	4.71
SJ008	9	0.30	0.01	3.33	4	0.49	0.03	6.12	0			
SJ011	10	0.28	0.01	3.39	8	0.36	0.01	2.95	8	0.35	0.01	2.02
SJ012	10	0.32	0.01	3.95	1	0.41	-	-	1	0.38	-	-
SJ019	9	0.25	0.02	6.67	4	0.34	0.05	13.24	4	0.31	0.04	11.29

note: A * indicates a sandbar sample.

Table 22- NRTL values for the 150-212μm fractions of the littoral samples.

	INTEGRATION METHOD 1				INTEGRATION METHOD 2				INTEGRATION METHOD 3			
sample	n	NRTL	STDEV	% STDEV	n	NRTL	STDEV	% STDEV	n	NRTL	STDEV	% STDEV
*SJ059	10	0.54	0.02	2.93	7	0.52	0.02	2.91	8	0.59	0.01	2.40
SJ058	10	0.40	0.03	7.12	9	0.38	0.02	6.14	9	0.44	0.03	7.58
*SJ057	10	0.51	0.03	4.96	8	0.47	0.03	6.77	8	0.56	0.03	5.68
SJ056	10	0.42	0.02	4.52	10	0.45	0.02	3.51	10	0.49	0.02	4.52
*SJ055	9	0.47	0.02	4.26	6	0.48	0.02	3.40	6	0.52	0.02	3.14
SJ054	10	0.43	0.02	4.41	10	0.45	0.01	2.81	10	0.49	0.02	3.87
*SJ052B	9	0.45	0.02	4.44	6	0.45	0.02	5.44	8	0.50	0.02	4.95
SJ052A	10	0.38	0.01	2.50	10	0.43	0.01	2.21	10	0.45	0.01	1.41
SJ051	10	0.37	0.02	5.98	9	0.42	0.01	2.38	9	0.44	0.02	4.55
SJ049	7	0.38	0.02	3.98	7	0.36	0.01	2.10	7	0.42	0.01	2.70
SJ030	10	0.33	0.01	2.87	9	0.41	0.02	5.69	9	0.41	0.01	3.25
SJ073	10	0.36	0.02	6.15	8	0.39	0.02	4.53	8	0.43	0.02	4.11
SJ029	10	0.32	0.01	3.95	9	0.38	0.01	1.75	9	0.38	0.01	2.63
SJ026	10	0.35	0.01	3.61	9	0.36	0.02	4.63	9	0.40	0.01	3.33
SJ025	10	0.37	0.01	3.42	7	0.43	0.02	3.52	7	0.45	0.02	3.36
SJ024	10	0.35	0.01	3.61	8	0.44	0.01	2.41	8	0.43	0.01	3.29
SJ071	10	0.34	0.02	5.58	6	0.41	0.03	6.97	6	0.42	0.02	4.86
SJ023	10	0.27	0.01	2.34	7	0.32	0.01	3.54	7	0.33	0.01	3.44
SJ070	9	0.33	0.02	6.06	5	0.38	0.03	8.24	5	0.41	0.02	4.36
SJ003	10	0.38	0.06	16.64	7	0.39	0.02	4.85	7	0.45	0.08	16.80
SJ004	8	0.30	0.02	5.89	7	0.32	0.04	12.99	7	0.34	0.03	8.89
SJ005	9	0.29	0.01	2.30	6	0.36	0.02	5.67	6	0.36	0.02	4.54
SJ006	4	0.34	0.03	7.35	4	0.44	0.03	5.68	4	0.42	0.01	2.38
SJ007	10	0.30	0.02	5.27	7	0.42	0.02	4.50	7	0.37	0.01	3.06
SJ008	10	0.32	0.01	3.95	9	0.39	0.01	3.42	9	0.39	0.01	2.56
SJ009	10	0.30	0.01	4.22	9	0.35	0.02	6.67	9	0.36	0.02	4.63
SJ010	5	0.31	0.01	2.89	4	0.36	0.03	8.33	4	0.37	0.01	2.70
SJ011	10	0.29	0.01	3.27	7	0.40	0.01	2.83	7	0.36	0.01	3.15
SJ012	10	0.30	0.01	3.16	10	0.39	0.02	5.68	10	0.38	0.01	3.33
SJ013	10	0.28	0.01	3.39	8	0.32	0.02	5.52	8	0.33	0.02	5.36
SJ014	10	0.28	0.02	7.91	8	0.35	0.02	6.06	8	0.36	0.01	3.93
SJ015	10	0.27	0.01	4.68	8	0.37	0.02	5.73	8	0.34	0.02	6.24
SJ016	10	0.30	0.01	3.16	10	0.39	0.02	5.68	10	0.38	0.01	3.33
SJ018	10	0.33	0.01	3.83	8	0.40	0.02	4.42	8	0.41	0.02	4.31
SJ019	10	0.29	0.01	4.36	8	0.38	0.01	2.79	8	0.35	0.01	4.04

note: A * *indicates a sandbar sample.*

Table 23- NRTL values for the 212-250μm fractions of the littoral samples.

	INTEGRATION METHOD 1				INTEGRATION METHOD 2				INTEGRATION METHOD 3			
sample	n	NRTL	STDEV	% STDEV	n	NRTL	STDEV	% STDEV	n	NRTL	STDEV	% STDEV
*SJ059	8	0.41	0.01	3.45	5	0.42	0.01	3.19	5	0.46	0.01	2.92
SJ058	10	0.31	0.02	7.14	7	0.34	0.02	4.45	7	0.37	0.03	7.15
*SJ057	8	0.33	0.02	7.50	4	0.39	0.04	8.97	4	0.43	0.03	6.98
SJ056	10	0.29	0.01	3.27	10	0.37	0.03	7.69	10	0.36	0.01	2.64
*SJ055	6	0.33	0.02	4.95	3	0.34	0.04	11.89	3	0.37	0.03	9.36
SJ054	9	0.36	0.03	8.33	3	0.40	0.03	7.22	3	0.47	0.05	11.06
*SJ052B	10	0.35	0.02	4.52	7	0.40	0.01	2.83	7	0.43	0.01	2.64
SJ052A	10	0.30	0.01	3.16	9	0.38	0.01	2.63	9	0.37	0.01	2.70
SJ051	10	0.31	0.01	4.08	8	0.38	0.02	4.65	8	0.38	0.01	3.72
SJ050	10	0.36	0.02	6.15	9	0.40	0.02	5.83	9	0.41	0.02	5.69
SJ049	7	0.27	0.01	4.20	7	0.35	0.01	2.16	7	0.34	0.01	3.33
SJ030	9	0.28	0.02	5.95	7	0.38	0.02	5.97	7	0.35	0.02	6.48
*SJ072	10	0.30	0.01	4.22	6	0.41	0.03	6.97	6	0.38	0.02	4.30
SJ073	9	0.28	0.01	4.76	7	0.36	0.01	3.15	7	0.35	0.01	3.24
SJ029	7	0.29	0.02	5.21	5	0.33	0.01	2.71	5	0.36	0.01	2.48
SJ027	9	0.33	0.03	9.09	8	0.35	0.02	5.05	8	0.39	0.03	7.25
SJ026	9	0.26	0.01	3.85	5	0.35	0.01	3.83	5	0.33	0.01	2.71
SJ025	8	0.27	0.01	3.93	7	0.40	0.02	4.72	7	0.34	0.01	3.33
SJ024	8	0.28	0.01	2.53	7	0.35	0.01	3.24	7	0.34	0.01	2.22
SJ071	10	0.29	0.02	5.45	8	0.41	0.02	4.31	8	0.37	0.01	2.87
SJ070	7	0.24	0.02	9.45	7	0.35	0.01	2.16	7	0.30	0.02	5.04
SJ003	9	0.26	0.01	3.85	6	0.40	0.02	4.08	6	0.33	0.02	4.95
SJ004	10	0.26	0.01	2.43	9	0.34	0.02	4.90	9	0.33	0.01	3.03
SJ005	8	0.26	0.02	8.16	7	0.35	0.02	6.48	7	0.31	0.02	7.32
SJ006	10	0.28	0.01	3.39	8	0.35	0.02	5.05	8	0.35	0.01	3.03
SJ007	10	0.27	0.01	2.34	10	0.40	0.02	3.95	10	0.34	0.01	2.79
SJ008	6	0.25	0.01	3.27	6	0.36	0.01	2.27	6	0.31	0.01	3.95
SJ009	8	0.24	0.01	5.89	4	0.31	0.01	3.23	4	0.29	0.01	3.45
SJ010	10	0.26	0.01	4.87	6	0.36	0.02	5.67	6	0.32	0.02	5.10
SJ011	9	0.25	0.01	2.67	6	0.35	0.01	3.50	6	0.32	0.01	2.55
SJ013	7	0.27	0.01	4.20	4	0.31	0.01	3.23	4	0.32	0.01	3.13
SJ014	8	0.23	0.01	4.61	6	0.30	0.01	4.08	6	0.29	0.01	2.82
SJ015	10	0.29	0.01	2.18	6	0.38	0.01	2.15	6	0.37	0.01	2.21
SJ016	8	0.27	0.01	3.93	3	0.29	0.03	9.95	3	0.32	0.02	5.41
SJ018	5	0.24	0.00	1.86	2	0.33	0.02	6.43	2	0.30	0.02	7.07
SJ019	7	0.27	0.02	7.00	1	0.32	-	-	1	0.37	-	-

note: A * indicates a sandbar sample.

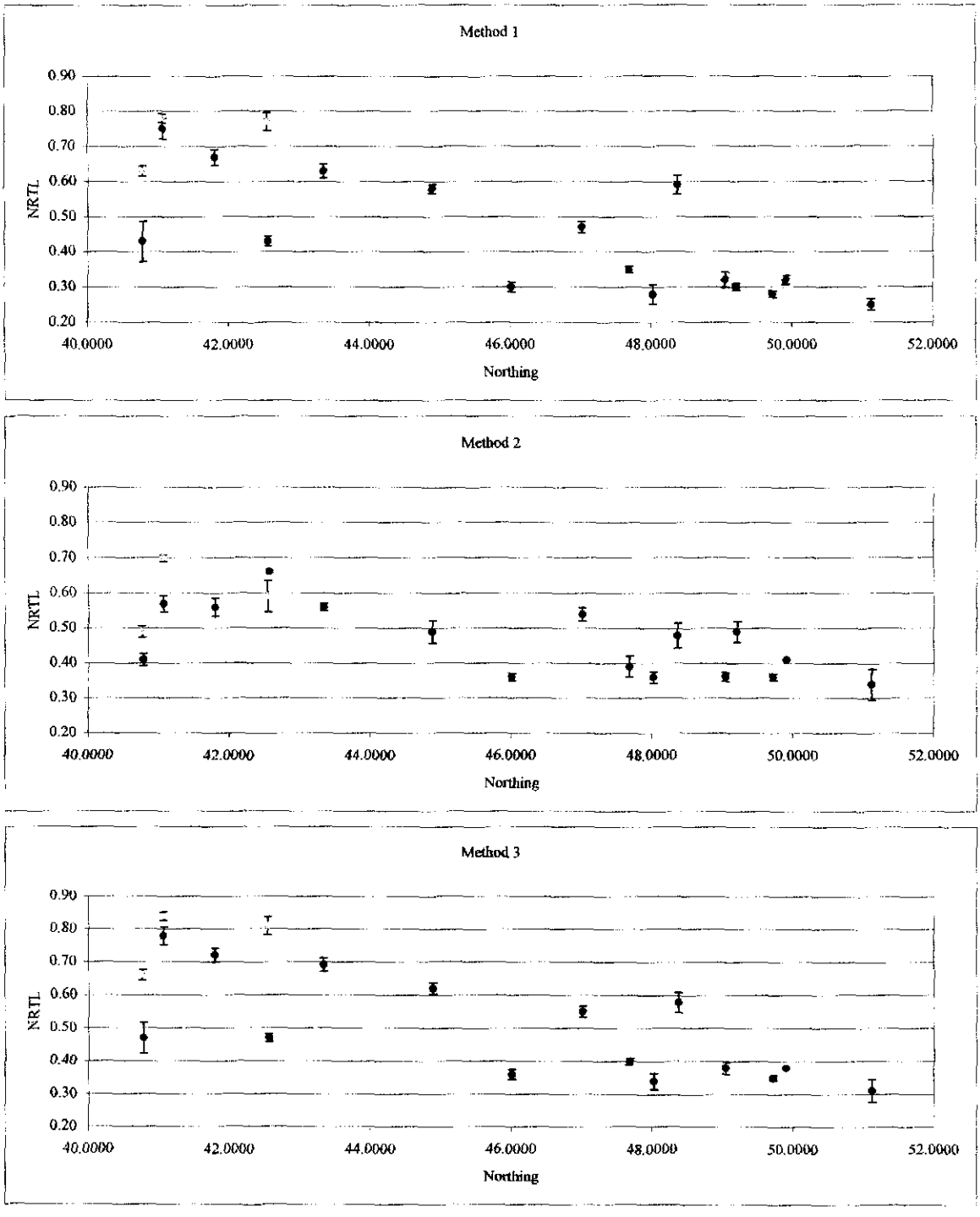

Figure 46- NRTL trends for the 90-150μm grain size fraction.

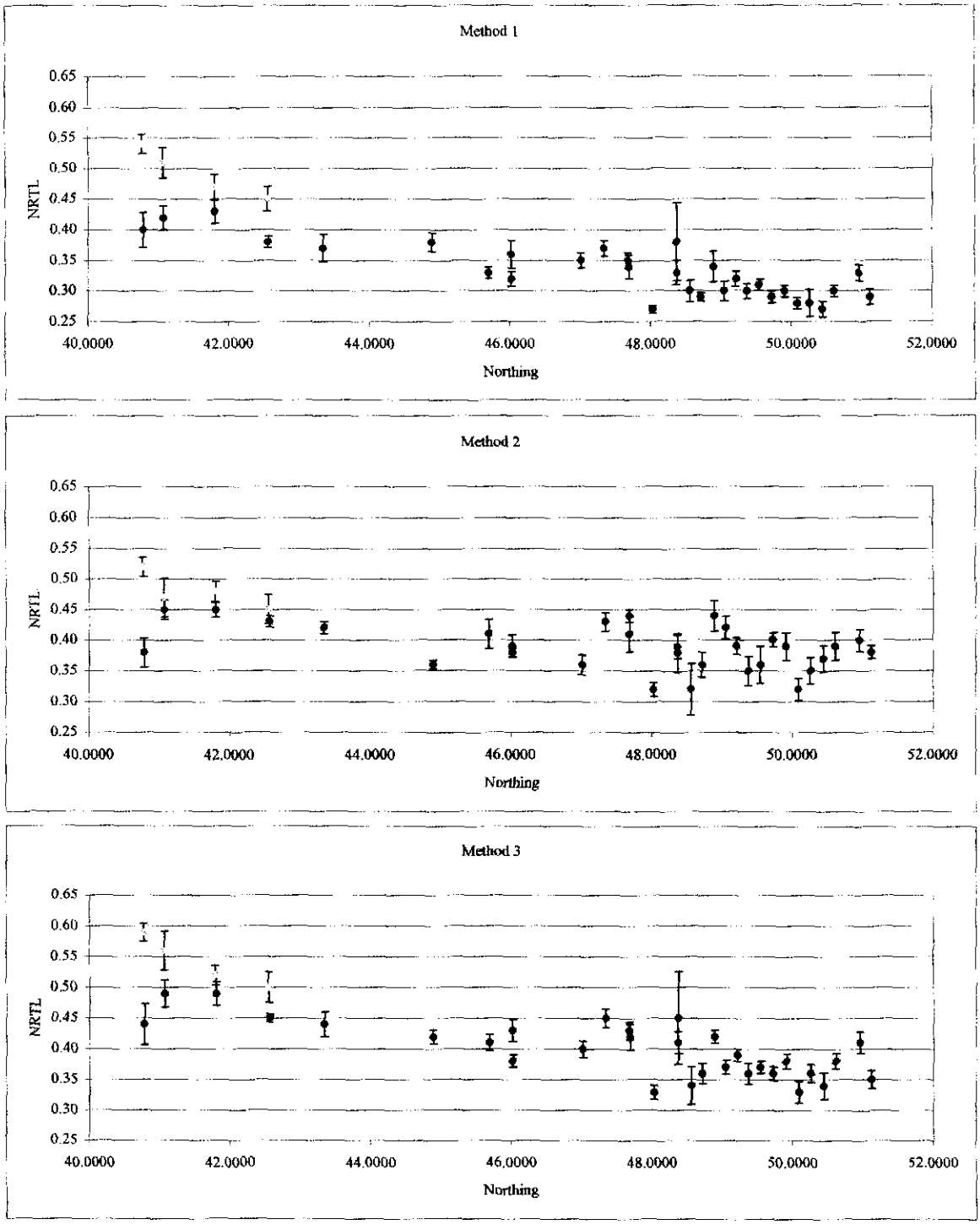

Figure 47- NRTL trends for the 150-212μm grain size fraction.

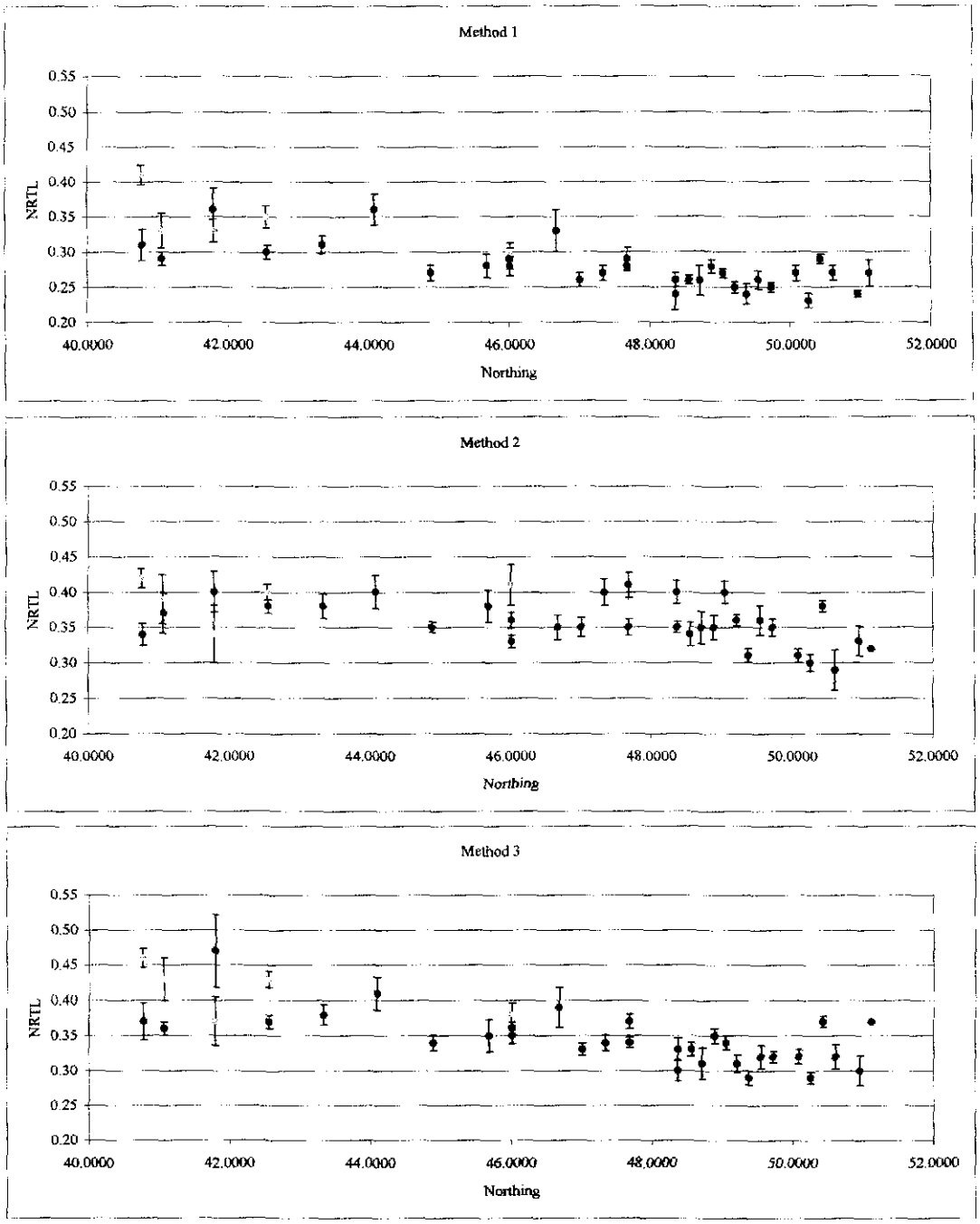

Figure 48- NRTL trends for the 212-250μm grain size fraction.

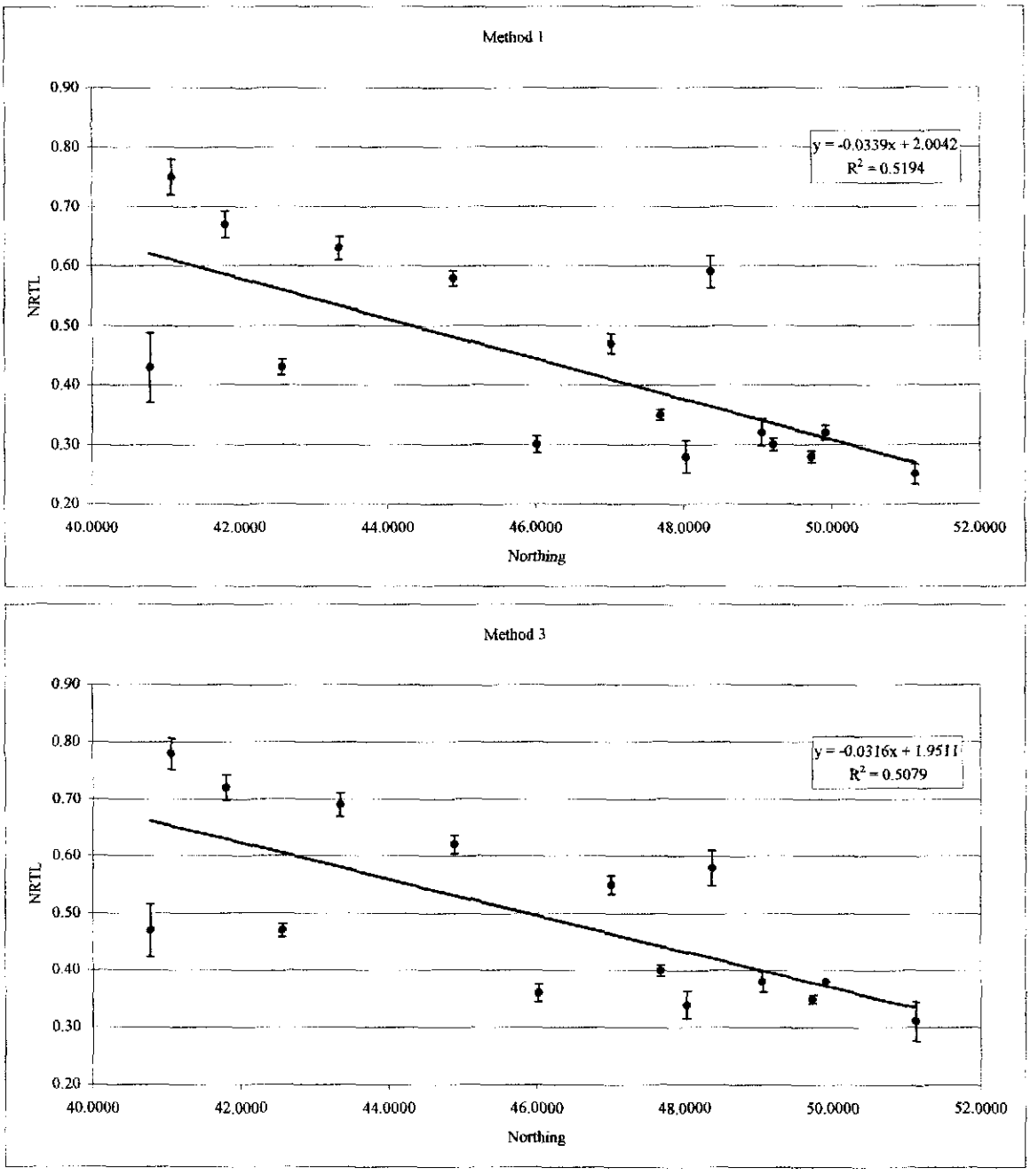

Figure 49- NRTL trends for the 90-150μm grain size fraction. Sandbar samples have been excluded.

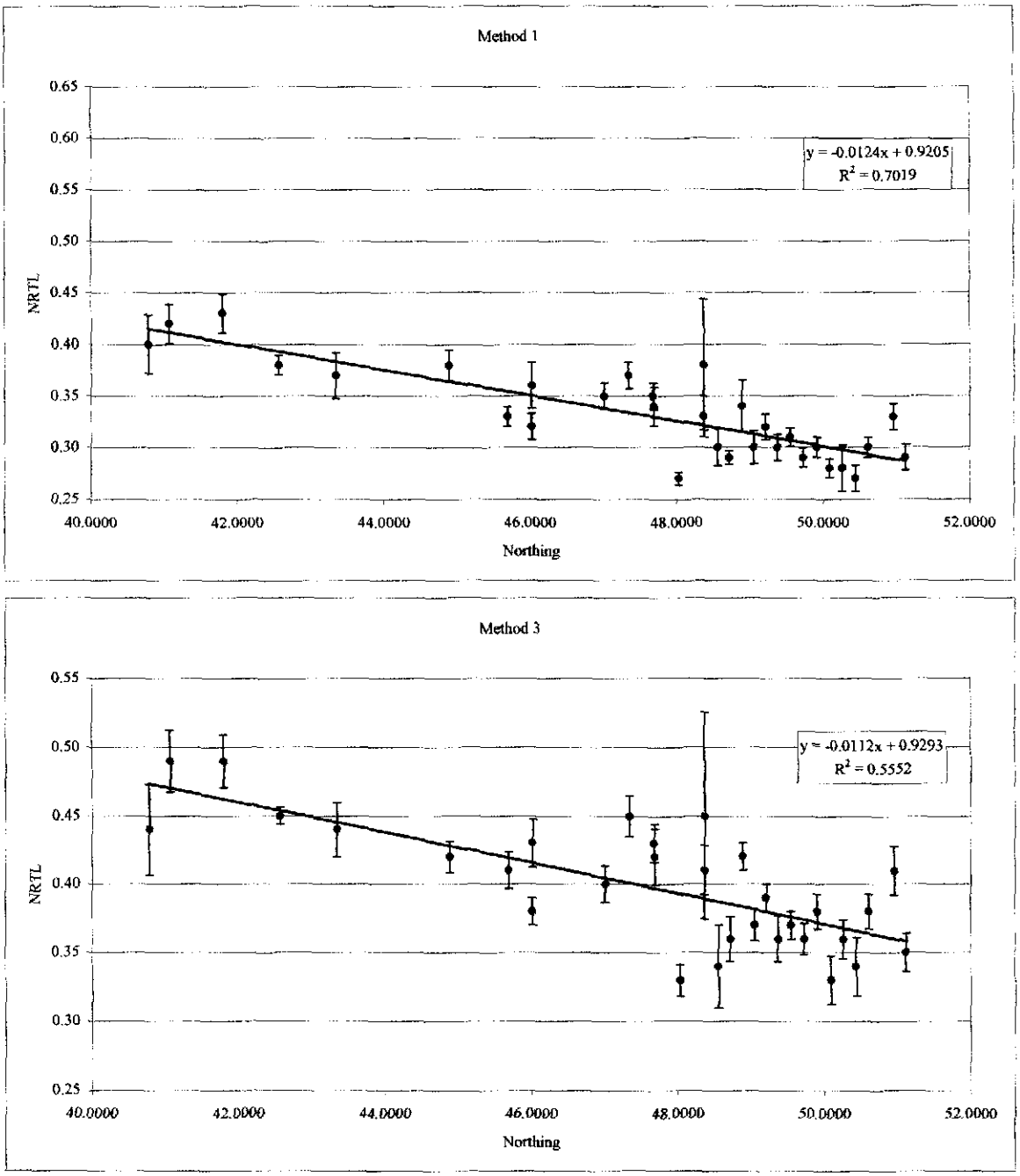

Figure 50- NRTL trends for the 150-212μm grain size fraction. Sandbar samples have been excluded.

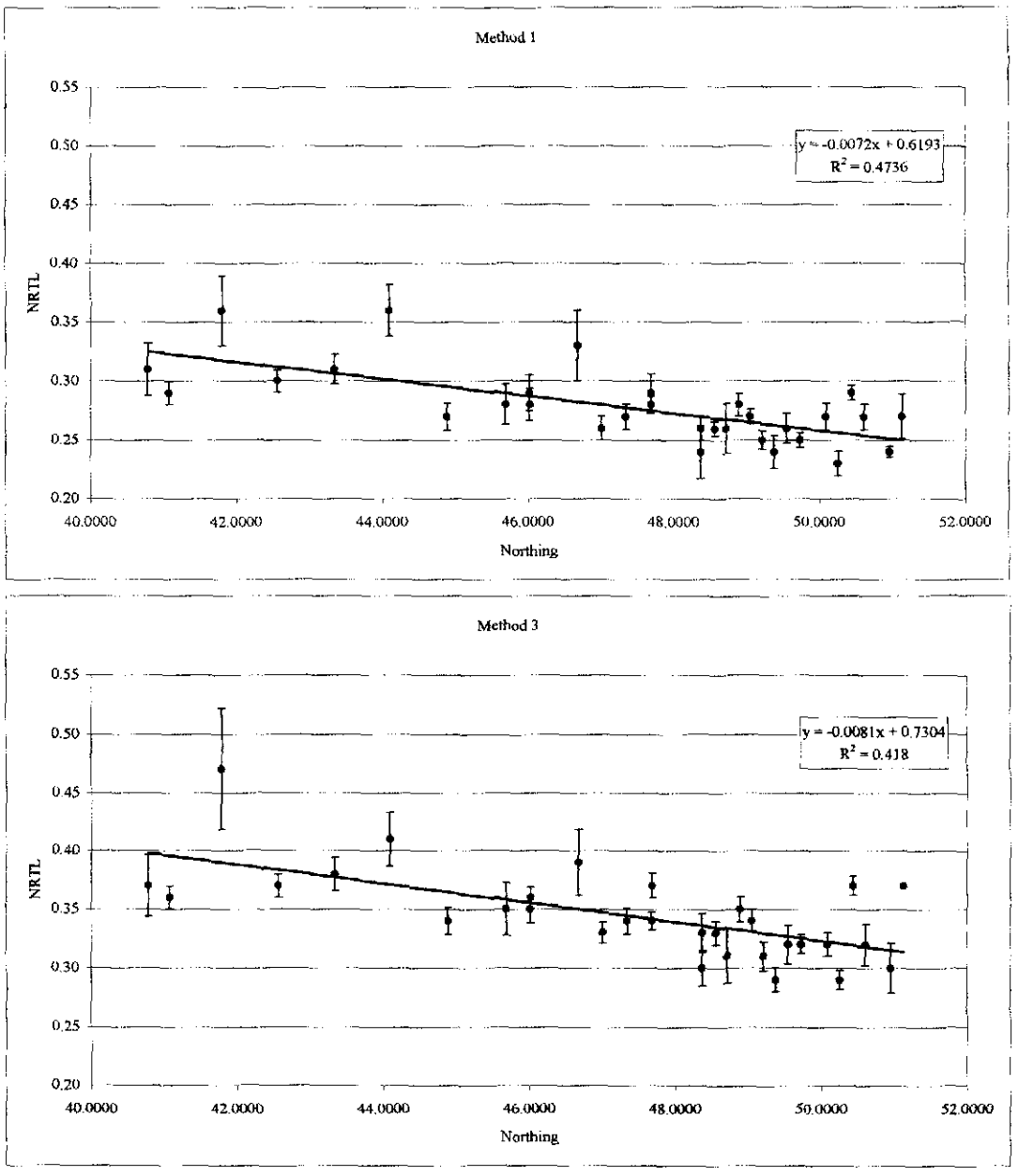

Figure 51- NRTL trends for the 212-250μm grain size fraction. Sandbar samples have been excluded.

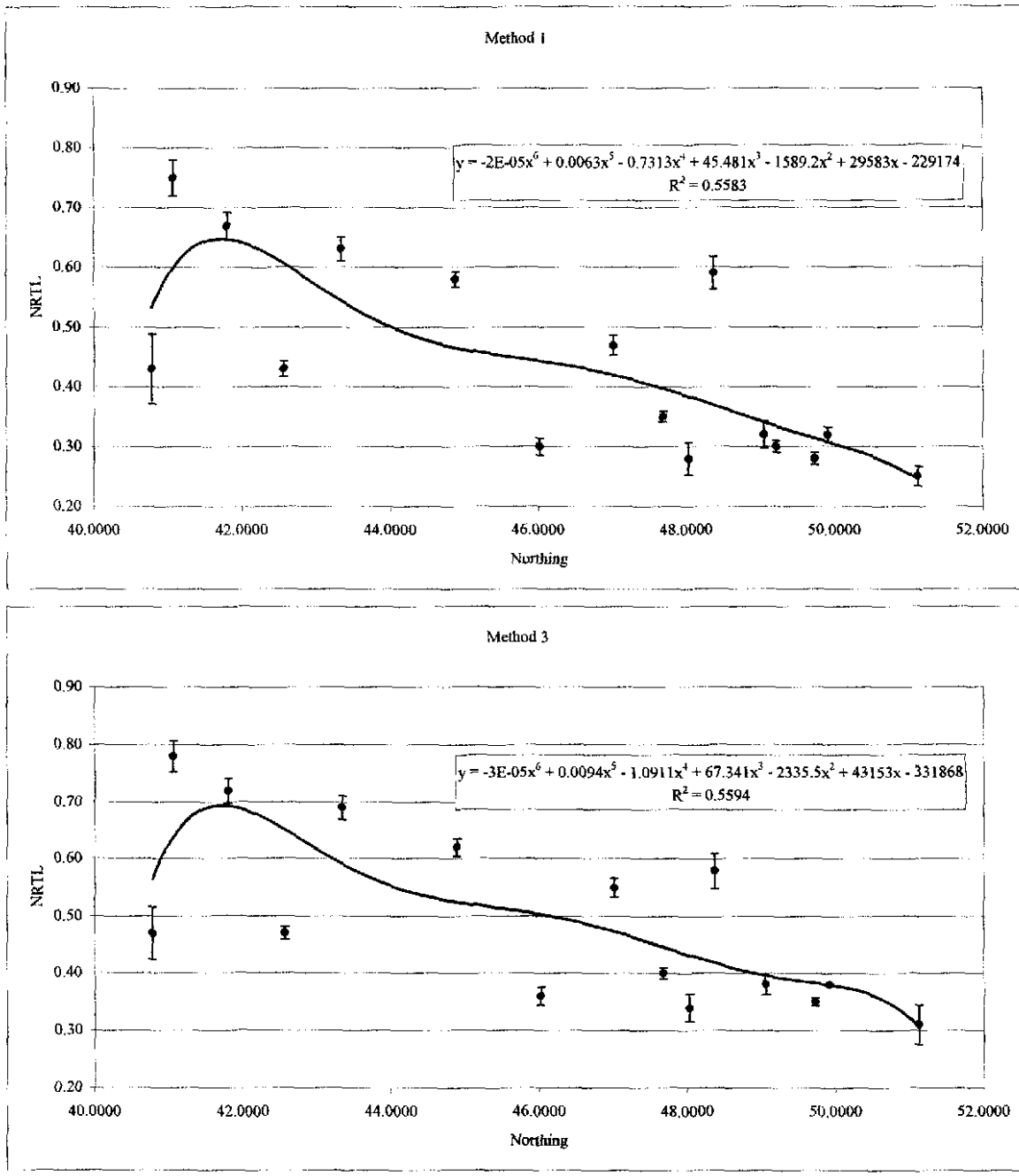

Figure 52- NRTL trends for the 90-150μm grain size fraction. Sandbar samples have been excluded.

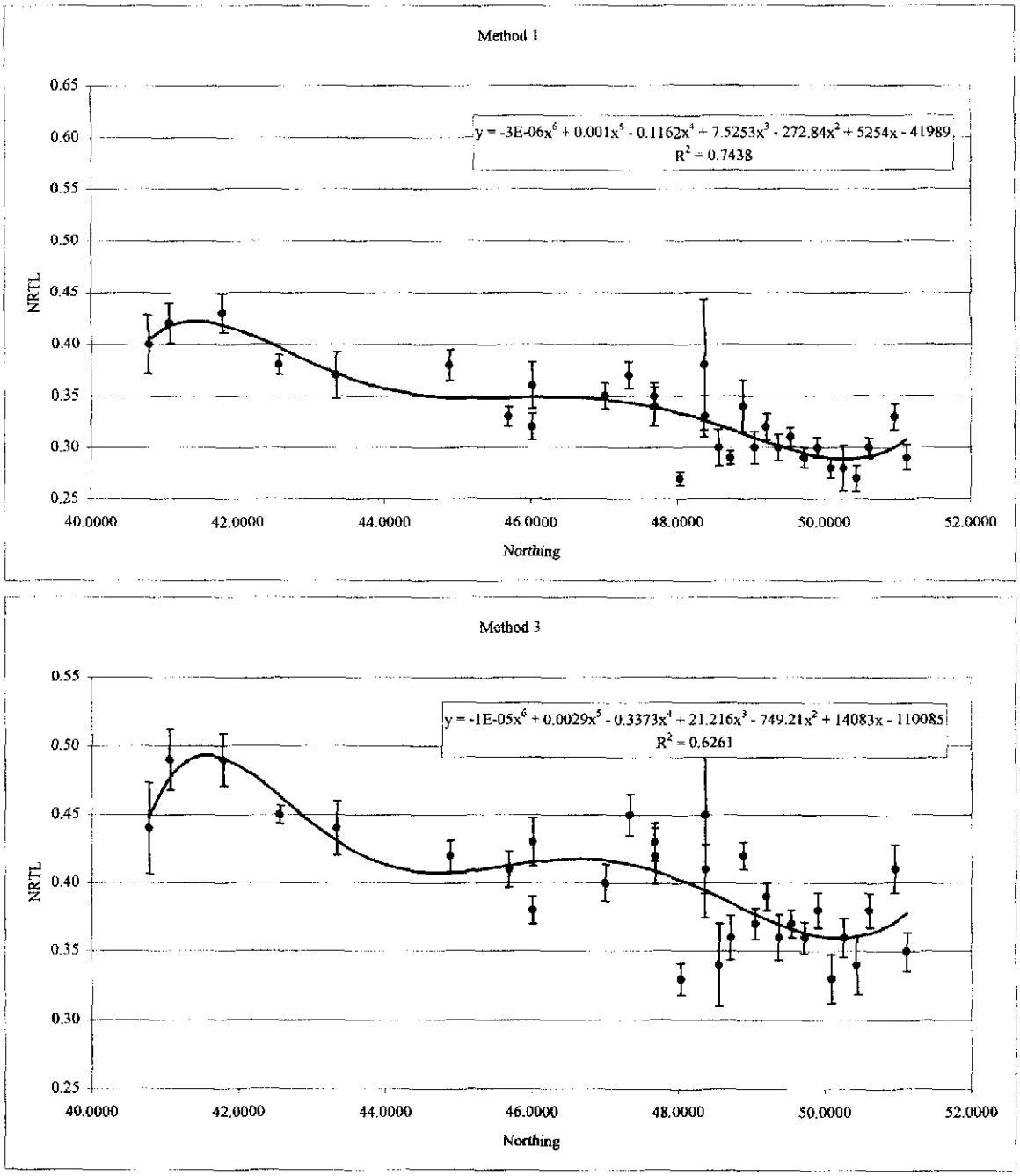

Figure 53- NRTL trends for the 150-212μm grain size fraction. Sandbar samples have been excluded.

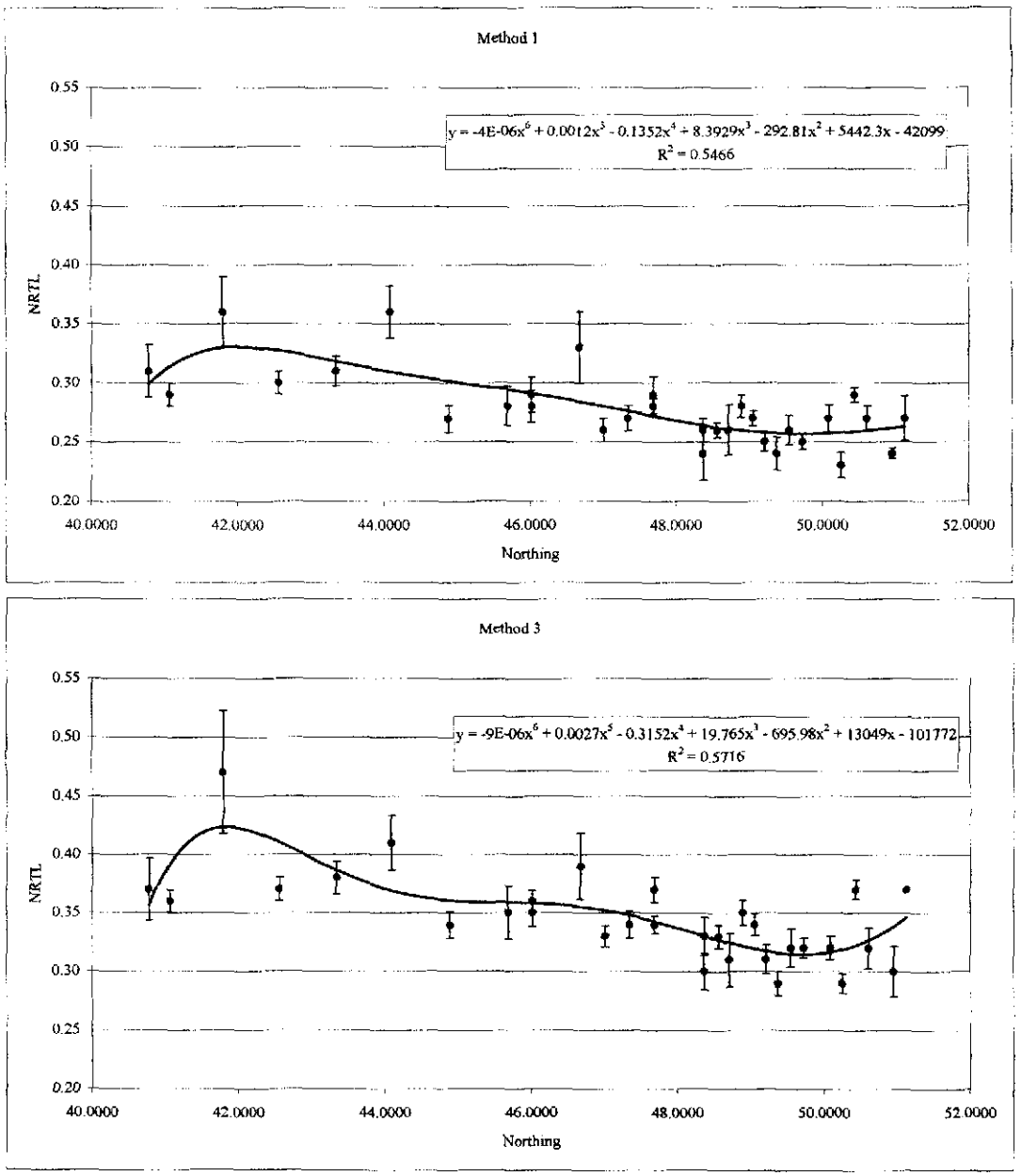

Figure 54- NRTL trends for the 212-250μm grain size fraction. Sandbar samples have been excluded.

Table 24- Summary of R^2 values for each method

	Linear Trend		Polynomial Trend	
grain size (μm)	method 1	method 3	method 1	method 3
90-150	0.52	0.51	0.56	0.56
150-212	0.70	0.56	0.74	0.63
212-250	0.47	0.42	0.55	0.57

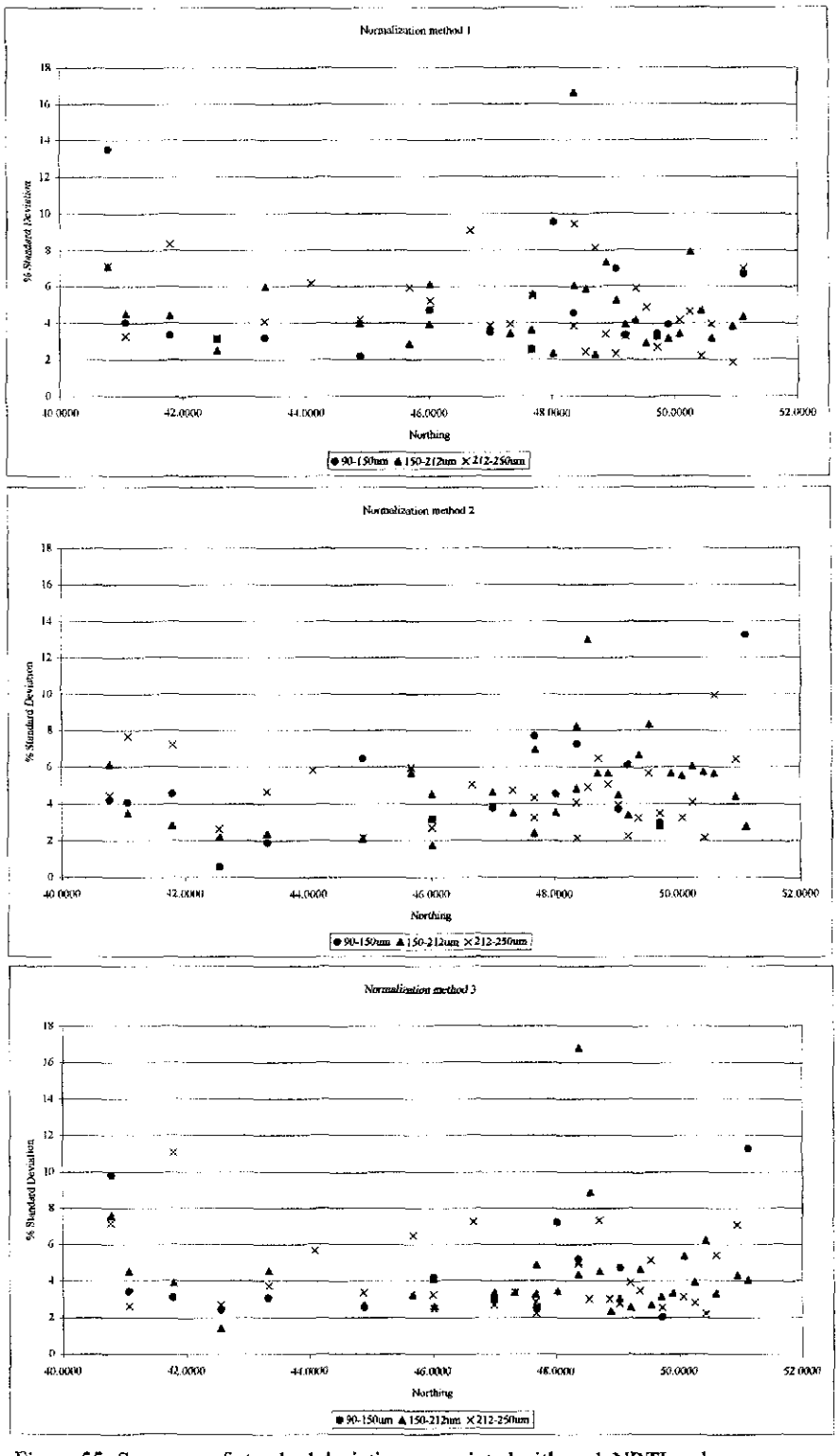

Figure 55- Summary of standard deviations associated with each NRTL value.

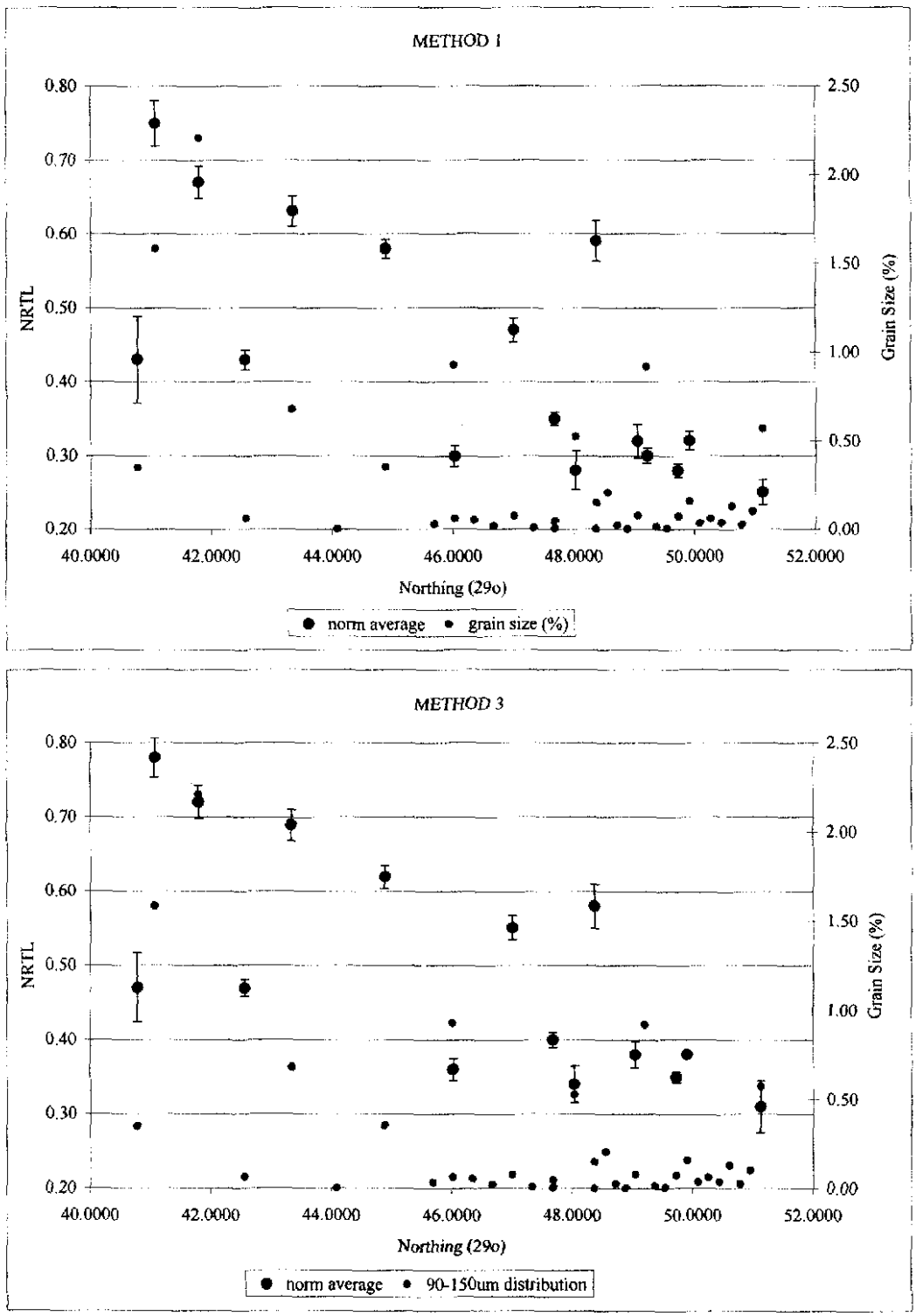

Figure 56- 90-150μm NRTL. The grain size distribution has been superimposed on the NRTL data. Sandbar samples have been excluded.

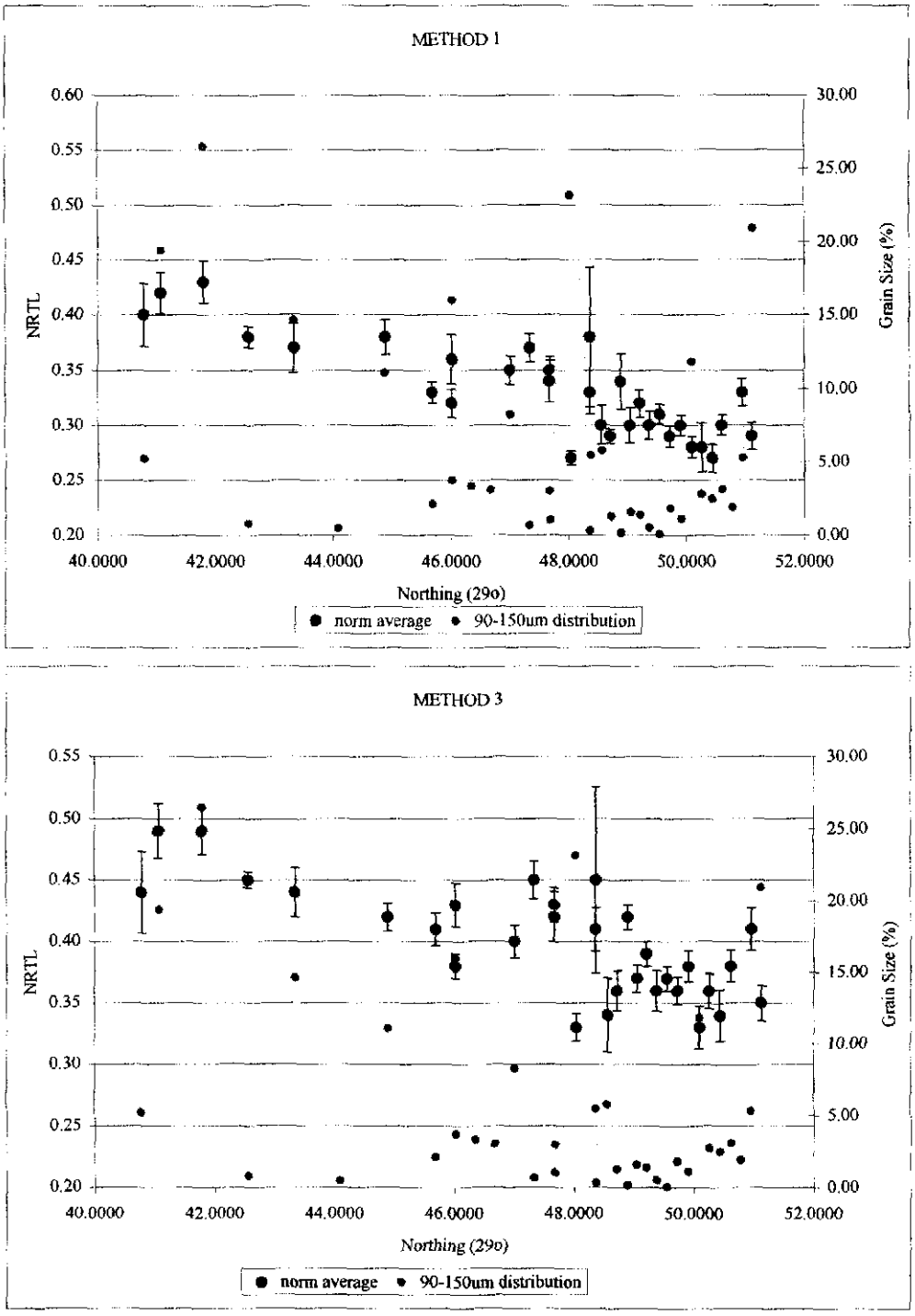

Figure 57- 150-212μm NRTL. The grain size distribution has been superimposed on the NRTL data. Sandbar samples have been excluded.

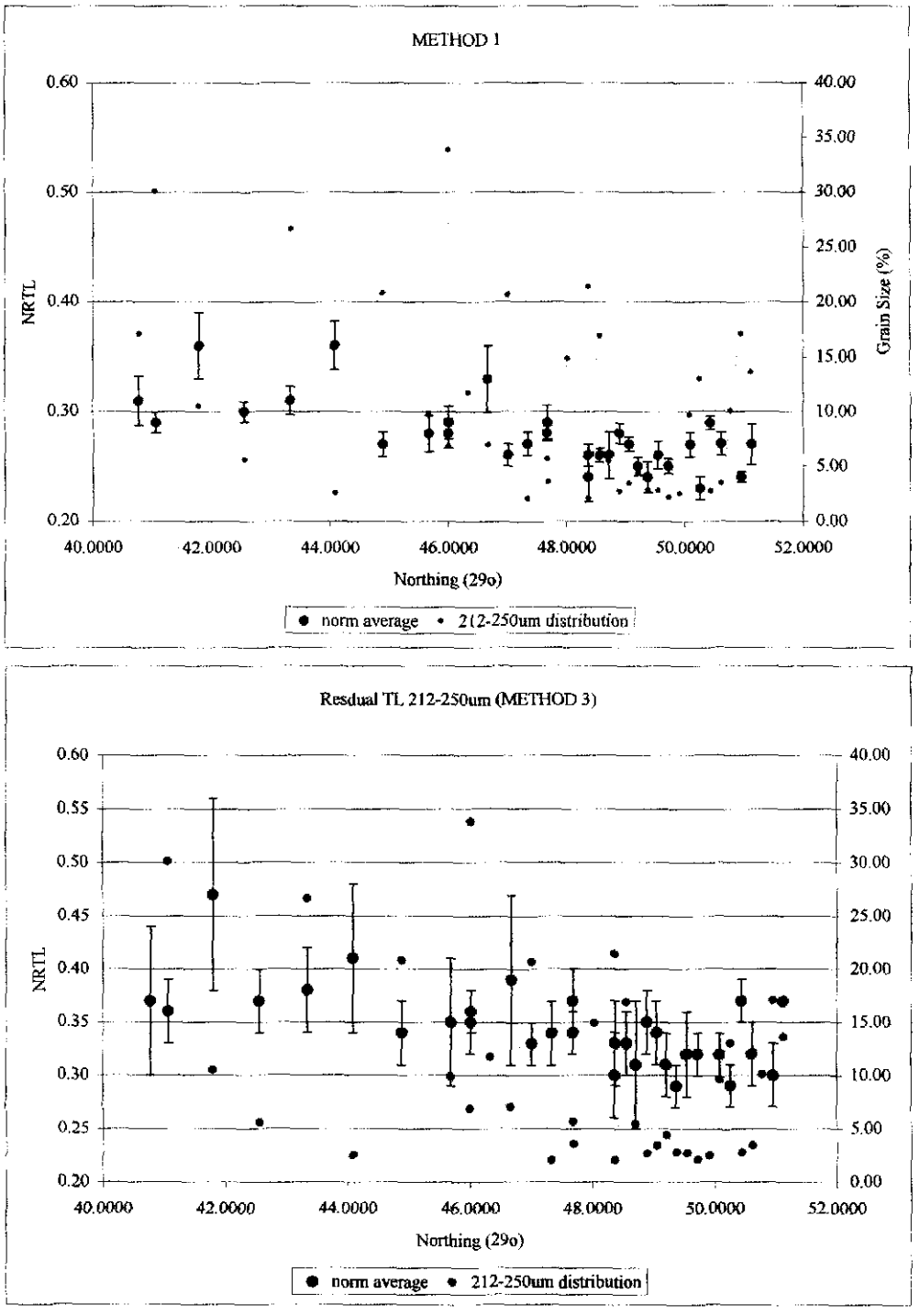

Figure 58- 212-250μm NRTL. The grain size distribution has been superimposed on the NRTL data. *Sandbar samples have been excluded.*

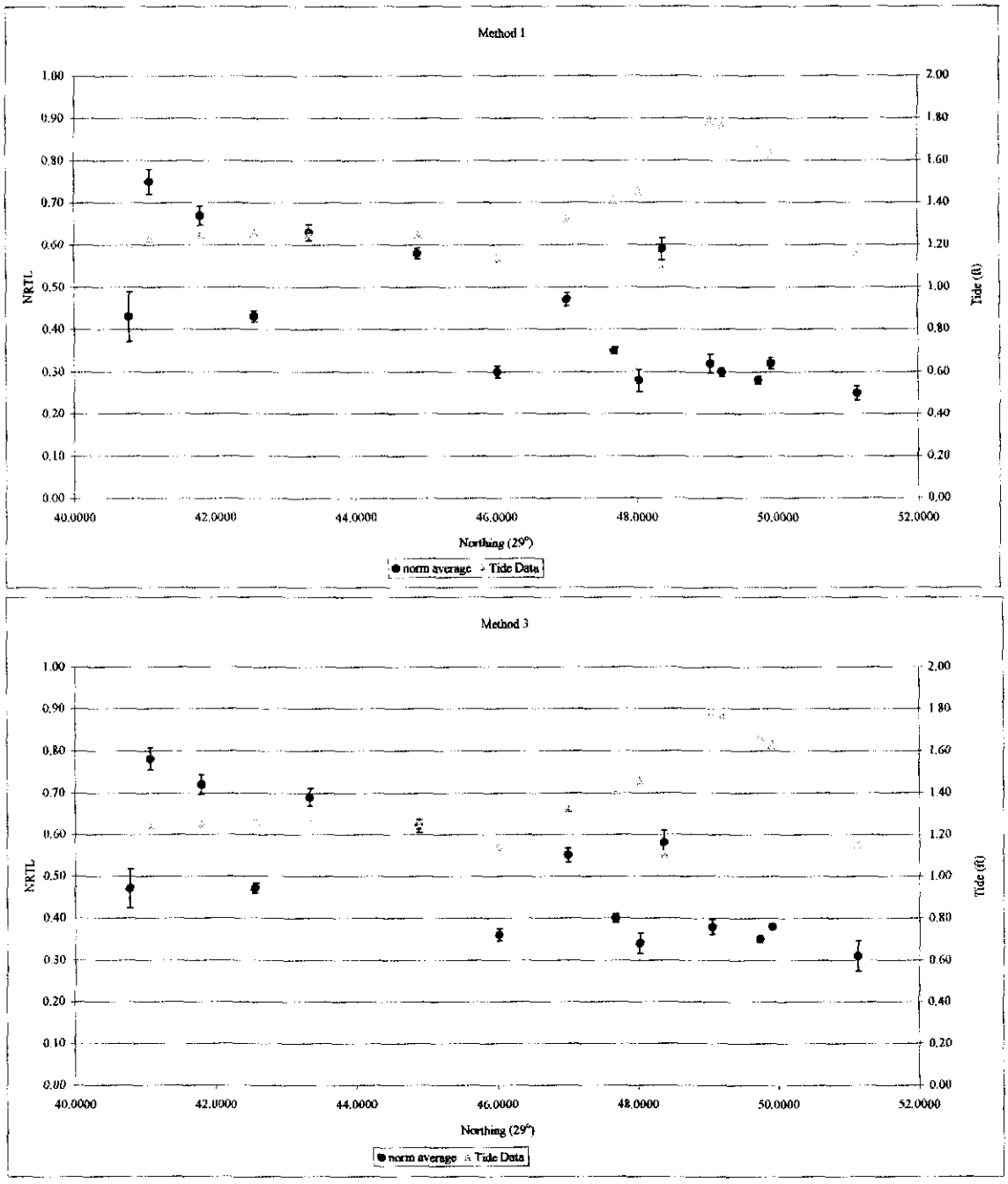

Figure 59- Relationship between NRTL and tide height for the 90-150μm grain size fractions

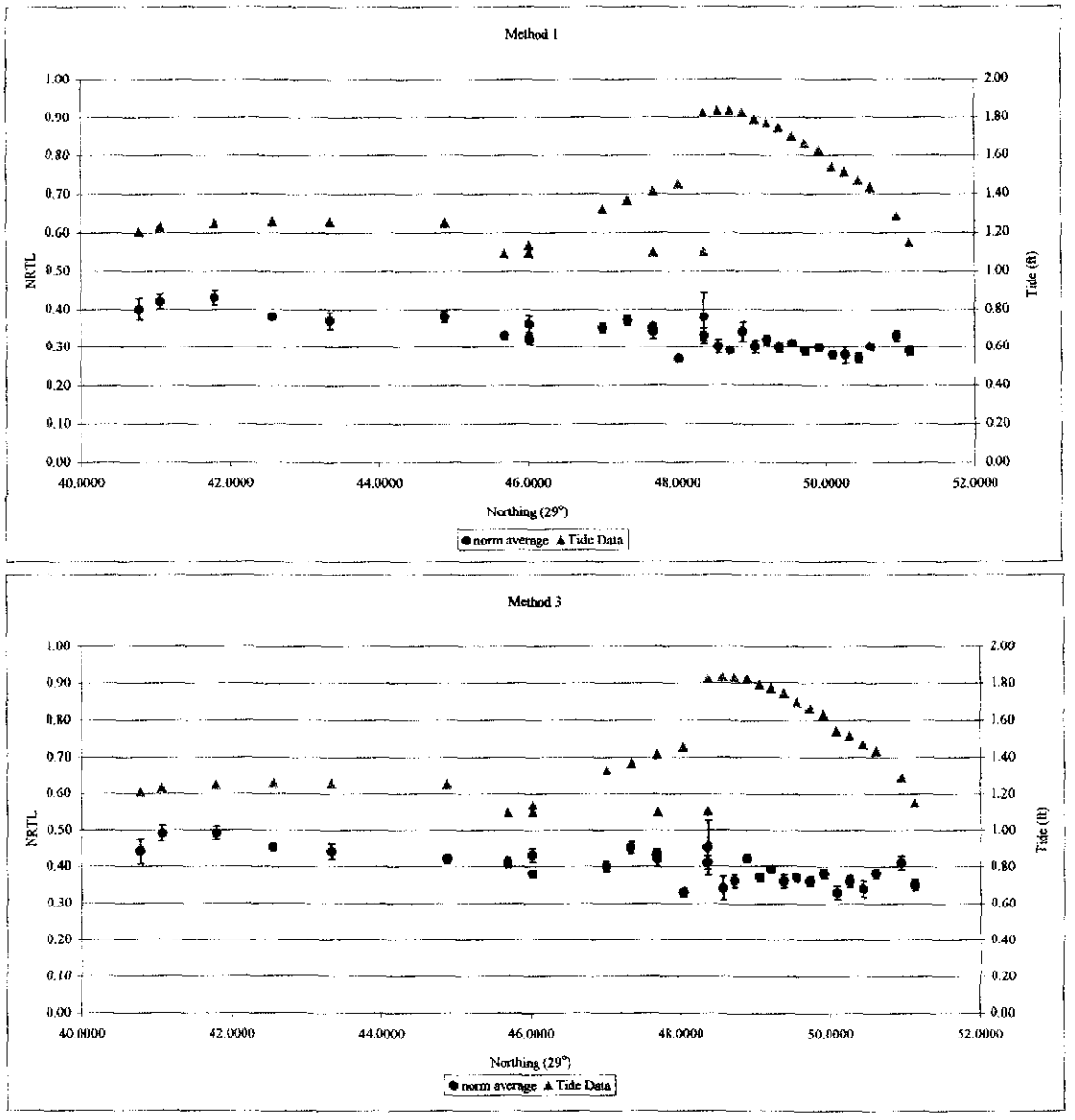

Figure 60- Relationship between NRTL and tide height for the 150-212μm grain size fractions

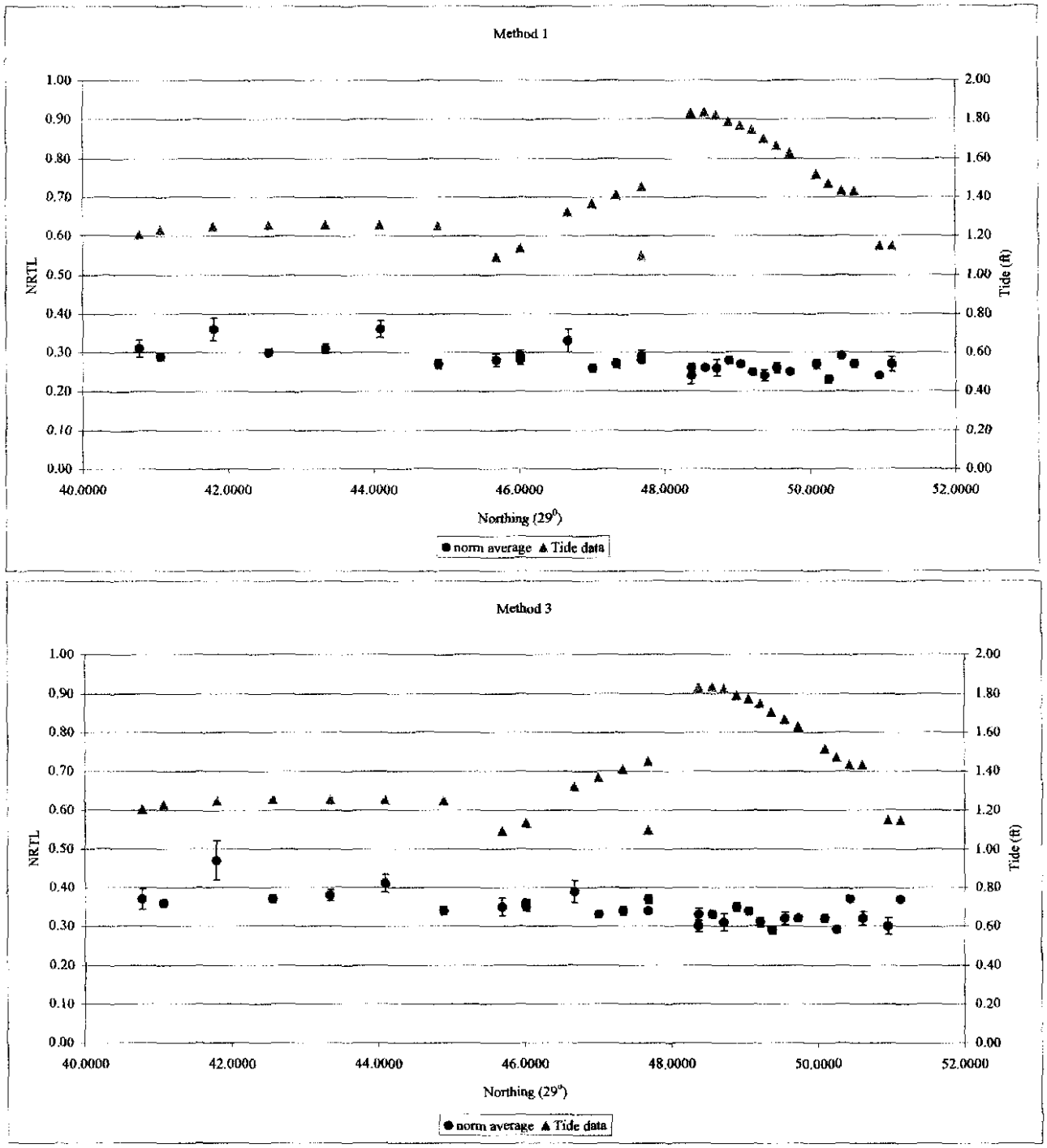

Figure 61- Relationship between NRTL and tide height for the 212-250μm grain size fractions

Table 25- Comparison of samples collected at the same location but on different days

	90-150μm		150-212μm		212-250μm	
sample	method 1	method 3	method 1	method 3	method 1	method 3
SJ003 (August 31, 2001)	-	-	0.38 +/- 0.06	0.45 +/- 0.08	0.26 +/- 0.01	0.33 +/- 0.02
SJ070 (September 6, 2001)	0.59 +/- 0.03	0.58 +/- 0.03	0.33 +/- 0.02	0.41 +/- 0.02	0.24 +/- 0.02	0.30 +/- 0.02
SJ024 (September 1, 2001)	0.35 +/- 0.01	0.40 +/- 0.01	0.35 +/- 0.01	0.43 +/- 0.01	0.28 +/- 0.01	0.34 +/- 0.01
SJ071 (September 6, 2001)	-	-	0.34 +/- 0.02	0.42 +/- 0.02	0.29 +/- 0.02	0.37 +/- 0.01
SJ029 (September 1, 2001)	0.30 +/- 0.01	0.36 +/- 0.02	0.32 +/- 0.01	0.38 +/- 0.01	0.29 +/- 0.02	0.36 +/- 0.01
SJ073 (September 6, 2001)	-	-	0.36 +/- 0.02	0.43 +/- 0.02	0.28 +/- 0.01	0.35 +/- 0.01

Table 26- Comparison of results obtained from 10 aliquot and 48 aliquot measurements.

	INTEGRATION METHOD 1				INTEGRATION METHOD 3			
Grain Size (μm)	n	norm	STDEV	% STDEV	n	norm	STDEV	% STDEV
90-150um	9	0.63	0.02	3.2	8	0.69	0.02	2.9
	45	0.57	0.01	1.8	41	0.63	0.009	1.4
150-212um	10	0.37	0.02	5.4	9	0.44	0.02	4.5
	46	0.33	0.006	1.8	42	0.4	0.006	1.5
212-250um	10	0.31	0.01	3.2	8	0.38	0.01	2.6
	43	0.28	0.01	3.6	40	0.34	0.01	2.9

all measurements were done using sample SJ051

Table 27- Dose variation near monazite and zircon grains

Sample	Hot Grain	Quartz/Heavy Mineral diameters (μm)	Dose Ratios			
			0	100	200	300
SJ14B	Zircon	110/150	9.41	3.37	2.00	1.51
		110/70	3.05	1.40	1.15	1.07
		70/70	4.45	1.50	1.18	1.08
	Monazite	110/150	71.18	19.32	8.82	5.09
		110/70	19.50	4.18	2.15	1.54
		70/70	33.11	5.14	2.40	1.61
SJ042A	Zircon	110/150	14.69	4.85	2.63	1.83
		110/70	4.33	1.64	1.25	1.11
		70/70	6.61	1.82	1.30	1.13
	Monazite	110/150	115.24	30.82	13.72	7.65
		110/70	31.11	6.18	2.87	1.88
		70/70	53.26	7.73	3.27	2.00
SJ048A	Zircon	110/150	16.22	5.29	2.81	1.92
		110/70	4.70	1.72	1.27	1.13
		70/70	7.23	1.91	1.33	1.15
	Monazite	110/150	128.00	34.15	15.14	8.39
		110/70	34.47	6.75	3.08	1.98
		70/70	59.10	8.49	3.52	2.11
SJ048B	Zircon	110/150	5.26	2.20	1.51	1.26
		110/70	2.04	1.20	1.08	1.04
		70/70	2.74	1.26	1.09	1.04
	Monazite	110/150	36.53	10.27	4.96	3.07
		110/70	10.36	2.61	1.58	1.27
		70/70	17.25	3.09	1.71	1.31
SJ252A	Zircon	110/150	13.31	4.47	2.47	1.75
		110/70	3.99	1.58	1.22	1.10
		70/70	6.04	1.74	1.27	1.12
	Monazite	110/150	103.70	27.81	12.44	6.98
		110/70	28.07	5.65	2.69	1.79
		70/70	47.98	7.05	3.04	1.90
SJ252B	Zircon	110/150	15.87	5.19	2.77	1.90
		110/70	4.61	1.70	1.27	1.12
		70/70	7.09	1.89	1.33	1.14
	Monazite	110/150	125.04	33.38	14.82	8.22
		110/70	33.69	6.62	3.04	1.96
		70/70	57.75	8.31	3.47	2.08
SJ252C	Zircon	110/150	18.88	6.04	3.13	2.09
		110/70	5.35	1.84	1.32	1.15
		70/70	8.32	2.07	1.39	1.17
	Monazite	110/150	150.21	39.95	17.62	9.69
		110/70	40.33	7.76	3.45	2.15
		70/70	69.26	9.80	3.97	2.30
SJ298-39	Zircon	110/150	1.25	1.07	1.03	1.02
		110/70	1.06	1.01	1.00	1.00
		70/70	1.10	1.01	1.01	1.00
	Monazite	110/150	3.08	1.54	1.23	1.12
		110/70	1.55	1.09	1.03	1.02
		70/70	1.95	1.12	1.04	1.02
SJ298-40	Zircon	110/150	18.08	5.81	3.03	2.04
		110/70	5.15	1.80	1.31	1.14
		70/70	8.00	2.02	1.37	1.17
	Monazite	110/150	143.52	38.20	16.87	9.30
		110/70	38.56	7.46	3.34	2.10
		70/70	66.20	9.40	3.83	2.25

*values shown are ratios of the average total dose for an etched grain to the total dose from the matrix at grain separations of 0, 100, 200 and 300 μm

Table 28- Maximum equivalent dose accounted for by proximity to a heavy mineral grain

					maximum dose possible if contact with quartz is considered				maximum dose possible if contact with monazite is considered			
sample	grain size (μm)	mask size (mm)	mean DE (Gy)	quartz/zircon diameters (μm)	separation of 0 μm	separation of 100 μm	separation of 200 μm	separation of 300 μm	separation of 0 μm	separation of 100 μm	separation of 200 μm	separation of 300 μm
SJ148	150-212	8	0.34	110/150	3.20	1.15	0.68	0.51	24.20	6.57	3.00	1.73
				110/70	1.04	0.47	0.29	0.26	6.03	1.42	0.73	0.52
		5	0.36	110/150	3.39	1.21	0.72	0.54	25.63	6.96	3.17	1.83
				110/70	1.10	0.50	0.31	0.28	7.02	1.50	0.77	0.55
		3	0.37	110/150	3.48	1.25	0.74	0.56	26.34	7.15	3.26	1.88
				110/70	1.13	0.52	0.43	0.40	7.21	1.55	0.80	0.57
		1	0.21	110/150	1.98	0.71	0.42	0.32	14.95	4.06	1.85	1.07
				110/70	0.64	0.29	0.24	0.22	4.09	0.88	0.45	0.32
	212-250	5	0.35	110/150	3.29	1.18	0.70	0.53	24.91	6.76	3.09	1.78
				110/70	1.07	0.49	0.30	0.27	6.82	1.46	0.75	0.54
		1	0.40	110/150	3.76	1.35	0.80	0.60	28.47	7.73	3.53	2.03
				110/70	1.22	0.56	0.46	0.43	7.80	1.67	0.86	0.62
SJ042A	150-212	8	0.17	110/150	2.50	0.83	0.45	0.31	19.59	5.24	2.33	1.30
				110/70	0.74	0.28	0.21	0.19	5.29	1.05	0.49	0.32
		5	0.16	110/150	2.35	0.78	0.42	0.29	18.44	4.93	2.20	1.22
				110/70	0.69	0.26	0.20	0.18	4.98	0.99	0.46	0.30
		3	0.15	110/150	2.20	0.73	0.39	0.27	17.29	4.62	2.06	1.15
				110/70	0.65	0.25	0.19	0.17	4.67	0.93	0.43	0.28
		1	0.20	110/150	2.94	0.97	0.53	0.37	23.05	6.16	2.74	1.53
				110/70	0.87	0.33	0.25	0.22	6.22	1.24	0.57	0.38
	212-250	8	0.17	110/150	2.50	0.83	0.45	0.31	19.59	5.24	2.33	1.30
				110/70	0.74	0.28	0.21	0.19	5.29	1.05	0.49	0.32
		5	0.16	110/150	2.20	0.73	0.39	17.29	17.29	4.62	2.06	1.15
				110/70	0.65	0.25	0.19	0.17	4.67	0.93	0.43	0.28
		3	0.15	110/150	2.20	0.73	0.39	0.27	17.29	4.62	2.06	1.15
				110/70	0.65	0.25	0.19	0.17	4.67	0.93	0.43	0.28
SJ048A	150-212	8	0.03	110/150	0.49	0.16	0.08	0.06	3.84	1.02	0.45	0.25
				110/70	0.14	0.05	0.04	0.03	1.03	0.20	0.09	0.06
		5	0.03	110/150	0.49	0.16	0.08	0.06	3.84	1.02	0.45	0.25
				110/70	0.22	0.06	0.04	0.03	1.03	0.20	0.09	0.06
		3	0.03	110/150	0.49	0.16	0.08	0.06	3.84	1.02	0.45	0.25
				110/70	0.06	0.00	0.00	0.00	1.03	0.20	0.09	0.06
	212-250	8	0.04	110/150	0.65	0.22	0.11	0.08	5.12	1.37	0.61	0.34
				110/70	0.19	0.07	0.05	0.05	1.38	0.27	0.12	0.08
		5	0.03	110/150	1.14	0.37	0.20	0.13	8.96	2.39	1.06	0.59
				110/70	0.33	0.12	0.09	0.08	2.41	0.47	0.22	0.14
SJ048B	150-212	8	0.05	110/150	0.26	0.11	0.08	0.06	1.83	0.51	0.25	0.15
				110/70	0.10	0.06	0.05	0.05	0.52	0.13	0.08	0.06
		5	0.05	110/150	0.26	0.11	0.08	0.06	1.83	0.51	0.25	0.15
				110/70	0.10	0.06	0.05	0.05	0.52	0.13	0.08	0.06
		7	0.05	110/150	0.26	0.11	0.08	0.06	1.83	0.51	0.25	0.15
				110/70	0.10	0.06	0.05	0.05	0.52	0.13	0.08	0.06
		1	0.12	110/150	0.63	0.26	0.15	0.15	4.38	1.23	0.59	0.37
				110/70	0.24	0.14	0.13	0.12	1.24	0.31	0.19	0.15
	212-250	8	0.05	110/150	0.26	0.11	0.08	0.06	1.83	0.51	0.25	0.15
				110/70	0.10	0.06	0.05	0.05	0.52	0.13	0.08	0.06
		5	0.04	110/150	0.21	0.09	0.06	0.05	1.46	0.41	0.20	0.12
				110/70	0.08	0.05	0.04	0.04	0.41	0.10	0.06	0.05
		3	0.05	110/150	0.26	0.11	0.08	0.06	1.83	0.51	0.25	0.15
				110/70	0.10	0.06	0.05	0.05	0.52	0.13	0.08	0.06
SJ152A	150-212	8	0.44	110/150	5.06	1.96	1.08	0.77	45.61	12.24	5.47	3.07
				110/70	1.76	0.69	0.54	0.49	12.35	2.49	1.18	0.79
		5	0.39	110/150	5.19	1.74	0.96	0.68	40.44	10.82	4.85	2.72
				110/70	1.56	0.62	0.48	0.43	10.95	2.20	1.05	0.70
		3	0.46	110/150	6.12	2.05	1.13	0.80	47.70	12.79	5.72	3.21
				110/70	1.84	0.73	0.56	0.51	12.91	2.60	1.24	0.83
		1	0.48	110/150	6.39	2.14	1.18	0.84	49.78	13.35	5.97	3.35
				110/70	1.92	0.76	0.59	0.53	13.47	2.71	1.29	0.86
	212-250	8	0.41	110/150	5.46	1.83	1.01	0.72	42.52	11.40	5.10	2.86
				110/70	1.64	0.65	0.50	0.45	11.51	2.52	1.10	0.73
		5	0.35	110/150	4.66	1.56	0.86	0.61	36.30	9.73	4.35	2.44
				110/70	1.40	0.55	0.43	0.39	9.82	1.98	0.94	0.63
		3	0.38	110/150	5.06	1.70	0.94	0.66	39.41	10.57	4.73	2.65
				110/70	1.52	0.60	0.46	0.42	10.67	2.13	1.02	0.68
		1	0.66	110/150	8.78	2.95	1.63	1.15	68.44	18.35	8.21	4.61
				110/70	2.64	1.04	0.81	0.73	18.51	3.55	1.77	1.18
SJ252B	150-212	8	0.36	110/150	5.71	1.87	1.00	0.69	45.01	12.02	5.33	2.96
				110/70	1.66	0.61	0.46	0.40	12.13	2.38	1.09	0.70
		5	0.36	110/150	5.71	1.87	1.00	0.69	45.01	12.02	5.33	2.96
				110/70	1.66	0.61	0.46	0.40	12.13	2.38	1.09	0.70
		3	0.39	110/150	6.19	2.02	1.08	0.74	48.77	13.02	5.78	3.21
				110/70	1.80	0.66	0.49	0.44	13.14	2.58	1.18	0.76
		1	0.61	110/150	9.68	3.16	1.69	1.16	76.23	20.36	9.04	5.02
				110/70	2.81	1.04	0.77	0.69	20.93	4.04	1.85	1.19
	212-250	8	0.38	110/150	6.03	1.97	1.05	0.72	47.52	12.68	5.63	3.12
				110/70	1.75	0.65	0.48	0.43	12.80	2.52	1.15	0.74
		5	0.37	110/150	5.87	1.92	1.02	0.70	46.27	12.35	5.48	3.04
				110/70	1.71	0.63	0.47	0.42	12.47	2.45	1.12	0.72
		3	0.36	110/150	5.71	1.87	1.00	0.69	45.01	12.02	5.33	2.96
				110/70	1.66	0.61	0.46	0.40	12.13	2.38	1.09	0.70
		1	0.64	110/150	9.98	2.78	1.22	0.84	58.02	14.69	6.52	3.62
				110/70	2.03	0.75	0.56	0.49	14.82	2.91	1.34	0.86
SJ252C	150-212	8	0.41	110/150	7.74	2.43	1.28	0.86	61.59	16.38	7.22	3.97
				110/70	2.19	0.76	0.54	0.47	16.53	3.18	1.41	0.88
		5	0.39	110/150	7.36	2.33	1.22	0.81	58.58	15.58	6.87	3.78
				110/70	2.09	0.73	0.53	0.45	15.73	3.03	1.34	0.84
		3	0.36	110/150	6.80	2.17	1.13	0.75	54.08	14.38	6.34	3.49
				110/70	1.93	0.66	0.48	0.41	14.52	2.79	1.24	0.77
		1	0.56	110/150	10.57	3.35	1.75	1.17	84.12	22.37	9.87	5.43
				110/70	3.09	1.03	0.74	0.64	22.68	4.35	1.93	1.20
	212-250	8	0.41	110/150	7.74	2.42	1.28	0.86	61.59	16.38	7.22	3.97
				110/70	2.19	0.76	0.54	0.47	16.53	3.18	1.41	0.88
		5	0.39	110/150	7.36	2.35	1.22	0.81	58.58	15.58	6.87	3.78
				110/70	2.09	0.72	0.51	0.45	15.73	3.03	1.34	0.84
		3	0.38	110/150	7.18	2.29	1.19	0.79	57.08	15.18	6.70	3.68
				110/70	2.05	0.70	0.50	0.44	15.32	2.93	1.31	0.82
		1	0.73	110/150	13.78	4.41	2.28	1.52	109.66	29.16	12.86	7.07
				110/70	3.90	1.24	0.96	0.84	29.44	5.67	2.52	1.57
SJ398-30	125-250	8	0.14	110/150	0.14	0.12	0.11	0.11	0.34	0.19	0.14	0.12
				110/70	0.12	0.11	0.11	0.11	0.17	0.12	0.11	0.11
		5	0.1	110/150	0.12	0.11	0.10	0.10	0.31	0.15	0.12	0.11
				110/70	0.11	0.10	0.10	0.10	0.15	0.11	0.10	0.10
		3	0.1	110/150	0.12	0.11	0.10	0.10	0.31	0.15	0.12	0.11
				110/70	0.11	0.10	0.10	0.10	0.15	0.11	0.10	0.10
		1	1.1	110/150	1.33	1.18	1.15	1.12	3.39	1.70	1.33	1.23
				110/70	1.17	1.11	1.10	1.10	1.20	1.39	1.14	1.12
	250-300	8	0.12	110/150	0.13	0.12	0.12	0.12	0.37	0.19	0.13	0.13
				110/70	0.13	0.12	0.12	0.12	0.19	0.13	0.12	0.12
		5	0.11	110/150	0.14	0.12	0.11	0.11	0.34	0.17	0.14	0.12
				110/70	0.12	0.11	0.11	0.11	0.17	0.12	0.11	0.11
		3	0.12	110/150	0.15	0.13	0.12	0.12	0.37	0.19	0.15	0.13
				110/70	0.13	0.12	0.12	0.12	0.19	0.13	0.12	0.12
SJ398-40	125-250	8	0.04	110/150	0.72	0.23	0.12	0.08	5.74	1.53	0.67	0.37
				110/70	0.21	0.07	0.05	0.05	1.54	0.30	0.13	0.08
		5	0.04	110/150	0.72	0.23	0.12	0.08	5.74	1.53	0.67	0.37
				110/70	0.21	0.07	0.05	0.05	1.54	0.30	0.13	0.08
		3	0.05	110/150	0.90	0.29	0.15	0.10	7.18	1.91	0.84	0.47
				110/70	0.26	0.09	0.07	0.06	1.93	0.37	0.17	0.11
		1	0.08	110/150	1.43	0.46	0.24	0.16	11.48	3.06	1.35	0.74
				110/70	0.41	0.14	0.10	0.09	3.08	0.60	0.27	0.17
	250-300	8	0.04	110/150	0.72	0.23	0.12	0.08	5.74	1.53	0.67	0.37
				110/70	0.21	0.07	0.05	0.05	1.54	0.30	0.13	0.08
		5	0.04	110/150	0.72	0.23	0.12	0.08	5.74	1.53	0.67	0.37
				110/70	0.21	0.07	0.05	0.05	1.54	0.30	0.13	0.08
		3	0.15	110/150	2.71	0.87	0.45	0.31	21.53	5.73	2.53	1.40
				110/70	0.77	0.27	0.20	0.17	5.78	1.12	0.50	0.32

not considering quartz/heavy mineral diameters of 70/70 because outside of grain size fractions

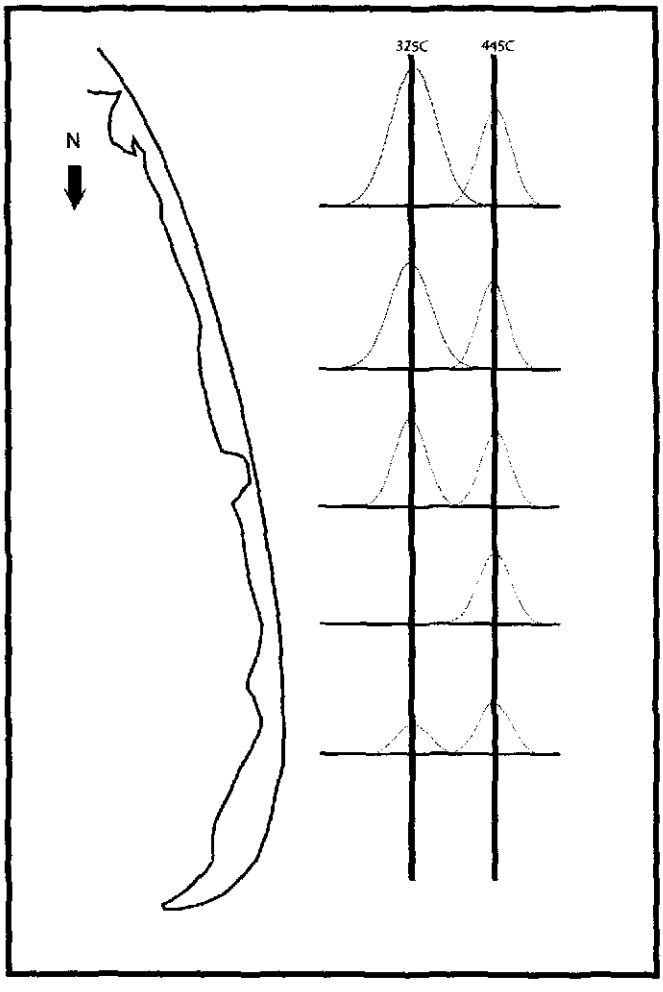

Figure 62- Disappearance of the low temperature TL peak. Both the low and high temperature peaks are being reduced as sunlight exposure increases. However, the high temperature peak is reduced at a slower rate.

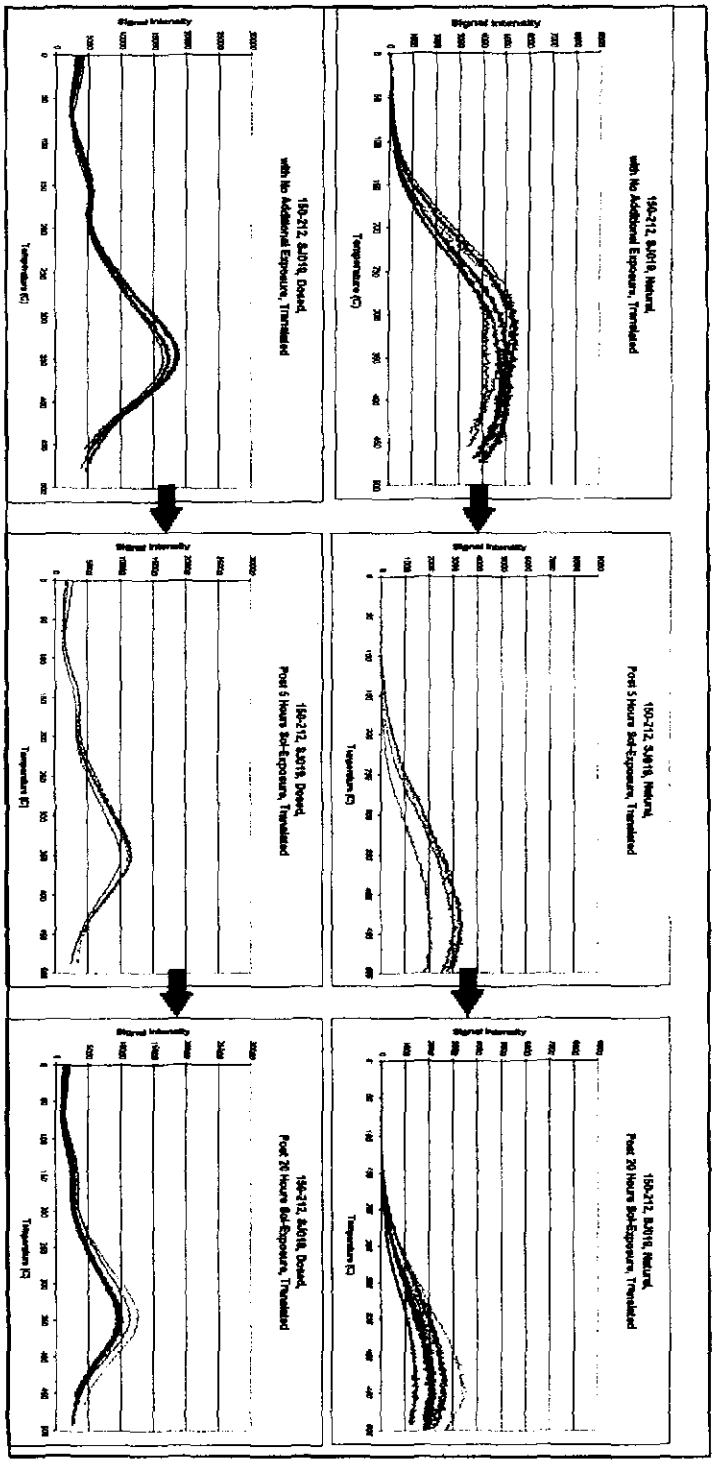

Figure 63- Solar exposure experiments performed by Keizars (2003). With increasing solar exposure there is a corresponding loss of the high temperature peak.

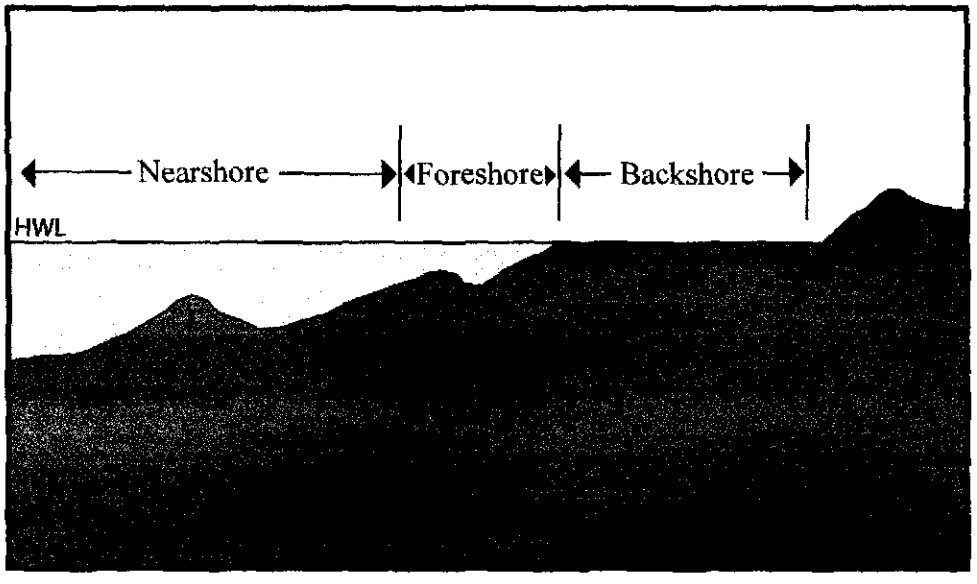

Figure 64- Typical beach profile (Ritter, 1986)

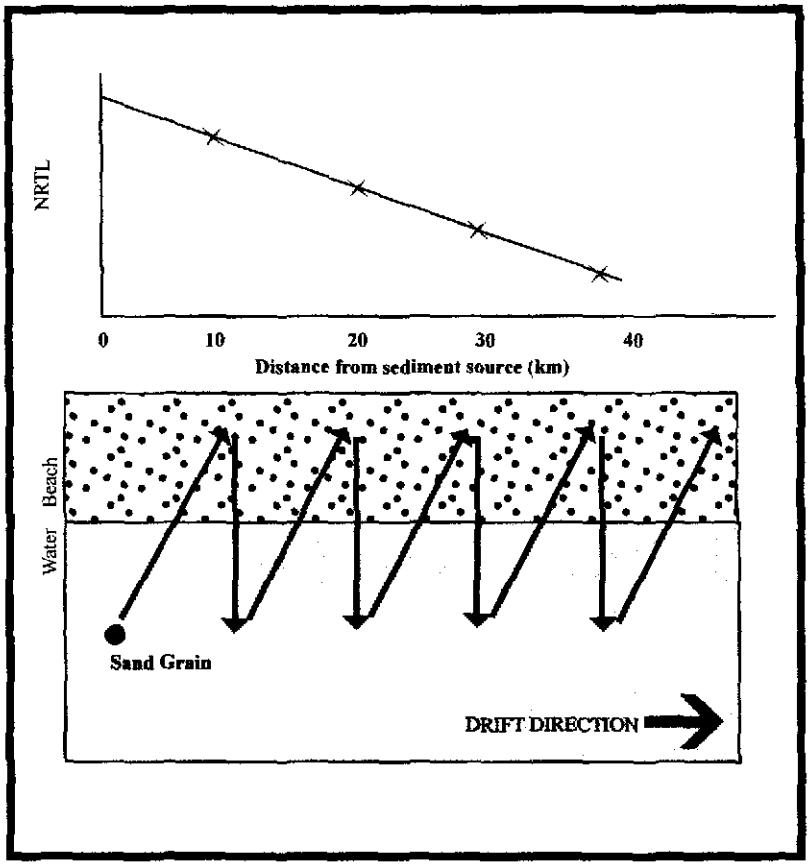

Figure 65- Movement of a sand grain across the beach/water interface as it travels within the longshore current. The natural residual thermoluminescence signal (NRTL) is reduced with increasing distance from the sediment source. (modified from Keizars, 2003)

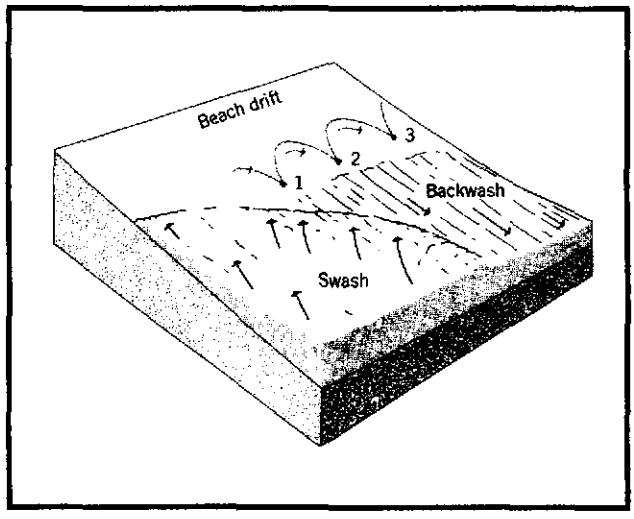

Figure 66- Swash and Backwash (Strahler, 1975)

REFERENCES

Adamiec, G. and Aitken, M. 1998. Dose rate conversion factors: update. *Ancient TL.* v16: 37-50.

Aitken, M.J. 1985. Thermoluminescence Dating. London: Academic Press.

Aitken, M.J. 1994. Optical dating: a non-specialist review. *Quaternary Geochronology.* v13: 503-508.

Aitken, M.J. 1998. An Introduction to Optical Dating: The Dating of Quaternary Sediments by the use of Photon-Stimulated Luminescence. New York: Oxford University Press.

Aubrey, D.G. and Gaines, A.G. 1982. Rapid formation and degradation of barrier spits in areas with low rates of littoral drift. *Marine Geology.* v49: 257-278.

Ballarini, M., Wallinga, J., Murray, A.S., Van Heteren, S., Oost, A.P., Bos, A.J.J. and van Eijk, C.W.E. 2003. Optical dating of young coastal dunes on a decadal time scale. *Quaternary Science Reviews.* v22 (10-13): 1011-1017.

Bard, E. 1998. Geochemical and geophysical implications of the radiocarbon calibration. *Geochimica et Cosmochimica Acta.* v62 (12): 2025-2038.

Benchley, E.D. and Bense, J.A. 2000. Archaeology and history of St. Joseph Peninsula State Park-Phase 1 Investigations. University of West Florida Archaeology Institute. Report of Investigations, No.89.

Berger, G. 1988. Dating quaternary events by luminescence. *Geological Society of America.* Special Paper 227: 13-50.

Berger, G. 1990. Effectiveness of natural zeroing of the thermoluminescence in sediments. *Journal of Geophysical Research.* v95 (B8): 12375-12397.

Berger, G. 1995. Progress in luminescence dating methods for quaternary sediments. In N.W. Ritter and N.R. Catto (eds). Dating methods for quaternary deposits. Newfoundland: Geological Association of Canada.

Boggs, S. 1995. Principles of Sedimentology and Stratigraphy. New Jersey: Prentice-Hall Inc.

Bøtter-Jensen, L., Bulur, E., Duller, G.A.T. and Murray, A.S. 2000. Advances in luminescence instrument systems. *Radiation Measurements.* v516: 523-528.

Brennan, B.J., Lyons, R.G. and Philips, S.W. 1991. Attenuation of alpha particle track dose for spherical grains. *Nuclear Tracks and Radiation Measurements*. v18 (1/2): 249-253.

Brennan, B.J. 2003. Beta doses to spherical grains. *Radiation Measurements*. [in press].

Bruno, R.O. and Goble, C.G. 1977. Longshore transport at a littoral barrier. *Proceedings of the 15th international conference on coastal engineering*: 1203-1222.

Carter, R.W.G., Devoy, R.J.N. and Shaw, J. 1989. Late Holocene sea levels in Ireland. *Journal of Quaternary Science*. v4: 7-24.

Critical erosion area maps, Florida, USA. (2001). FDEP. Available: www.dep.state.fl.us/beaches/publications/pdf/eroar-nw.pdf. [downloaded May 6, 2003].

Davis, R.A. 1997. The evolving coast. New York: Scientific American Library.

Donoghue, J.F. and Greenfield, M.B. 1991. Radioactivity of heavy mineral sands as an indicator of coastal sand transport processes. *Journal of Coastal Research*. v7(1): 189-201.

Donoghue, J.F. and Tanner, W.F. 1992. Quaternary terraces and shorelines of the Panhandle Florida region. *Quaternary Coasts of the United States: Marine and Lacustrine Systems, SEPM Special Pub*. 48: 233-241.

Donoghue, J.F. 1993. Late Wisconsinian and Holocene depositional history, northeastern Gulf of Mexico. *Marine Geology*. v112:185-205.

Duane, D.B. and James, W.R. 1980. Littoral transport in the surf zone elucidated by an Eulerian sediment tracer experiment. *Journal of Sedimentary Petrology*. v50: 929-942.

Duller, G. 1998. Luminescence dating using single aliquots: methods and applications. *Radiation Measurements*. v24(3): 217-226.

Eichenholtz, M.E., Pirkle, E.C. and Pirkle, F.L. 1989. Sediment characteristics of selected beach ridges along Florida's northeastern coast. *Southeastern Geology*. v30:155-167.

Elfrink, B. and Baldock, T. 2002. Hydrodynamic and sediment transport in the swash zone: a review and perspectives. *Coastal Engineering*. v45: 149-167.

Faulkner, E.L. 1986. Introduction to Prospecting. British Columbia Ministry of Energy, Mines and Petroleum Resources, Mineral Resources Division, Geological Survey Branch.

Fernald, E.A. and Purdum, E.D. 1992. Atlas of Florida. Gainsville, Florida: University Press of Florida.

Folk, R.L. 1974. Petrology of Sedimentary Rocks. Texas: Hemphill Publishing Co.

Folz, R. and Mercier, N. 1999. A single-aliquot OSL protocol using bracketing regenerative doses to accurately determine equivalent doses in quartz. *Radiation Measurements*. v30: 503-508.

Forrest, B. 2001. UV/VIS absorption of littoral zone sediment. McMaster University. B.Sc. Thesis.

Foster, G.A., Healy, T.R. and DeLarge, W.P. 1996. Presaging beach nourishment from a nearshore dredge dump mound, Mt. Maunganui Beach, New Zealand. *Journal of Coastal Research*. v12: 395-405.

Foster, E.R. and Cheng, J. 2001. Shoreline change rate estimates, Gulf county. Florida Department of Environmental Protection Office of Beaches and Coastal Systems, *Report No. BCS-01-02.*

Godfrey-Smith, D.I., Huntley, D.J. and Chen, W.H. 1988. Optical dating studies of quartz and feldspar sediment extracts. *Quaternary Science Reviews*. v7: 373-380.

Gorsline, D.S. 1966. Dynamic characteristics of West Florida Gulf Coast beaches. *Marine Geology*. v4: 187-206.

Hatchett, L. Bathymetric map of the St. Joseph Peninsula, 1998, 1:200,000. "FDEP Reconnaissance level sand search for the Florida Panhandle". [available online]: http://sandpan.urs-tally.com.

Hellegaard, J. 1995. Eroding confidence. *Explore Magazine* (University of Florida). v1(1): 1-2.

Hsu, K.J. 1960. Texture and mineralogy of the recent sands of the Gulf Coast. *Journal of Sedimentary Petrology*. v30 (3): 380-403.

Huntley, D.J. 1985. On the zeroing of the thermoluminescence of sediments. *Physics and Chemistry of Minerals*. v12: 122-127.

Huntley, D.J., Godfrey-Smith, D.I. and Thewalt, M.L.W. 1985. Optical dating of sediments. *Nature*. v313: 105-107.

Huntley, D.J. and Lian, O.B. 1999. Using optical dating to determine when a sediment was last exposed to sunlight. *GSC Bulletin*. v534: 211-215.

Hurricane Evacuation Route and Beach Management on St. Joseph Peninsula-Feasibility and design study. FDEP project no. 50698. Coastal Tech and Preble-Rish Inc. Consulting Engineers. 1998.

Hutt, G.I. and Raukas, A. 1995. Thermoluminescence dating of sediments. In Dating Methods for Quaternary Deposits. Eds. N.W. Rutter and N.R. Catto. Newfoundland: Geological Association of Canada.

Johnson, J.W. 1957. The littoral drift problem at shoreline harbors. *Journal of Waterways and Harbors Division*. v83: 1-37.

Jungner, H., Korjonen, K., Heikkinen, O. and Wiedmann, A.M. 2001. Luminescence and radiocarbon dating of a dune series at Cape Kiwanda, Oregon, USA. *Quaternary Science Reviews*. v20: 811-814.

Keizars, K. 2003. Analysis of littoral drift on St. Joseph Peninsula, Florida, using natural residual thermoluminescence. McMaster University. B.Sc. Thesis.

Komar, P.D. and Inman, P. 1970. Longshore sand transport on beaches. *Journal of Geophysical Research*. v75 (30): 5514-5527.

Kunte, P.D., Wagle, B.G. and Sugimori, Y. 2003. Sediment transport and depth variation study of the Gulf of Kutch using remote sensing. *International Journal of Remote Sensing*. v24 (11): 2253-2263.

Lalou, C. and Valladas, G. 1989. Thermoluminescence dating. In Roth, E. and Poty, B. (eds). Nuclear Methods of Dating. Paris: CEA.

Lamont, M.M., Percival, H.F., Pearlstine, L.G., Colwell, S.V., Kitchens, W.M. and Carthy, R.R. 1997. The Cape San Blas Ecological Study. US Geological Survey/Biological Resources Division, Florida Cooperative Fish and Wildlife Research Unit. Technical Report No. 57. 209 pp.

Mejdahl, V. 1979. Thermoluminescence dating: Dose attenuation in quartz grains. *Archaeometry*. v21: 61-72.

Mejdahl, V. and Christiansen, H.H. 1994. Procedures used for luminescence dating of sediment. *Quaternary Science Reviews*. v13: 403-406.

Missimer, T. 1973. Growth rates of beach ridges on Sanibel Island, Florida. *Transactions-Gulf Coast Association of Geological Societies*. v23: 383-388.

Murray, A.S., Roberts, R.G. and Wintle, A.G. 1997. Equivalent dose measurement using a single aliquot of quartz. *Radiation Measurements*. v27(2): 171-184.

Murray, A.S. and Wintle, A.G. 2000. Luminescence dating of quartz using an improved single-aliquot regenerative dose protocol. *Radiation Measurements*. v32: 57-73.

Murray, A.S. and Wintle, A.G. 2002. The single aliquot regenerative dose protocol: potential for improvements in reliability. [in press]

Murray-Wallace, C.V., Banerjee, D., Bourman, R.P., Olley, J. and Brooke, B.P. 2002. Optically stimulated luminescence dating of Holocene relict foredunes, Guichen Bay, South Australia. *Quaternary Science Reviews*. v21: 1077-1086.

Pabich, W.J. 1995. A sedimentological study of a replenished beach: Revere Beach, Massachusetts, M.Sc. Thesis. Department of Geology, Duke University, Durham, North Carolina.

Pettijohn, F.J. 1949. Sedimentary Rocks. New York: Harper and Brothers.

Pieper, K.D. 2001. Thermoluminescence of quartz and feldspar sand grains as a tracer of nearshore environmental processes in the southeastern Mediterranean Sea. *Unpublished B.Sc. Thesis.*

Prescott, J.R. and Hutton, J.T. 1988. Cosmic ray and gamma ray dosimetry for TL and ESR. *Nuclear Tracks and Radiation Measurements*. v14: 223-227.

Reed, A.J. and Wells, J.T. 2000. Sediment distribution patterns offshore of a renourished beach: Atlantic Beach and Fort Macon, North Carolina. *Journal of Coastal Research.* v16(1): 88-98.

Rees-Jones, J. 1995. Optical dating of young sediments using fine-grain quartz. *Ancient TL*. v13 (2): 9-14.

Richardson, C.A. 2001. Residual luminescence signals in modern coastal sediments. *Quaternary Science Reviews*. v20: 887-892.

Rink, W.J. and Odom, A.L. 1991. Natural alpha recoil particle radiation and ionizing radiation sensitivities in quartz detected with EPR: Implications for geochronometry. *Nuclear Tracks and Radiation Measurements* D. v18: 163-173.

Rink, W.J., Rhodes, E.J. and Grun, R. 1994. Thermoluminescence from igneous and natural hydrothermal vein quartz: dose response after optical bleaching. *Radiation Measurements*. v23: 159-173.

Rink, W.J. 1999. Quartz luminescence as a light-sensitive indicator of sediment transport in coastal processes. *Journal of Coastal Research*. v15 (1): 148-154.

Rink, W.J. and Pieper, K.D. 2001. Quartz thermoluminescence in a storm deposit and welded beach ridge. *Quaternary Science Reviews*. v20: 815-820.

Rink, W.J. 2003. Thermoluminescence of quartz and feldspar sand grains as a tracer of nearshore environmental processes in the southeastern Mediterranean Sea. *Journal of Coastal Research*. v19: 723-730.

Ritter, D.F. 1986. Process Geomorphology. Iowa: Wm. C. Brown Publishers.

Rizk, F. 1991. The Late Holocene Development of St. Joseph Spit. Florida State University. *PhD dissertation*. 379pp.

Shepard, F.P. 1950. Beach cycles in southern California. Technical memo. 20, Beach Erosion Board, Corps of Engineers.

Smith, B.W., Aitken, M.J., Rhodes, E.J., Robinson, P.D. and Geldard, D.M. 1986. Optical dating: methodological aspects. *Radiation Protection Dosimetry*. v17: 229-233.

Spooner, N.A. 1987. The effect of light on the thermoluminescence of quartz. *Unpublished M.Sc. thesis*. University of Adelaide.

Stapor, F.W. and Tanner, W.F. 1973. Errors in the pre-holocene C-14 scale. *Transactions-Gulf Coast Association of Geological Societies*. v23: 351-354.

Stapor, F.W., Mathews, T.D. and Lindfors-Kearns, F.E. 1991. Barrier island progradation and Holocene sea level history in southwest Florida. *Journal of Coastal Research*. v7(3): 815-838.

State of Florida Department of Natural Resources. St. Joseph Peninsula [LIDAR images]: Photogrammetric methods aerial cartographers of America, Inc. 1998.

Stewart, R.A. and Gorsline, D.S. 1962. Recent sedimentary history of St. Joseph Bay, Florida. *Sedimentology*. v1: 256-286.

Stokes, S. 1992. Optical dating of young (modern) sediments using quartz: Results from a selection of depositional environments. *Quaternary Science Reviews*. v11: 153-159.

Stone, G.W. and Stapor, F.W. 1996. A nearshore sediment transport model for the northeast Gulf of Mexico Coast, USA. *Journal of Coastal Research.* v12(3): 786-792.

Stone, G.W., Armbruster, C.K., Grymes, J.M. and Huh, O.K. 1996. Researchers study impact of Hurricane Opal on Florida coast. *EOS.* v77: 181.

Strahler, A.N. 1975. Physical Geography. Toronto: John Wiley and Sons, Inc.

Tanner, W.F. 1963. Nearly ideal drift system along the Florida Panhandle coast. *Geol. Soc. Am. Spec. Paper* 73: 311.

Tanner, W.F. 1975. Historical changes, Florida "Big Bend" coast. *Transactions-Gulf Coast Association of Geological Societies.* v25: 379.

Tanner, W.F. 1987. The beach: Where is the "river of sand"? *Journal of Coastal Research.* v3(3): 377-386.

Tanner, W.F. 1988. Beach ridge data and sea level history from the Americas. *Journal of Coastal Research.* v4(1): 81-91.

Tanner, W.F. 1991. The "Gulf of Mexico" late Holocene sea level curve and river delta history. *Transactions-Gulf Coast Association of Geological Societies.* v61: 583-589.

United States Department of the Interior Geological Survey. St. Joseph Point Quadrangle, Florida- Gulf County [map]. 1:24,000. 7.5 minute series orthophotomap. Colorado: USGS, 1982.

United States Department of the Interior Geological Survey. Port St. Joe Quadrangle, Florida- Gulf County [map]. 1:24,000. 7.5 minute series orthophotomap. Colorado: USGS, 1982.

United States Department of the Interior Geological Survey. Cape San Blas Quadrangle, Florida- Gulf County [map]. 1:24,000. 7.5 minute series orthophotomap. Colorado: USGS, 1982.

United States Department of the Interior Geological Survey. St. Joseph Peninsula Quadrangle, Florida- Gulf County [map]. 1:24,000. 7.5 minute series orthophotomap. Colorado: USGS, 1982.

USGS. 1999. Digital orthoquadrangles. "Terra Server USA." Posted 2001. 2m x 2m resolution. [available online]: http://terraserver-usa.com.

van Rijn, L.C., Walstra, D.J.R., Grasmeijer, B., Sutherland, J., Pan, S. and Sierra, J.P. 2003. The predictability of cross-shore bed evolution of sandy beaches at the time scale of storms and seasons using process-based profile models. *Coastal Engineering*. v47 (3): 295-327.

Von Drehle, W. 1973. A sedimentary investigation of the large linear sand bodies exposed in the Gulf County, Florida, canal. *Unpublished M.Sc. Thesis*. Florida State University, Tallahassee, 119p.

Williams, J.M. and Duedall, I.W. 1997. Florida Hurricanes and Tropical Storms. Gainesville: University Press of Florida.

Wintle, A.G. 1993. Recent developments in optical dating of sediments. *Radiation Protection Dosimetry*. V74(1/4): 627-635.

Wintle, A.G., Clarke, M.L., Musson, F.M., Orford, J.D. and Devoy, R.J.N. 1998. Luminescence dating of recent dunes on Inch Spit, Dingle Bay, Southwest Ireland. *The Holocene*. v8(3): 331-339.

Woodroffe, C.D. 2002. Coasts: form, processes and evolution. Cambridge: Cambridge University Press.

APPENDIX A- Heavy mineral deposit at SJ298

APPENDIX B- unshifted TL curves

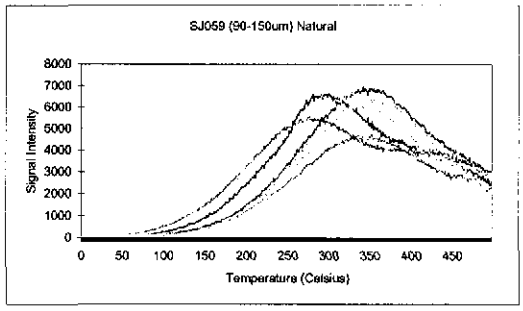
SJ059 (90-150um) Natural
Signal Intensity
Temperature (Celsius)

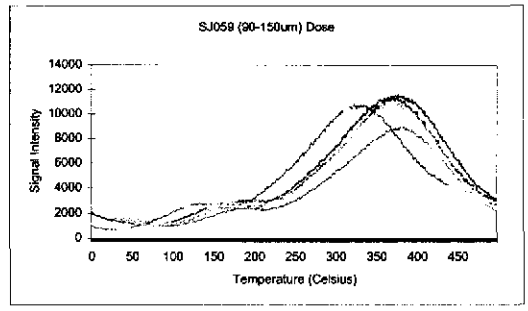
SJ059 (90-150um) Dose
Signal Intensity
Temperature (Celsius)

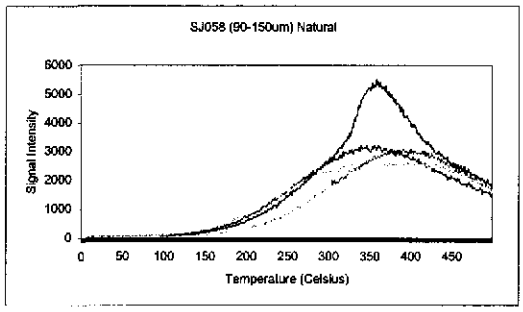
SJ058 (90-150um) Natural
Signal Intensity
Temperature (Celsius)

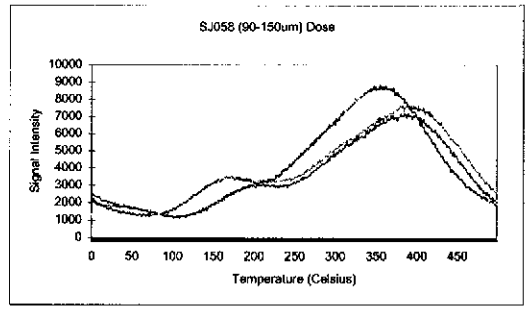
SJ058 (90-150um) Dose
Signal Intensity
Temperature (Celsius)

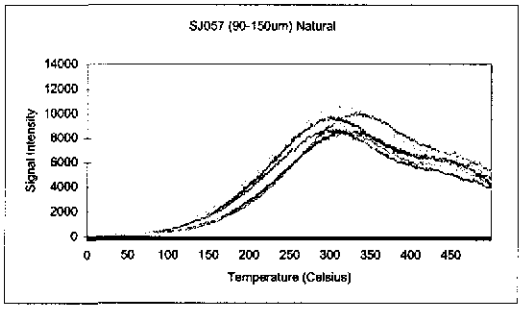
SJ057 (90-150um) Natural
Signal Intensity
Temperature (Celsius)

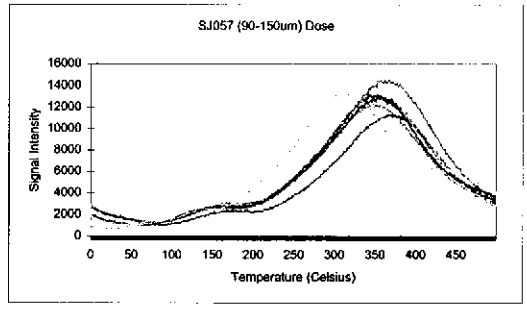
SJ057 (90-150um) Dose
Signal Intensity
Temperature (Celsius)

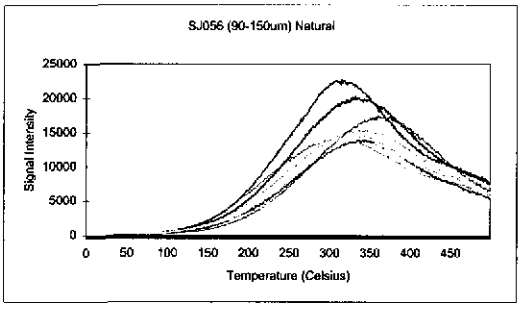
SJ056 (90-150um) Natural
Signal Intensity
Temperature (Celsius)

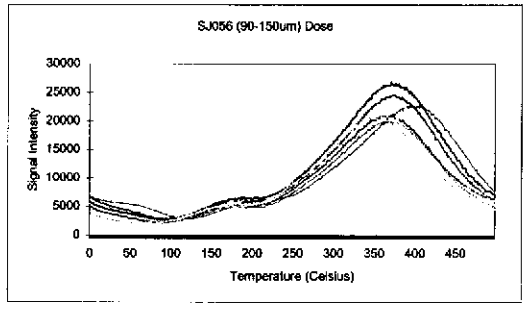
SJ056 (90-150um) Dose
Signal Intensity
Temperature (Celsius)

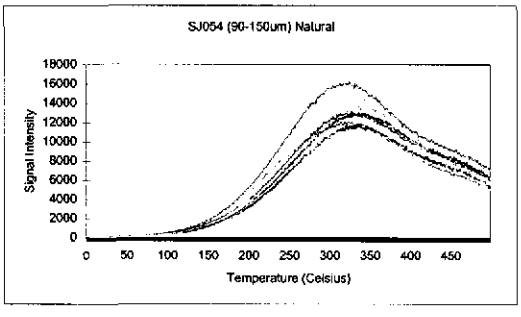
SJ054 (90-150um) Natural
Signal Intensity
Temperature (Celsius)

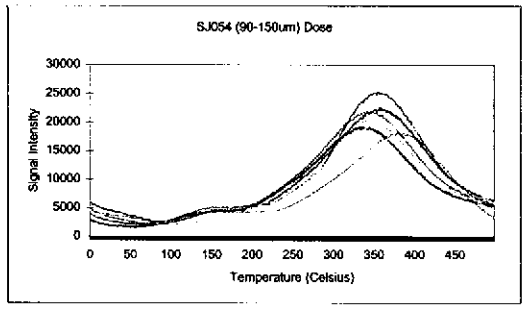
SJ054 (90-150um) Dose
Signal Intensity
Temperature (Celsius)

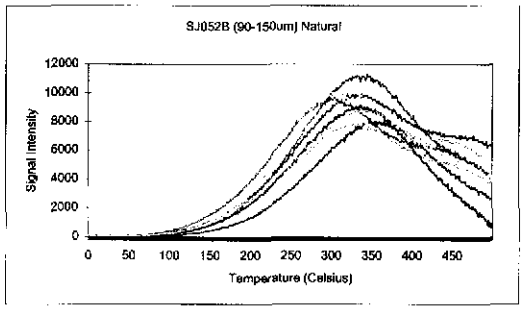
SJ052B (90-150um) Natural
Signal Intensity
Temperature (Celsius)

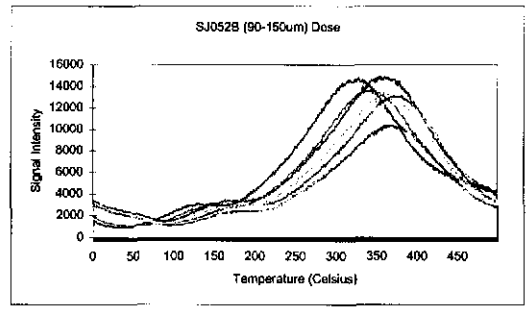
SJ052B (90-150um) Dose
Signal Intensity
Temperature (Celsius)

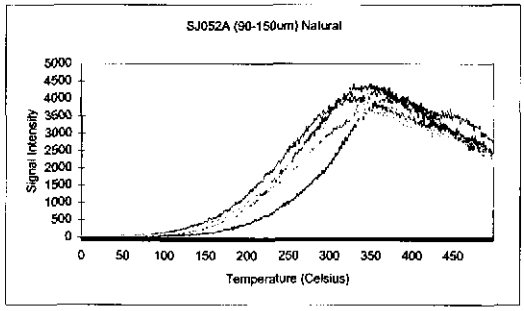
SJ052A (90-150um) Natural
Signal Intensity
Temperature (Celsius)

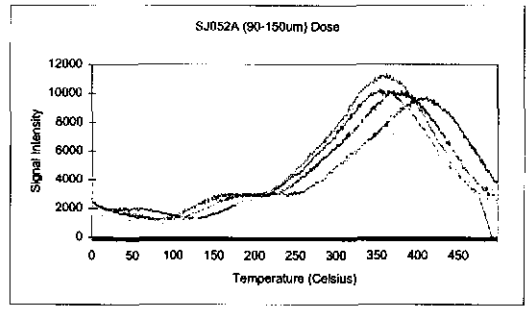
SJ052A (90-150um) Dose
Signal Intensity
Temperature (Celsius)

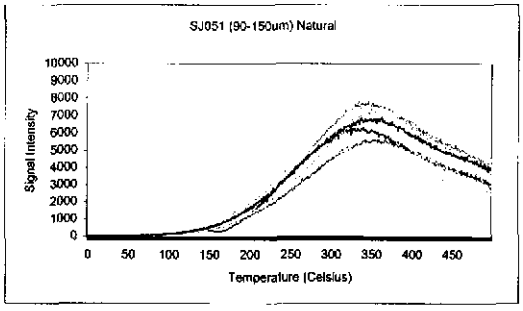
SJ051 (90-150um) Natural
Signal Intensity
Temperature (Celsius)

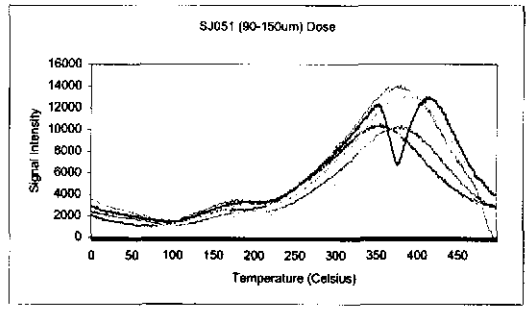
SJ051 (90-150um) Dose
Signal Intensity
Temperature (Celsius)

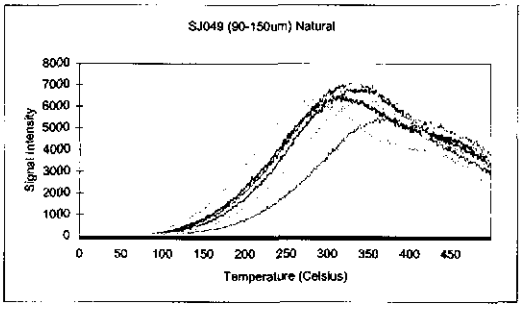
SJ049 (90-150um) Natural
Signal Intensity
Temperature (Celsius)

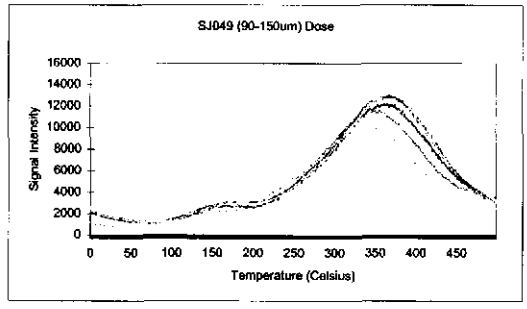
SJ049 (90-150um) Dose
Signal Intensity
Temperature (Celsius)

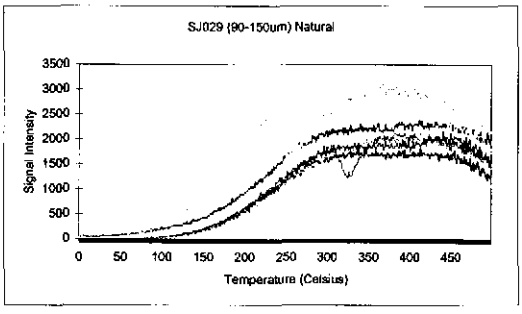
SJ029 (90-150um) Natural
Signal Intensity
Temperature (Celsius)

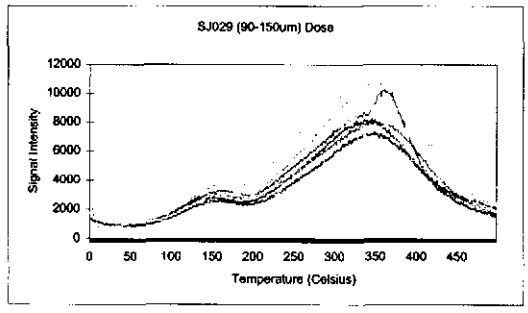
SJ029 (90-150um) Dose
Signal Intensity
Temperature (Celsius)

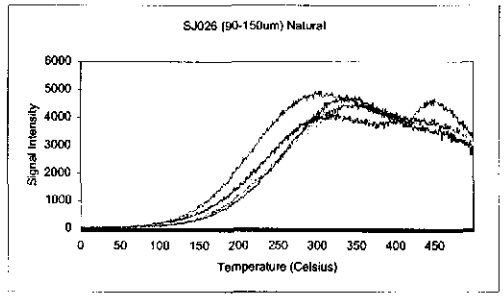
SJ026 (90-150um) Natural
Signal Intensity
Temperature (Celsius)

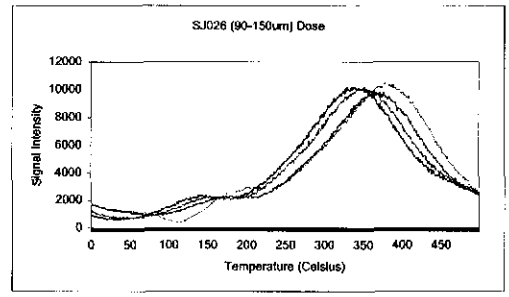
SJ026 (90-150um) Dose
Signal Intensity
Temperature (Celsius)

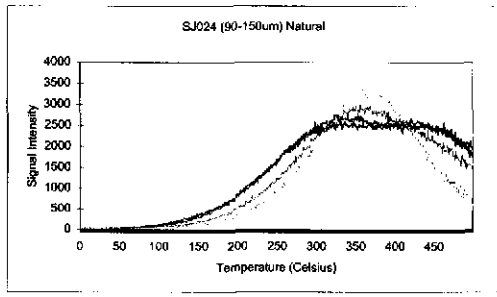
SJ024 (90-150um) Natural
Signal Intensity
Temperature (Celsius)

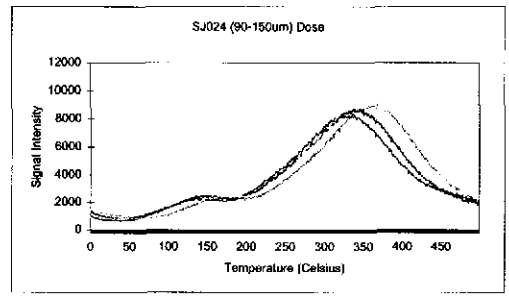
SJ024 (90-150um) Dose
Signal Intensity
Temperature (Celsius)

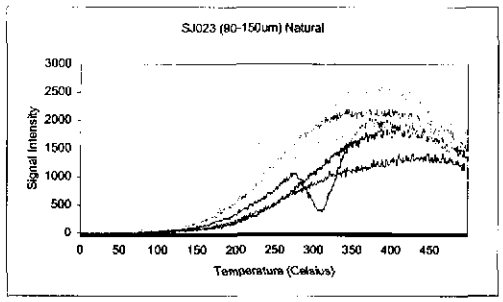
SJ023 (90-150um) Natural
Signal Intensity
Temperature (Celsius)

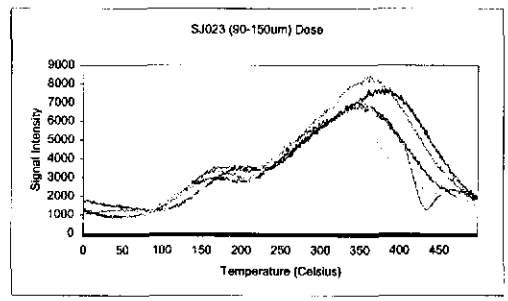
SJ023 (90-150um) Dose
Signal Intensity
Temperature (Celsius)

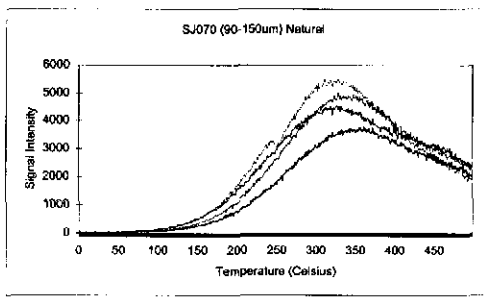
SJ070 (90-150um) Natural
Signal Intensity
Temperature (Celsius)

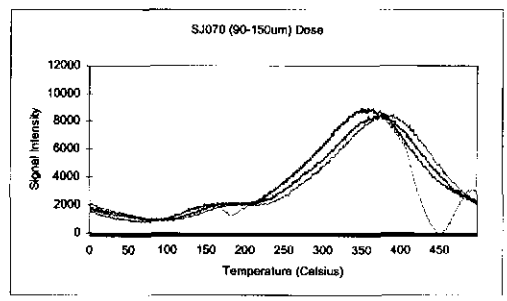
SJ070 (90-150um) Dose
Signal Intensity
Temperature (Celsius)

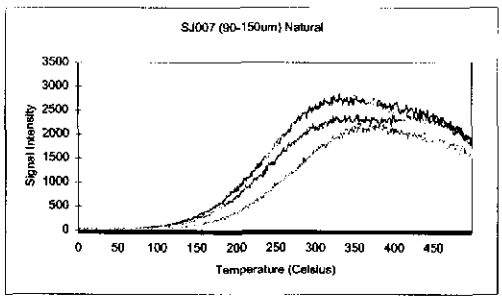
SJ007 (90-150um) Natural
Signal Intensity
Temperature (Celsius)

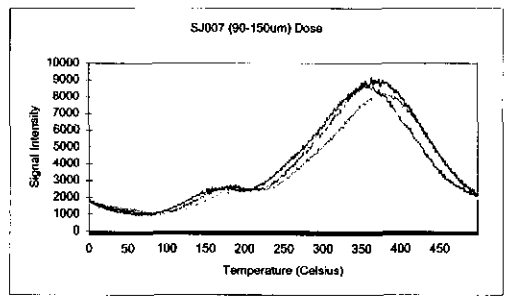
SJ007 (90-150um) Dose
Signal Intensity
Temperature (Celsius)

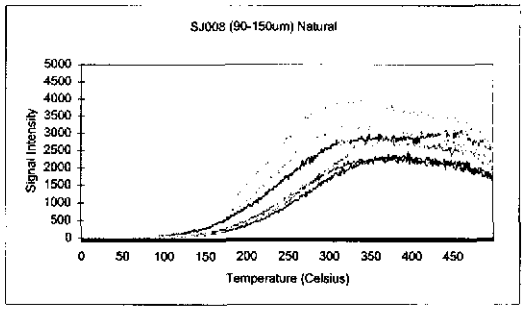
SJ008 (90-150um) Natural
Signal Intensity
Temperature (Celsius)

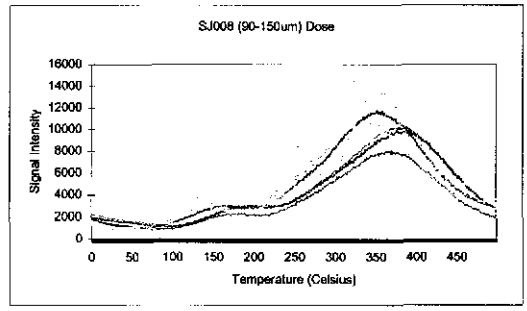
SJ008 (90-150um) Dose
Signal Intensity
Temperature (Celsius)

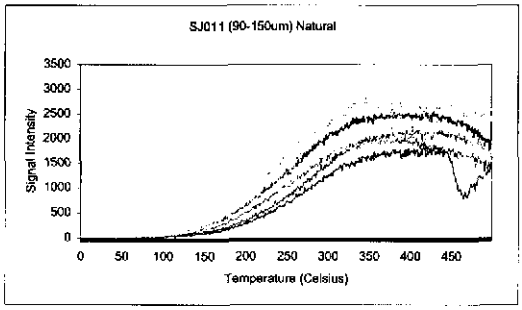
SJ011 (90-150um) Natural
Signal Intensity
Temperature (Celsius)

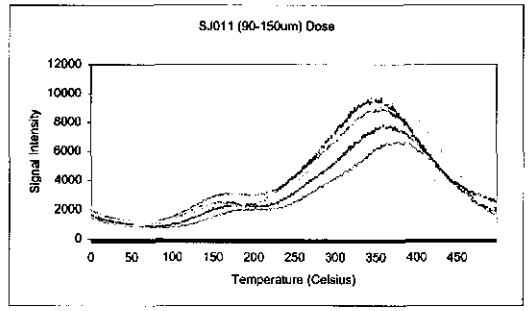
SJ011 (90-150um) Dose
Signal Intensity
Temperature (Celsius)

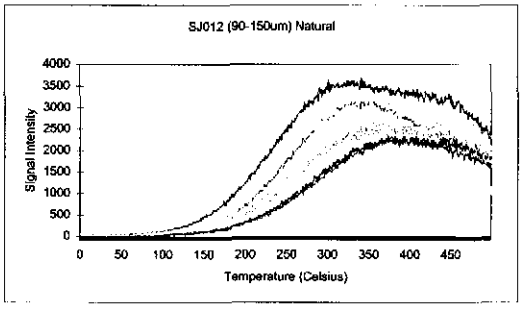
SJ012 (90-150um) Natural
Signal Intensity
Temperature (Celsius)

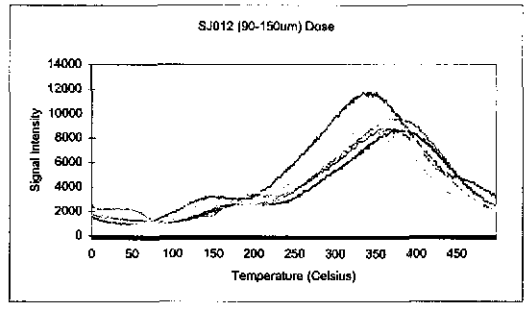
SJ012 (90-150um) Dose
Signal Intensity
Temperature (Celsius)

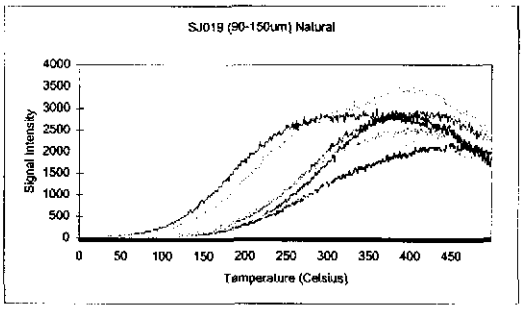
SJ019 (90-150um) Natural
Signal Intensity
Temperature (Celsius)

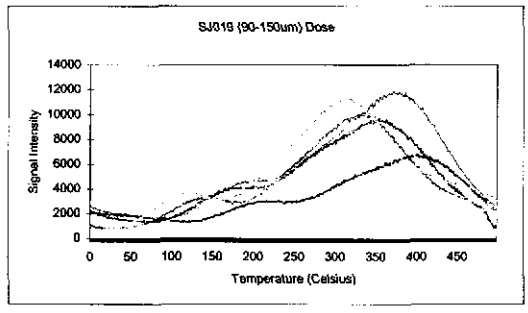
SJ019 (90-150um) Dose
Signal Intensity
Temperature (Celsius)

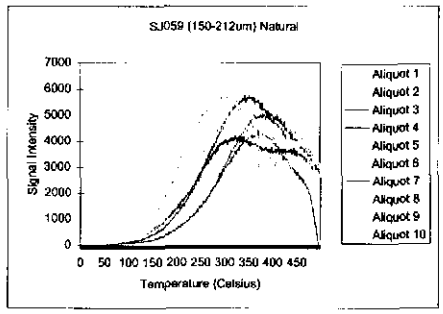
SJ059 (150-212um) Natural
Signal Intensity
Temperature (Celsius)
Aliquot 1
Aliquot 2
Aliquot 3
Aliquot 4
Aliquot 5
Aliquot 6
Aliquot 7
Aliquot 8
Aliquot 9
Aliquot 10

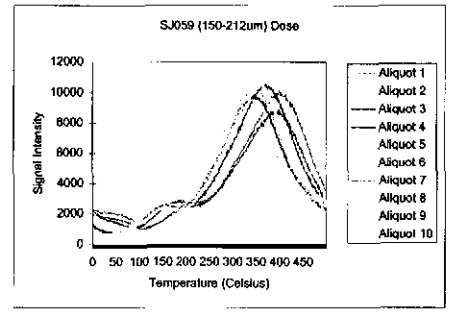
SJ059 (150-212um) Dose
Signal Intensity
Temperature (Celsius)
Aliquot 1
Aliquot 2
Aliquot 3
Aliquot 4
Aliquot 5
Aliquot 6
Aliquot 7
Aliquot 8
Aliquot 9
Aliquot 10

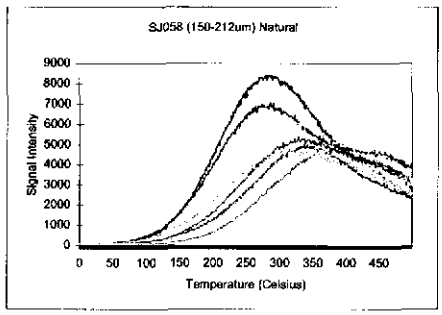
SJ058 (150-212um) Natural
Signal Intensity
Temperature (Celsius)

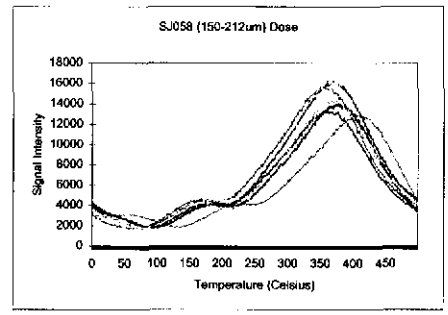
SJ058 (150-212um) Dose
Signal Intensity
Temperature (Celsius)

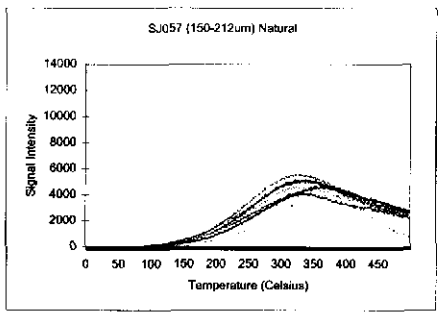
SJ057 (150-212um) Natural
Signal Intensity
Temperature (Celsius)

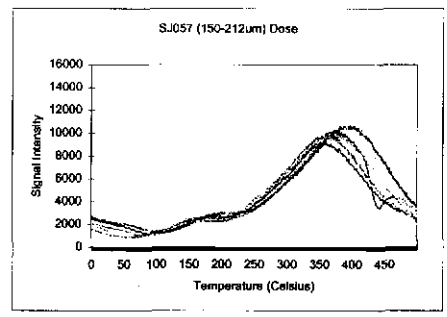
SJ057 (150-212um) Dose
Signal Intensity
Temperature (Celsius)

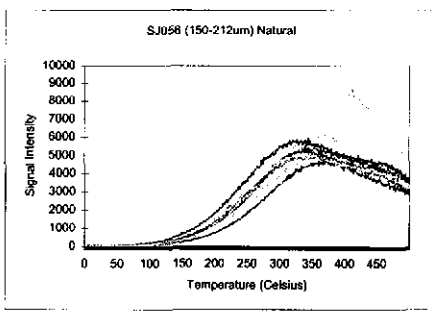
SJ056 (150-212um) Natural
Signal Intensity
Temperature (Celsius)

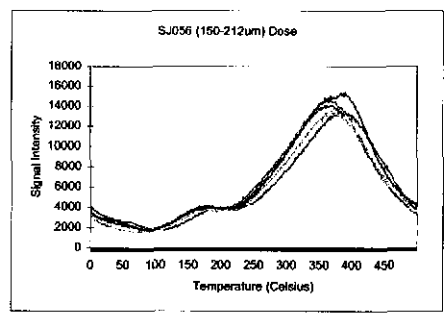
SJ056 (150-212um) Dose
Signal Intensity
Temperature (Celsius)

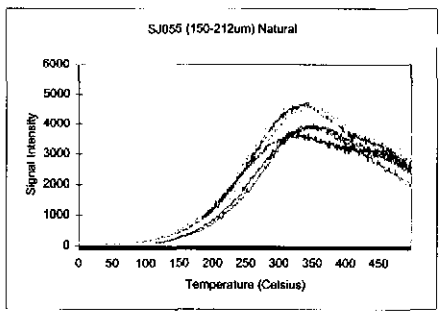
SJ055 (150-212um) Natural
Signal Intensity
Temperature (Celsius)

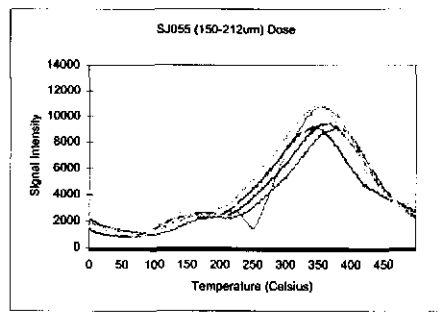
SJ055 (150-212um) Dose
Signal Intensity
Temperature (Celsius)

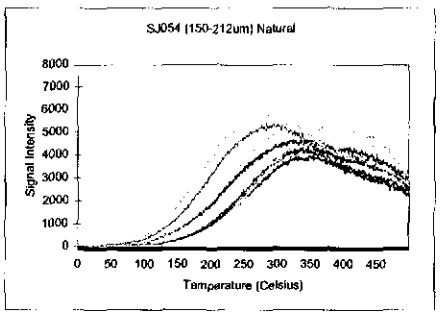
SJ054 (150-212um) Natural
Signal Intensity
Temperature (Celsius)

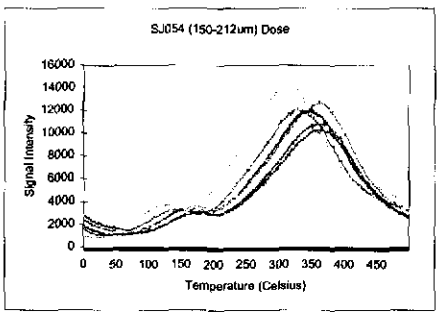
SJ054 (150-212um) Dose
Signal Intensity
Temperature (Celsius)

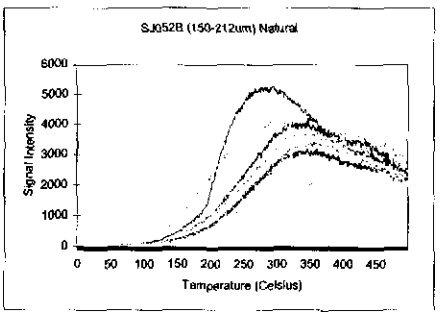
SJ052B (150-212um) Natural
Signal Intensity
Temperature (Celsius)

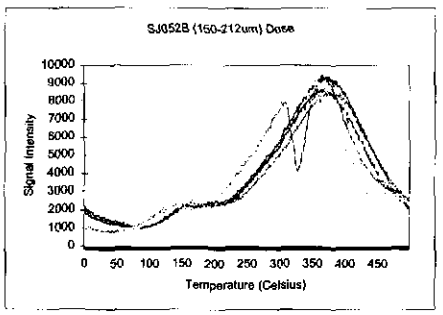
SJ052B (150-212um) Dose
Signal Intensity
Temperature (Celsius)

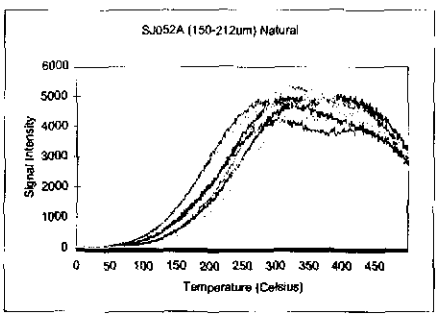
SJ052A (150-212um) Natural
Signal Intensity
Temperature (Celsius)

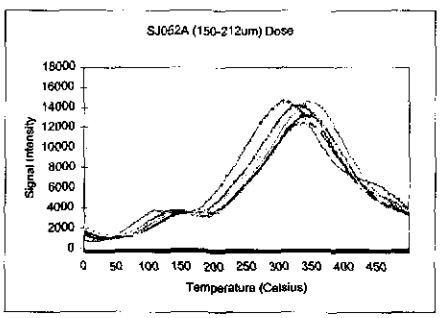
SJ052A (150-212um) Dose
Signal Intensity
Temperature (Celsius)

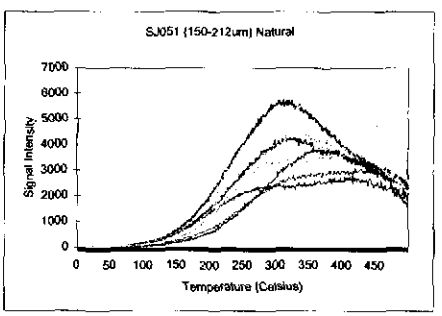
SJ051 (150-212um) Natural
Signal Intensity
Temperature (Celsius)

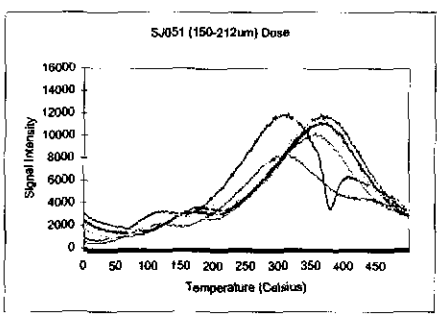
SJ051 (150-212um) Dose
Signal Intensity
Temperature (Celsius)

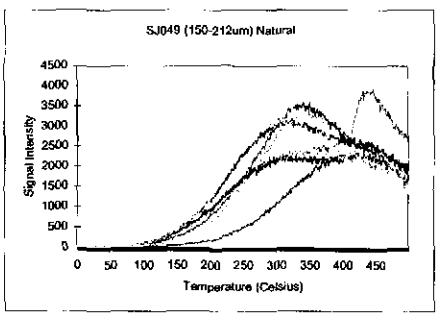
SJ049 (150-212um) Natural
Signal Intensity
Temperature (Celsius)

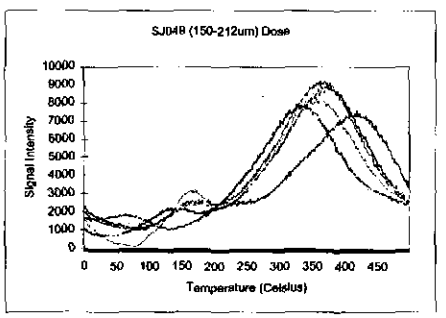
SJ049 (150-212um) Dose
Signal Intensity
Temperature (Celsius)

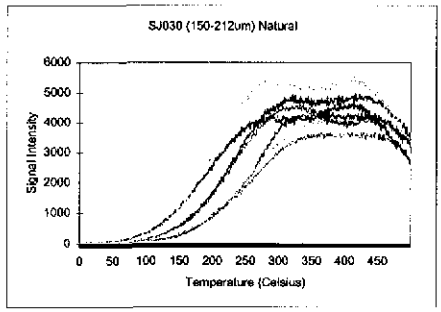
SJ030 (150-212um) Natural
Signal Intensity
Temperature (Celsius)

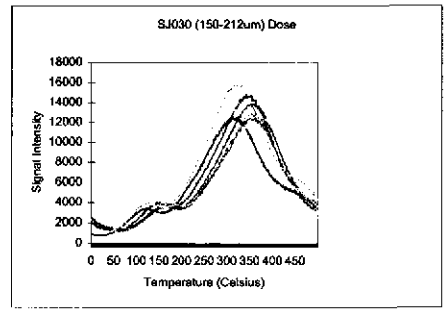
SJ030 (150-212um) Dose
Signal Intensity
Temperature (Celsius)

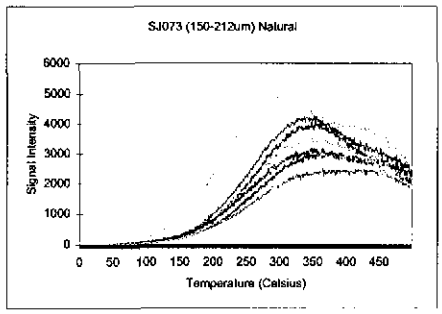
SJ073 (150-212um) Natural
Signal Intensity
Temperature (Celsius)

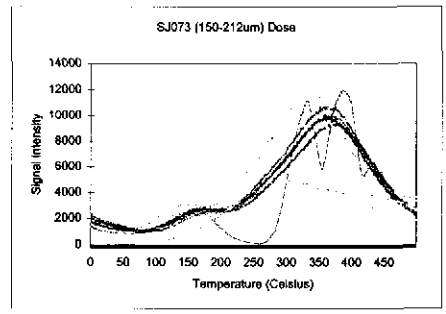
SJ073 (150-212um) Dose
Signal Intensity
Temperature (Celsius)

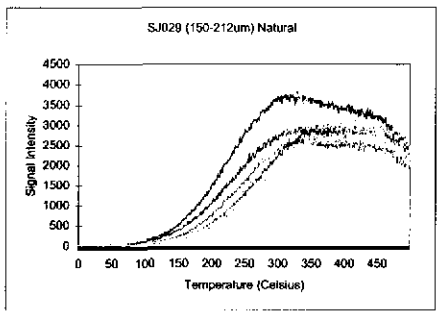
SJ029 (150-212um) Natural
Signal Intensity
Temperature (Celsius)

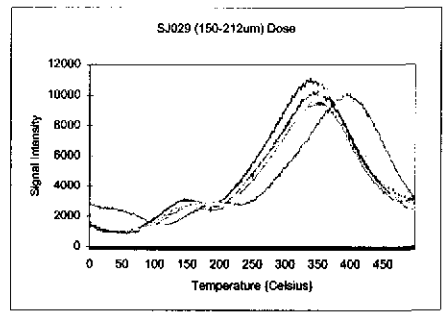
SJ029 (150-212um) Dose
Signal Intensity
Temperature (Celsius)

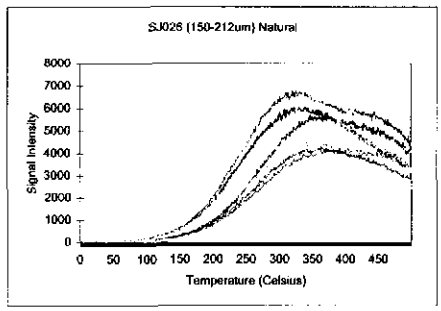
SJ026 (150-212um) Natural
Signal Intensity
Temperature (Celsius)

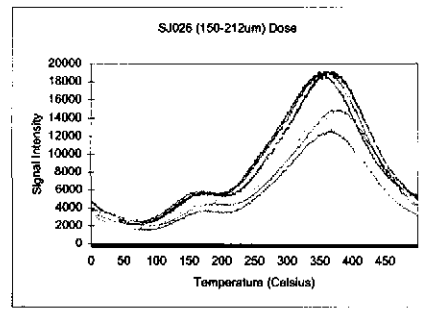
SJ026 (150-212um) Dose
Signal Intensity
Temperature (Celsius)

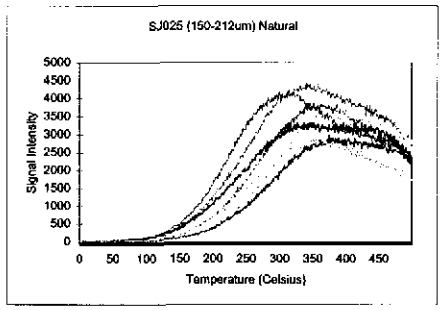
SJ025 (150-212um) Natural
Signal Intensity
Temperature (Celsius)

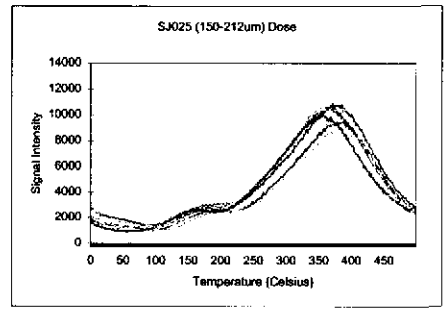
SJ025 (150-212um) Dose
Signal Intensity
Temperature (Celsius)

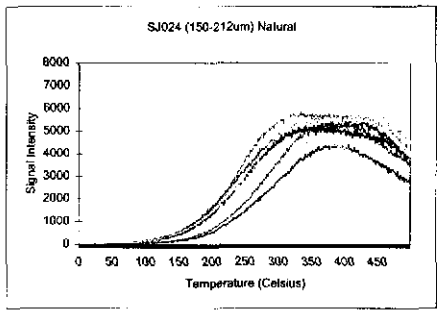
SJ024 (150-212um) Natural
Signal Intensity
Temperature (Celsius)

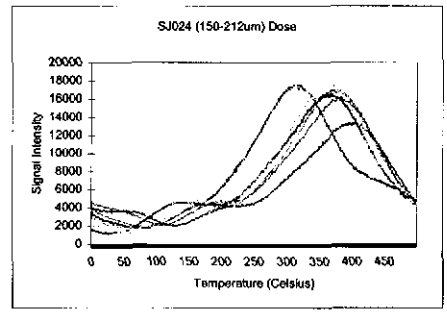
SJ024 (150-212um) Dose
Signal Intensity
Temperature (Celsius)

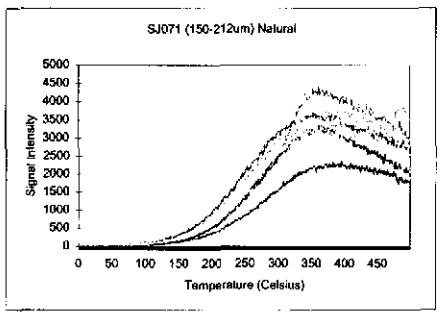
SJ071 (150-212um) Natural
Signal Intensity
Temperature (Celsius)

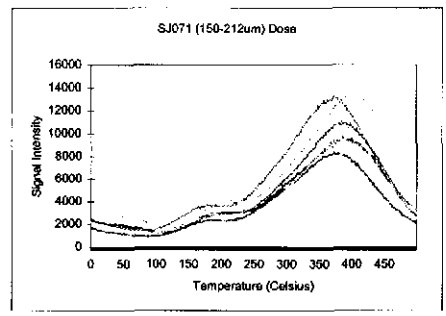
SJ071 (150-212um) Dose
Signal Intensity
Temperature (Celsius)

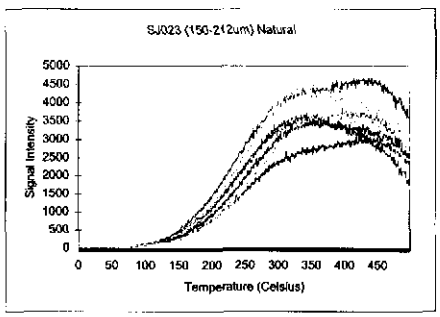
SJ023 (150-212um) Natural
Signal Intensity
Temperature (Celsius)

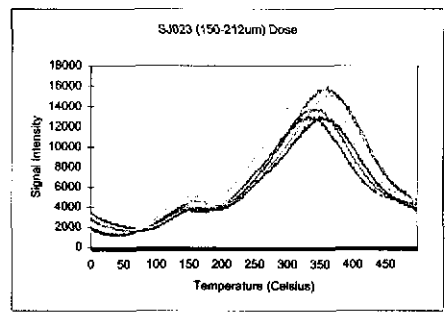
SJ023 (150-212um) Dose
Signal Intensity
Temperature (Celsius)

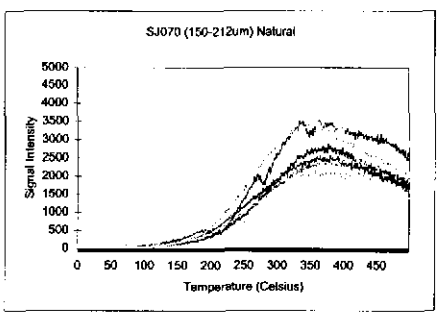
SJ070 (150-212um) Natural
Signal Intensity
Temperature (Celsius)

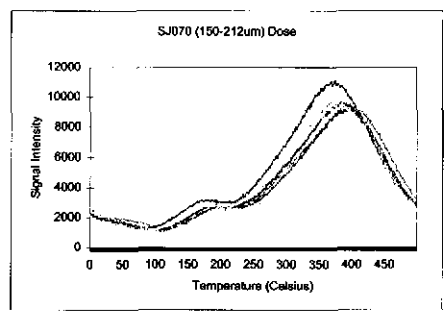
SJ070 (150-212um) Dose
Signal Intensity
Temperature (Celsius)

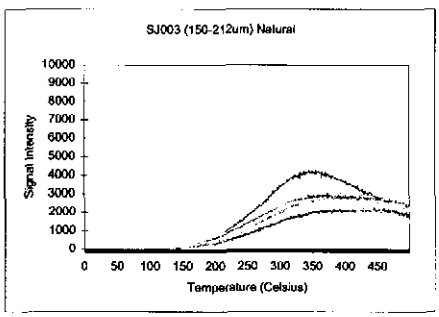
SJ003 (150-212um) Natural
Signal Intensity
Temperature (Celsius)

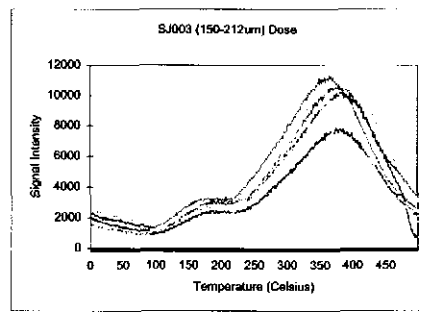
SJ003 (150-212um) Dose
Signal Intensity
Temperature (Celsius)

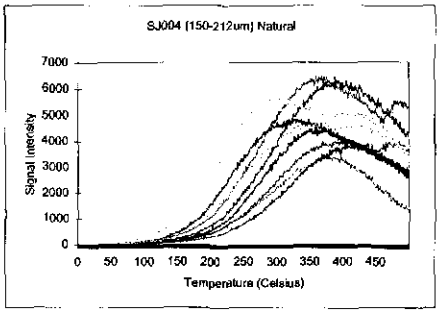
SJ004 (150-212um) Natural
Signal Intensity
Temperature (Celsius)

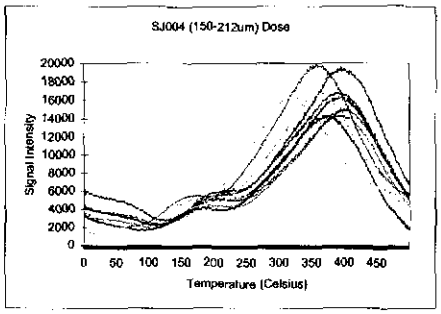
SJ004 (150-212um) Dose
Signal Intensity
Temperature (Celsius)

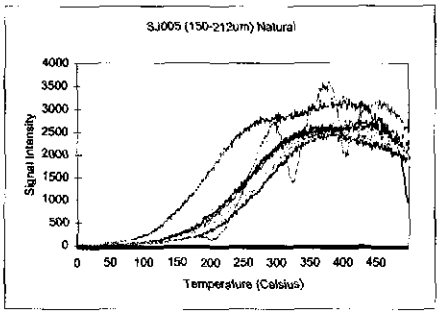
SJ005 (150-212um) Natural
Signal Intensity
Temperature (Celsius)

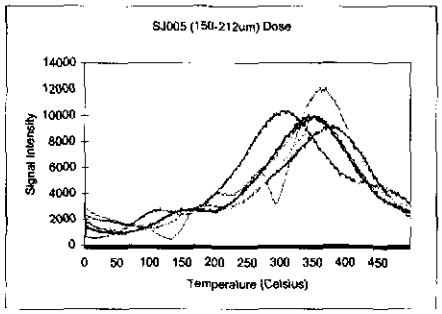
SJ005 (150-212um) Dose
Signal Intensity
Temperature (Celsius)

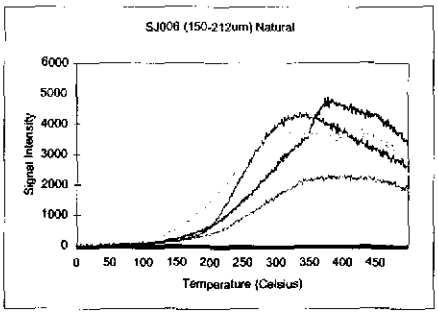
SJ006 (150-212um) Natural
Signal Intensity
Temperature (Celsius)

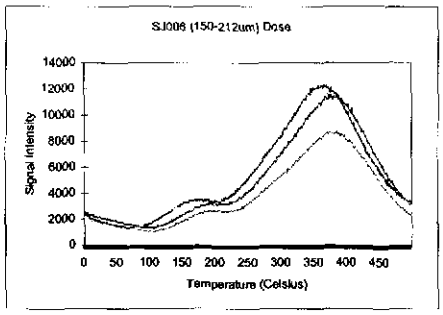
SJ006 (150-212um) Dose
Signal Intensity
Temperature (Celsius)

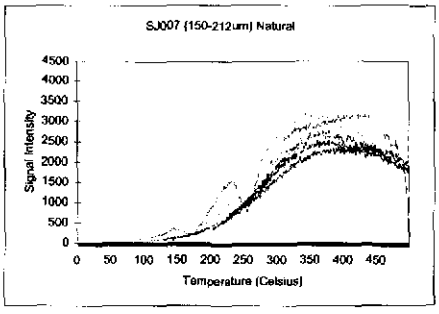
SJ007 (150-212um) Natural
Signal Intensity
Temperature (Celsius)

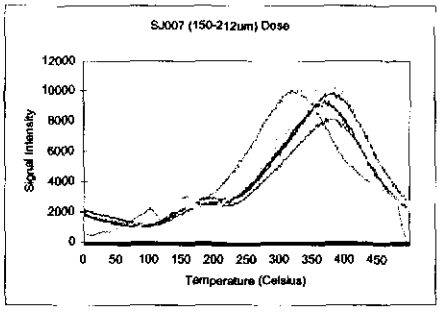
SJ007 (150-212um) Dose
Signal Intensity
Temperature (Celsius)

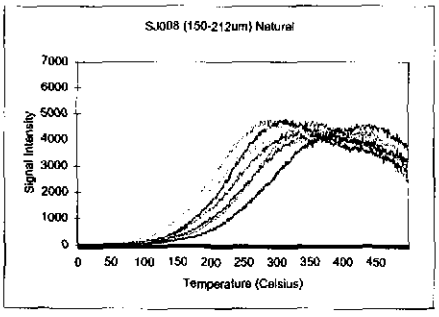
SJ008 (150-212um) Natural
Signal Intensity
Temperature (Celsius)

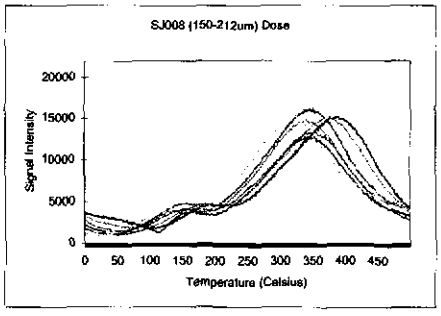
SJ008 (150-212um) Dose
Signal Intensity
Temperature (Celsius)

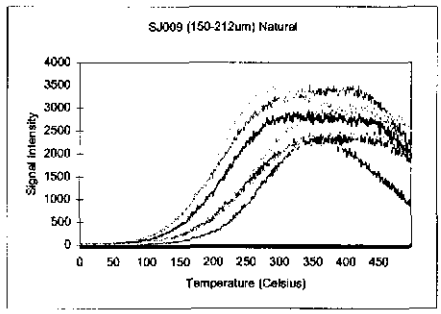
SJ009 (150-212um) Natural
Signal Intensity
Temperature (Celsius)

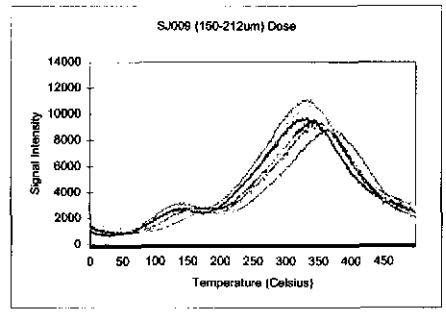
SJ009 (150-212um) Dose
Signal Intensity
Temperature (Celsius)

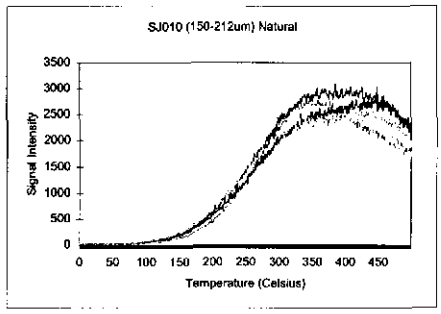
SJ010 (150-212um) Natural
Signal Intensity
Temperature (Celsius)

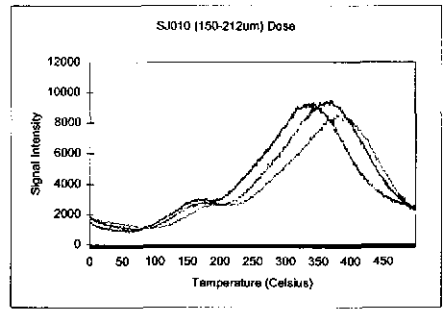
SJ010 (150-212um) Dose
Signal Intensity
Temperature (Celsius)

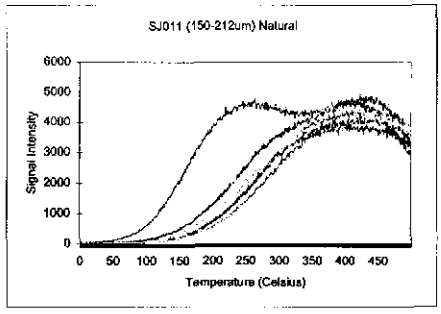
SJ011 (150-212um) Natural
Signal Intensity
Temperature (Celsius)

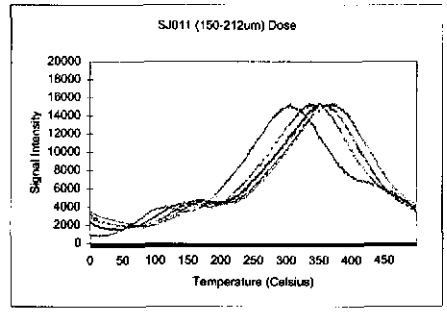
SJ011 (150-212um) Dose
Signal Intensity
Temperature (Celsius)

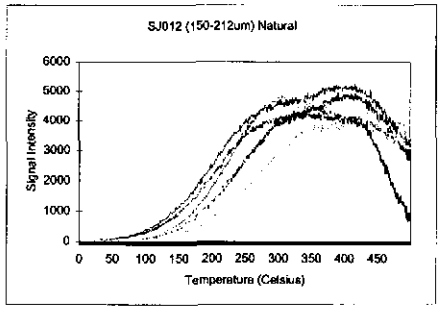
SJ012 (150-212um) Natural
Signal Intensity
Temperature (Celsius)

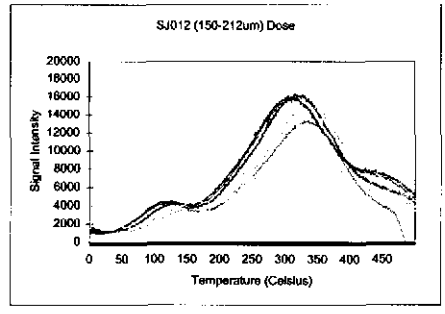
SJ012 (150-212um) Dose
Signal Intensity
Temperature (Celsius)

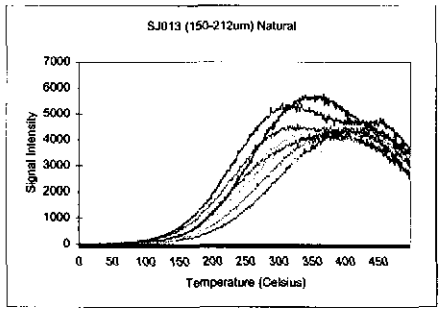
SJ013 (150-212um) Natural
Signal Intensity
Temperature (Celsius)

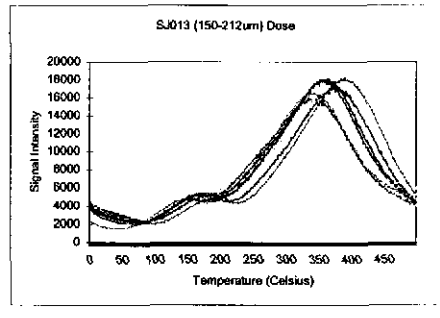
SJ013 (150-212um) Dose
Signal Intensity
Temperature (Celsius)

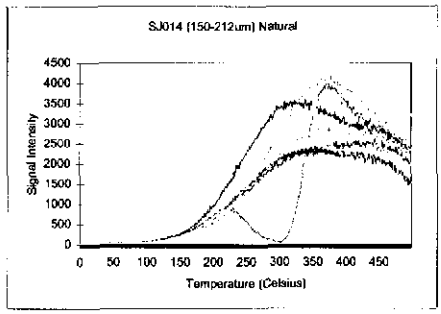
SJ014 (150-212um) Natural
Signal Intensity
Temperature (Celsius)

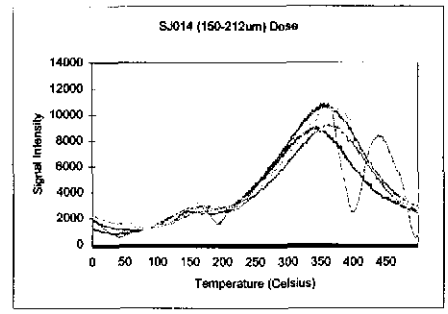
SJ014 (150-212um) Dose
Signal Intensity
Temperature (Celsius)

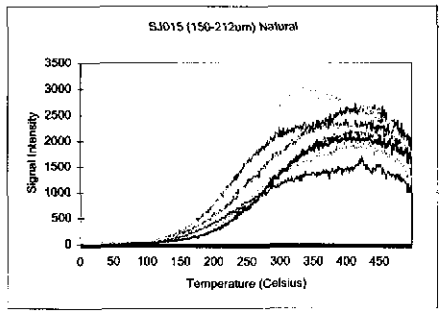
SJ015 (150-212um) Natural
Signal Intensity
Temperature (Celsius)

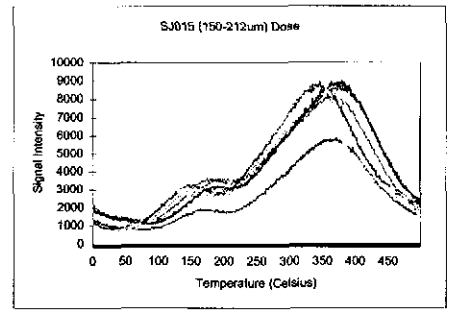
SJ015 (150-212um) Dose
Signal Intensity
Temperature (Celsius)

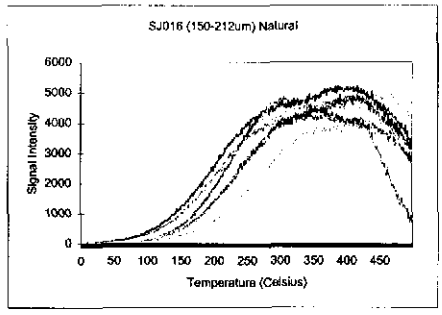
SJ016 (150-212um) Natural
Signal Intensity
Temperature (Celsius)

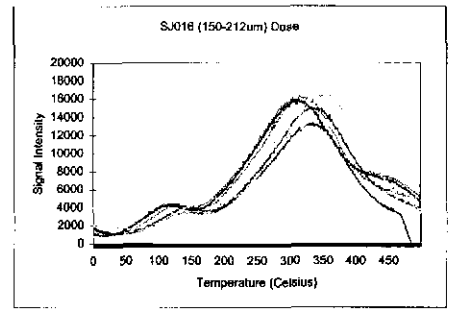
SJ016 (150-212um) Dose
Signal Intensity
Temperature (Celsius)

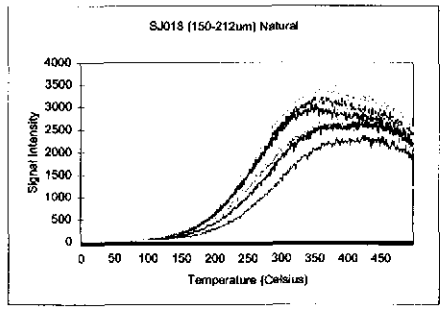
SJ018 (150-212um) Natural
Signal Intensity
Temperature (Celsius)

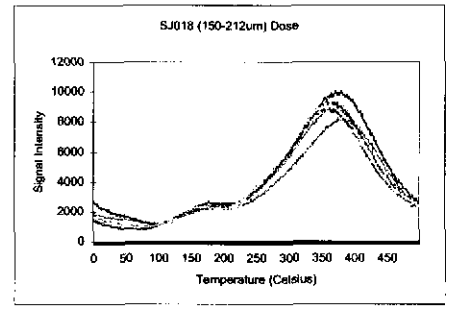
SJ018 (150-212um) Dose
Signal Intensity
Temperature (Celsius)

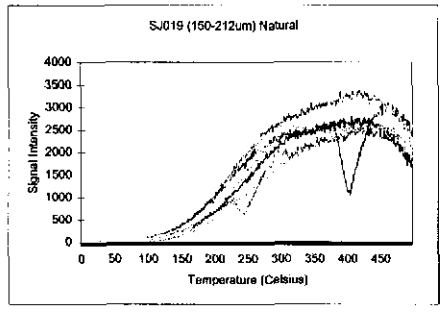
SJ019 (150-212um) Natural
Signal Intensity
Temperature (Celsius)

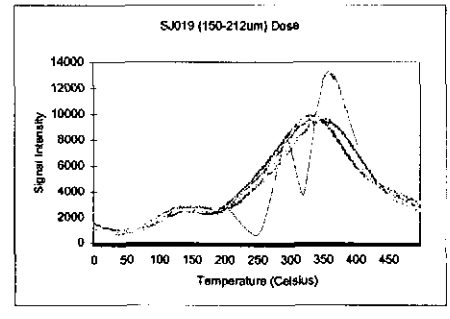
SJ019 (150-212um) Dose
Signal Intensity
Temperature (Celsius)

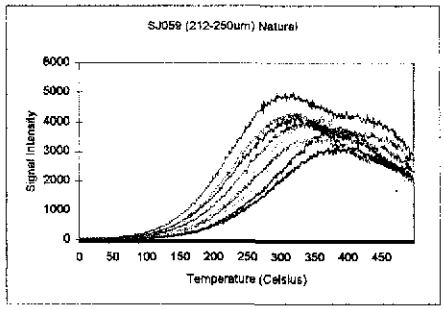
SJ059 (212-250um) Natural
Signal Intensity
Temperature (Celsius)

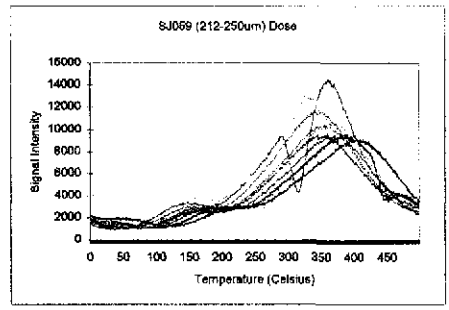
SJ059 (212-250um) Dose
Signal Intensity
Temperature (Celsius)

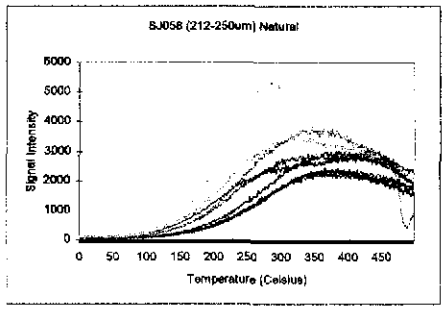
SJ058 (212-250um) Natural
Signal Intensity
Temperature (Celsius)

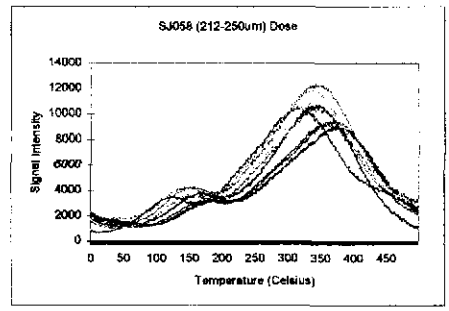
SJ058 (212-250um) Dose
Signal Intensity
Temperature (Celsius)

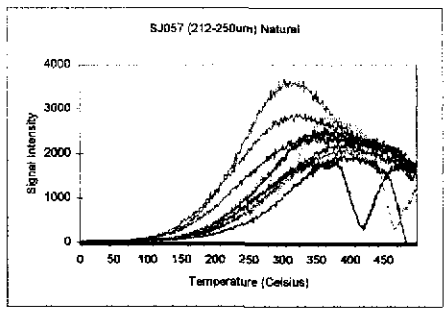
SJ057 (212-250um) Natural
Signal Intensity
Temperature (Celsius)

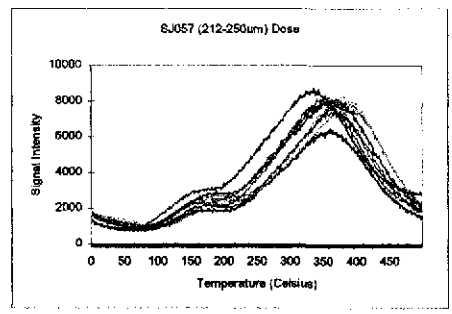
SJ057 (212-250um) Dose
Signal Intensity
Temperature (Celsius)

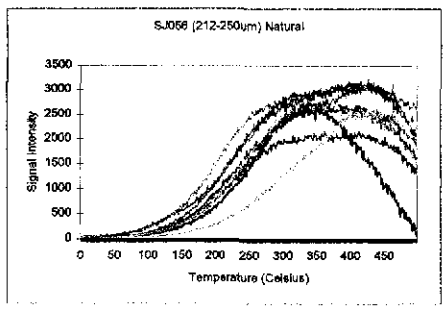
SJ056 (212-250um) Natural
Signal Intensity
Temperature (Celsius)

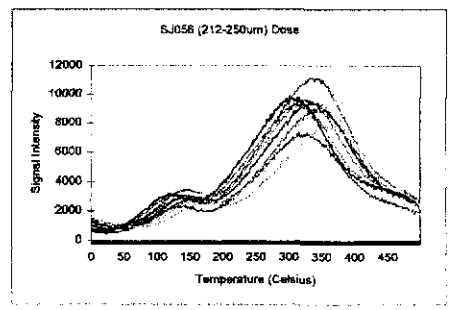
SJ056 (212-250um) Dose
Signal Intensity
Temperature (Celsius)

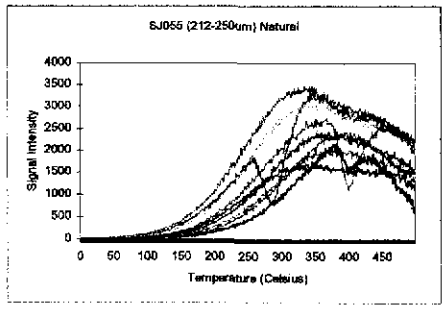
SJ055 (212-250um) Natural
Signal Intensity
Temperature (Celsius)

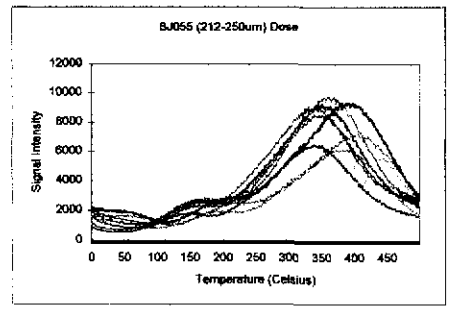
SJ055 (212-250um) Dose
Signal Intensity
Temperature (Celsius)

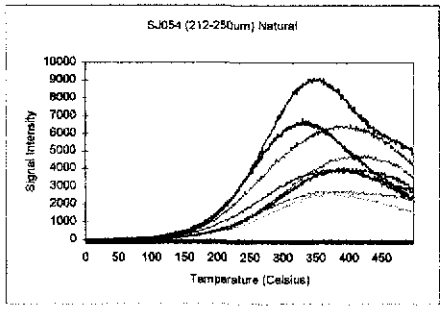
SJ054 (212-250um) Natural
Signal Intensity
Temperature (Celsius)

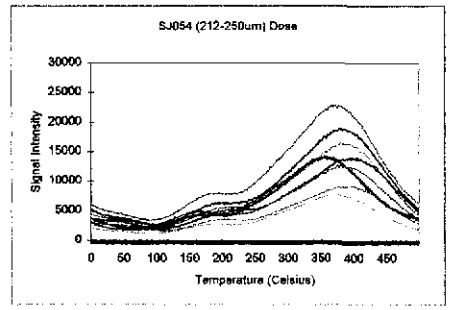
SJ054 (212-250um) Dose
Signal Intensity
Temperature (Celsius)

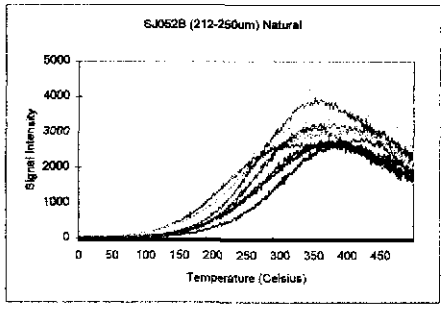
SJ052B (212-250um) Natural
Signal Intensity
Temperature (Celsius)

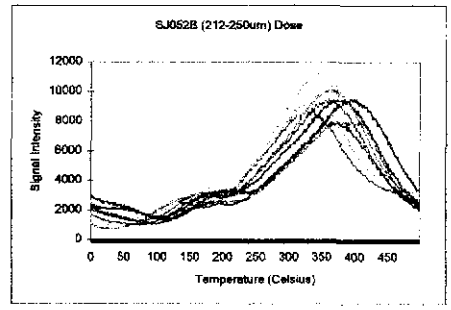
SJ052B (212-250um) Dose
Signal Intensity
Temperature (Celsius)

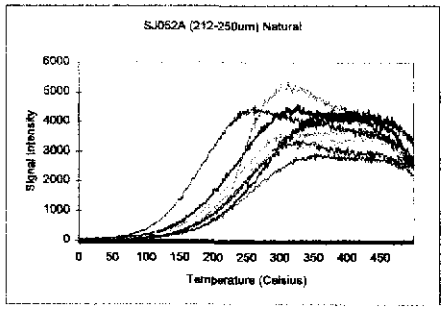
SJ052A (212-250um) Natural
Signal Intensity
Temperature (Celsius)

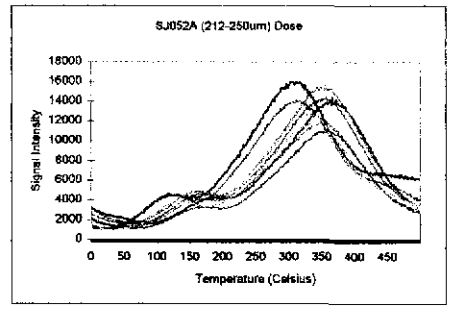
SJ052A (212-250um) Dose
Signal Intensity
Temperature (Celsius)

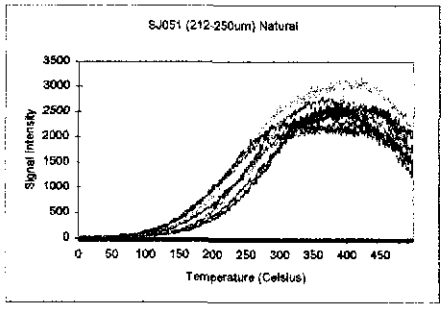
SJ051 (212-250um) Natural
Signal Intensity
Temperature (Celsius)

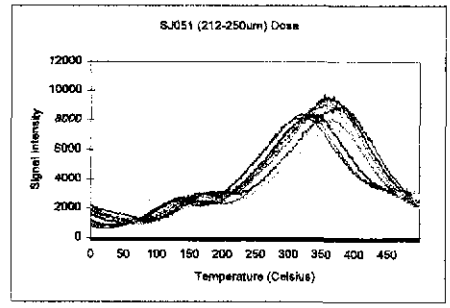
SJ051 (212-250um) Dose
Signal Intensity
Temperature (Celsius)

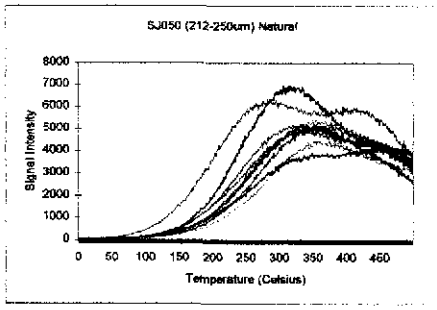
SJ050 (212-250um) Natural
Signal Intensity
Temperature (Celsius)

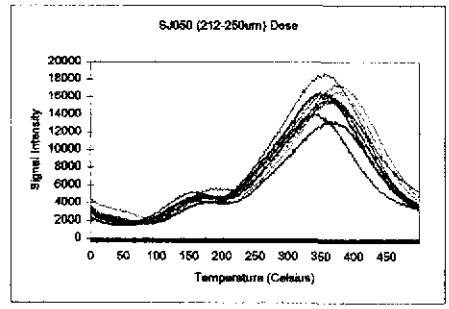
SJ050 (212-250um) Dose
Signal Intensity
Temperature (Celsius)

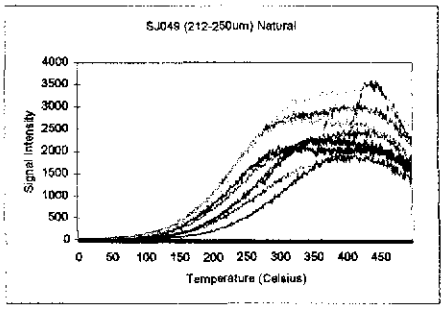
SJ049 (212-250um) Natural
Signal Intensity
Temperature (Celsius)

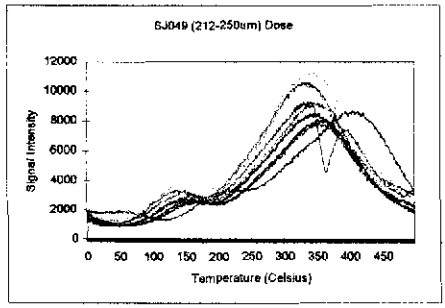
SJ049 (212-250um) Dose
Signal Intensity
Temperature (Celsius)

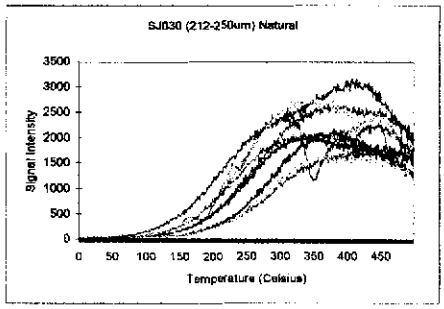
SJ030 (212-250um) Natural
Signal Intensity
Temperature (Celsius)

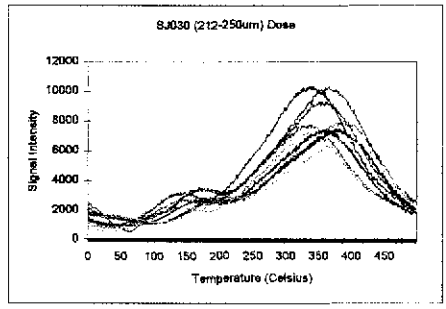
SJ030 (212-250um) Dose
Signal Intensity
Temperature (Celsius)

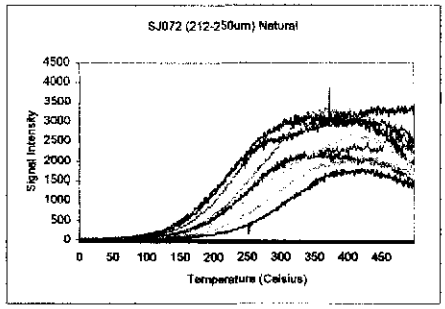
SJ072 (212-250um) Natural
Signal Intensity
Temperature (Celsius)

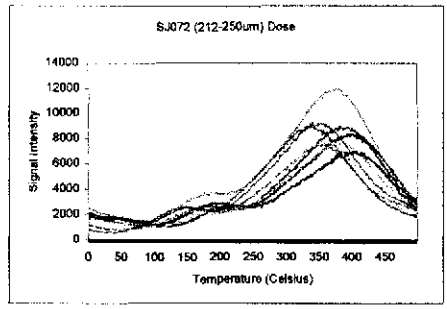
SJ072 (212-250um) Dose
Signal Intensity
Temperature (Celsius)

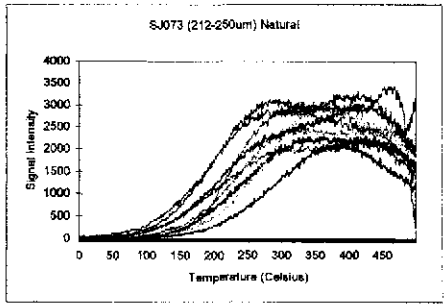
SJ073 (212-250um) Natural
Signal Intensity
Temperature (Celsius)

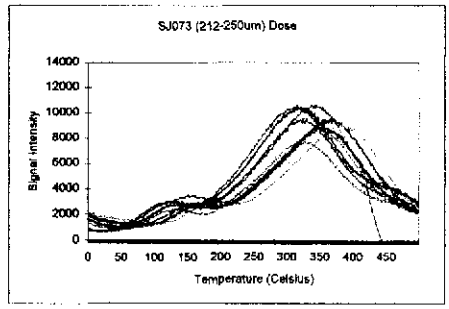
SJ073 (212-250um) Dose
Signal Intensity
Temperature (Celsius)

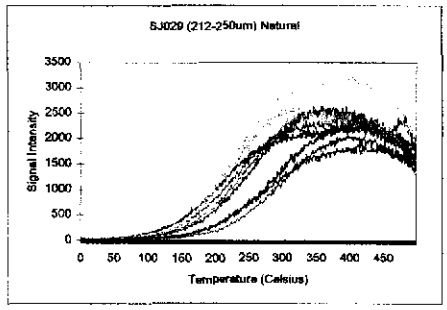
SJ029 (212-250um) Natural
Signal Intensity
Temperature (Celsius)

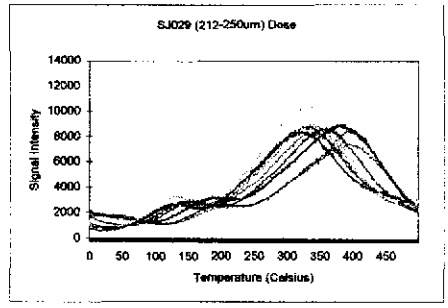
SJ029 (212-250um) Dose
Signal Intensity
Temperature (Celsius)

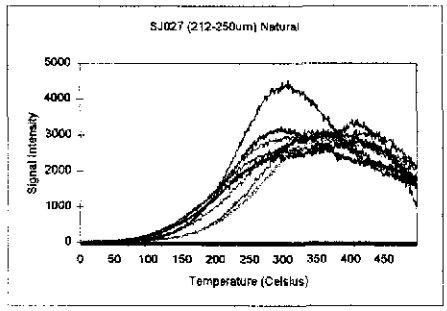
SJ027 (212-250um) Natural
Signal Intensity
Temperature (Celsius)

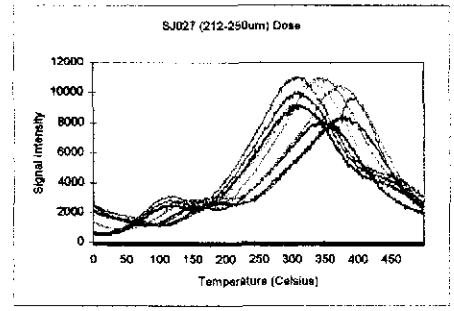
SJ027 (212-250um) Dose
Signal Intensity
Temperature (Celsius)

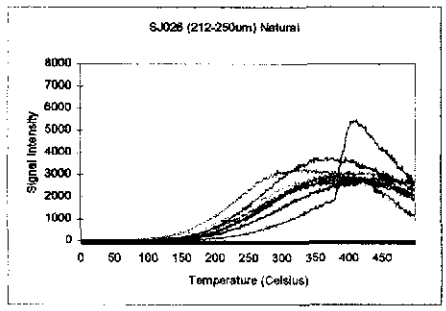
SJ028 (212-250um) Natural
Signal Intensity
Temperature (Celsius)

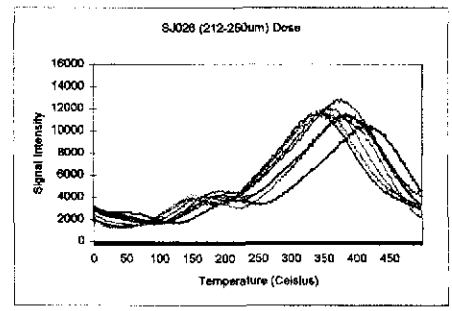
SJ028 (212-250um) Dose
Signal Intensity
Temperature (Celsius)

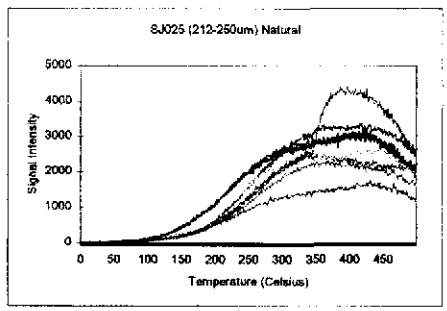
SJ025 (212-250um) Natural
Signal Intensity
Temperature (Celsius)

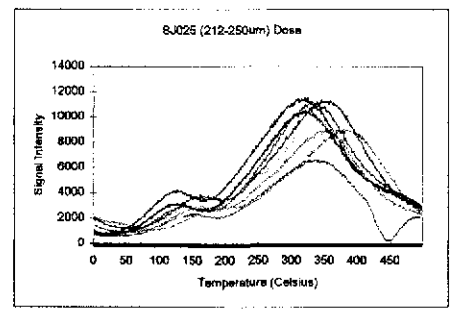
SJ025 (212-250um) Dose
Signal Intensity
Temperature (Celsius)

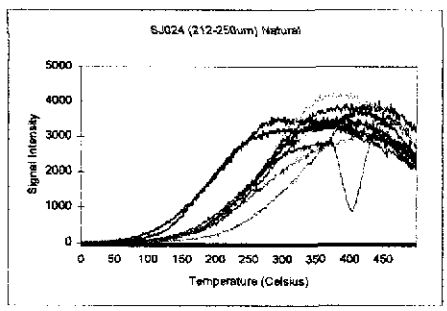
SJ024 (212-250um) Natural
Signal Intensity
Temperature (Celsius)

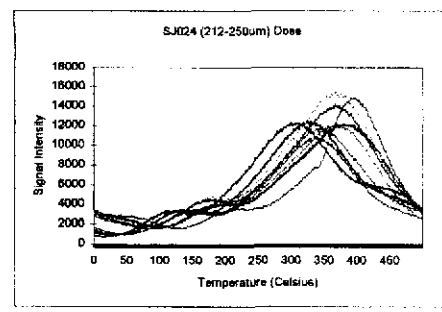
SJ024 (212-250um) Dose
Signal Intensity
Temperature (Celsius)

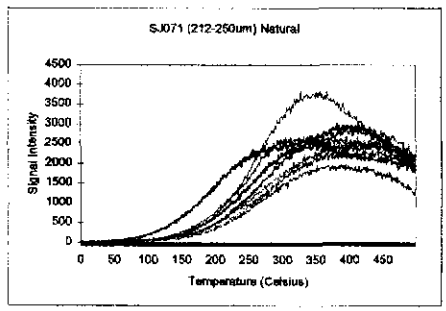
SJ071 (212-250um) Natural
Signal Intensity
Temperature (Celsius)

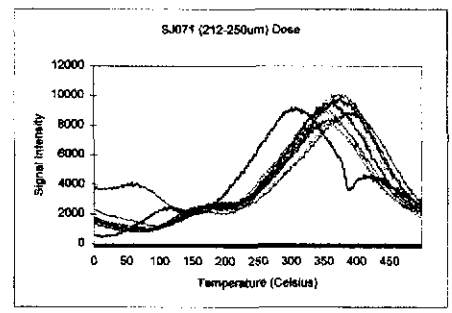
SJ071 (212-250um) Dose
Signal Intensity
Temperature (Celsius)

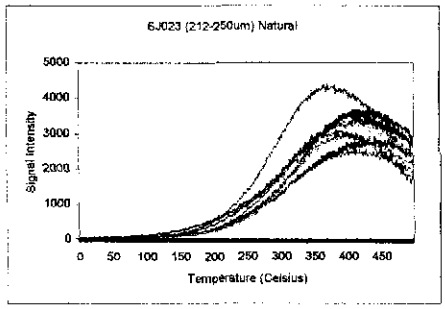
SJ023 (212-250um) Natural
Signal Intensity
Temperature (Celsius)

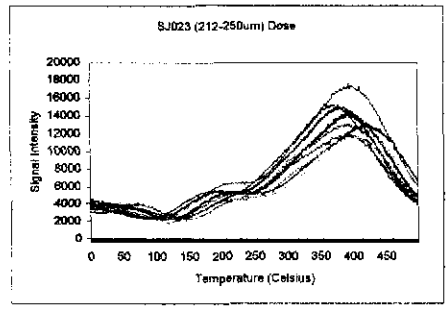
SJ023 (212-250um) Dose
Signal Intensity
Temperature (Celsius)

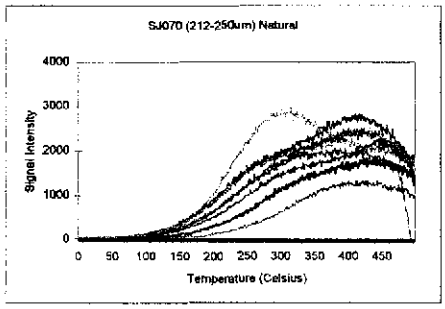
SJ070 (212-250um) Natural
Signal Intensity
Temperature (Celsius)

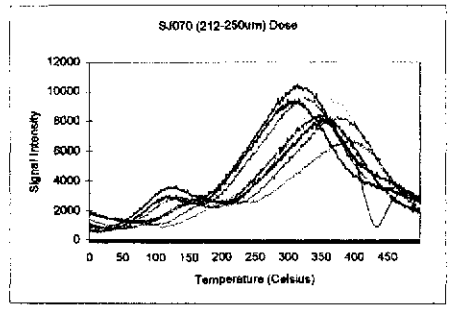
SJ070 (212-250um) Dose
Signal Intensity
Temperature (Celsius)

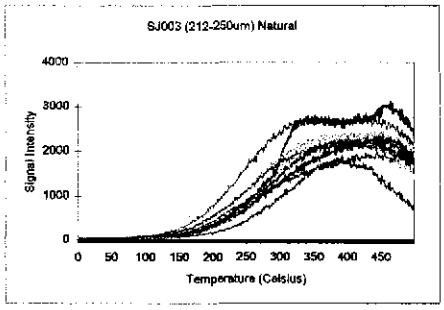
SJ003 (212-250um) Natural
Signal Intensity
Temperature (Celsius)

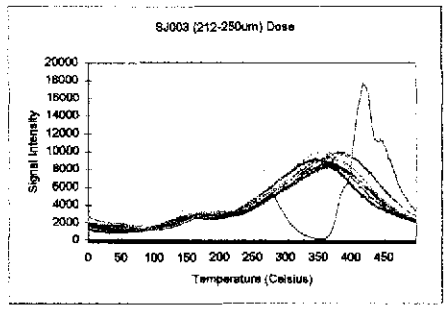
SJ003 (212-250um) Dose
Signal Intensity
Temperature (Celsius)

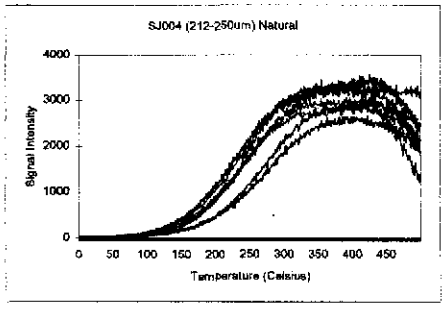
SJ004 (212-250um) Natural
Signal Intensity
Temperature (Celsius)

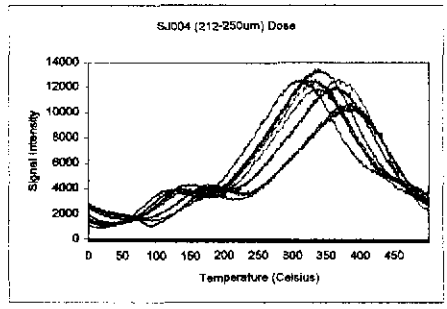
SJ004 (212-250um) Dose
Signal Intensity
Temperature (Celsius)

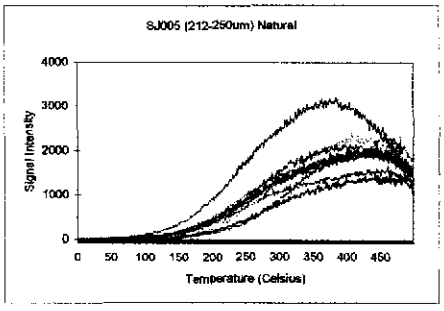
SJ005 (212-250um) Natural
Signal Intensity
Temperature (Celsius)

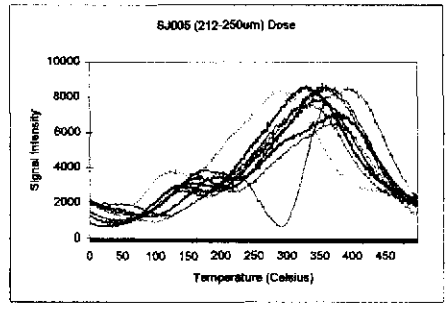
SJ005 (212-250um) Dose
Signal Intensity
Temperature (Celsius)

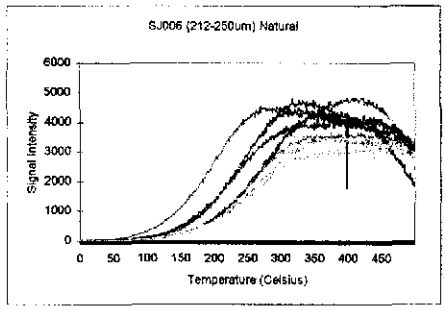
SJ006 (212-250um) Natural
Signal Intensity
Temperature (Celsius)

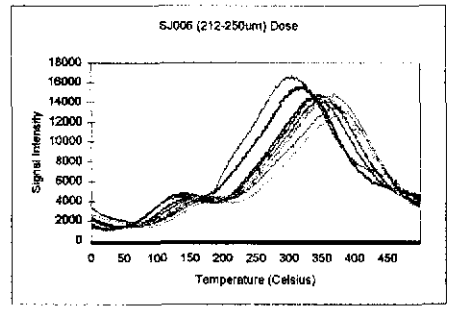
SJ006 (212-250um) Dose
Signal Intensity
Temperature (Celsius)

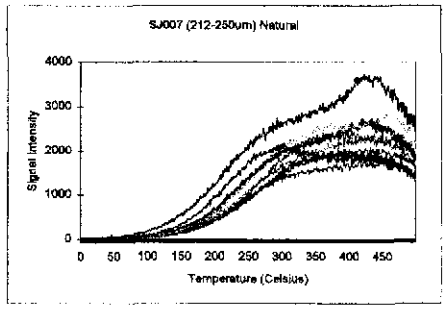
SJ007 (212-250um) Natural
Signal Intensity
Temperature (Celsius)

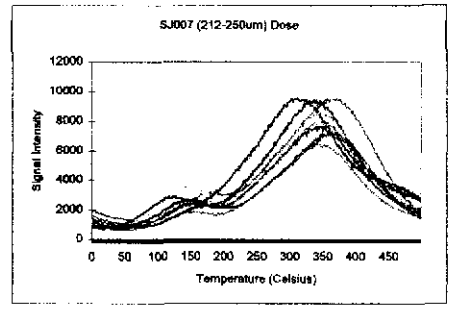
SJ007 (212-250um) Dose
Signal Intensity
Temperature (Celsius)

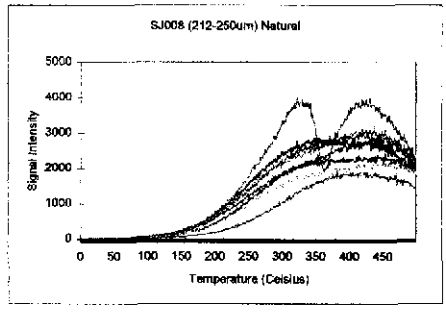
SJ008 (212-250um) Natural
Signal Intensity
Temperature (Celsius)

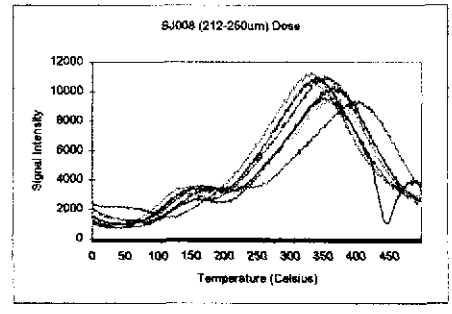
SJ008 (212-250um) Dose
Signal Intensity
Temperature (Celsius)

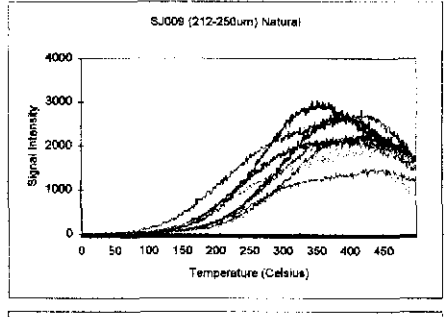
SJ009 (212-250um) Natural
Signal Intensity
Temperature (Celsius)

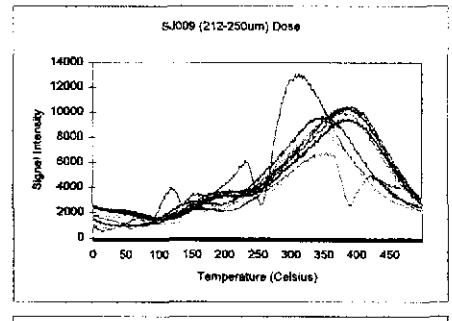
SJ009 (212-250um) Dose
Signal Intensity
Temperature (Celsius)

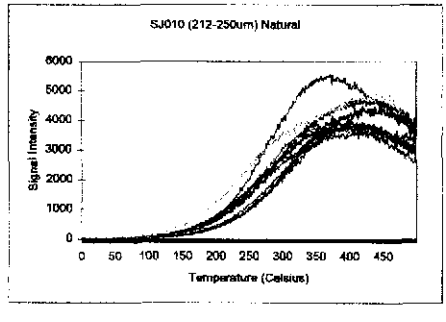
SJ010 (212-250um) Natural
Signal Intensity
Temperature (Celsius)

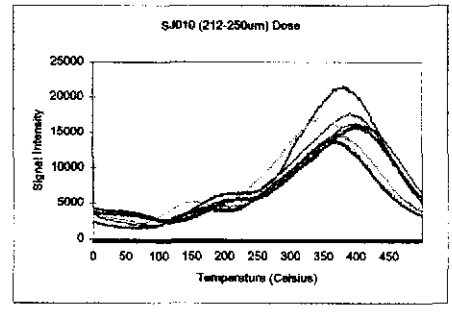
SJ010 (212-250um) Dose
Signal Intensity
Temperature (Celsius)

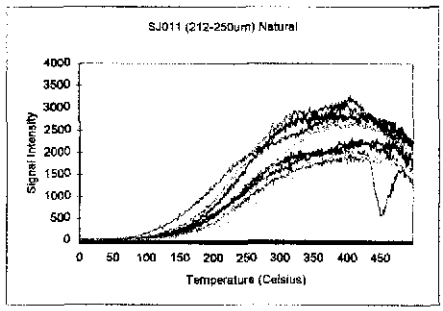
SJ011 (212-250um) Natural
Signal Intensity
Temperature (Celsius)

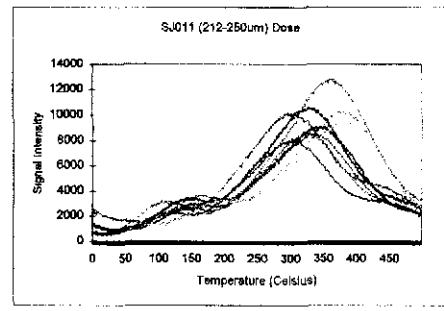
SJ011 (212-250um) Dose
Signal Intensity
Temperature (Celsius)

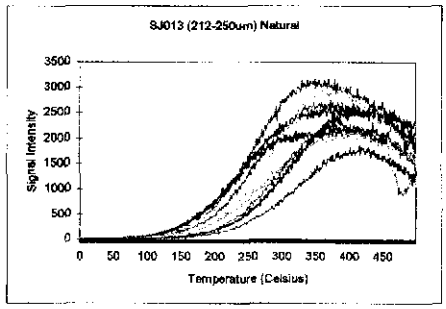
SJ013 (212-250um) Natural
Signal Intensity
Temperature (Celsius)

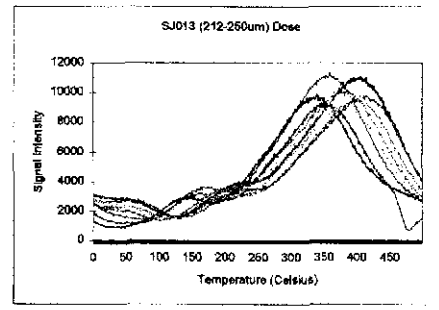
SJ013 (212-250um) Dose
Signal Intensity
Temperature (Celsius)

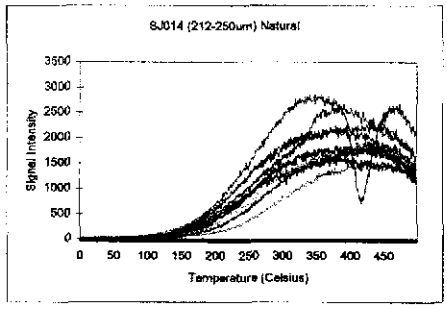
SJ014 (212-250um) Natural
Signal Intensity
Temperature (Celsius)

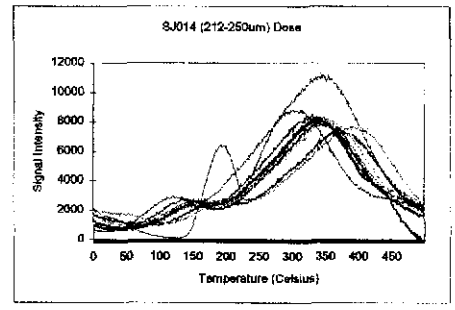
SJ014 (212-250um) Dose
Signal Intensity
Temperature (Celsius)

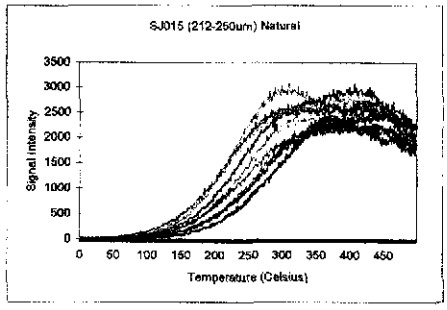
SJ015 (212-250um) Natural
Signal Intensity
Temperature (Celsius)

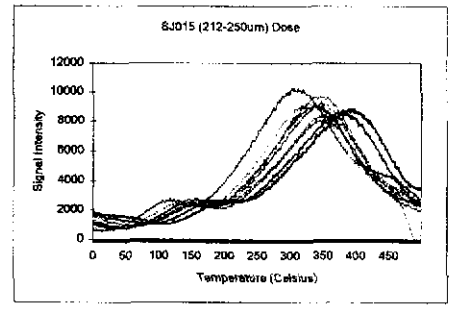
SJ015 (212-250um) Dose
Signal Intensity
Temperature (Celsius)

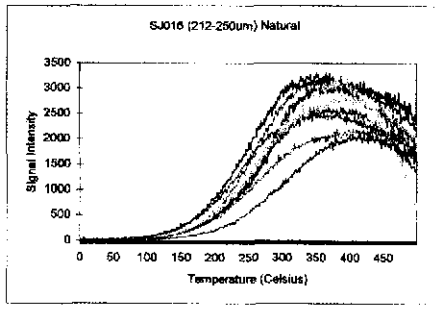
SJ016 (212-250um) Natural
Signal Intensity
Temperature (Celsius)

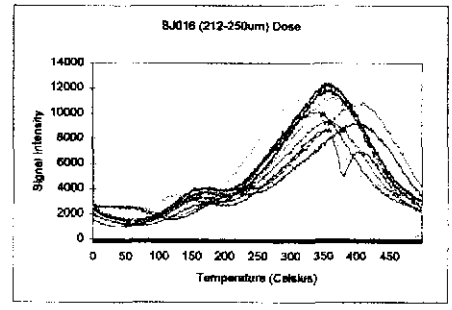
SJ016 (212-250um) Dose
Signal Intensity
Temperature (Celsius)

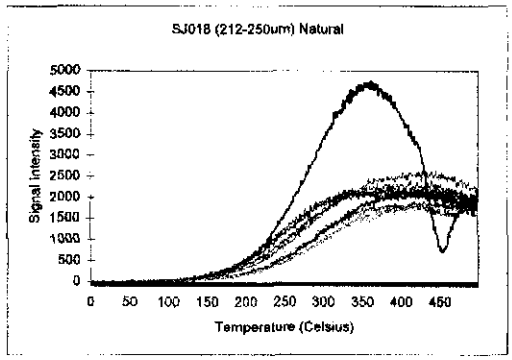
SJ018 (212-250um) Natural
Signal Intensity
5000
4500
4000
3500
3000
2500
2000
1500
1000
500
0
0 50 100 150 200 250 300 350 400 450
Temperature (Celsius)

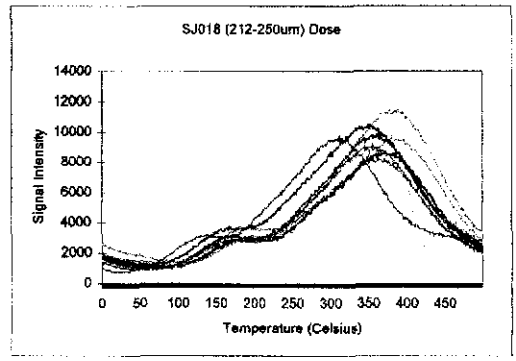
SJ018 (212-250um) Dose
Signal Intensity
14000
12000
10000
8000
6000
4000
2000
0
0 50 100 150 200 250 300 350 400 450
Temperature (Celsius)

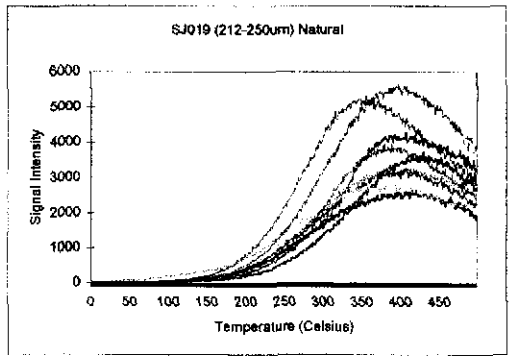
SJ019 (212-250um) Natural
Signal Intensity
6000
5000
4000
3000
2000
1000
0
0 50 100 150 200 250 300 350 400 450
Temperature (Celsius)

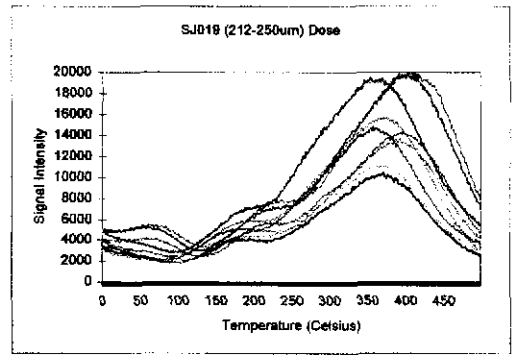
SJ019 (212-250um) Dose
Signal Intensity
20000
18000
16000
14000
12000
10000
8000
6000
4000
2000
0
0 50 100 150 200 250 300 350 400 450
Temperature (Celsius)

APPENDIX C- shifted TL curves

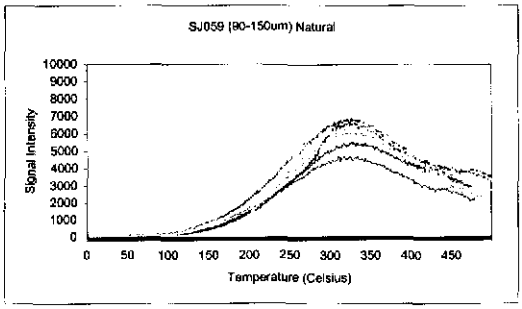
SJ059 (90-150um) Natural
Signal Intensity
Temperature (Celsius)

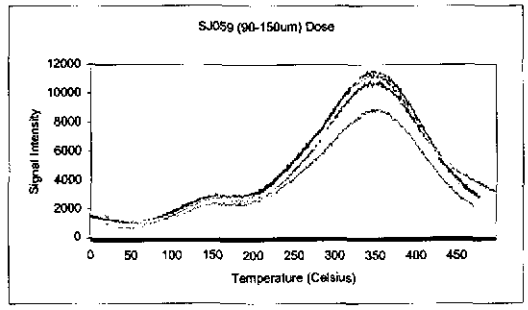
SJ059 (90-150um) Dose
Signal Intensity
Temperature (Celsius)

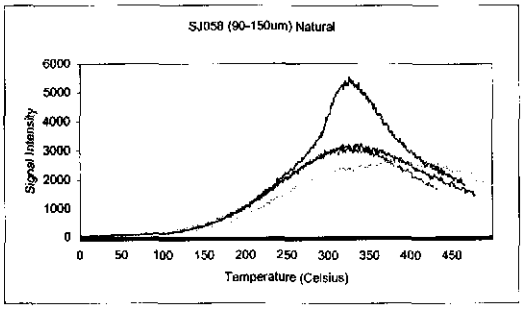
SJ058 (90-150um) Natural
Signal Intensity
Temperature (Celsius)

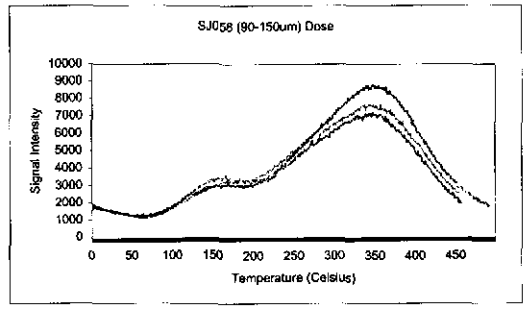
SJ058 (90-150um) Dose
Signal Intensity
Temperature (Celsius)

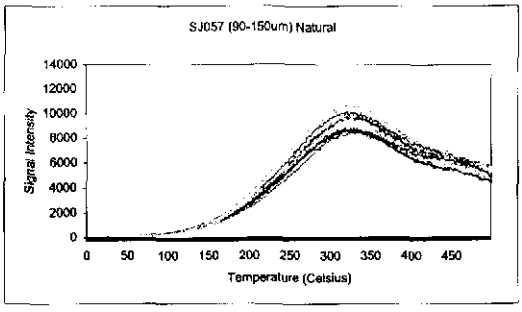
SJ057 (90-150um) Natural
Signal Intensity
Temperature (Celsius)

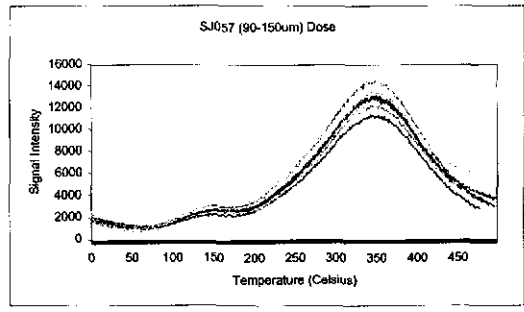
SJ057 (90-150um) Dose
Signal Intensity
Temperature (Celsius)

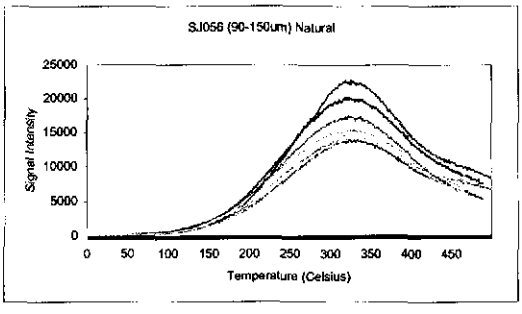
SJ056 (90-150um) Natural
Signal Intensity
Temperature (Celsius)

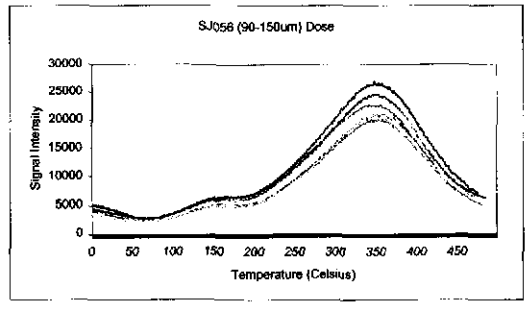
SJ056 (90-150um) Dose
Signal Intensity
Temperature (Celsius)

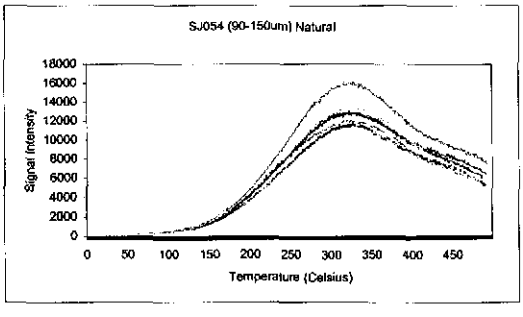
SJ054 (90-150um) Natural
Signal Intensity
Temperature (Celsius)

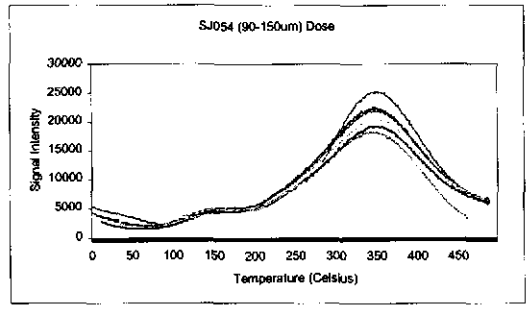
SJ054 (90-150um) Dose
Signal Intensity
Temperature (Celsius)

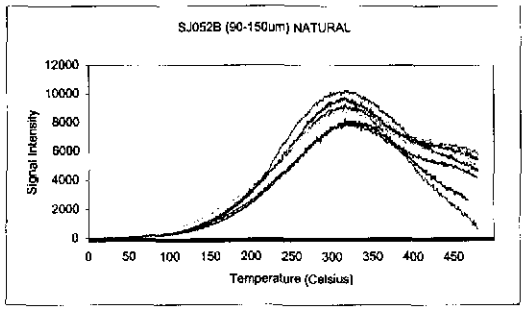
SJ052B (90-150um) NATURAL
Signal Intensity
Temperature (Celsius)

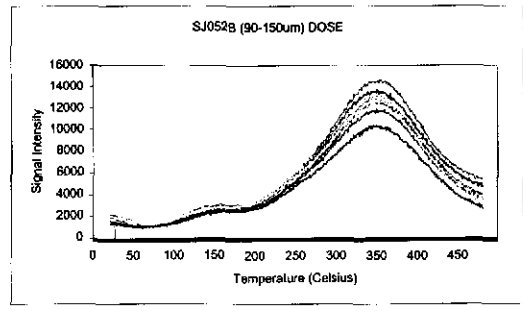
SJ052B (90-150um) DOSE
Signal Intensity
Temperature (Celsius)

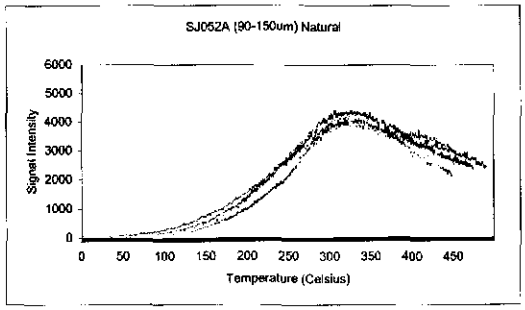
SJ052A (90-150um) Natural
Signal Intensity
Temperature (Celsius)

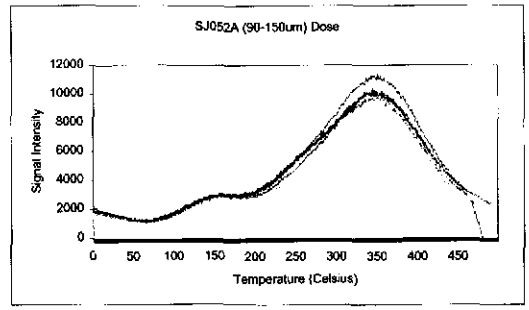
SJ052A (90-150um) Dose
Signal Intensity
Temperature (Celsius)

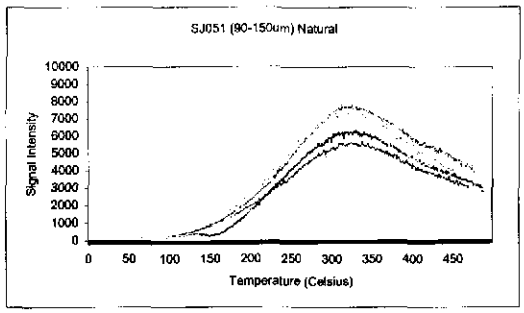
SJ051 (90-150um) Natural
Signal Intensity
Temperature (Celsius)

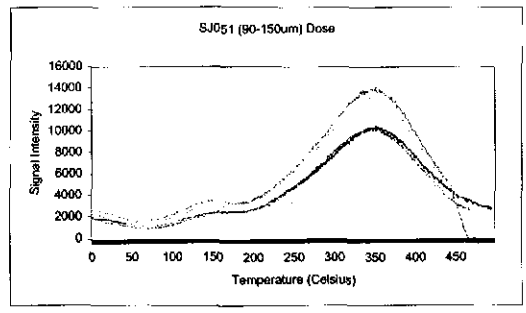
SJ051 (90-150um) Dose
Signal Intensity
Temperature (Celsius)

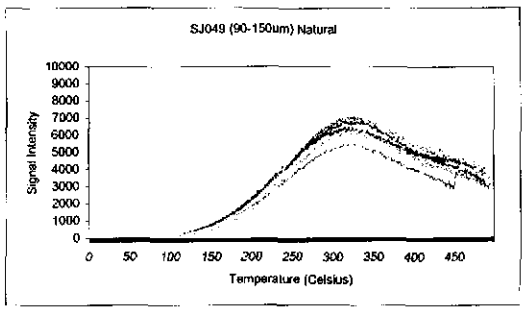
SJ049 (90-150um) Natural
Signal Intensity
Temperature (Celsius)

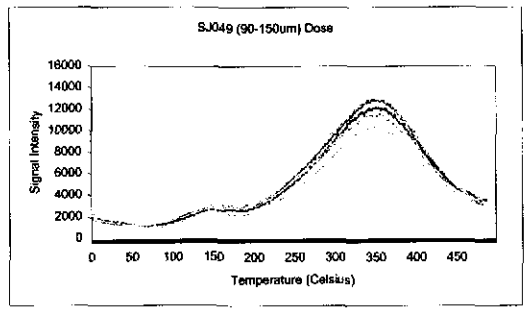
SJ049 (90-150um) Dose
Signal Intensity
Temperature (Celsius)

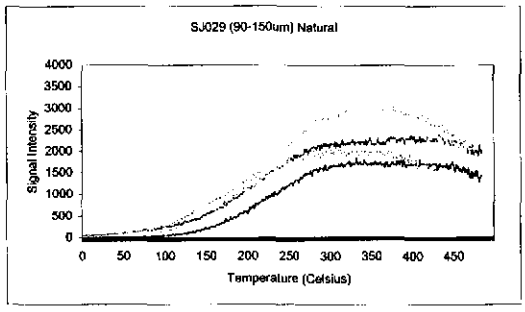
SJ029 (90-150um) Natural
Signal Intensity
Temperature (Celsius)

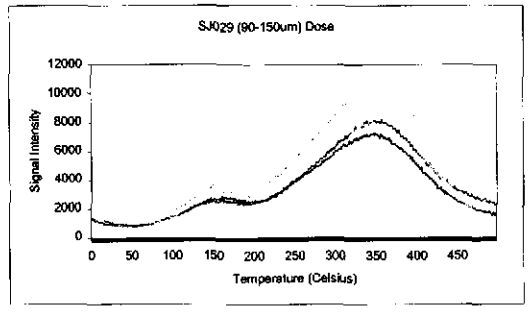
SJ029 (90-150um) Dose
Signal Intensity
Temperature (Celsius)

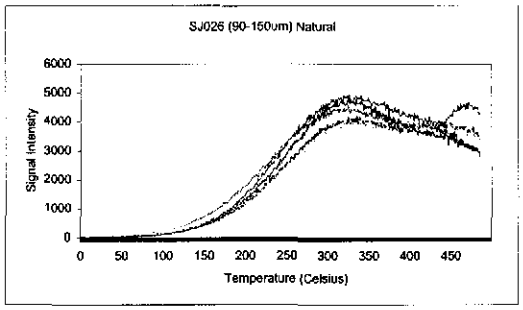
SJ026 (90-150um) Natural
Signal Intensity
Temperature (Celsius)

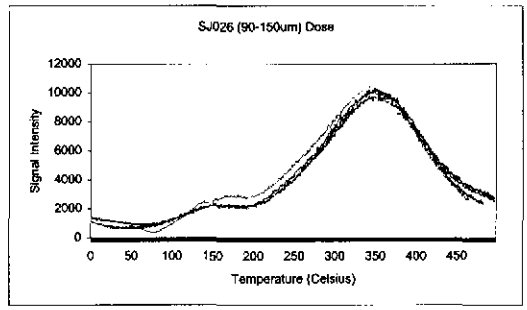
SJ026 (90-150um) Dose
Signal Intensity
Temperature (Celsius)

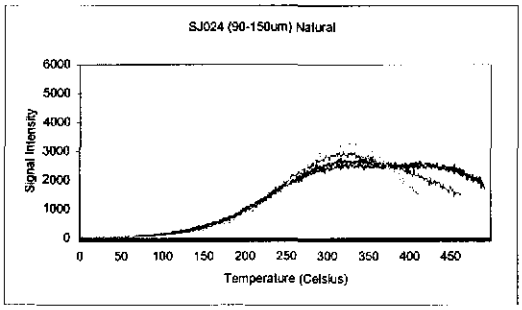
SJ024 (90-150um) Natural
Signal Intensity
Temperature (Celsius)

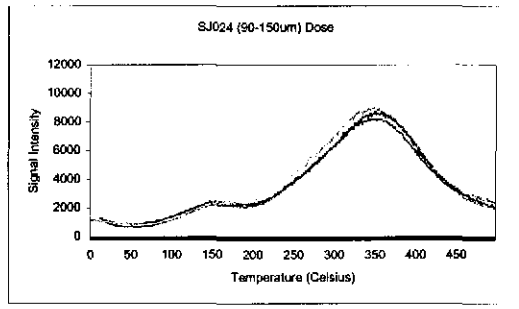
SJ024 (90-150um) Dose
Signal Intensity
Temperature (Celsius)

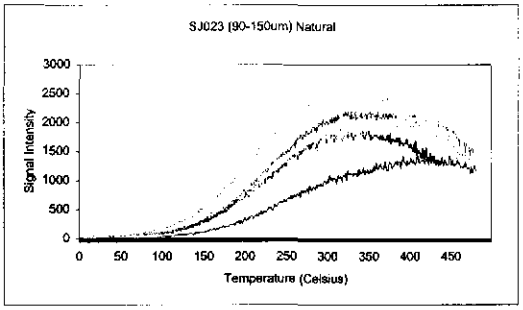
SJ023 (90-150um) Natural
Signal Intensity
Temperature (Celsius)

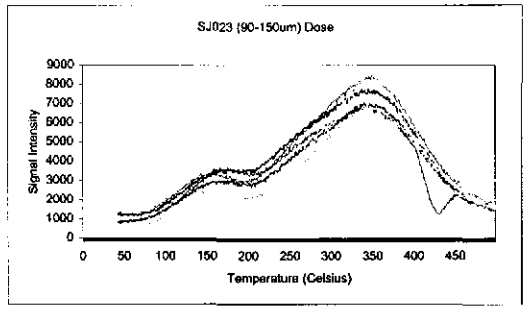
SJ023 (90-150um) Dose
Signal Intensity
Temperature (Celsius)

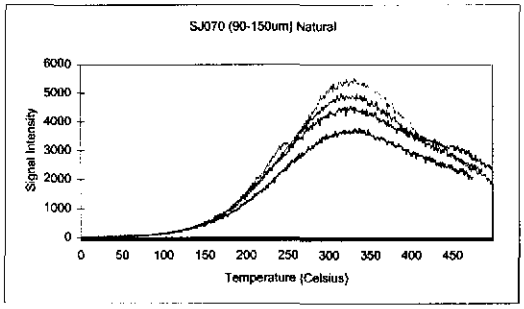
SJ070 (90-150um) Natural
Signal Intensity
Temperature (Celsius)

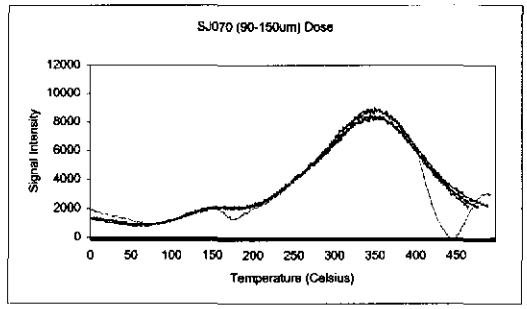
SJ070 (90-150um) Dose
Signal Intensity
Temperature (Celsius)

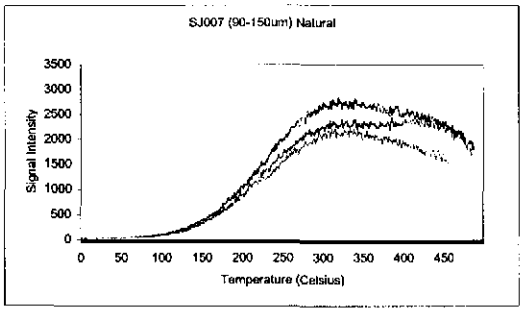
SJ007 (90-150um) Natural
Signal Intensity
Temperature (Celsius)

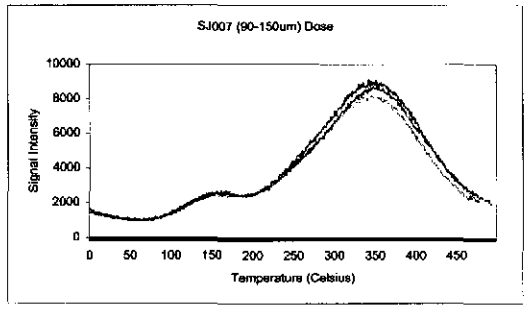
SJ007 (90-150um) Dose
Signal Intensity
Temperature (Celsius)

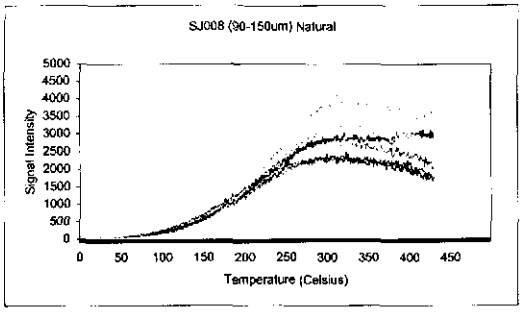
SJ008 (90-150um) Natural
Signal Intensity
Temperature (Celsius)

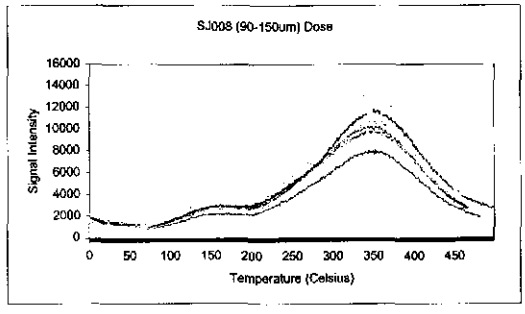
SJ008 (90-150um) Dose
Signal Intensity
Temperature (Celsius)

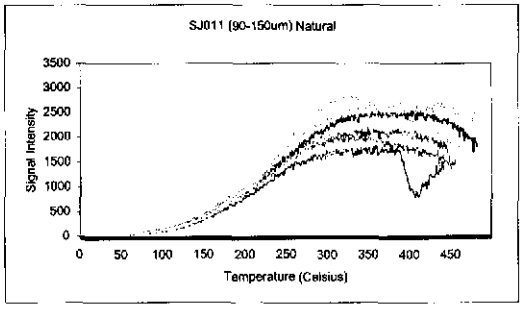
SJ011 (90-150um) Natural
Signal Intensity
Temperature (Celsius)

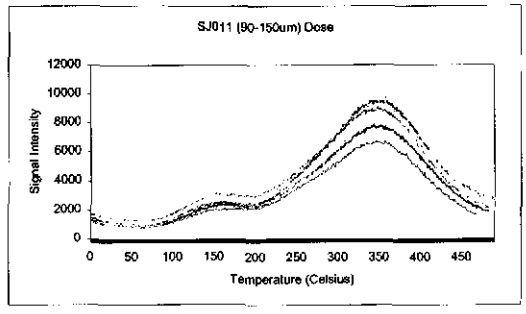
SJ011 (90-150um) Dose
Signal Intensity
Temperature (Celsius)

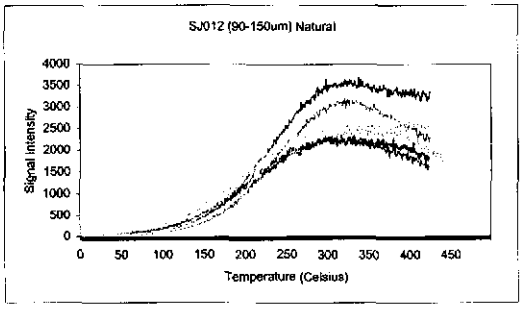
SJ012 (90-150um) Natural
Signal Intensity
Temperature (Celsius)

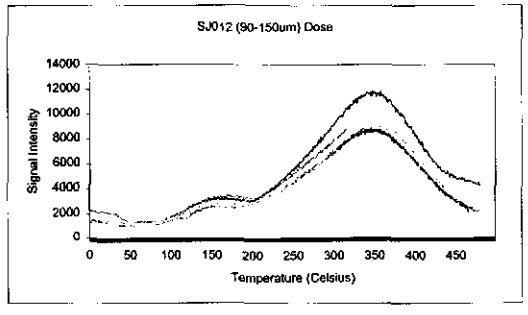
SJ012 (90-150um) Dose
Signal Intensity
Temperature (Celsius)

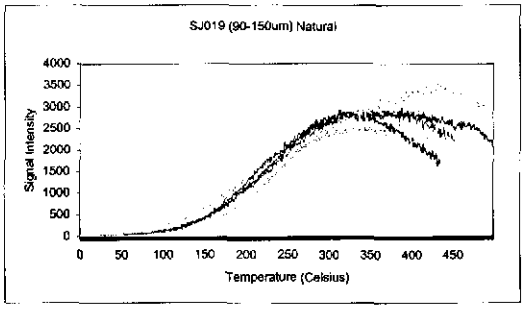
SJ019 (90-150um) Natural
Signal Intensity
Temperature (Celsius)

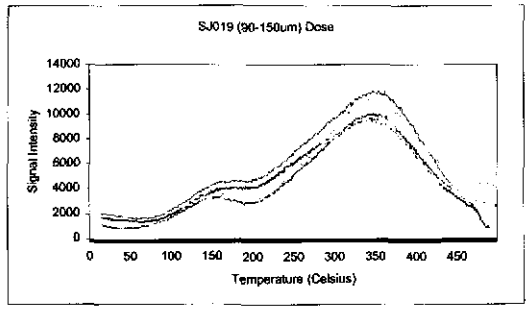
SJ019 (90-150um) Dose
Signal Intensity
Temperature (Celsius)

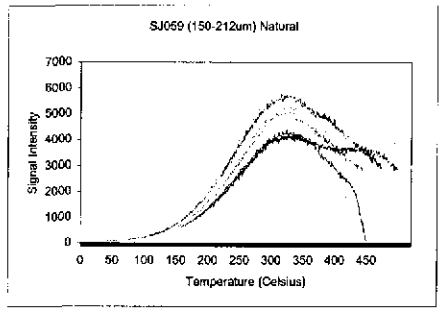
SJ059 (150-212um) Natural
Signal Intensity
Temperature (Celsius)

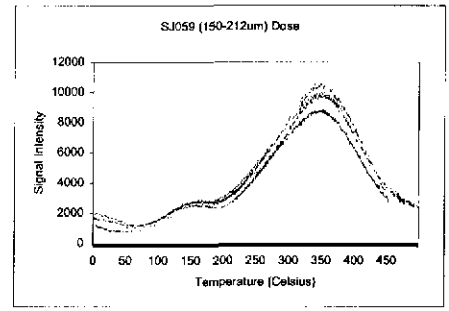
SJ059 (150-212um) Dose
Signal Intensity
Temperature (Celsius)

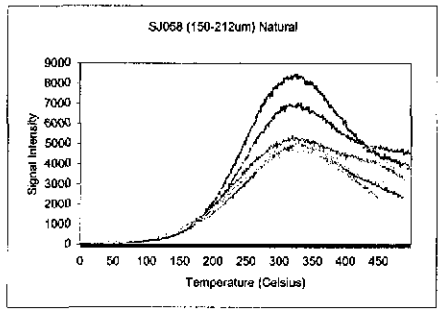
SJ058 (150-212um) Natural
Signal Intensity
Temperature (Celsius)

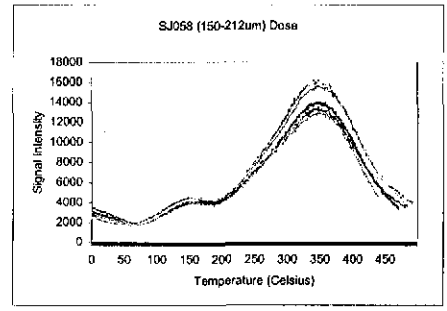
SJ058 (150-212um) Dose
Signal Intensity
Temperature (Celsius)

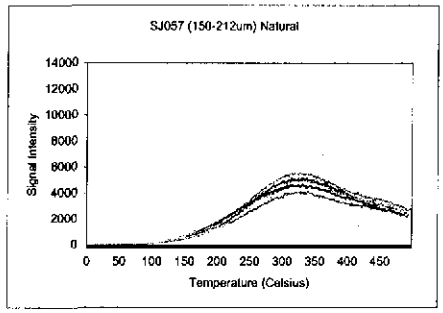
SJ057 (150-212um) Natural
Signal Intensity
Temperature (Celsius)

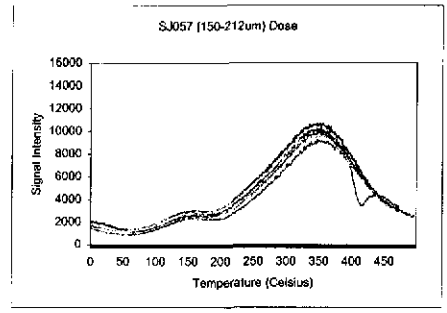
SJ057 (150-212um) Dose
Signal Intensity
Temperature (Celsius)

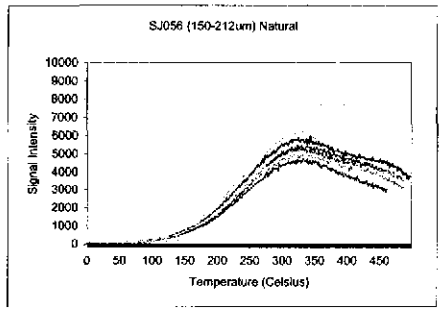
SJ056 (150-212um) Natural
Signal Intensity
Temperature (Celsius)

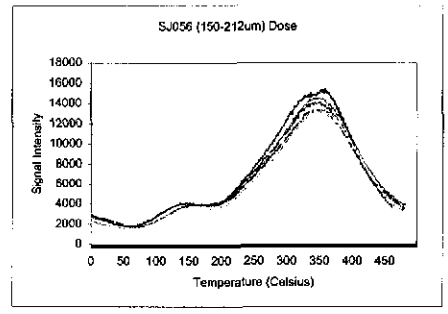
SJ056 (150-212um) Dose
Signal Intensity
Temperature (Celsius)

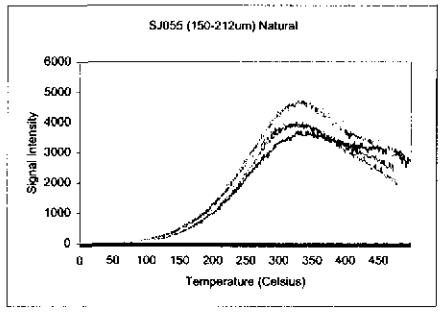
SJ055 (150-212um) Natural
Signal Intensity
Temperature (Celsius)

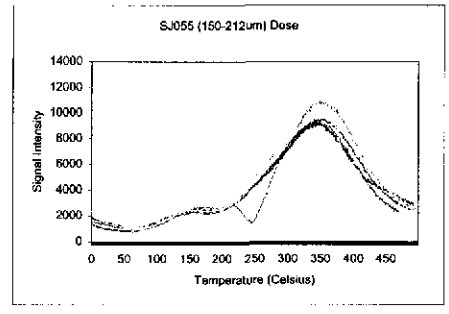
SJ055 (150-212um) Dose
Signal Intensity
Temperature (Celsius)

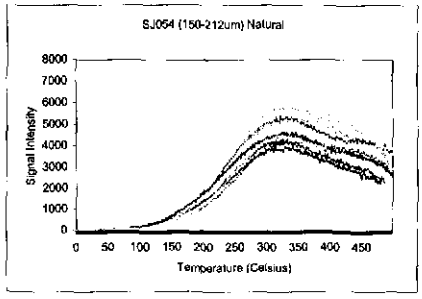
SJ054 (150-212um) Natural
Signal Intensity
Temperature (Celsius)

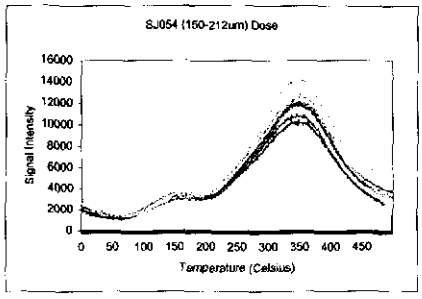
SJ054 (150-212um) Dose
Signal Intensity
Temperature (Celsius)

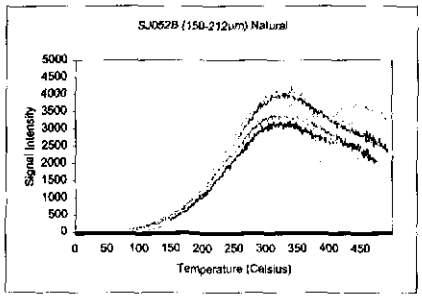
SJ052B (150-212um) Natural
Signal Intensity
Temperature (Celsius)

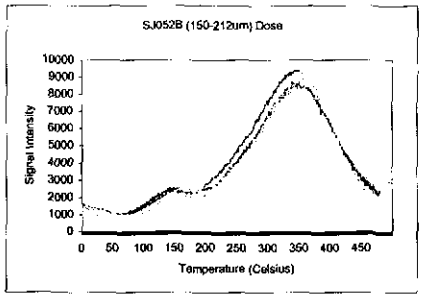
SJ052B (150-212um) Dose
Signal Intensity
Temperature (Celsius)

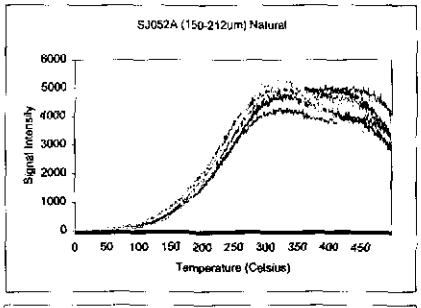
SJ052A (150-212um) Natural
Signal Intensity
Temperature (Celsius)

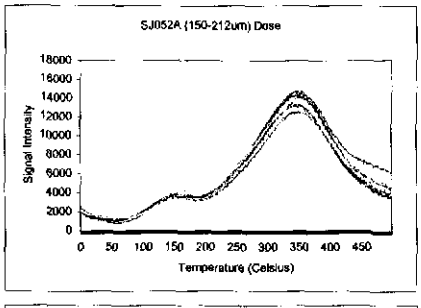
SJ052A (150-212um) Dose
Signal Intensity
Temperature (Celsius)

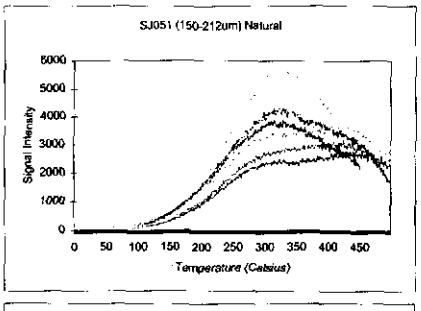
SJ051 (150-212um) Natural
Signal Intensity
Temperature (Celsius)

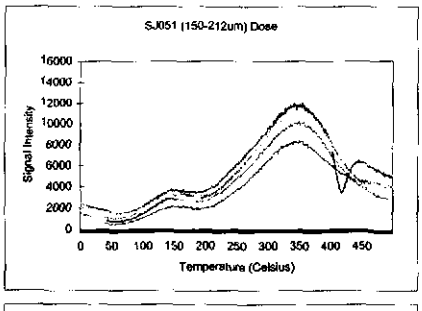
SJ051 (150-212um) Dose
Signal Intensity
Temperature (Celsius)

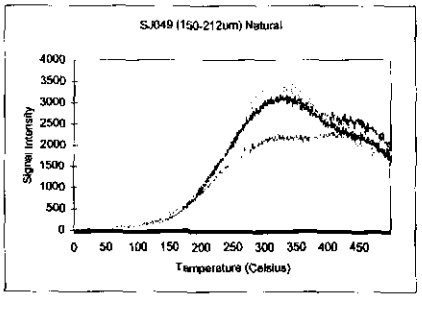
SJ049 (150-212um) Natural
Signal Intensity
Temperature (Celsius)

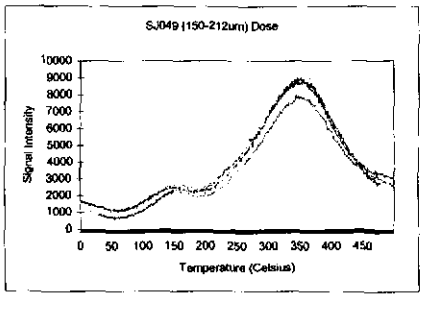
SJ049 (150-212um) Dose
Signal Intensity
Temperature (Celsius)

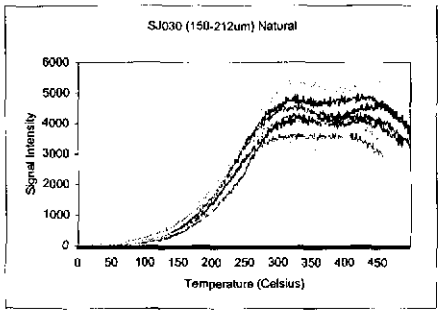
SJ030 (150-212um) Natural
Signal Intensity
Temperature (Celsius)

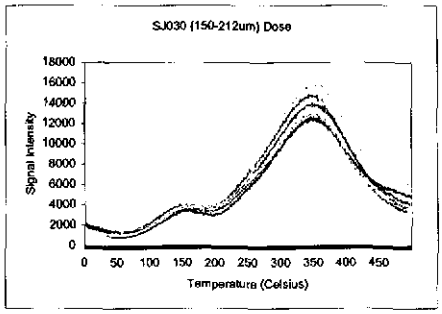
SJ030 (150-212um) Dose
Signal Intensity
Temperature (Celsius)

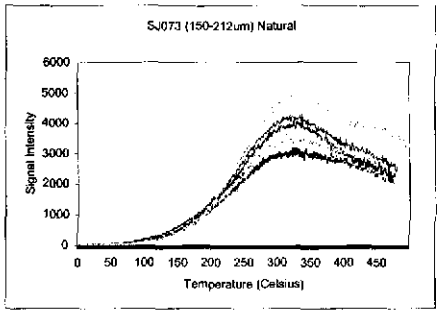
SJ073 (150-212um) Natural
Signal Intensity
Temperature (Celsius)

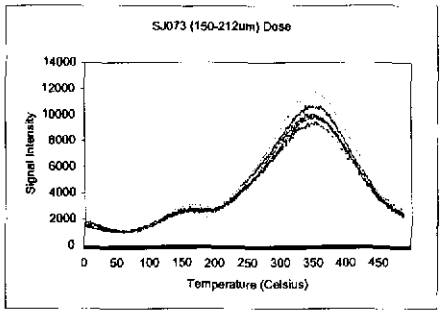
SJ073 (150-212um) Dose
Signal Intensity
Temperature (Celsius)

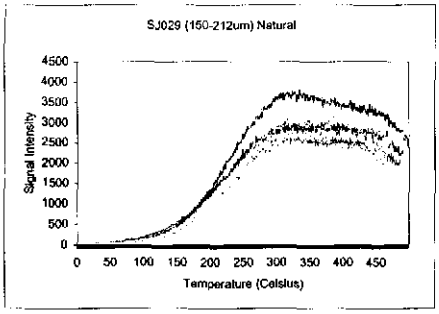
SJ029 (150-212um) Natural
Signal Intensity
Temperature (Celsius)

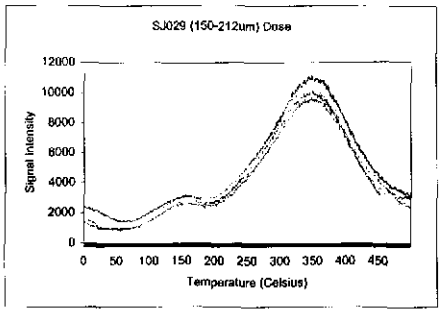
SJ029 (150-212um) Dose
Signal Intensity
Temperature (Celsius)

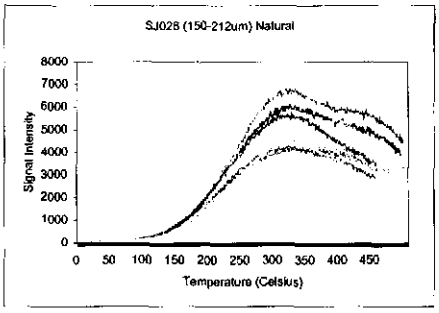
SJ028 (150-212um) Natural
Signal Intensity
Temperature (Celsius)

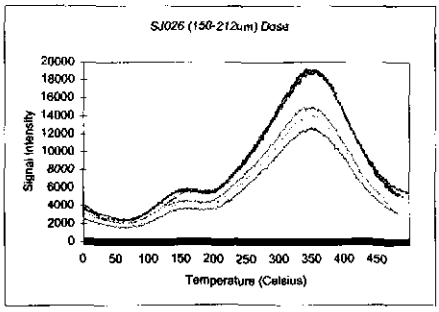
SJ026 (150-212um) Dose
Signal Intensity
Temperature (Celsius)

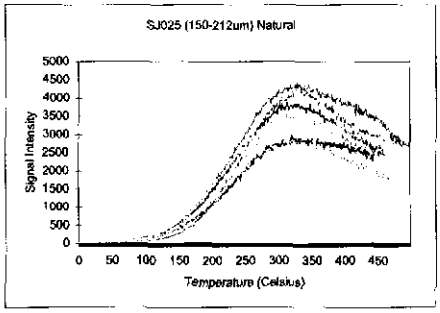
SJ025 (150-212um) Natural
Signal Intensity
Temperature (Celsius)

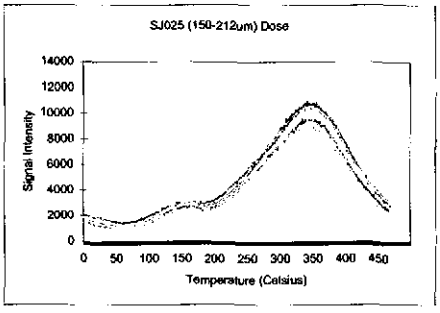
SJ025 (150-212um) Dose
Signal Intensity
Temperature (Celsius)

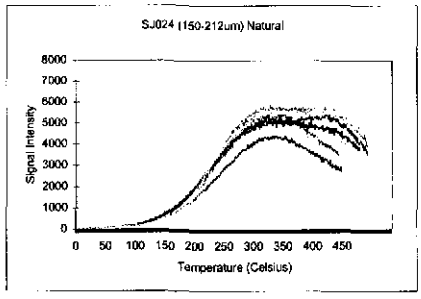
SJ024 (150-212um) Natural
Signal Intensity
Temperature (Celsius)

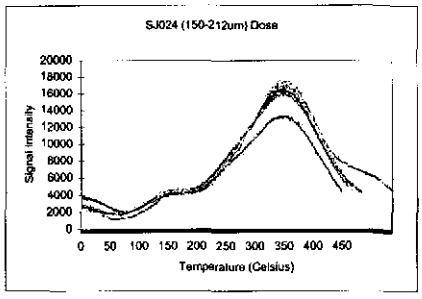
SJ024 (150-212um) Dose
Signal Intensity
Temperature (Celsius)

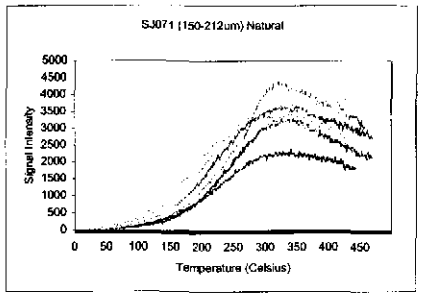
SJ071 (150-212um) Natural
Signal Intensity
Temperature (Celsius)

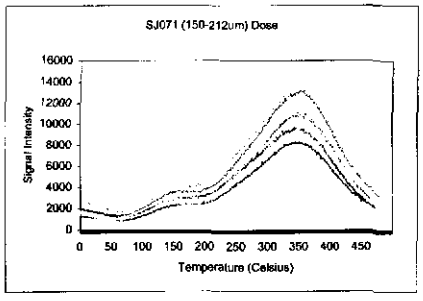
SJ071 (150-212um) Dose
Signal Intensity
Temperature (Celsius)

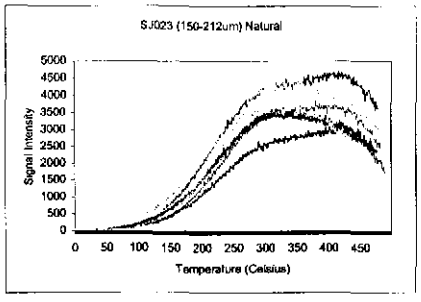
SJ023 (150-212um) Natural
Signal Intensity
Temperature (Celsius)

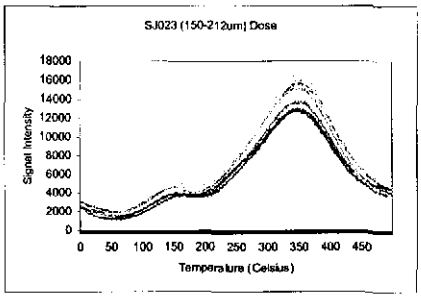
SJ023 (150-212um) Dose
Signal Intensity
Temperature (Celsius)

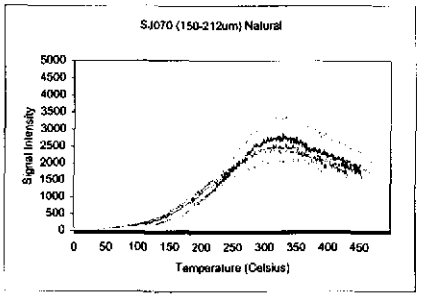
SJ070 (150-212um) Natural
Signal Intensity
Temperature (Celsius)

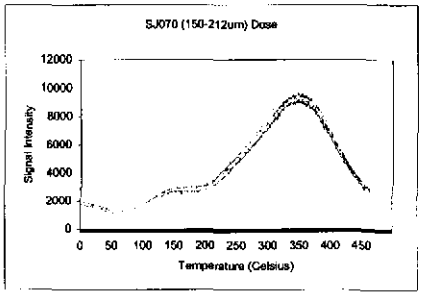
SJ070 (150-212um) Dose
Signal Intensity
Temperature (Celsius)

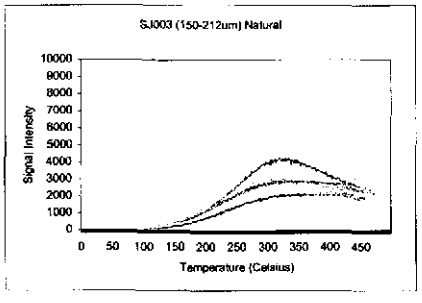
SJ003 (150-212um) Natural
Signal Intensity
Temperature (Celsius)

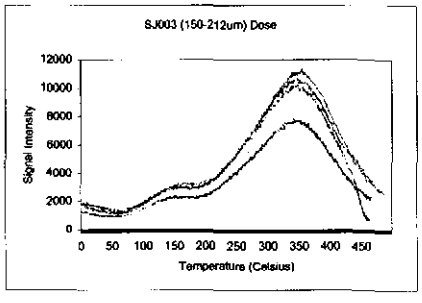
SJ003 (150-212um) Dose
Signal Intensity
Temperature (Celsius)

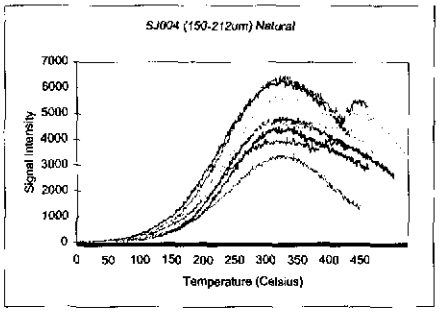
SJ004 (150-212um) Natural
Signal Intensity
Temperature (Celsius)

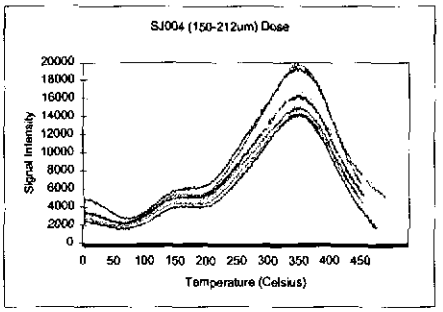
SJ004 (150-212um) Dose
Signal Intensity
Temperature (Celsius)

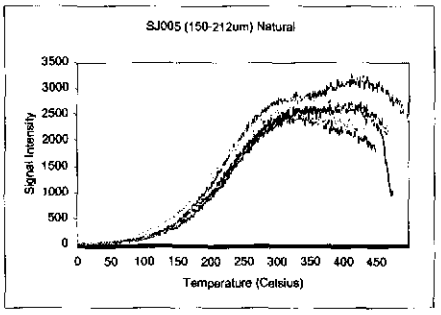
SJ005 (150-212um) Natural
Signal Intensity
Temperature (Celsius)

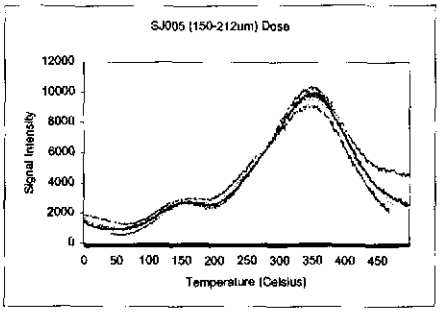
SJ005 (150-212um) Dose
Signal Intensity
Temperature (Celsius)

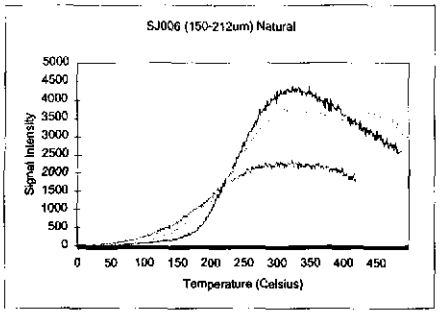
SJ006 (150-212um) Natural
Signal Intensity
Temperature (Celsius)

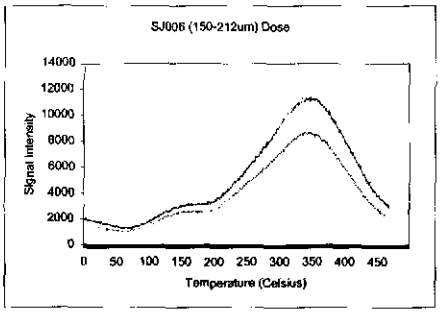
SJ006 (150-212um) Dose
Signal Intensity
Temperature (Celsius)

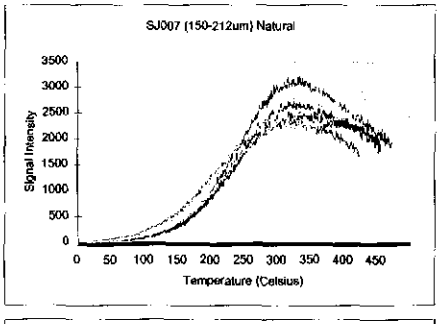
SJ007 (150-212um) Natural
Signal Intensity
Temperature (Celsius)

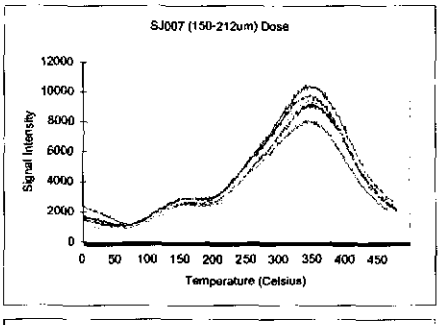
SJ007 (150-212um) Dose
Signal Intensity
Temperature (Celsius)

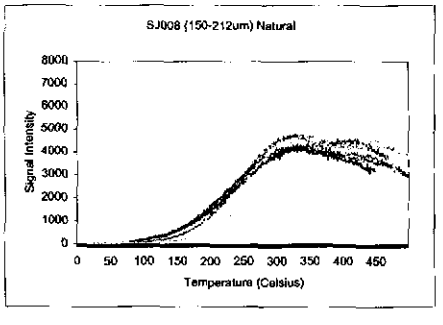
SJ008 (150-212um) Natural
Signal Intensity
Temperature (Celsius)

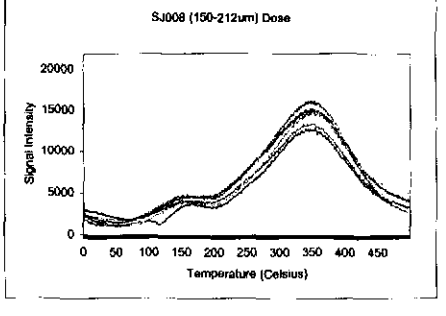
SJ008 (150-212um) Dose
Signal Intensity
Temperature (Celsius)

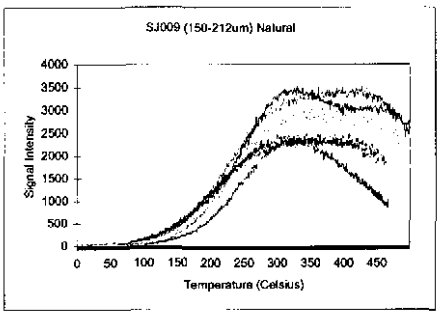
SJ009 (150-212um) Natural
Signal Intensity
Temperature (Celsius)

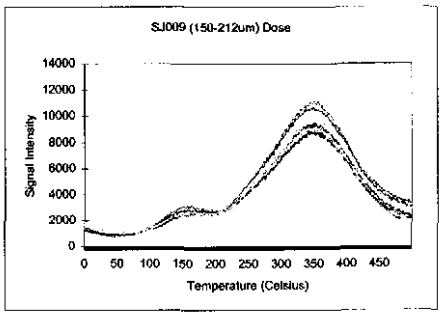
SJ009 (150-212um) Dose
Signal Intensity
Temperature (Celsius)

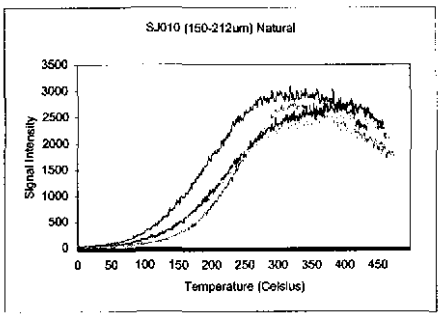
SJ010 (150-212um) Natural
Signal Intensity
Temperature (Celsius)

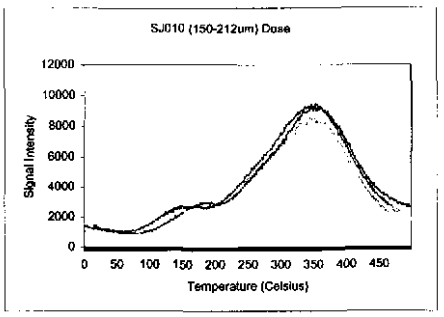
SJ010 (150-212um) Dose
Signal Intensity
Temperature (Celsius)

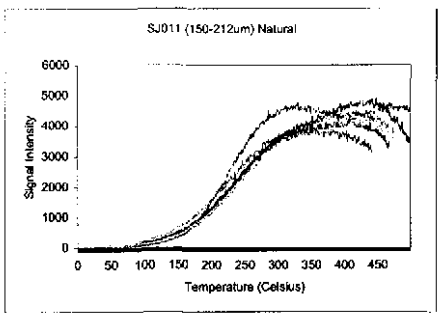
SJ011 (150-212um) Natural
Signal Intensity
Temperature (Celsius)

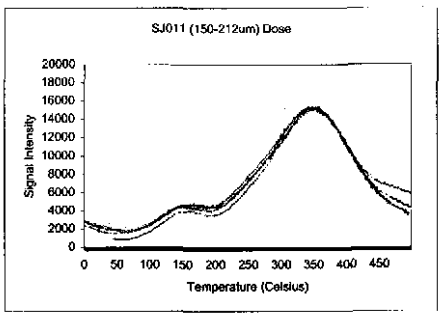
SJ011 (150-212um) Dose
Signal Intensity
Temperature (Celsius)

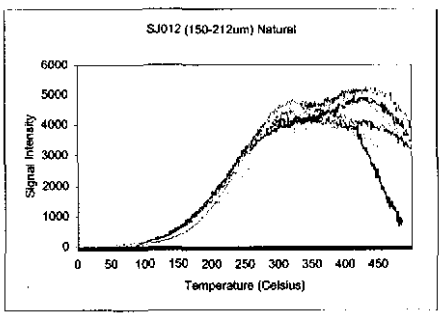
SJ012 (150-212um) Natural
Signal Intensity
Temperature (Celsius)

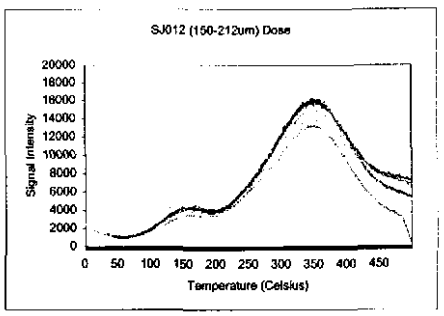
SJ012 (150-212um) Dose
Signal Intensity
Temperature (Celsius)

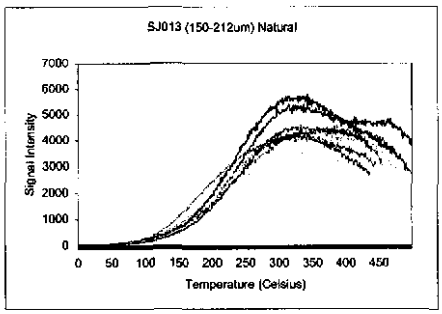
SJ013 (150-212um) Natural
Signal Intensity
Temperature (Celsius)

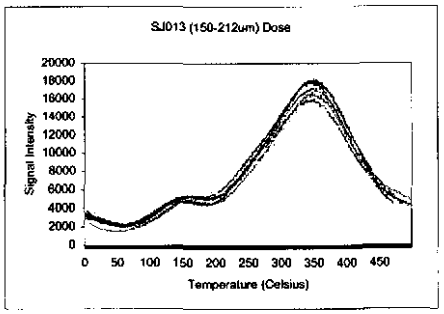
SJ013 (150-212um) Dose
Signal Intensity
Temperature (Celsius)

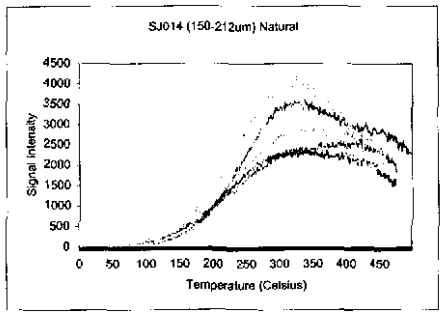
SJ014 (150-212um) Natural
Signal Intensity
Temperature (Celsius)

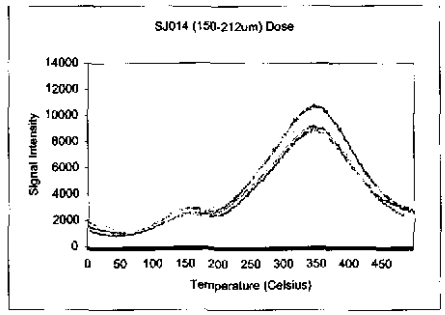
SJ014 (150-212um) Dose
Signal Intensity
Temperature (Celsius)

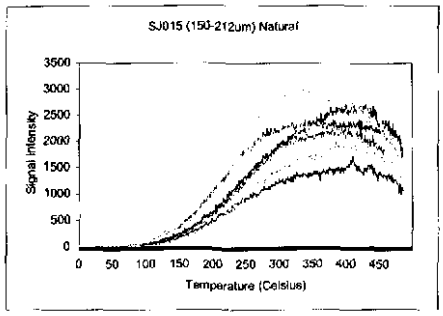
SJ015 (150-212um) Natural
Signal Intensity
Temperature (Celsius)

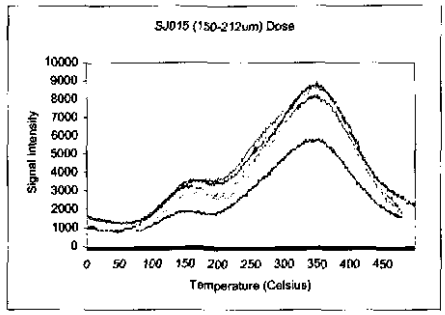
SJ015 (150-212um) Dose
Signal Intensity
Temperature (Celsius)

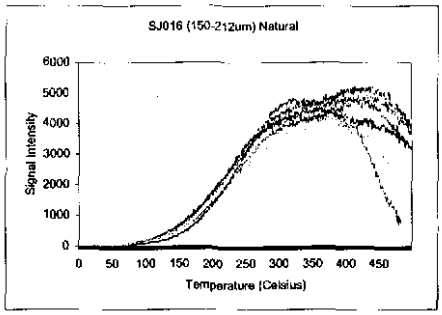
SJ016 (150-212um) Natural
Signal Intensity
Temperature (Celsius)

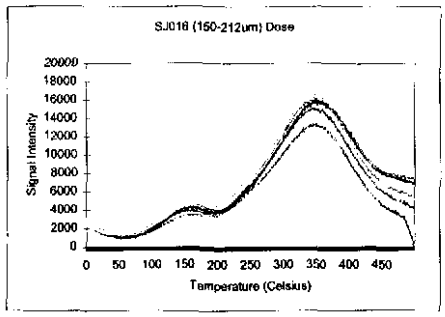
SJ018 (150-212um) Dose
Signal Intensity
Temperature (Celsius)

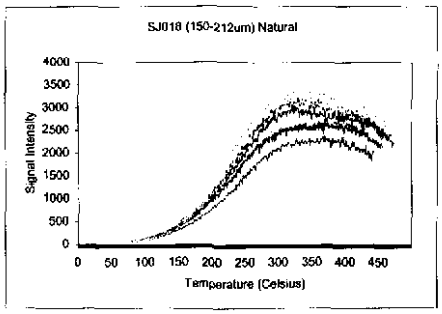
SJ018 (150-212um) Natural
Signal Intensity
Temperature (Celsius)

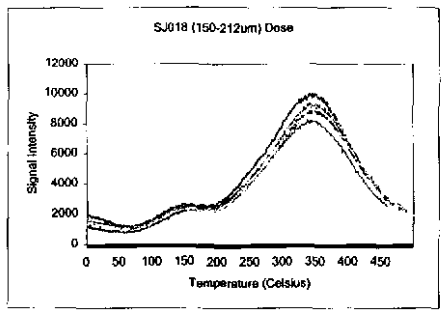
SJ018 (150-212um) Dose
Signal Intensity
Temperature (Celsius)

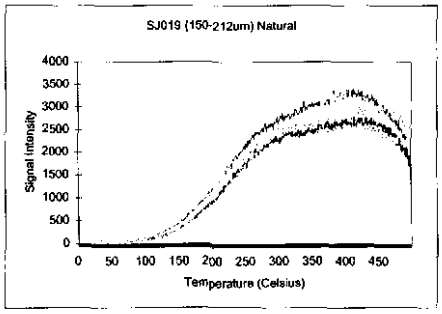
SJ019 (150-212um) Natural
Signal Intensity
Temperature (Celsius)

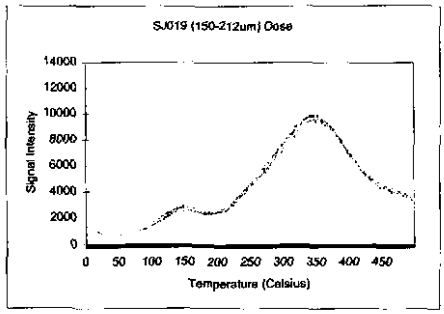
SJ019 (150-212um) Dose
Signal Intensity
Temperature (Celsius)

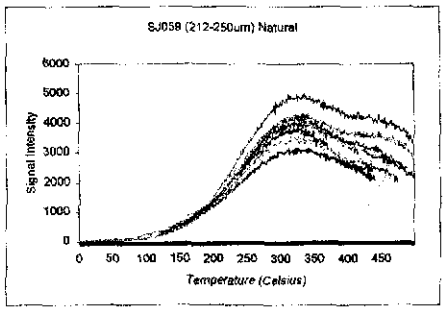
SJ059 (212-250um) Natural
Signal Intensity
Temperature (Celsius)

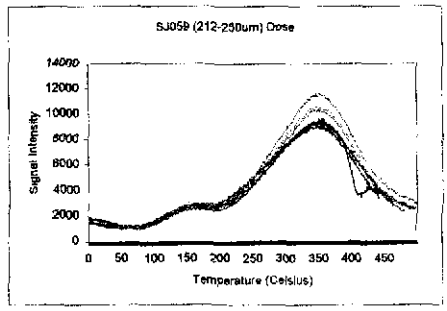
SJ059 (212-250um) Dose
Signal Intensity
Temperature (Celsius)

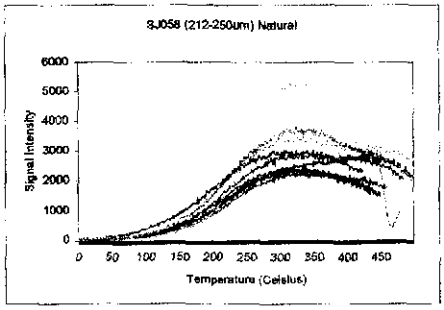
SJ058 (212-250um) Natural
Signal Intensity
Temperature (Celsius)

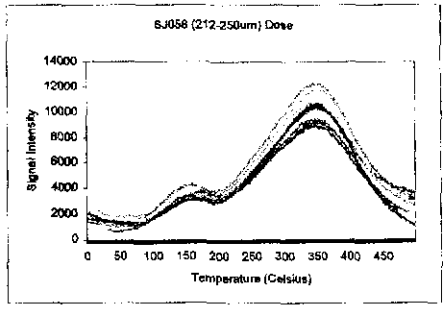
SJ058 (212-250um) Dose
Signal Intensity
Temperature (Celsius)

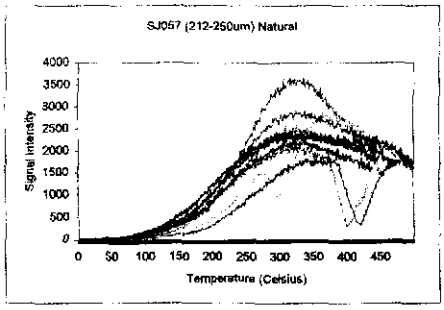
SJ057 (212-250um) Natural
Signal Intensity
Temperature (Celsius)

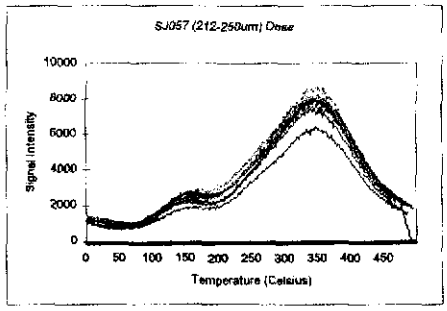
SJ057 (212-250um) Dose
Signal Intensity
Temperature (Celsius)

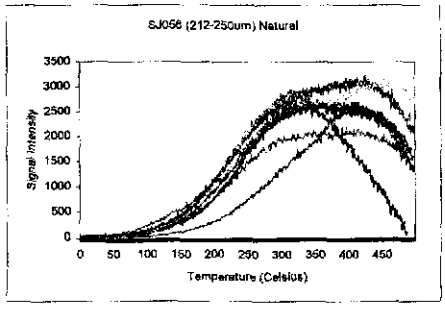
SJ056 (212-250um) Natural
Signal Intensity
Temperature (Celsius)

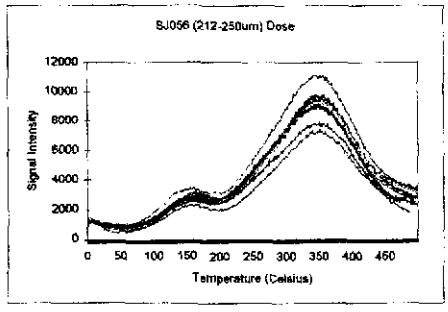
SJ056 (212-250um) Dose
Signal Intensity
Temperature (Celsius)

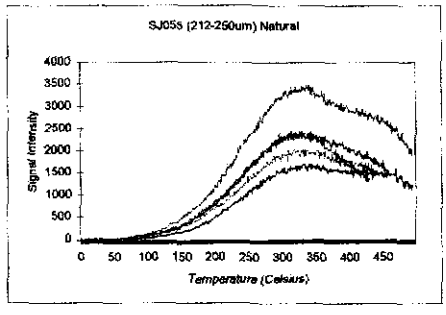
SJ055 (212-250um) Natural
Signal Intensity
Temperature (Celsius)

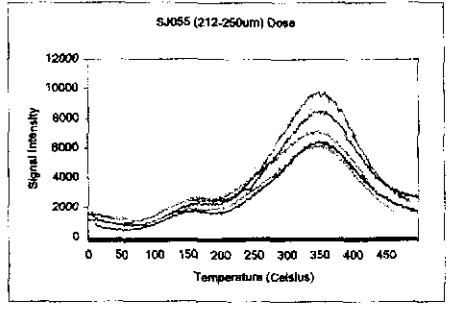
SJ055 (212-250um) Dose
Signal Intensity
Temperature (Celsius)

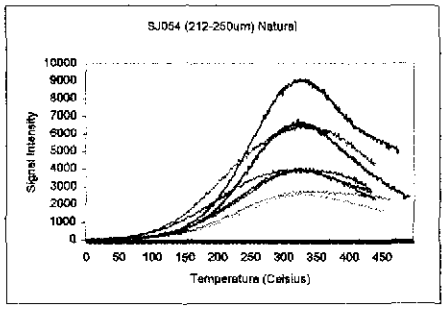
SJ054 (212-250um) Natural
Signal Intensity
Temperature (Celsius)

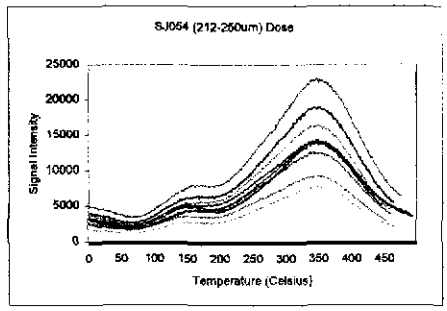
SJ054 (212-250um) Dose
Signal Intensity
Temperature (Celsius)

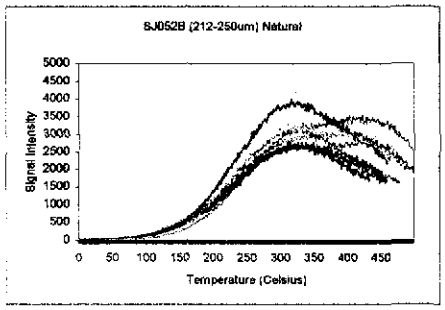
SJ052B (212-250um) Natural
Signal Intensity
Temperature (Celsius)

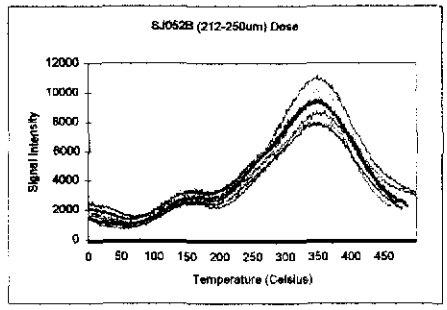
SJ052B (212-250um) Dose
Signal Intensity
Temperature (Celsius)

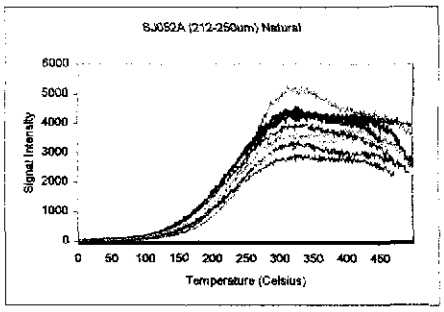
SJ052A (212-250um) Natural
Signal Intensity
Temperature (Celsius)

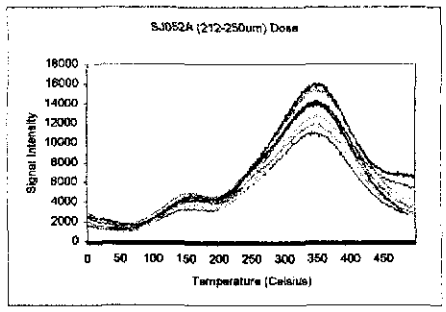
SJ052A (212-250um) Dose
Signal Intensity
Temperature (Celsius)

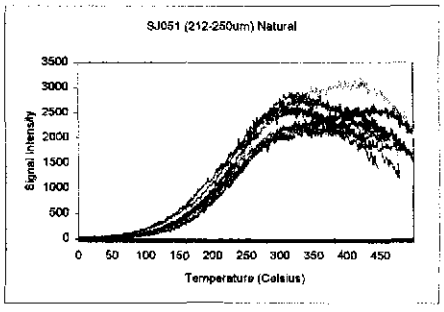
SJ051 (212-250um) Natural
Signal Intensity
Temperature (Celsius)

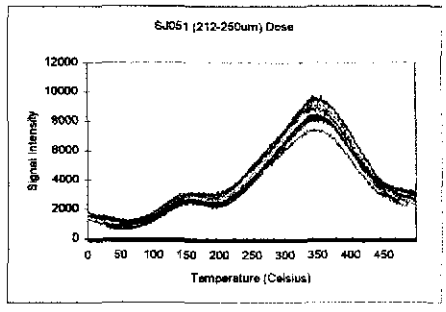
SJ051 (212-250um) Dose
Signal Intensity
Temperature (Celsius)

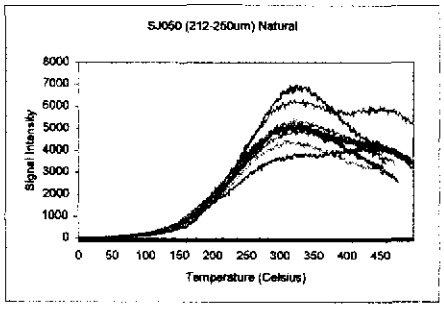
SJ050 (212-250um) Natural
Signal Intensity
Temperature (Celsius)

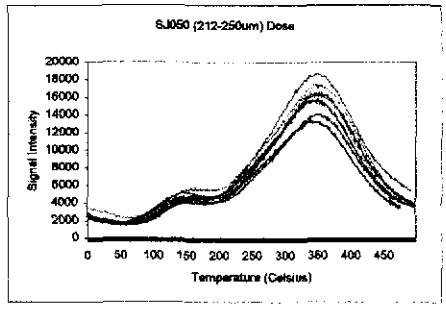
SJ050 (212-250um) Dose
Signal Intensity
Temperature (Celsius)

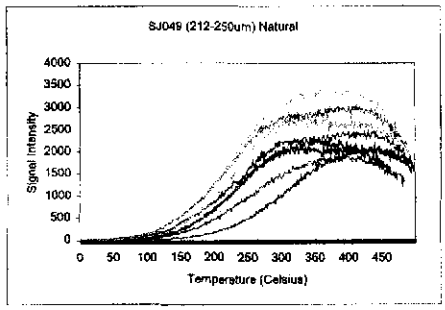
SJ049 (212-250um) Natural
Signal Intensity
Temperature (Celsius)

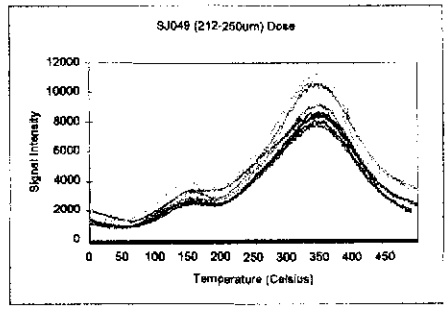
SJ049 (212-250um) Dose
Signal Intensity
Temperature (Celsius)

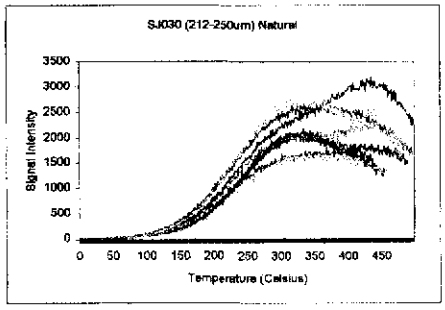
SJ030 (212-250um) Natural
Signal Intensity
Temperature (Celsius)

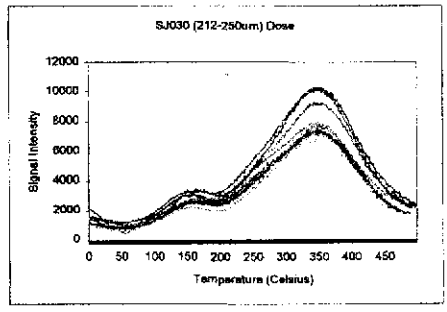
SJ030 (212-250um) Dose
Signal Intensity
Temperature (Celsius)

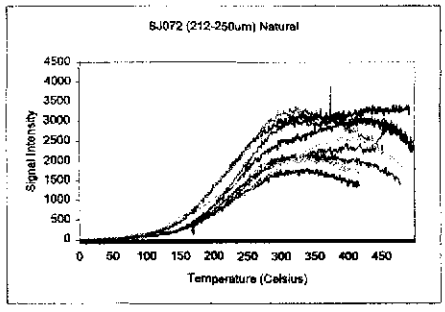
SJ072 (212-250um) Natural
Signal Intensity
Temperature (Celsius)

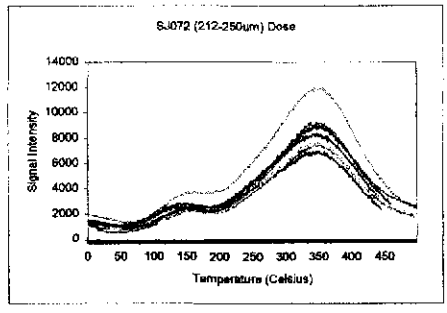
SJ072 (212-250um) Dose
Signal Intensity
Temperature (Celsius)

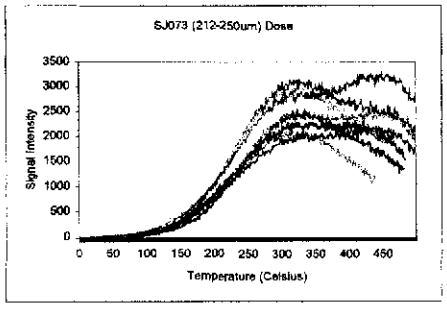
SJ073 (212-250um) Dose
Signal Intensity
Temperature (Celsius)

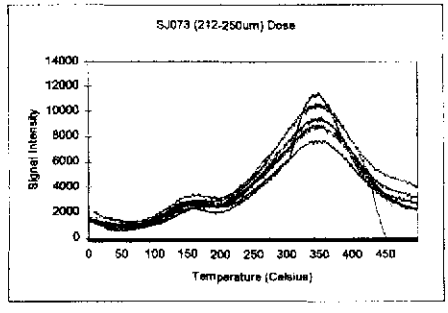
SJ073 (212-250um) Dose
Signal Intensity
Temperature (Celsius)

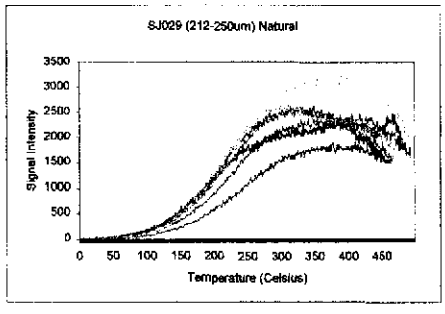
SJ029 (212-250um) Natural
Signal Intensity
Temperature (Celsius)

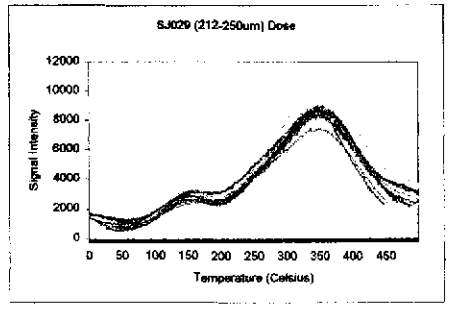
SJ029 (212-250um) Dose
Signal Intensity
Temperature (Celsius)

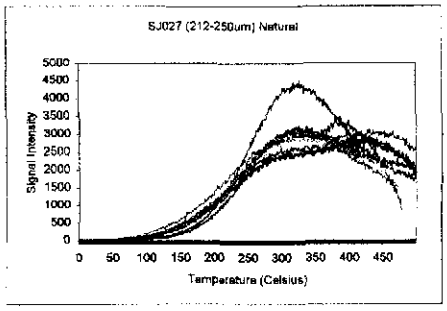
SJ027 (212-250um) Natural
Signal Intensity
Temperature (Celsius)

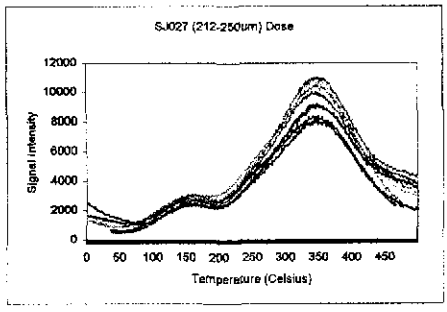
SJ027 (212-250um) Dose
Signal Intensity
Temperature (Celsius)

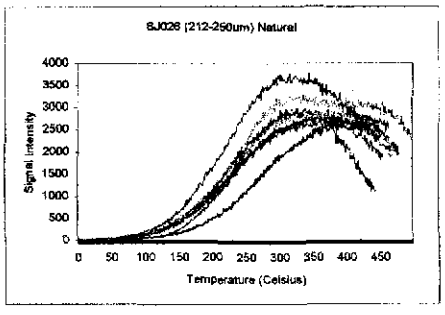
SJ026 (212-250um) Natural
Signal Intensity
Temperature (Celsius)

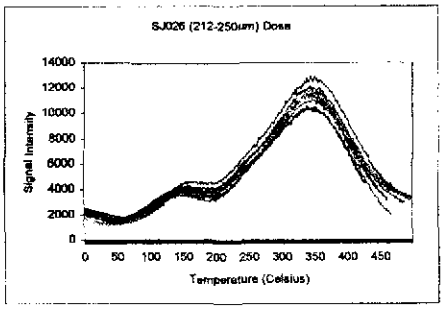
SJ026 (212-250um) Dose
Signal Intensity
Temperature (Celsius)

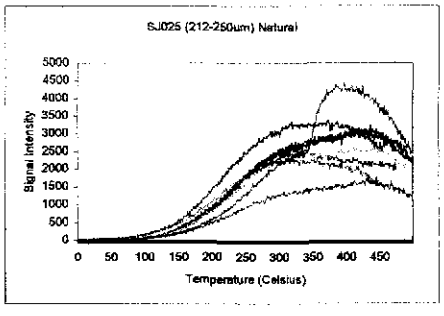
SJ025 (212-250um) Natural
Signal Intensity
Temperature (Celsius)

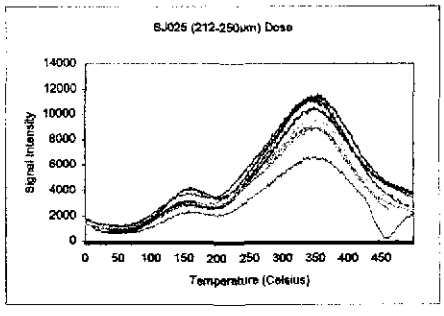
SJ025 (212-250um) Dose
Signal Intensity
Temperature (Celsius)

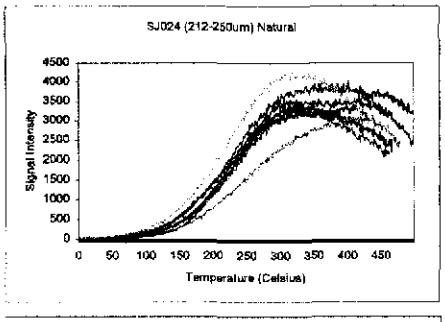
SJ024 (212-250um) Natural
Signal Intensity
Temperature (Celsius)

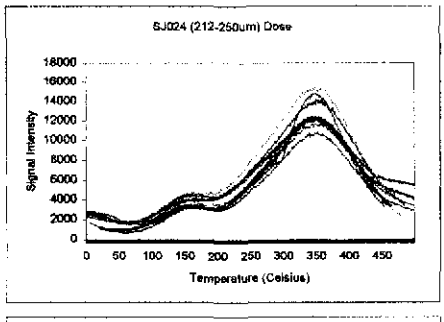
SJ024 (212-250um) Dose
Signal Intensity
Temperature (Celsius)

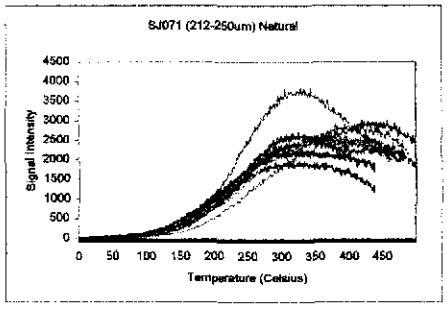
SJ071 (212-250um) Natural
Signal Intensity
Temperature (Celsius)

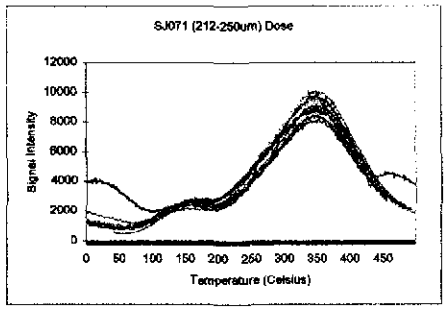
SJ071 (212-250um) Dose
Signal Intensity
Temperature (Celsius)

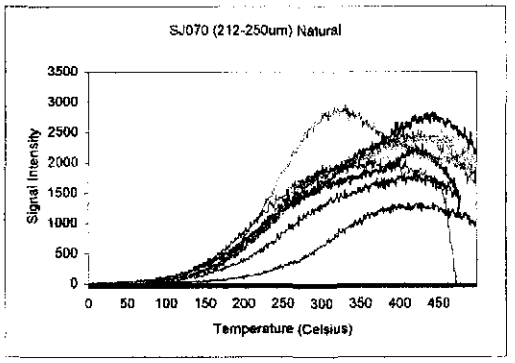
SJ070 (212-250um) Natural
Signal Intensity
Temperature (Celsius)

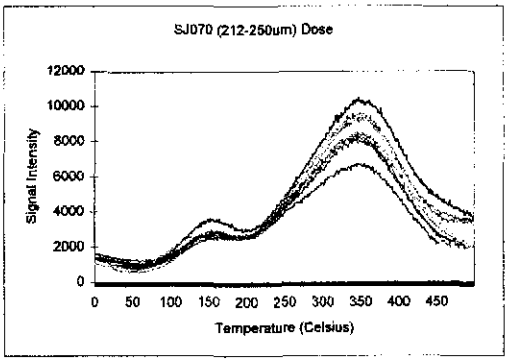
SJ070 (212-250um) Dose
Signal Intensity
Temperature (Celsius)

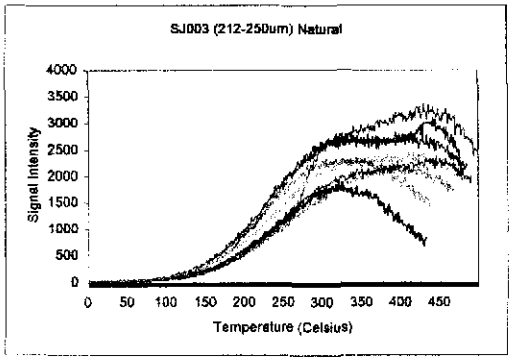
SJ003 (212-250um) Natural
Signal Intensity
Temperature (Celsius)

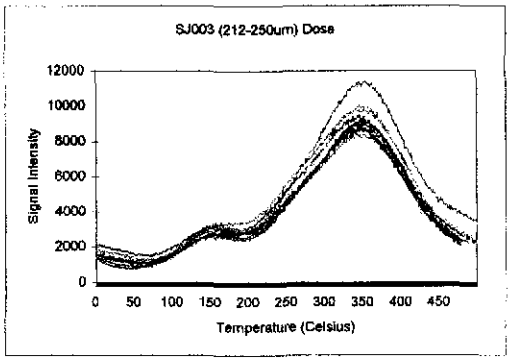
SJ003 (212-250um) Dose
Signal Intensity
Temperature (Celsius)

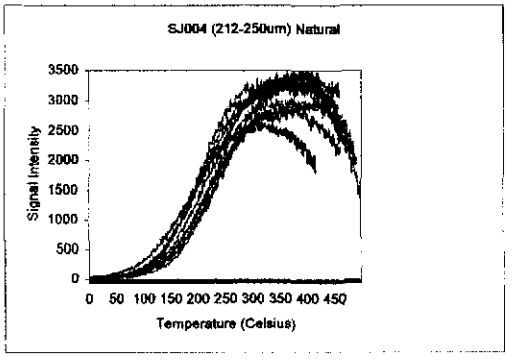
SJ004 (212-250um) Natural
Signal Intensity
Temperature (Celsius)

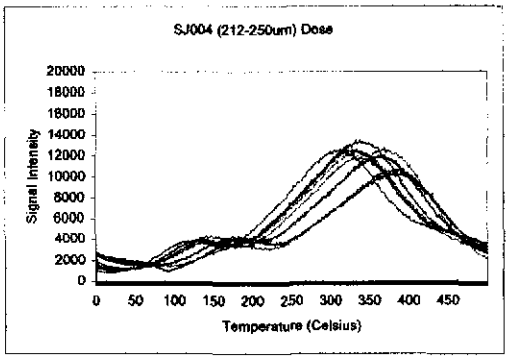
SJ004 (212-250um) Dose
Signal Intensity
Temperature (Celsius)

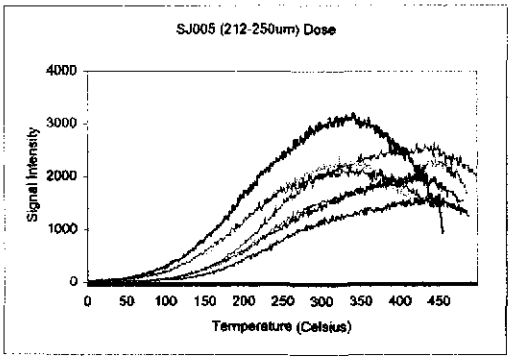
SJ005 (212-250um) Dose
Signal Intensity
Temperature (Celsius)

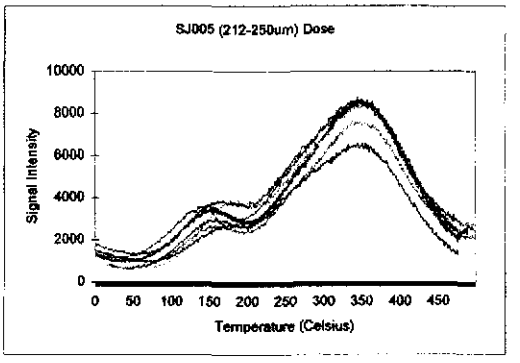
SJ005 (212-250um) Dose
Signal Intensity
Temperature (Celsius)

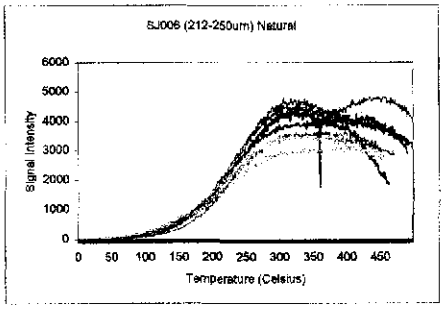
SJ006 (212-250um) Natural
Signal Intensity
Temperature (Celsius)

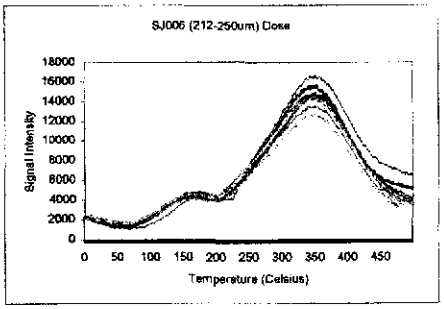
SJ006 (212-250um) Dose
Signal Intensity
Temperature (Celsius)

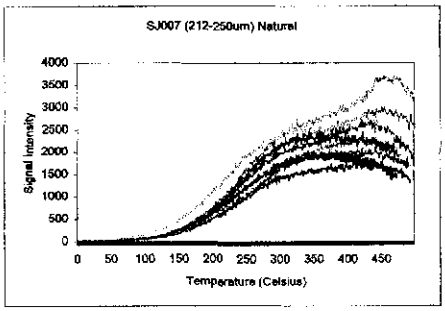
SJ007 (212-250um) Natural
Signal Intensity
Temperature (Celsius)

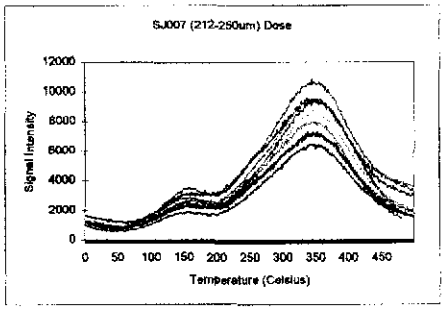
SJ007 (212-250um) Dose
Signal Intensity
Temperature (Celsius)

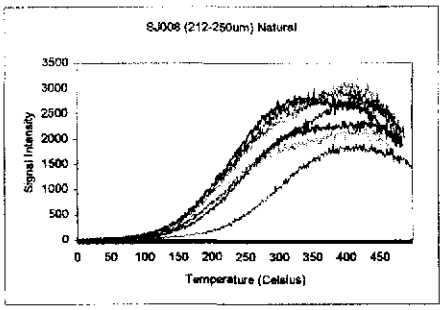
SJ008 (212-250um) Natural
Signal Intensity
Temperature (Celsius)

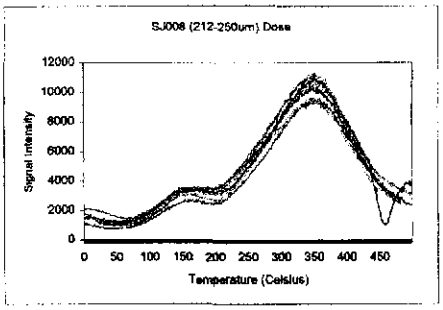
SJ008 (212-250um) Dose
Signal Intensity
Temperature (Celsius)

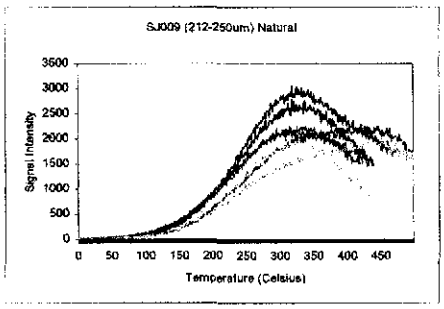
SJ009 (212-250um) Natural
Signal Intensity
Temperature (Celsius)

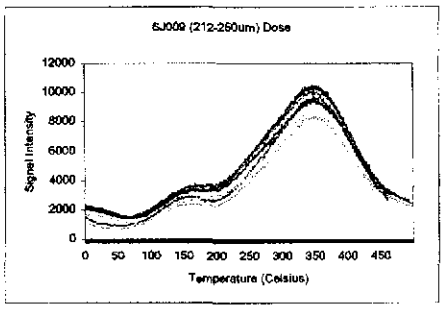
SJ009 (212-250um) Dose
Signal Intensity
Temperature (Celsius)

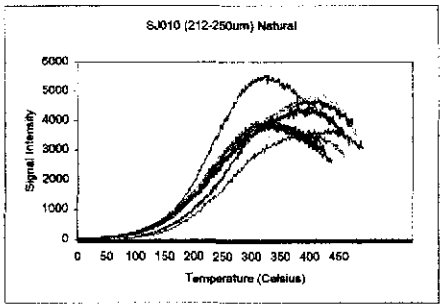
SJ010 (212-250um) Natural
Signal Intensity
Temperature (Celsius)

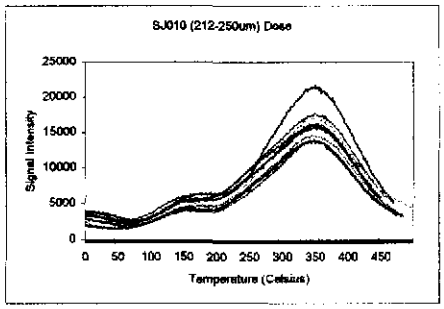
SJ010 (212-250um) Dose
Signal Intensity
Temperature (Celsius)

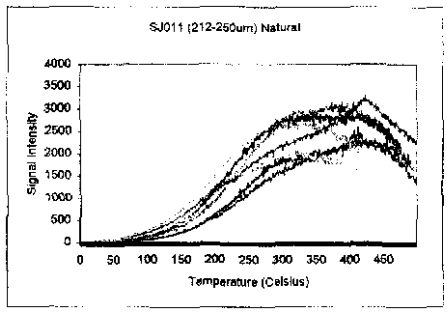
SJ011 (212-250um) Natural
Signal Intensity
Temperature (Celsius)

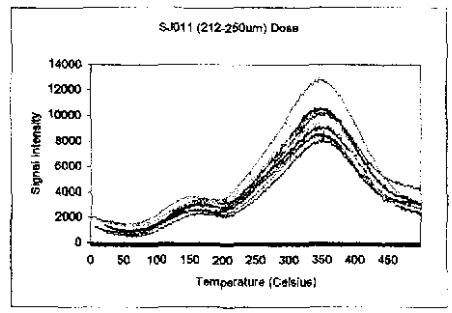
SJ011 (212-250um) Dose
Signal Intensity
Temperature (Celsius)

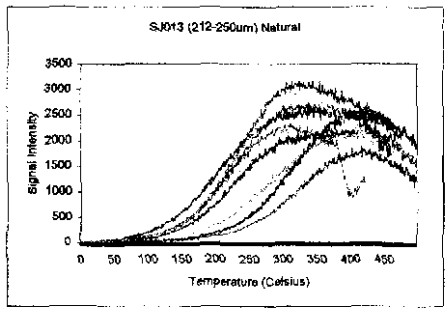
SJ013 (212-250um) Natural
Signal Intensity
Temperature (Celsius)

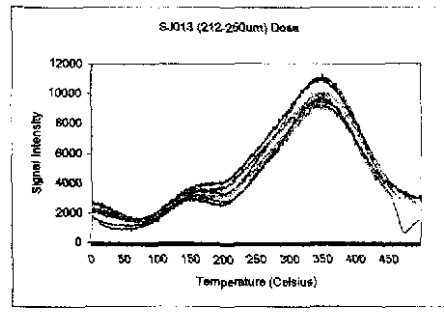
SJ013 (212-250um) Dose
Signal Intensity
Temperature (Celsius)

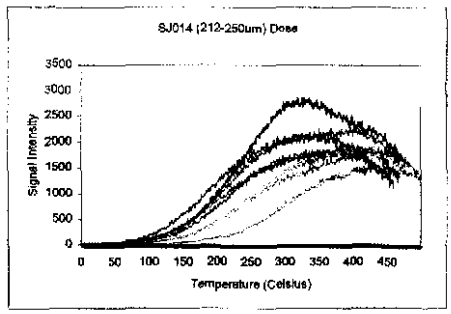
SJ014 (212-250um) Dose
Signal Intensity
Temperature (Celsius)

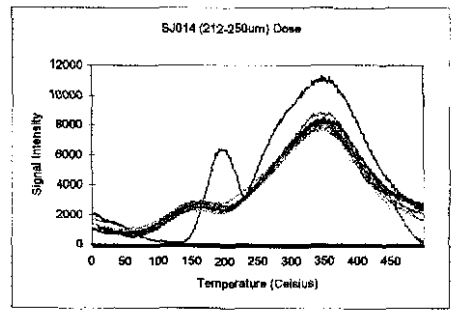
SJ014 (212-250um) Dose
Signal Intensity
Temperature (Celsius)

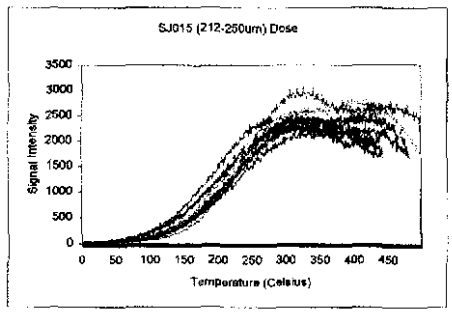
SJ015 (212-250um) Dose
Signal Intensity
Temperature (Celsius)

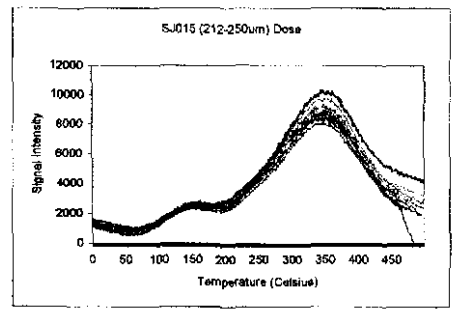
SJ015 (212-250um) Dose
Signal Intensity
Temperature (Celsius)

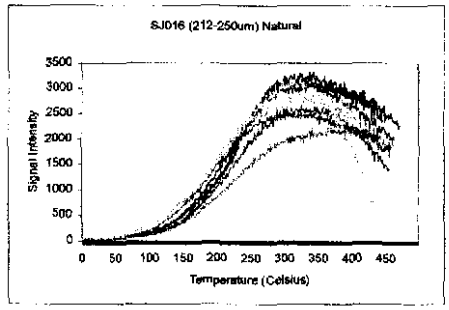
SJ016 (212-250um) Natural
Signal Intensity
Temperature (Celsius)

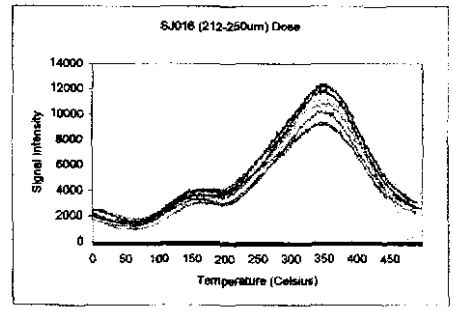
SJ016 (212-250um) Dose
Signal Intensity
Temperature (Celsius)

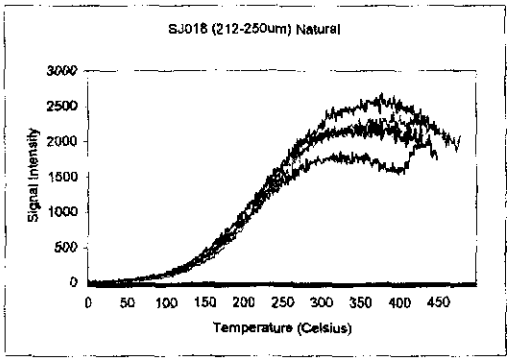
SJ018 (212-250um) Natural
Signal Intensity
3000
2500
2000
1500
1000
500
0
0 50 100 150 200 250 300 350 400 450
Temperature (Celsius)

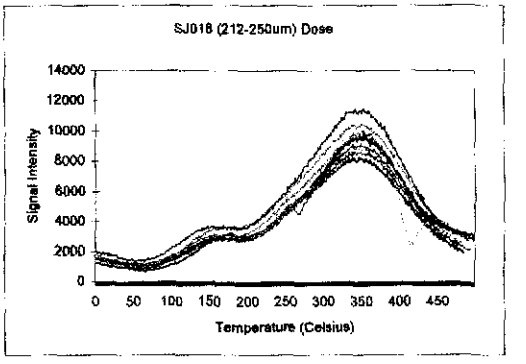
SJ018 (212-250um) Dose
Signal Intensity
14000
12000
10000
8000
6000
4000
2000
0
0 50 100 150 200 250 300 350 400 450
Temperature (Celsius)

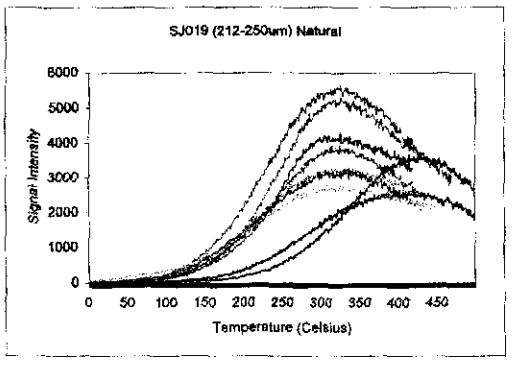
SJ019 (212-250um) Natural
Signal Intensity
6000
5000
4000
3000
2000
1000
0
0 50 100 150 200 250 300 350 400 450
Temperature (Celsius)

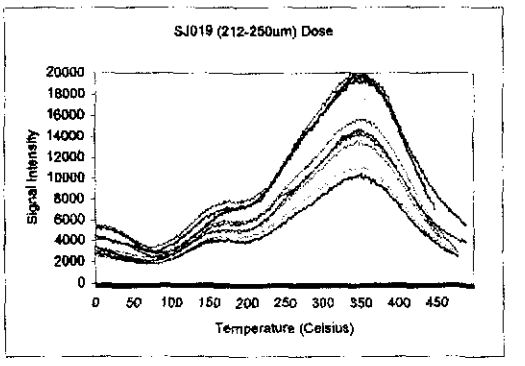
SJ019 (212-250um) Dose
Signal Intensity
20000
18000
16000
14000
12000
10000
8000
6000
4000
2000
0
0 50 100 150 200 250 300 350 400 450
Temperature (Celsius)